Université du Québec
Institut National de la Recherche Scientifique
Énergie Matériaux et Télécommunications

Enhanced fluorescence evanescent wave spectroscopy with integrated polymer optical waveguides

Par

Jalal Abdul-Hadi

Thèse présentée pour l'obtention du grade de
Philosophiae doctor (Ph.D.)
en sciences physique

Jury d'évaluation

Président du jury et examinateur interne	Prof. Jinyang Liang INRS-EMT
Examinateur externe	Prof. Narayanswamy Sivakumar Concordia University
Examinateur externe	Prof. Krishnan Venkatakrishnan Ryerson University
Directeur de recherche	Prof. Marc Andre Gauthier INRS-EMT
Codirecteur de recherche	Prof. Muthukumaran Packirisamy Concordia University

RÉSUMÉ

INTRODUCTION

La détection d'analytes biologiques et chimiques est requise dans plusieurs domaines de la biologie, biochimie et biomédicale en général. Les procédures standard pour la détection de ces analytes sont souvent longues et complexes. Heureusement, la recherche dans ce domaine a progressée grandement durant les deux dernières décennies et a permis la détection d'analytes biologiques et chimiques à l'aide de biocapteurs. Les biocapteurs sont des dispositifs analytiques comportant une partie de reconnaissance biologique qui permet de saisir sélectivement les bio-analytes à détecter. Un changement physico-chimique est provoqué suivant l'immobilisation des bio-analytes. Ce dernier est converti par un système de transduction à un signal mesurable par un dispositif électronique. Plusieurs types de transducteurs ont été développés, principalement des transducteurs utilisant des méthodes électrochimiques, optiques, piézoélectriques et thermiques comme intermédiaires pour la détection des bioéléments d'intérêts. Il est intéressant de noter que, comparés aux autres biocapteurs, les biocapteurs optiques offrent une sensibilité élevée, une détection rapide, une immunité aux interférences électromagnétiques, sont appropriés pour la miniaturisation et le multiplexage ainsi que la capacité de faire la détection sans marqueurs [3, 181-184]. Le mécanisme de détection de la plupart des biocapteurs optiques découle d'une propriété de la lumière lorsqu'elle est confinée dans un guide d'onde optique, appelé onde évanescente. En effet, décrite pour la première fois par Hirschfeld [185], l'onde évanescente apparaît après la réflexion totale d'une lumière incidente à la frontière entre deux milieux diélectriques, la lumière incidente se propageant à partir d'un milieu diélectrique à indice élevé et se reflétant totalement à la frontière avec le milieu diélectrique avec indice de réfraction inférieur. L'onde évanescente est un champ qui se fane de manière exponentielle à l'intérieur du milieu d'indice inférieur et sert à sonder les changements à proximité de la surface de la plate-forme. Les fibres optiques ont été les

premières et encore largement utilisées plates-formes de détection pour la bio-détection optique [1]. En effet, leur capacité à effectuer la détection à longue distance avec une bonne flexibilité géométrique est attrayante pour de nombreuses applications biomédicales [186]. Cependant, le principal inconvénient des fibres optiques est leur fragilité. En particulier lorsque leur gaine est retirée ou soumise à un effilage extrême pour permettre au cœur d'être exposé à un échantillon, par exemple pour une détection par absorption [165, 187] ou une détection par fluorescence [188, 189]. Les guides d'ondes planaires sont une alternative aux fibres optiques car ils fournissent une plate-forme plus robuste. De plus, ils permettent la miniaturisation et la structuration de matériaux biologiques tels que des anticorps ou des antigènes pour des analyses multi-analytique en temps réel. Différentes méthodes optiques ont été utilisées avec le guide d'onde planaire comme plate-forme pour la détection biologique, telles que la résonance de plasmons de surface (RPS) [190], la résonance de plasmons de surface localisée (RPSL) [191], l'émission couplée de plasmons de surface (ECPS) [192], la symétrie inverse [193], la spectroscopie de fluorescence par ondes évanescentes [194], etc. La spectroscopie de fluorescence à ondes évanescentes combine, entre autres, le sondage qui est restreint à la surface du champ évanescent avec la sensibilité et la spécificité élevées fournies par les fluorophores. Bien que les guides d'ondes planaires se soient révélés adaptés à la détection biologique et à la miniaturisation, ils sont généralement intégrés dans une configuration complexe et volumineuse [195]. Pour miniaturiser complètement les composants et traitements optiques, ainsi que pour incorporer un système micro-fluidique, les guides d'ondes rectangulaires (guides d'ondes bidimensionnels) conviennent mieux. En effet, les guides d'ondes rectangulaires peuvent être conçus dans une large gamme de structures optiques pour les applications de bio-détection telles que les résonateurs à micro-anneaux [196], les résonateurs à réseau de Bragg [197], les coupleurs directionnels [198], les interféromètres [87], etc. Jusqu'à maintenant les matériaux à base de silicium ont été les plus populaires pour la fabrication de composants optique intégrés [113] et ont également été utilisés pour la fabrication de guides d'ondes rectangulaires dans des capteurs optiques intégrés à ondes évanescentes [114-116]. Bien que les matériaux inorganiques composent la plus grande partie des composants optiques intégrés, les propriétés particulières des matériaux

polymères en font un support intéressant pour l'optique intégrée [117]. Leur procédé de fabrication plus simple et leur facilité d'intégration comparés aux matériaux minéraux en font un choix attrayant, en particulier pour l'industrie des télécommunications optiques [118]. En effet, les polymères peuvent être fabriqués par embossage [119] et estampage [120], ce qui offre la possibilité d'une fabrication bon marché et à grand volume. D'autres méthodes de fabrication ont également été utilisées pour des polymères tels que la photolithographie directe [86], l'ablation au laser [121], la gravure ionique réactive (*reactive ion etching*, RIE) [122], le "dip-floating" [123], l'écriture par faisceau d'électrons (*e-beam*) [124], etc. Comparés à la silice et au silicium, les polymères ont une faible conductivité thermique mais un coefficient thermo-optique élevé, ce qui est idéal pour l'actionnement thermique [125]. Cette propriété permet de développer des dispositifs thermo-optiques de hautes performances [126-128]. Une autre propriété intéressante est que les guides d'ondes en polymère ont la capacité d'être flexibles. Cette caractéristique unique a été utilisée à juste titre pour développer des interconnexions optiques flexibles [129, 130] ou des capteurs de contrainte [131, 132] avec des matériaux polymères. De plus, les polymères ont été utilisés dans les biocapteurs optiques comme matériau pour fabriquer différents types de plates-formes de détection telles que des guides d'ondes planaires [133], guides d'ondes à nervure inversée [134], micro-résonateurs [135], interféromètres [136], guides d'ondes rectangulaires [74], etc. En ce qui concerne les mesures de bio-détection, les analytes contaminent la plate-forme de détection après la liaison, ce qui peut altérer la réponse des futures analyses. Par conséquent, comme les polymères sont peu coûteux et faciles à fabriquer, ils conviennent parfaitement aux biocapteurs jetables [137]. Une grande variété de matériaux polymères convient aux dispositifs optiques intégrés tels que les acrylates [138], les polyimides [139], les polycarbonates [140], les oléfines [141] et les époxydes [142]. SU-8, une résine photosensible négative à base d'époxy développée en 1989 par IBM, s'est révélée très utile comme matériau de choix pour les guides d'ondes optiques intégrés en raison de sa transparence sur une large gamme de longueurs d'onde [86], sa haute résolution [143], sa résistance mécanique [144] et sa biocompatibilité [145, 146] à des fins de détection biologique. Pour cette raison, le SU-8 sera utilisé dans ce travail comme matériau de base des guides d'ondes.

Pour résumé, notre motivation pour cette thèse découle du fait que les technologies optiques de bio-détection par détection à fluorescence offrent, pour la plupart, une grande sensibilité et des applications utiles. Toutefois, en termes de miniaturisation, de production en série et d'analyse au d'intervention, seuls les guides d'ondes planaires et rectangulaires se distinguent. L'un des inconvénients des guides d'ondes planaires est que le couplage de la lumière à l'entrée ou à la sortie est encombrant et ne permet pas une intégration planaire totale de tous les composants optiques. De plus, sa structure intrinsèque ne permet pas beaucoup de flexibilité en termes de mise en forme géométrique. Au contraire, les guides d'ondes rectangulaires conviennent parfaitement à la fabrication planaire monolithique, y compris l'intégration d'autres composants optiques, au couplage optique sans alignement et à la conception de microstructures élaborées pour la manipulation optique. Ces caractéristiques sont favorables aux systèmes de laboratoire sur puce, qui peuvent être intégrés à la micro-fluidique pour la distribution des solutions biochimiques aux plates-formes de détection. Le matériau polymère choisi pour le noyau des guides d'ondes pour cette thèse était la résine photosensible SU-8 polymérisée pour ses propriétés avantageuses pour nos applications. En effet, nos travaux portent sur la lumière visible et le SU-8 présente une très bonne transparence pour les longueurs d'onde comprises entre ~ 400 et 800 nm [78]. En outre, le SU-8 permet une haute résolution de fabrication [79, 80], ce qui est crucial pour de faibles pertes de propagation. Et puisque les guides d'ondes ont été soumis à un rinçage et à des manipulations rigoureuses, la solidité structurelle remarquable du SU-8 [81] était essentielle pour effectuer les tâches expérimentales. De plus, la biocompatibilité du SU-8 permettait d'utiliser des échantillons biologiques pour la bio-détection [82]. Pour toutes ces raisons, les guides d'ondes rectangulaires en SU-8 ont été préférés pour effectuer ce travail qui se concentre sur l'amélioration des performances de la spectroscopie de fluorescence à ondes évanescentes avec des guides d'ondes en polymère à des fins de bio-détection.

Avant de tester les guides d'ondes SU-8 pour la spectroscopie de fluorescence à ondes évanescentes, la fabrication et la caractérisation des guides d'ondes en SU-8 ont été effectuées pour des substrats de silice et de quartz.

FABRICATION ET CARACTÉRISATION DES GUIDES D'ONDES EN SU-8 SUR SUBSTRATS DE SILICE ET QUARTZ

La fabrication et la caractérisation de guides d'ondes optiques SU-8 monomode et multimode ont été effectuées par plusieurs groupes [86, 91-95]; bien que la plupart de ces études utilisent des substrats en dioxyde de silicium, en verre ou en polymère. Cependant, des substrats alternatifs tels que le quartz fondu offrent d'autres avantages. Étant donné que le quartz fondu, par rapport à d'autres verres, est constitué uniquement de silice, il représente un substrat alternatif intéressant pour les guides d'ondes optiques. Contrairement à l'épaisse couche d'oxyde de silicium sur une plaquette de silicium, cela simplifie le processus et évite l'absorption optique par le substrat de silicium sous-jacent. De plus, il offre un meilleur confinement puisque son indice de réfraction est légèrement inférieur à celui de l'oxyde de silicium, offre une plate-forme plus robuste et est complètement transparent (possibilité d'illuminer les guides d'ondes optiques à partir de la base en cas de microscopie à fluorescence ou de bio-détection). De plus, un substrat d'indice de réfraction plus faible contribue à augmenter la profondeur de pénétration du champ évanescent dans la gaine, cette propriété est utilisée dans une plus grande mesure par le guide d'ondes à symétrie inverse pour détecter les bactéries et les cellules vivantes [96]. Cette section présente le protocole de fabrication de guides d'ondes SU-8 de 10 × 5 µm avec de l'air comme gaine sur un substrat de quartz fondu par photolithographie UV. Les pertes de propagation optique à 635 nm sont rapportées et comparées à des guides d'ondes équivalents fabriqués en utilisant le protocole standard sur un substrat en dioxyde de silicium.

Les guides d'ondes SU-8/silice ont été fabriqués suivant les indications du fabricant pour une épaisseur de 5 µm. Qui se résume à deux sessions de spin coating à 500 rpm pour 10s et à 3000 rpm pour 30s. Suivi d'un *soft bake* (SB) (pré-cuisson) à 65˚C pour 2 min et à 95˚C pour 5 min. Ensuite, une exposition UV (9 mW·cm^{-2}) de 18 s a permis le transfert du motif du masque à la résine. Après cela, deux sessions de *post-exposure bake* (PEB) (cuisson après exposition) ont eu lieu à 65˚C pour 1 min et à 95˚C pour 2 min. Finalement,

le développement du motif c'est fait par l'immersion de la résine dans le développeur pour SU-8 pour 2 min et un *hard bake* (HB) (recuit) à 150˚C pour 1h.

À notre connaissance, il s'agit de la première étude portant sur la préparation de guides d'ondes SU-8 sur un substrat de quartz fondu. Une plaquette de quartz fondu de quatre pouces de diamètre et d'un mm d'épaisseur a été choisie comme substrat et la résine SU-8 a été choisie comme matériau du cœur pour les guides d'ondes. Pour assurer une adhérence et une uniformité optimales de la résine photosensible, la surface du quartz devait être modifiée. En effet, une surface de quartz fondu contient moins de groupes OH que la silice, ce qui la rend plus hydrophobe. Cela a entraîné une plus grande contraction de la résine photosensible après le revêtement par centrifugation. Pour augmenter la mouillabilité de la surface, la plaquette de quartz fondu a été hydroxylée par exposition à un plasma d'oxygène pendant 1 min. Tout en rendant la surface de quartz fondu plus hydrophile, le traitement au plasma d'oxygène a diminué l'adhérence de la résine en raison de l'eau adsorbée, ce qui a entraîné des trous dans la résine après le revêtement par centrifugation et un relâchement des guides d'ondes après développement. Afin de réduire le caractère hydrophile, la surface a été chauffée à 150℃ pendant 2 minutes et demie sur une plaque chauffante après le traitement au plasma à l'oxygène. En utilisant les mêmes conditions de revêtement par centrifugation que pour le substrat en oxyde de silicium, la résine se répartit uniformément sur la surface. Après le revêtement par centrifugation, la résine photosensible a été développée comme pour le substrat en dioxyde de silicium, bien que la délamination des guides d'ondes ait été observée et accompagnée de fissuration. Comme le quartz fondu et le dioxyde de silicium ont presque les mêmes coefficients de dilatation thermique, ce phénomène ne devrait pas être à l'origine de la fissuration. Cette adhésion suggérée entre le polymère et la surface de quartz fondu était la cause de ce phénomène. En effet, un problème similaire a été rapporté par Keller *et al.* [97] pour les films minces SU-8 sur des plaquettes de silicium. L'approche adoptée par les auteurs pour éviter la fissuration consistait à promouvoir une densité de réticulation plus élevée de la résine en augmentant la concentration de solvant. Une façon d'y parvenir est de réduire la température du SB de 65℃ à la température ambiante et de la maintenir sur une période plus longue. La délamination, qui est principalement causée par le stress de la polymérisation, peut également être

réduite en abaissant la température du PEB (T_{PEB}) et en augmentant sa durée. Tous ces paramètres, y compris les conditions d'exposition, doivent être équilibrés pour conserver une bonne résolution et ont été optimisés empiriquement. La procédure optimisée, pour l'épaisseur de guide d'onde désirée (5 µm) est la suivante : après revêtement par centrifugation, le substrat revêtu de SU-8 a été laissé à température ambiante (23 °C) pendant 225 min. Pour empêcher la résine de coller au masque, elle a été séchée pendant 30 s en maintenant la plaquette avec le côté de la résine face vers le bas à une distance de 2 pouces de la plaque chauffante (65 °C), de sorte que seule la surface sèche. Ensuite, le masque a été fixé dans l'alignement du masque, la résine a été exposée à la lumière ultraviolette pendant 15s, suivie d'un PEB consistant à chauffer la plaquette à partir de la température ambiante jusqu'à 55 °C à une vitesse de 5 °C·min^{-1} et en maintenant cette température pendant 65 minutes. Pour éviter tout stress thermique, la plaquette a été refroidie directement sur la plaque chauffante pendant 15 min, après avoir éteint la plaque chauffante. Le motif a été développé pendant 2 min dans le développeur de SU-8 et rincé. Cela a été suivi d'un HB à 150 °C pendant 1 h, comme pour le protocole des guides d'ondes SU-8 sur silice.

Le procédé de fabrication pour les guides d'ondes SU-8/quartz a procuré des parois latérales plus lisses et a préservé les dimensions anticipées du masque pour ces derniers comparativement aux guides d'ondes SU-8/silice, comme observé sur les images SEM à la Figure 2.4. La performance des guides d'ondes SU-8/quartz et SU-8/silice pour les pertes de propagation optique a été testée avec la méthode "cut-back" pour une lumière de longueur d'onde λ = 635 nm pour la polarisation TE et TM. Cette méthode requiert de mesurer l'intensité de la lumière de sortie pour différentes longueurs de guide d'ondes. Les résultats sont présentés à la Figure 2.7. Comme attendue, la plus faible rugosité des guides d'ondes SU-8/quartz a entraîné moins de perte de propagation optique comparativement aux guides d'ondes SU-8/silice. En effet, des pertes optiques pour la polarisation TE de 0,58 dB·cm^{-1} et 1,44 dB·cm^{-1} et pour la polarisation TM de 0,73 dB·cm^{-1} et 1,16 dB·cm^{-1} ont été mesurées pour les guides d'ondes SU-8/quartz et SU-8/silice, respectivement. Aussi, le procédé de fabrication pour les guides d'ondes SU-8/quartz a résulté à moins de stress structurel sur les guides d'ondes SU-8/quartz comparativement aux guides d'ondes SU-8/silice. Ce qui a eu pour effet d'augmenter l'indice de réfraction

du SU-8 pour le procédé SU-8/quartz comparativement au procédé SU-8/silice en raison de son état plus détendu [105]. Comme révélées par des mesures d'ellipsométrie, Figure 2.8.

En conclusion, la caractérisation optique des guides d'ondes SU-8/quartz a révélé des pertes de propagation optique plus faibles et une augmentation de l'indice de réfraction du SU-8 par rapport aux guides d'ondes SU-8/silice. De plus, il a été mesuré que le substrat de quartz avait un indice de réfraction inférieur à celui de la couche de silice. Différents indices de réfraction pour les cœurs et les substrats se traduiront par une asymétrie différente.

La prochaine section aura pour objet d'étudier les performances des deux guides d'ondes en tenant compte des différentes caractéristiques de chacun. En effet, différentes pertes de propagation et asymétries entre les guides d'ondes SU-8/quartz et SU-8/silice affecteront la fluorescence de sortie des guides d'ondes susmentionnés.

SPECTROSCOPIE DE FLUORESCENCE PAR COUPLAGE D'ONDES ÉVANESCENTES DES GUIDES D'ONDES SU-8/SILICE ET SU-8/QUARTZ

Divers procédés ont été développés pour augmenter la sensibilité de la spectroscopie de fluorescence à ondes évanescentes de guides d'ondes plans ou rectangulaires tels que des réseaux [147], des microcavités [148], une fluorescence renforcée par plasmons de surface [149], etc. Comme mentionné précédemment, un nouveau procédé de fabrication de guides d'ondes SU-8 sur quartz mis au point par Abdul-Hadi *et al.* [150] a démontré des pertes de propagation optique plus faibles et un indice de réfraction accru du cœur de SU-8. Ces caractéristiques ont été exploitées pour augmenter la sensibilité de la spectroscopie de fluorescence à ondes évanescentes. Cette section vise à évaluer l'effet du nouveau procédé de fabrication du guide d'onde SU-8/quartz [150] sur la spectroscopie de fluorescence à ondes évanescentes et à le comparer à un guide d'onde SU-8/silice fabriqué selon le protocole standard. Nos travaux précédents étaient axés sur le développement de guides d'ondes en polymère à faibles pertes optiques. De plus, l'indice de réfraction du cœur SU-8 sur quartz était plus élevé en raison des particularités du processus de fabrication. Aussi, avec un substrat d'indice de réfraction plus faible, le guide d'ondes SU-8/quartz présente un paramètre d'asymétrie inférieur à celui du guide d'ondes SU-8 / silice. Ces caractéristiques du guide d'onde SU-8/quartz obtenues à partir du processus de fabrication optimisé de nos travaux précédents seront utilisées pour augmenter le rendement de fluorescence de la spectroscopie de fluorescence à ondes évanescentes. Afin d'étudier l'effet des paramètres de conception sélectionnés sur la sensibilité des plates-formes de détection, des simulations 3D FDTD avec des dipôles de courant émetteurs sans dimension à orientation et en phase aléatoire pour les guides d'ondes SU-8 sur des substrats de quartz et de silice ont été utilisées pour comparer le couplage de fluorescence des deux plates-formes de détection. De plus, une méthode de calcul combinant la méthode de l'indice effectif à l'approche de propagation modale développée par Srivastava *et al.* [157] a été utilisée pour calculer l'efficacité de la collecte de fluorescence pour des sources proches d'une surface de guide d'ondes planaire, mais

pour des paramètres variants dont l'indice de réfraction du cœur et du substrat et les dimensions du guide d'ondes.

Une surface diélectrique à proximité d'un dipôle rayonnant, dans notre cas un fluorophore, modifie la distribution angulaire de la lumière émise [152] tout en provoquant un rétrocouplage de la fluorescence dans le milieu diélectrique [153]. La lumière qui se propage dans le diélectrique se situe en partie sous l'angle critique, dit «lumière autorisée» [154], et en partie au-dessus de l'angle critique, appelé «lumière interdite» [154]. La lumière se propageant au-dessus de l'angle critique peut être guidée si une autre couche est ajoutée en tant que substrat si son indice de réfraction est inférieur à la couche diélectrique, sachant que le dipôle est également situé dans un milieu d'indice inférieur à la couche diélectrique. Cette disposition s'appelle un guide d'ondes (Figure 3.4), où la couche diélectrique joue le rôle de couche de guide pour la lumière. Dans ce travail, les fluorophores sont liés à une protéine BSA et dilués dans une solution tampon (PBS). Étant donné que la solution tampon était principalement composée d'eau, son indice de réfraction est d'environ 1,33. L'Alexa Fluor 647 a été choisi comme colorant fluorescent lequel pouvant être excité avec une lumière de 635 nm et ayant un pic d'émission à une longueur d'onde d'environ λ = 671 nm. La molécule BSA, dans ce travail, peut être vue comme un ellipsoïde prolongé avec des diamètres de 14 nm et 4 nm de taille [155] avec un degré de marquage de 4. Par conséquent, la distance entre le fluorophore et l'interface PBS-SU-8 est approximativement 10 nm. La lumière dans la zone interdite est guidée à travers, par exemple, le guide d'ondes SU-8/quartz formé par la solution tampon, le cœur SU-8 et le substrat de quartz, Figure. 3.4. Il a été démontré que lorsqu'un fluorophore est excité à proximité d'un milieu à indice de réfraction élevé, il émet des ondes évanescentes qui sont transformées en ondes planes se propageant par le milieu [153]. L'émission du fluorophore est couplée au champ évanescent du ou des modes guidés (Figure 3.4). Ce phénomène est appelé couplage évanescent et est utilisé pour détecter des entités biologiques marquées et immobilisées sur le guide d'ondes en mesurant la lumière de fluorescence guidée à la sortie du guide d'ondes. L'efficacité de la collecte de fluorescence donne la proportion de la lumière provenant des sources capturées et guidées par le guide d'ondes.

La méthode numérique 3D FDTD a été utilisée pour évaluer la différence relative des rendements de collecte de fluorescence entre les guides d'ondes avec une couche fluorescente Alexa-647 de 10 nm située au sommet ou sur les côtés des guides d'ondes. Tout d'abord, une étude avec un modèle 3D FDTD des guides d'ondes SU-8/quartz et SU-8/silice avec des fluorophores simulés proches de la surface des guides d'ondes a été réalisée pour évaluer l'efficacité de la collecte à la sortie du guide. Des dipôles émetteurs sans dimension ont été utilisés pour simuler les fluorophores Alexa-647. Comme mentionné ci-dessus, la molécule de BSA a été estimée à une taille de 10 nm. Les dipôles étaient alors situés à une distance de 10 nm des guides d'ondes et également espacés les uns des autres d'une distance de 10 nm. Les fluorophores simulés étaient uniformément distribués d'une extrémité à l'autre de la partie supérieure et latérale des guides d'ondes. La simulation a été réalisée avec le logiciel FDTD *Fullwave* de Synopsis. Recouvrir avec des fluorophores simulés de l'extrémité gauche à l'extrémité droite le long du haut et de bas en haut pour les côtés du guide d'onde nécessiterait respectivement 1001 et 1002 fluorophores simulés, s'ils sont espacés les uns des autres d'une distance de 10 nm. Cette quantité de fluorophores simulés dépassait les limites du logiciel. Seuls 32 fluorophores simulés sont autorisés à la fois. Une série de simulations avec chaque simulation ayant le nombre maximum de fluorophores simulés a été réalisée jusqu'à couvrir complètement une ligne de 10 µm le long du haut ou bien les deux lignes de 5 µm sur les côtés des guides d'ondes. (Plus de détails sont présentés à la section 3.5 et à la Figure 3.6). Les rapports entre les puissances moyennes de quatre distributions différentes de phases et de dipôles d'orientation choisis de manière aléatoire pour le dessus, les côtés et le dessus /côtés des guides d'ondes SU-8/quartz et SU-8/silice sont présentés dans le Tableau 3.2.

D'après les résultats du Tableau 3.2, le guide d'ondes SU-8/quartz présente une efficacité de collecte de la fluorescence plus élevée que le guide d'ondes SU-8/silice pour tous les côtés des guides d'ondes. Si le guide d'ondes rectangulaire est approximé par 2 guides d'ondes planaires, le guide d'ondes planaire d'indice le long de l'axe des y aura un paramètre d'asymétrie TE / TM [151] de 0,88 / 1,78 pour le guide d'ondes SU-8 sur quartz et 0,98/1,94 8 pour le guide d'onde SU-8 sur silice. Les paramètres d'asymétrie des guides d'ondes planaires variant d'indice le long de l'axe x seront nuls. Il a été montré

dans [157] qu'une asymétrie plus basse augmente l'efficacité de la collecte de fluorescence. Par conséquent, l'efficacité de collecte était supérieure pour le dessus du guide d'ondes. Bien que les paramètres d'asymétrie soient nuls pour les côtés des guides d'ondes, l'indice du cœur du guide d'ondes SU-8/quartz est supérieur à l'indice du cœur du guide d'ondes SU-8/silice. Il a également été montré dans [158] qu'un cœur d'indice plus élevé augmente l'efficacité de la collecte de fluorescence. En effet, un indice de cœur plus élevé augmente le couplage de la lumière des fluorophores émetteurs en augmentant le confinement de la lumière près de l'interface cœur/gaine. Tandis qu'un indice de substrat plus élevé entraîne plus de puissance des modes dans le substrat, ce qui entraîne moins de puissance dans la gaine résultant en une diminution de l'efficacité de la collecte de fluorescence. Le guide d'ondes SU-8/quartz fabriqué selon le nouveau procédé de [150] présente à la fois un indice de cœur supérieur et un indice de substrat inférieur à celui de SU-8/silice, ce qui en fait un meilleur choix pour la spectroscopie de fluorescence à ondes évanescentes.

La dérivation du calcul de la collecte de fluorescence pour des sources ponctuelles émettrices à la proximité de la surface de guides d'ondes planaires a été prise de [157]. Cela a résulté à une efficacité de collecte de fluorescence pour le mode TE pour une épaisseur de couche fluorescente t_c équivalente à l'équation 4.6. En substituant le champ électrique transversal $\vec{E}_\nu$ par le champ magnétique transversal $\vec{H}_\nu$ et la fonction de mode du champ magnétique dans la direction y pour les trois régions du guide d'onde prises dans [176], l'efficacité de collecte de la fluorescence pour le mode TM pour une épaisseur de couche fluorescente t_c équivaut à l'équation 4.7. Étant donné que des guides d'ondes rectangulaires étaient utilisés dans ce travail, le calcul de l'efficacité de la collecte de la fluorescence a été effectué à l'aide de la méthode de l'indice effectif. La méthode de l'indice effectif [179] suppose que le champ électromagnétique, avec l'utilisation de la séparation de variable, peut être exprimé par l'équation 4.11. En insérant Eq.4.11 dans l'équation scalaire de Helmholtz et en y introduisant la variable $k_0{}^2 n_{eff}^2(y)$, l'équation résultante peut être séparée en deux équations indépendantes qui ressemblent aux équations de deux guides d'ondes en plaque unidimensionnelles, voir équation 4.12 & 4.13. Le guide d'ondes rectangulaire sera ensuite traité comme deux guides d'ondes en

plaque distincts pour lesquels l'indice effectif du premier guide d'ondes en plaque sera utilisé comme indice de réfraction du cœur du second guide d'ondes en plaque. Après avoir trouvé l'indice effectif du premier guide d'ondes en plaque avec l'équation 4.12, il était possible d'évaluer l'efficacité de collecte de fluorescence pour les modes TE ou TM pour une couche fluorescente sur le dessus ou sur le côté du guide d'onde. En effet, l'efficacité de collecte de fluorescence est similaire à l'Eq.4.6 & Eq.4.7 mais avec les fonctions de mode de Eq.4.13 avec la variable x ou y dépendamment si la couche fluorescente se trouvant au sommet ou sur le côté du guide d'ondes. La méthode de l'indice effectif a été préférée à la méthode numérique 3D FDTD pour cette analyse tridimensionnelle de l'efficacité de la collecte de la fluorescence avec la variation des paramètres du guide d'onde, car la méthode numérique 3D FDTD prendrait énormément de temps à cet égard. Néanmoins, les valeurs absolues des rendements de collecte obtenus avec cette méthode ne doivent pas être considérées comme très précises, car elles ne prennent pas en compte les nœuds et anti-nœuds des modes pour une analyse tridimensionnelle rendant le champ évanescent discontinu à l'interface cœur-gaine. De plus, comme le rapport largeur/hauteur est de 2 (10 × 5 µm), le calcul de l'efficacité de la collecte de la fluorescence n'est pas très précis, mais est censé être utilisé comme une approche plus rapide que les simulations 3D FDTD pour évaluer qualitativement l'impact de différents paramètres sur l'efficacité de collection de fluorescence d'un guide d'onde rectangulaire.

L'efficacité de la collecte de fluorescence en fonction de l'épaisseur du cœur, de l'indice de réfraction du cœur et de l'indice de réfraction du substrat avec leurs paramètres d'asymétrie respectifs sont illustrés par les Figures 4.8 à 4.10.

Aussi, afin de voir la portée de la lumière d'excitation, les profondeurs de pénétration pour une lumière d'excitation de 635 nm de longueur d'onde ont été calculées pour chaque mode, pour le dessus et le côté des deux guides d'ondes (pour la polarisation TE) (Figure 4.12). Les profondeurs de pénétration dépassent largement (plus de 10 fois) l'épaisseur de la bio-couche de fluorescence de 10 nm.

Les détails de l'expérience de spectroscopie sont présentés à la section 3.6. Les résultats sont illustrés sur les courbes de calibrations pour la spectroscopie de fluorescence à

ondes évanescentes du BSA-Alexa 647 immobilisé sur des guides d'ondes SU-8/quartz et SU-8/silice à la Figure 3.11.

De nombreux paramètres peuvent affecter la spectroscopie de fluorescence à couplage évanescent entre les guides d'ondes SU-8/quartz et SU-8/silice. Le processus de fabrication peut influer sur les dimensions des guides d'ondes. Comme indiqué dans [150], la largeur du guide d'ondes SU-8/Quartz (~ 10 µm) est environ 10% plus grande que celle du guide d'ondes SU-8/silice (~ 9 µm) en raison des différents protocoles de fabrication. Comme le montre la Figure 4.8, la différence entre l'efficacité de collecte de fluorescence des deux guides d'ondes était relativement constante pour une largeur plus grande et pour des guides d'ondes hautement multimodaux. La plus grande largeur fournit une plus grande surface qui permettrait à plus d'analyte marqué de se fixer au guide d'ondes, conduisant à un couplage de fluorescence plus élevé. Cette caractéristique doit être prise en compte lors de la comparaison des courbes d'étalonnage des deux guides d'ondes. En revanche, comme on le voit dans [150], les épaisseurs des guides d'ondes sont similaires et ne devraient pas affecter la sortie de fluorescence. La variation de l'efficacité de collecte de la fluorescence due au changement d'indice du cœur ou du substrat était sensiblement la même pour les deux guides d'ondes (Figures 4.9 à 4.10). D'après les courbes d'étalonnage (Figure 3.11), la sensibilité des guides d'ondes SU-8/quartz était supérieure à celle des guides d'ondes SU-8/silice. L'amélioration de la sensibilité peut être déterminée par le rapport de la pente des équations de régression linéaire, ce qui donne une amélioration de 17% de la sensibilité des guides d'ondes SU-8/quartz comparativement aux guides d'ondes SU-8/silice. En outre, les limites de détection ont été de 0,24 et 0,69 nmol·L^{-1} pour les guides d'ondes SU-8/quartz et SU-8/silice, respectivement. Comme expliqué ci-dessus, les asymétries et perte de propagation optique inférieures dues au choix des substrats et aux particularités des processus de fabrication ayant conduit à des indices de réfraction différents ont entraîné un couplage évanescent de fluorescence plus important et des pertes optiques moindres de la fluorescence guidée. Cela a conduit à un plus grand rendement de fluorescence à la sortie du guide d'onde SU-8/quartz pour une concentration d'analyte marquée similaire. Bien que les intervalles linéaires doivent être similaires puisque les protocoles d'immobilisation étaient similaires pour les deux guides

d'ondes, la petite différence observée entre les intervalles linéaires des deux guides d'ondes était probablement due à des erreurs expérimentales. Selon [150], les pertes de propagation optique, déterminées pour la polarisation TE, pour les deux guides d'ondes, différaient de celles évaluées avec la polarisation TM. Compte tenu de cela et du fait que la polarisation de la lumière à l'entrée des guides d'ondes a été mesurée à 41° du plan de la surface du substrat, la lumière de sortie guidée devrait être 48% plus élevée pour le guide d'ondes SU-8/quartz en calculant les pertes optiques des deux guides d'ondes avec les valeurs de la Figure 3.3 par rapport à la polarisation de la lumière d'entrée mesurée. En outre, à partir des simulations 3D FDTD, la valeur moyenne du rapport des 4 distributions (avec des fluorophores simulés phasés et orientés de manière aléatoire) pour l'efficacité de la collecte de fluorescence totale pour les deux guides d'onde a été évaluée à 5,4 ± 1,4% (erreur = écart-type), Tableau 3.2. Les calculs antérieurs avec la méthode de calcul combinant l'approche de propagation modale et la méthode d'indice effectif montraient que les rapports entre l'efficacité de collecte de fluorescence entre les guides d'ondes SU-8/quartz et SU-8/silice étaient évalués à environ 18% pour le haut et 10% pour les côtés des guides d'ondes. Par conséquent, la moyenne correspondra à environ 15% d'augmentation pour le guide d'ondes SU-8/quartz, conformément à ces calculs.

En bref, les résultats de la méthode de calcul et des simulations 3D FDTD ont montré que l'asymétrie inférieure augmentait de 15% ou bien de 5,4 ± 1,4% l'efficacité de collecte de la fluorescence en plus des pertes de propagation optique réduites de 48%. Ainsi, environ 73% ou bien 63% de plus de lumière guidée atteindra la sortie du guide d'ondes SU-8/quartz (tenant compte de sa surface supérieure de 10%). En revanche, une augmentation moyenne de la sortie de fluorescence de 46 ± 18% a été observée, comme indiqué précédemment. Compte tenu de ces valeurs, l'augmentation de la sortie de fluorescence mesurée est inférieure à celle prévue.

Étonnamment, c'est la première fois que la spectroscopie de fluorescence a été réalisée avec couplage direct sur un guide d'onde SU-8 sur quartz rectangulaire. Le cœur en SU-8 et le substrat de quartz étant tous deux transparents à la lumière visible pourraient offrir la possibilité d'effectuer une microscopie à fluorescence à partir du bas du substrat en même temps qu'une spectroscopie de fluorescence. Cela pourrait être pratique si des

canaux micro-fluidiques étaient collés sur le dessus de la puce. De plus, le procédé de fabrication utilisé pour le guide d'ondes SU-8/quartz [150] augmente convenablement l'indice de réfraction du cœur et adoucit les parois latérales du guide d'ondes, ce qui est favorable à la spectroscopie de fluorescence à ondes évanescentes, comme le montre ce travail. Ce procédé de fabrication pourrait également être appliqué à d'autres matériaux à résine photosensible pour guides d'ondes rectangulaires destinés à la spectroscopie de fluorescence à ondes évanescentes. Cela étant dit, le processus de fabrication pourrait être grandement amélioré si d'autres paramètres, tels que la température et l'humidité, étaient contrôlés. Ces paramètres pourraient notamment influer sur la concentration de solvant dans la résine photosensible pendant la longue pré-cuisson spécifique au processus de fabrication du guide d'ondes SU-8/quartz, ce qui est un facteur crucial pour obtenir des parois de guide d'ondes plus lisses, comme indiqué dans [150]. Par conséquent, cela pourrait modifier les pertes de propagation optique de temps en temps. Par conséquent, également la lumière de fluorescence guidée de sortie.

Les deux sections précédentes prouvent qu'il était possible d'augmenter le rendement de fluorescence des guides d'ondes en diminuant les pertes de propagation optique et en augmentant l'indice de réfraction du cœur en ajustant les paramètres du processus de fabrication. Bien que la fluorescence de sortie puisse encore être augmentée avec un contrôle accru des paramètres de fabrication et une optimisation plus poussée, elle atteindrait un seuil si, de façon hypothétique, les parois du guide d'ondes étaient dépourvues de rugosité et l'indice central du SU-8 ne dépasserait probablement pas 1,6 pour la lumière de fluorescence (λ = 671 nm). Ainsi, pour améliorer les performances du capteur, une autre voie a été empruntée à la prochaine section en augmentant la surface de détection, ce qui a ensuite augmenté le rendement en fluorescence. Le design choisi était le guide d'ondes en cascade pour sa capacité à permettre un couplage direct simple pour la fibre d'entrée/sortie tout en augmentant la surface d'immobilisation pour les cibles marquées.

GUIDE D'ONDES EN POLYMÈRE OPTIQUE EN CASCADE POUR UNE SPECTROSCOPIE DE FLUORESCENCE À ONDES ÉVANESCENTES AMELIORÉE

Comme mentionné précédemment, les guides d'ondes rectangulaires peuvent être conçus dans une large gamme de structures optiques pour des applications de bio-détection telles que les résonateurs à micro-anneaux [196], les résonateurs à réseau de Bragg [197], les coupleurs directionnels [198], les interféromètres [87], etc. Parmi d'autres, le design de guides d'ondes en cascade d'Ozhikandathil *et al.* [70] a été proposé pour augmenter la sensibilité de la spectroscopie de fluorescence à ondes évanescentes. Le guide d'ondes en cascade, fabriqué avec un cœur et des substrats de silice, a été testé pour la détection des hormones de croissance recombinantes marquées, à une concentration aussi faible que 25 ng·mL^{-1}. Dans cette section, le design du guide d'ondes en cascade sera fabriqué avec des guides d'onde en SU-8 sur silice et testé pour la spectroscopie de fluorescence à ondes évanescentes avec différentes concentrations de biotine-Alexa 647. Des simulations avec la *beam propagation method* (méthode de propagation du faisceau) seront également utilisées pour analyser l'excitation et la lumière de fluorescence guidée à travers les capteurs.

Le design choisi repose sur l'augmentation de la surface d'immobilisation des cibles marquées afin d'accroître la fluorescence de sortie. Pour y parvenir, un guide d'ondes initial est scindé en deux, créant deux branches qui sont ensuite scindées en deux, créant ainsi quatre branches enfin scindées en deux, créant ainsi huit branches. À partir de ces huit branches, le même processus est effectué en sens inverse. Par conséquent, les branches se recombinent successivement jusqu'à l'obtention d'un seul guide de sortie (Figure 5.1b). Un guide d'ondes droit unique est fabriqué à côté du guide d'ondes en cascade afin de comparer sa sensibilité à la spectroscopie de fluorescence à ondes évanescentes, Figure 5.1a. Le substrat utilisé est une couche de silice de 5 µm oxydée à partir d'une plaquette de silicium. Les cœurs des guides d'ondes (10 × 5 µm) ont été fabriqués avec de la résine photosensible SU-8, Figure 5.1. Les dimensions de la configuration de guide d'ondes en cascade sont illustrées à la Figure 5.2. Les jonctions de séparation représentées à la Figure 5.2 sont constituées de deux guides d'ondes à

courbure en S. Les courbures en S sont constituées de deux arcs de même rayon configurés en forme de S. Les rayons des arcs des différentes jonctions de séparation du guide d'ondes en cascade ont été choisis très grands afin de minimiser les pertes optiques habituellement attribuées aux guides d'ondes courbés. De plus, les branches des jonctions sont très longues par rapport à la largeur entre les branches. Cette configuration a été choisie pour élargir très progressivement l'espace entre les branches des jonctions séparatrices de manière à minimiser les pertes optiques dues à la division de la lumière.

L'évaluation des pertes optiques de la lumière d'excitation a été réalisée à l'aide de simulations bidimensionnelles de la configuration du guide d'ondes en cascade originale et corrigée (incluant les défauts de fabrication), avec une source d'entrée simulée à l'aide de la *beam propagation method*. Les détails des simulations sont décrits à la section 5.4 du Chapitre 5 et les résultats de ces simulations sont présentés à la Figure 5.7. La moyenne des valeurs de puissance des simulations pour le design en cascade original est de 90% et 56% pour le design corrigé. Ces résultats indiquent que la résine supplémentaire due à la fabrication a eu un impact significatif sur la lumière d'excitation guidée. En outre, les pertes optiques de la lumière d'excitation à la sortie des guides d'ondes en cascade et la répartition de la lumière dans les branches ont été évaluées expérimentalement avec le montage optique illustré à la Figure 5.8. Les résultats de la caractérisation optique ont montré que les pertes optiques étaient supérieures de 75% à celles du guide d'onde unique (Figure 5.10), mais que la répartition de la lumière était relativement bien répartie entre les huit branches du guide d'onde en cascade (Figure 5.9).

Il est supposé qu'en raison de la plus grande surface d'immobilisation, la fluorescence de sortie des analytes marqués du guide d'ondes en cascade serait supérieure à celle d'un seul guide d'ondes. Pour vérifier cette affirmation, la sensibilité des différents capteurs sera étudiée par une expérience de spectroscopie de fluorescence à couplage d'ondes évanescentes avec la biotine-Alexa 647 comme cible modèle. Le montage expérimental et les étapes d'immobilisation de la biotine-Alexa 647 utilisées à cet effet sont illustrées aux Figures 5.12 et 5.13 respectivement.

Les courbes de calibration de la spectroscopie de fluorescence à ondes évanescentes de la biotine-Alexa 647 immobilisée sur les guides d'ondes simples et en cascade (Figure 5.14) ont montré que les guides d'ondes en cascade entraînaient une sensibilité 1,39 fois supérieure à celle d'un guide d'ondes unique. De manière surprenante, la surface disponible pour l'immobilisation des guides d'ondes en cascade est d'environ 1900 000 μm^2 et de 576 000 μm^2 pour le guide d'onde unique, ce qui devrait entraîner une augmentation de la sensibilité de 3.30 fois si l'on ne tenait compte que de la surface d'immobilisation. Pour étudier la différence entre l'augmentation de sensibilité attendue si seule la surface d'immobilisation est prise en compte et les résultats expérimentaux, une analyse de la fluorescence guidée couplée aux guides d'ondes a été réalisée. Étant donné que l'émission de fluorescence provient des fluorophores Alexa 647 liés aux molécules de biotine, il est prévu que le couplage de la lumière de fluorescence apparaisse sur la totalité de la surface des guides d'ondes où le biotine-Alexa 647 fluor est immobilisé. Cependant, le nombre de fluorophores est immense et simuler chaque fluorophore serait impossible. Pour cette raison, des sources stratégiquement positionnées dans la configuration du capteur génèrent les modes guidés autorisés par les guides d'ondes. En effet, la lumière de fluorescence se couple à tous les modes guidés des guides d'ondes. Comme le montre la Figure 5.15, onze sources sont positionnées pour simuler la lumière de fluorescence couplée dans différentes sections du capteur pour le design original et corrigé. Les résultats des simulations sont présentés dans le Tableau 5.1 pour chaque source pour le design original et corrigé. À la lumière des résultats de la simulation présentés dans le Tableau 5.1, les émissions lumineuses des fluorophores couplées aux guides d'ondes ne peuvent pas toutes être guidées à travers le guide d'ondes de sortie en raison de la restriction due à l'ordre de leurs modes, ce qui pourrait altérer considérablement la fluorescence de sortie. Ce phénomène pourrait expliquer en partie l'écart entre le rapport des aires d'immobilisation (3,30) et le rapport de sensibilité (1,39). De plus, le surplus de résine affectant les jonctions de division et de recombinaison provoque des pertes optiques qui ajoutent à la différence entre ces rapports. Les résultats de la simulation montrent les limites du design en cascade présentées dans ce travail. En effet, le nombre de niveaux de division est limité par le nombre de modes autorisés dans le guide d'onde de sortie. Par conséquent, seule

une partie de la puissance lumineuse de la fluorescence couplée aux guides d'onde atteindra la sortie du capteur. Il est compréhensible que, chaque fois, qu'il y ait une division environ la moitié de la puissance est perdue, car la moitié des modes ne seront pas guidés dans le guide de sortie. Si on ne prend en compte que ce phénomène, il n'y aura aucune différence entre le guide d'onde unique et le guide d'ondes en cascade en termes de sensibilité. Cependant, en réalité, les modes les plus élevés sont beaucoup plus affectés par la rugosité des flancs du guide d'ondes. En effet, cela a été démontré par Tien *et al.* [201], qu'à partir du 4ème mode, la puissance optique est réduite de 14 fois par rapport au mode fondamental. Compte tenu de cela, il est compréhensible que les modes inférieurs aient plus de chances d'atteindre le guide d'ondes de sortie. Des études complémentaires devraient être réalisées pour évaluer dans quelle mesure les pertes modales affectent la fluorescence de sortie. Néanmoins, le guide d'ondes en cascade présentait toujours une sensibilité accrue par rapport au guide d'ondes unique. De plus, comme la biotine marquée est très proche de la surface des guides d'ondes, le couplage sera plus efficace pour les modes guidés inférieurs, car la puissance de leurs champs évanescents est concentrée près de la surface. Comme le montre la Figure 5.7 et le Tableau 5.2, le design du guide d'ondes en cascade est affecté de manière significative par les pertes optiques dues à la résine supplémentaire entre les jonctions de division ou de recombinaison. À cet effet, il serait avantageux que les guides d'ondes en cascade soient fabriqués avec une méthode de fabrication permettant une résolution plus élevée tel que la lithographie par faisceaux d'électrons.

Le design du guide d'ondes en cascade a augmenté avec succès la sensibilité comparativement au guide d'ondes droit. Cependant, les pertes optiques dues aux jonctions multiples et à la restriction modale du guide d'onde de sortie pour guider les signaux de fluorescence avec des modes qu'il ne pouvait pas supporter ont gêné le rendement en fluorescence attendu de l'augmentation de la surface d'immobilisation. Afin de résoudre ces problèmes, de nouveaux designs tels que les guides d'ondes doublés et triplés ont été développés comme présentés dans la section suivante.

GUIDES D'ONDES POLYMÈRES OPTIQUES DOUBLÉS ET TRIPLÉS POUR LA SPECTROSCOPIE DE FLUORESCENCE À ONDES ÉVANESCENTES AMELIORÉE

Dans ce travail, une augmentation de la sensibilité de la détection de fluorescence est proposée en augmentant la surface d'immobilisation, en multipliant le nombre de guides d'ondes multimodes à l'aide de séparateurs à double et triple jonctions. Dans cette section, les séparateurs à double et triple jonction ont été conçus pour des guides d'ondes multimodes SU-8 sur silice (10 × 5 µm) afin de multiplier le nombre de guides d'ondes comme moyen d'augmenter la surface d'immobilisation des analytes marqués. De plus, les guides d'ondes non seulement se divisent mais se recombinent à la sortie pour bénéficier du couplage de fluorescence accru. Ce travail présente l'optimisation d'une jonction double et triple pour assurer une distribution uniforme de la lumière d'excitation à l'aide de simulations numériques et expérimentations. En outre, une expérience de spectroscopie de fluorescence à ondes évanescentes avec biotine-Alexa 647 (en tant qu'analyte modèle) a été réalisée pour évaluer l'amélioration de la détection par fluorescence des guides d'ondes doublés et triplés par rapport à un seul guide d'ondes. Enfin, une étude modale a été réalisée avec des simulations numériques pour traiter les pertes optiques des différents modes aux jonctions de séparation.

L'approche adoptée pour concevoir la configuration du capteur consistait à augmenter la surface d'immobilisation des cibles marquées, pour ainsi augmenter la quantité de lumière de fluorescence guidée provenant du couplage évanescent de la fluorescence au guide d'ondes. Le guide d'ondes doublé, Figure 6.1b, commence par un guide d'onde droit qui se divise en deux guides d'onde droits à l'aide d'une jonction en Y et se recombine à nouveau pour former un guide d'onde droit à la sortie. Le guide d'ondes triplé, Figure 6.1c, a la même configuration que le guide d'ondes doublé, à la différence qu'un guide d'ondes droit supplémentaire va de l'entrée à la sortie. Le guide d'ondes unique, Figure 6.1a, a été ajouté pour comparer sa sensibilité pour la spectroscopie de fluorescence à ondes évanescentes à celle des guides d'ondes doublé et triplé. Les cœurs des guides d'ondes étaient constitués de résine photosensible SU-8 et le substrat était une couche de silice de 5 µm oxydée à partir d'une plaquette de silicium, Figure 6.1.

Les jonctions séparatrices pourraient causer des pertes optiques pour la lumière d'excitation entrante. Pour cette raison, des simulations numériques avec la *beam propagation method* afin d'optimiser la configuration de la jonction de division pour des pertes optiques plus faibles. Les simulations ont été effectuées en faisant varier la longueur de la jonction de division pour mesurer la puissance à la sortie des branches des jonctions. Comme observé sur la Figure 6.4 c, à partir d'environ 1000 µm de longueur de jonction de division, la puissance dans la branche de jonction à double division reste constante à environ 50%. En ce qui concerne la répartition de la puissance lumineuse dans la branche du diviseur de guides d'ondes triplé, la puissance varie périodiquement, comme indiqué à la Figure 6.4d. Pour une répartition uniforme de la lumière dans les branches du diviseur de guide d'ondes triplé, la puissance dans la branche devrait atteindre 33%. Différentes longueurs de jonction de séparation du guide d'ondes triplé pourraient permettre une distribution de puissance de 33% dans les branches en raison de la nature périodique de la fonction. Puisqu'une longueur définitive doit être choisie pour la fabrication du guide d'ondes, une longueur de 2377 µm a été choisie pour la jonction de division du guide d'ondes triplé, Figure 6.4d. Il est important de mentionner qu'après la fabrication, le design a été légèrement modifié en raison des limites de la lithographie UV. En effet, comme le montre la Figure 6.9ab, une résine supplémentaire remplit la jonction au début de la jonction de séparation. Pour cette raison, le design original sera corrigé en tenant compte de cette résine supplémentaire. Les designs originaux des guides d'ondes doublé et triplé illustrés à la Figure 6.4ab et les designs corrigés illustrés à la Figure 6.6ab seront utilisés pour l'étude modale présentée à la Figure 6.7. Comme le montre la Figure 6.7a, la puissance dans la branche du guide d'ondes doublé (design original) était stable à 50%. Le design du guide d'ondes doublé corrigé est légèrement différent en raison de l'altération de la transition progressive de l'ouverture de la jonction provenant du matériau supplémentaire. Néanmoins, la puissance moyenne est de 49%, ce qui est un changement insignifiant. Pour le design original du guide d'ondes triplé (Figure 6.7b), la puissance dans la branche du côté du diviseur triple est en moyenne de 23%. Pour vérifier la répartition de la lumière d'excitation dans les branches des guides d'ondes doublés et triplés, ainsi que pour comparer les pertes optiques à la sortie des deux designs, la lumière de sortie des facettes a été

visualisée à l'aide du montage optique illustré à la Figure 6.10. La Figure 6.12 montre que les pertes de propagation optique du guide d'ondes unique sont environ 33% inférieures à celles du guide d'ondes doublé et triplé. Ceci était prévu puisque les jonctions contribueraient à plus de pertes optiques. Il est intéressant de noter que les Figures 6.12 et 6.13 montrent que les intensités de sortie moyennes totales de la fin et du milieu des guides d'ondes (Total doublé, Total triplé) des guides doublé et triplé diffèrent que légèrement les uns des autres. L'intensité des sorties des branches du guide d'onde doublé diffère de 18% et les branches du guide d'onde triplé varient de 29% pour la branche gauche et de 9% pour la branche droite par rapport à la branche médiane. Cette distribution inégale est probablement due à des défauts de fabrication. En effet, une plus grande quantité de lumière sera guidée vers la branche où se trouve plus de "résine supplémentaire" à l'ouverture de la séparation de la jonction. En outre, l'alignement de la fibre d'entrée par rapport à la facette d'entrée du guide d'ondes pourrait être un facteur dans la distribution de la lumière. Néanmoins, la lumière d'excitation est raisonnablement bien répartie dans les branches des guides d'ondes doublés et triplés pour l'application envisagée.

Maintenant que la distribution de la lumière d'excitation le long des branches des jonctions de séparation et les pertes optiques des designs de guides d'ondes doublées et triplées ont été analysées et prouvé appropriées, le rendement de fluorescence des différents designs peut être étudié avec une expérience de spectroscopie de fluorescence à couplage d'ondes évanescentes. Le montage expérimental utilisé à cet effet est présenté à la Figure 6.16. Les courbes d'étalonnage de la spectroscopie de fluorescence à ondes évanescentes de la biotine-Alexa 647 immobilisée sur des guides d'ondes simples, doublés et triplés en SU-8/silice peuvent être consultées à la Figure 6.18. Où des limites de détections de 15 pg·mL^{-1}, 10 pg·mL^{-1} et 7 pg·mL^{-1} ont été trouvés pour les guides d'ondes simples, doublés et triplés, respectivement. De plus, les courbes d'étalonnage ont révélé une augmentation de 1,5 et 2 fois de la sensibilité pour les guides d'ondes doublés et triplés, respectivement, par rapport au guide d'ondes simple. La surface disponible pour l'immobilisation de la cible marquée (la surface de la jonction non exposée à la solution a été soustraite) est de 576 000 µm^2, 992000 µm^2 et 1408000 µm^2 pour les guides d'ondes simples, doublés et triplés. Ce qui se traduit par une surface

d'immobilisation de 1,7 et 2,4 fois plus grande pour les guides d'ondes doublés et triplés par rapport au guide d'ondes unique. Il en résulte une différence de 20% et 40% entre les résultats expérimentaux pour les guides d'ondes doublés et triplés, respectivement. Pour étudier cette divergence, des simulations de la lumière de fluorescence guidée couplée de manière évanescente à travers les capteurs ont été effectuées pour évaluer les pertes optiques dues aux jonctions de séparation.

Comme observé à partir des résultats expérimentaux sur la lumière d'excitation, les jonctions séparatrices provoquent des pertes optiques significatives (33%) par rapport au guide d'ondes unique. Les simulations ont également montré que les jonctions séparatrices des guides d'ondes doublés et triplés entraînaient des pertes optiques, mais dans une moindre mesure (5% à 8%), Figure 6.15. De la même manière, les jonctions séparatrices devraient également causer des pertes optiques à la lumière de fluorescence couplée de manière évanescente. En effet, la lumière de fluorescence couplée de manière évanescente est guidée à travers les guides d'ondes, donc à travers les jonctions séparatrices. Pour analyser l'impact des 2 jonctions de séparation sur la lumière de fluorescence guidée, tous les modes confinés dans la direction x pour les indices effectifs liés aux modes confinés dans la direction y (9 modes) sont injectés aux entrées des capteurs et de la jonction de recombinaison comme illustrés sur les Figures 6.19 a-d avec le "Launch mode". Les résultats de ces simulations sont présentés dans le Tableau 6.1.

Comme pour le guide d'ondes en cascade, les résultats de la simulation montrent les limites du design des guides doublés et triplés présentés dans ce travail. En effet, le nombre de niveaux de division est limité par le nombre de modes autorisés dans le guide d'onde de sortie. Par conséquent, seule une partie de la puissance lumineuse de la fluorescence couplée aux guides d'onde atteindra la sortie du capteur. Il est compréhensible que lorsqu'il y ait une division en deux ou trois de la jonction environ la moitié ou bien le deux tiers de la puissance est perdue, car la moitié ou bien le deux tiers des modes ne seront pas guidés dans le guide de sortie. Au vu de ces résultats, il apparaîtra pour un guide d'onde doublé ou triplé qu'il doit offrir une sortie de fluorescence guidée égale à celle d'un guide d'onde unique si on suppose que la lumière de fluorescence se couple de manière égale dans tous les modes guidés et ne subit aucune

perte à travers les capteurs. Néanmoins, en supposant qu'il y ait en réalité une rugosité sur les parois des guides d'ondes, les modes d'ordre supérieur fuiront davantage que les modes d'ordre inférieur. En effet, il a été rapporté par Tien *et al.* [201], à partir du 4$^{\text{ème}}$ mode, les pertes optiques dues à la diffusion de surface de la rugosité sont 14 fois supérieures à celles du mode fondamental. En outre, la puissance des modes d'ordre inférieur est concentrée plus près de la surface du guide d'onde que les modes d'ordre supérieur, ce qui permet d'obtenir un meilleur rendement de couplage de fluorescence puisque les cibles marquées ne se trouvent qu'à quelques nanomètres de la surface. Considérant les arguments en faveur des pertes optiques inférieures des modes guidés inférieurs par rapport aux modes d'ordre supérieur en raison de la rugosité et de l'efficacité de couplage plus élevée pour l'ordre de mode inférieur, l'amélioration de la sensibilité du guide d'ondes doublé (1,5 fois) et triplé (2 fois) comparée au guide d'ondes unique correspondant presque au rapport de surface entre les guides d'ondes doublé (1,7 fois) et triplé (2,4 fois) est compréhensible. De plus, les résultats des simulations du Tableau 6.1 montrent que la jonction recombinante pourrait limiter le nombre de modes pouvant être guidés à travers le guide d'onde de sortie à partir de la fluorescence couplée à partir des guides d'onde droits suivant les jonctions de séparation. Cela pourrait expliquer l'écart de 20% et 40% entre les valeurs d'augmentation de la sensibilité (1,5-2) et du rapport de surface (1,7-2,4).

CONCLUSION & TRAVAUX FUTURS

Conclusion générale

Le but de ce travail était d'améliorer et d'étudier les performances de la spectroscopie de fluorescence à ondes évanescentes et a été réalisé de deux manières: d'une part, en développant un nouveau procédé de fabrication des guides d'onde SU-8 sur quartz et, d'autre part, en concevant de nouvelles géométries de capteurs optiques pour une surface accrue d'immobilisation.

Le nouveau procédé de fabrication des guides d'ondes SU-8/quartz s'est avéré efficace pour diminuer la rugosité des parois latérales du guide d'onde, réduisant ainsi les pertes de propagation optique et augmentant du même coup le rendement de la lumière de fluorescence guidée venant du couplage évanescent des analytes marqués. En plus de cela, l'augmentation de l'indice de réfraction du cœur de SU-8 due aux paramètres particuliers du protocole de fabrication avec l'indice de réfraction inférieur du substrat de quartz a abaissé l'asymétrie du guide d'onde par rapport à un guide d'onde standard SU-8/silice, bénéficiant ainsi l'efficacité de collection de la fluorescence des guides d'ondes pour des fluorophores proches de leur surface. Le plus grand rendement en fluorescence à la sortie du guide d'onde SU-8/quartz comparé au guide d'onde standard SU-8/silice a été étudié numériquement à l'aide de deux méthodes: par des simulations 3D FDTD de dipôles de courant ponctuels émetteurs à proximité des guides d'ondes et avec une méthode de calcul combinant l'approche de propagation modale pour des guides d'ondes planaires avec la méthode d'indice effectif. Les deux méthodes de calcul ont prédit une augmentation de l'efficacité de collection de la fluorescence des guides d'ondes SU-8/quartz fabriqués avec le nouveau protocole par rapport aux guides d'onde standard SU-8/silice. À notre connaissance, c'était la première fois que des simulations 3D FDTD aussi précises étaient effectuées pour déterminer l'efficacité de collection de la fluorescence des guides d'ondes. En outre, pour la première fois, une méthode de calcul a été développée pour évaluer l'efficacité de la collecte de fluorescence pour des guides d'ondes rectangulaires pour divers paramètres. En raison des limitations du procédé de fabrication permettant de réduire les pertes de propagation optique ou d'augmenter l'indice du cœur des guides d'ondes, de nouveaux designs ont été développés,

permettant une plus grande surface pour l'immobilisation des cibles marquées. Tous les designs ont été comparés à un seul guide d'onde droit en termes de sensibilité pour évaluer leurs rendements. Le premier design, le guide d'onde en cascade, augmentait la surface d'immobilisation des cibles marquées en utilisant des ramifications qui partaient d'un guide d'entrée droit et se recombinaient en un autre guide d'onde de sortie droit. Le design a réussi à augmenter la sensibilité du capteur, mais pas à la hauteur de l'agrandissement de la surface d'immobilisation. Cela était dû au grand nombre de jonctions-Y nécessaires au doublement des guides d'ondes. En outre, plus les ramifications étaient doublées, plus l'ordre du mode de la lumière de fluorescence couplée/guidée atteignant le guide d'onde de sortie était important. Ceci a eu pour résultat que seulement une partie de la lumière de fluorescence couplée de manière évanescente a été collectée. Par conséquent, cela a diminué l'effet d'une surface d'immobilisation agrandie pour les analytes marqués. Pour contrer ces obstacles, deux nouveaux designs ont été développés avec seulement 2 jonctions-Y pour réduire les pertes de propagation optique et seulement 2 ou 3 guides d'ondes droits, exploitant au maximum la surface d'immobilisation, permettant d'abaisser l'ordre du mode de la lumière de fluorescence couplée de manière évanescente atteignant le guide d'onde de sortie.

La sensibilité des biocapteurs optiques à guides d'onde doublés et triplés s'est révélée être presque proportionnelle à l'élargissement de la zone d'immobilisation par rapport à un guide d'onde unique. Pour avoir une meilleure idée de la performance de ces capteurs, leurs courbes de calibration pour la détection de différentes concentrations de biotine-Alexa 647 ont été tracées ensemble, comme le montre la Figure 7.1. De toute évidence, le guide d'onde triplé présentait la plus grande sensibilité (2 fois supérieure à celle du guide d'onde unique), la LD la plus basse (7 pg·mL^{-1}) et le rendement en fluorescence de sortie le plus élevé par rapport aux autres capteurs. De manière surprenante, le guide d'onde en cascade semble comparable au guide d'onde doublé en termes de rendement en fluorescence sortie et de sensibilité. La tendance observée est qu'un équilibre doit être maintenu entre le nombre de jonctions et la multiplication des guides d'ondes, c'est-à-dire la gestion entre les pertes optiques, la création de modes d'ordre élevé et l'augmentation de la zone d'immobilisation.

Travaux futurs

Le processus de fabrication du SU-8/quartz devrait principalement être axé sur l'exécution des tâches de fabrication dans un environnement à humidité contrôlée afin de garantir des performances constantes et optimales des guides d'ondes. De même, le même protocole de fabrication devrait en général être adapté pour différents polymères, substrats et avec différentes dimensions afin de l'établir comme référence pour les guides d'ondes optiques en polymères. Les futures études de caractérisation devraient fournir les profils de rugosité des parois latérales des guides d'ondes afin de mieux comprendre l'impact des différents procédés de fabrication et permettre des simulations numériques des pertes de propagation optique.

En outre, les simulations 3D FDTD permettant d'évaluer l'efficacité de la collecte de la fluorescence des guides d'ondes SU-8/quartz et SU-8/silice gagneraient à l'ajout des profils de rugosité au niveau des flancs. En effet, il pourrait fournir des résultats de simulation directement comparables aux résultats de la détection par spectroscopie de fluorescence à ondes évanescentes.

Quant à la méthode de calcul combinant l'approche de propagation modale pour l'efficacité de la collecte de la fluorescence pour les guides d'ondes planaires et la méthode de l'indice effectif, il convient de la comparer aux simulations 3D FDTD pour avoir une idée de l'erreur sur les valeurs absolues et relatives obtenues pour l'efficacité de collection de la fluorescence des guides d'ondes SU-8/quartz et SU-8/silice.

Les designs des guides d'ondes en cascade, doublés et triplés pourraient être améliorés en réduisant les pertes optiques des jonctions en créant des cônes (*tapers*) en 3D à variation progressive entre les branches qui tiendraient compte de la propagation de la lumière dans les deux directions transversales.

Aussi, un moyen ingénieux de limiter l'incapacité du guide de sortie à guider le signal de mode élevé formé par la recombinaison de signaux serait d'augmenter progressivement l'indice de réfraction de la dernière jonction jusqu'à la fin du guide de sortie, ce qui contribuerai à soutenir le grand nombre de signaux à mode d'ordre élevé. Le même résultat pourrait être obtenu en augmentant progressivement la jonction de

recombinaison finale en un guide de sortie de dimensions supérieures, ce qui permettra également de soutenir un plus grand nombre de signaux à mode d'ordre élevé.

Pour les futurs projets de bio-détection, les guides d'ondes doublés et triplés sont des designs prometteurs pour les plates-formes à multiple détection pour un système de laboratoire sur puce. En effet, puisqu'ils sont conçus avec des guides d'ondes droits, chaque guide d'ondes droit pourrait être modifié avec des anticorps spécifiques à différents analytes pour être ensuite exposé avec des analytes différents délivrés par des canaux micro-fluidiques. Une application intéressante serait l'évaluation de la pureté de l'eau qui nécessite la détection de plusieurs analytes en raison de la multitude de contaminants qu'elle contient. Avec des designs similaires au guide d'ondes doublé ou triplé, il serait possible de détecter une multitude de contaminants, mais la particularité de leurs conceptions permettrait également une puce miniaturisée entièrement plane, permettant une production en série, des coûts réduits et des dispositifs au point de diagnostic.

ABSTRACT

Research in optical biosensors has gained great interest in the last two decades. Although many optical technologies were developed, integrated optics technologies revealed to be popular due to their potential for quick detection, highly sensitive measurements and particularly for miniaturization. Indeed, miniaturization of an optical sensing device offer the possibility to integrate it in a lab-on-a-chip (LOC) system. Which consists, in the best scenario, of a device that takes care of the delivery of the bio or chemical samples to the sensing area with microfluidic channels and treatment of the detection signal in a single chip with micro dimensions. Optical sensing structures with nano to micro dimensions can then be easily integrated with microfluidics, hence ideal for LOC devices. Also, they surpass electrochemical sensors for this task since they are immune to electromagnetic interferences which could alter the detection results.

Optical sensing devices could be in many forms, but for the purpose of miniaturization channel waveguides are the best candidates. Indeed, the fabrication processes for channel waveguides benefited immensely from microelectronics circuits manufacturing technologies which have been refined for decades.

In this work, polymer channel waveguides were used as the sensing platforms for evanescent wave fluorescence spectroscopy among other optical bio sensing methods because of its high sensitivity and specificity.

Firstly, a novel fabrication process was developed for SU-8 polymer optical waveguides on a quartz substrate which revealed different characteristics than SU-8 polymer waveguides on a silica substrate fabricated with the standard protocol. They differed from each other mainly in their lower optical propagation losses and lower asymmetry.

The SU-8 on quartz waveguides were then compared with the SU-8 on silica waveguides for evanescent wave fluorescence spectroscopy to investigate the impact of the different parameters from the novel and standard fabrication protocols. Finite difference time domain (FDTD) simulations were performed to evaluate the impact of the different asymmetries of both SU-8/quartz and SU-8/silica waveguide on the fluorescence

collection efficiency for simulated emitting fluorophores. Also, an evanescent wave fluorescence spectroscopy experiment was performed with Alexa 647 labeled Bovine serum albumin (BSA) molecules to evaluate the sensitivity of both waveguides for fluorescence detection. In brief, the FDTD simulations showed an increase in the fluorescence collection efficiency for the SU-8/quartz waveguide compared to the SU-8/silica waveguide and the experimental results revealed that the SU-8/quartz waveguide offered a greater sensitivity than the SU-8/silica waveguide.

Moreover, to evaluate the impact of the variations of the different parameters (dimensions, core & substrate refractive indices) of both the SU-8/quartz and SU-8/silica waveguides on the fluorescence collection efficiency, a new calculation method was developed. This calculation method combined a modal propagation approach to find the fluorescence collection efficiency for planar waveguides with the effective index method.

Finally, new geometries were designed with the purpose of increasing the area of immobilization of the labeled targets for increased sensitivity. Namely, the cascaded, doubled and tripled waveguides. The geometries of these new designs were first optimized for the excitation light propagation with numerical simulations (beam propagation method) and then by experimental characterization. Evanescent wave fluorescence spectroscopy experiments with Alexa 647 labeled biotin were performed to compare their performance with a single straight waveguide. The experimental results revealed increased sensitivity for the new designs compared to the straight waveguide. Concentrations of Alexa 647-biotin as low as 15, 9, 10 and 7 pg·mL^{-1} were detected for the single, cascaded, doubled and tripled waveguides respectively. Experimental results were expected to be higher, taking into account the increased area of immobilization. To understand this discrepancy, additional numerical simulations with the beam propagation method were performed to analyze the optical losses of the evanescently coupled fluorescence guided throughout the sensors.

ACKNOWLEDGMENTS

CONTENTS

LIST OF TABLES

LIST OF FIGURES

NOMENCLATURE

2,4-D	2,4-dichlorophenoxyacetic acid
AFM	atomic force microscopy
AFM1	aflatoxin M1
AMF	5-(aminomethyl) fluorescein
APTES	(3-Aminopropyl)triethoxysilane
B.anthracis	bacillus anthracis
BPA	bisphenol A
BPSG	borophosphosilicate glass
BSA	bovine serum albumin
CCD	charged-coupled device
CdTe	cadmium telluride
dB	decibel
DI	deionized water
ELISA	enzyme-linked immunosorbent assays
F.C.E	fluorescence collection efficiency
FDTD	finite difference time domain
Hg	human immunoglobulin G
IgG	immunoglobulin G
LED	light emitting diode
LOC	lab-on-a-chip
LOD	limit of detection
LPCVD	low-pressure chemical vapour

MC-LR	microcystin-LR
MCLW	metal clad leaky waveguide
PA	protective antigen
PBS	phosphate buffer solution
PDMS	polydimethylsiloxane
PEB	post exposure bake
PECVD	plasma enhanced chemical vapor deposition
rbST	recombinant growth somatotropin
RIE	reactive ion etching
RMS	root mean square
SAF	supercritical angle fluorescence
SB	soft bake
SDS	sodium dodecyl sulfate
SEM	scanning electron microscope
SiO_2	silicon dioxide
$SiON_x$	silicon oxynitride
SP	surface plasmon
SPCE	surface plasmon coupled emission
SPR	surface plasmon resonance
SRSP	short range surface plasmon
Ta_2O_5	tantalum pentoxide
TE	transverse electric
TiO_2	titanium dioxide
TIR	total internal reflection

TIRF	total internal reflection fluorescence
TM	transverse magnetic
T_{PEB}	post exposure bake temperature

A	lower asymptote logistic curve
B	slope factor logistic curve
C	analyte concentration at the inflection point of the calibration curve
c	concentration
D	upper asymptote logistic curve
K	binding constant
L	length of planar waveguide
n	index of refraction
R	power radiated by a unit volume of a fluorophores layer to a unit solid angle
S	source strength
V	volume
W	planar waveguide width
x	analyte concentration
Y	response of the logistic curve

aTE	asymmetry parameter for the TE mode
aTM	asymmetry parameter for the TM mode
$\vec{E}_\nu$	transverse electric field of the related TE mode with index ν
$\vec{H}_\nu$	transverse magnetic field of the related TM mode with index ν

P_0	output power of the reference spectrum
P_{o-em}	waveguide output power of the labeled antigen emission
P_{rad}	total power radiated by the sources
P_{sat}	power at the saturation concentration
P_{wg}	total power coupled to the waveguide
P_{wg}^*	total power coupled to the waveguide + optical losses
$P_{wg}^* max$	measured fluorescence output for SU-8/Quartz at saturation
P_v	power carried by each mode
n_c	cladding refractive index
n_{eff}	effective index of refraction
n_f	core refractive index
n_s	substrate refractive index
t_c	thickness of fluorophore layer
γ_c	decay constant in the cladding
μ_0	magnetic permeability of vacuum
λ	wavelength
σ	standard deviation
Γ, Ω	normalized fluorescence power outputs
β	propagation constant
η	fluorescence collection efficiency
ψ, F	fluorescence intensity
ω	angular frequency

CHAPTER 1

INTRODUCTION

Fluorescence excitation and detection form the basis of many modern sensitive bio-sensing and bio-analytical techniques. In particular, restricting fluorescence to a highly confined space can lead to substantially increased sensitivity, reduced background signal, and can provide a means for selectively analyzing regions of interest within complex samples. Among the multiple ways this can be achieved, one powerful approach is to selectively excite fluorescence at the surface of a dielectric or metal using an evanescent wave or field generated at this location. An evanescent wave is a near-field whose intensity exhibits an exponential decay with distance from the location at which the wave was formed. In addition to selectively exciting fluorescence in proximity to the surface, collection can be restricted to the emission of surface-bound fluorophores by varying the angle of collection with respect to the surface.

The purpose of this introduction is to review the most common optical technologies (other than microscopy) in bio-sensing and bio-analysis based on fluorescence detection by evanescent wave excitation from total internal reflection of incident light on planar platforms (Total internal reflection fluorescence (TIRF), surface plasmon coupled emission (SPCE), long-range surface plasmon (LRSP) coupled emission, and metal-clad leaky waveguides (MCLW)) and from guided light in planar and rectangular waveguides.

The focus is placed on planar platform-based biosensors due to some of their particular characteristics that distinguish them from e.g., fiber optic based biosensors. More specifically, planar platforms provide more sturdiness, the possibility of preparing a lab-on-a-chip (LOC) combining multiple optical/microfluidic components, and the ability to spatially pattern their surface with recognition moieties for single or simultaneous detection of analytes. For a discussion of non-planar bio-sensors, such as fiber optics, the reader is referred to other excellent review papers on the topic [1, 2].

Given the vastness of the topics addressed herein as well as the overwhelming number of studies published each year in this field, many recent, important, and detailed review articles have been published on individual aspects discussed in this thesis [1-7]. Selected studies published from 2005, were taken as examples of the fluorescence detection technology they support.

1.1 Fluorescence sensing by excitation with evanescent waves from reflected incident light on planar platforms

An evanescent wave can be generated by directing light to the interface between two media where the refractive index of the incident medium is larger than the refractive index of the second medium. If the angle of incidence is above a specific "critical" angle, the light undergoes total internal reflection (TIR) with concurrent production of an evanescent wave to satisfy the boundary conditions of the electromagnetic field [8], Figure 1.1. This wave can extend up to a few hundred nanometers into the second medium and can therefore be used to probe analytes therein, based either on absorption/refractive index changes (label-free bio-sensing) [3] or emission phenomena (labeled bio-sensing) [4]. There exist numerous bio-sensor platforms that use the evanescent wave for detecting changes in the refractive index of the sensing area including: optical planar waveguides [9], optical fibers [1], surface plasmon resonance [6], interferometers [10], optical ring resonators [11], and photonic crystals [3]. Importantly, the evanescent wave can excite fluorophores, thus providing a means for very sensitive analyte detection. In this section, we successively discuss platforms which produce an evanescent wave at a dielectric–sample interface or at dielectric–metal-sample interface.
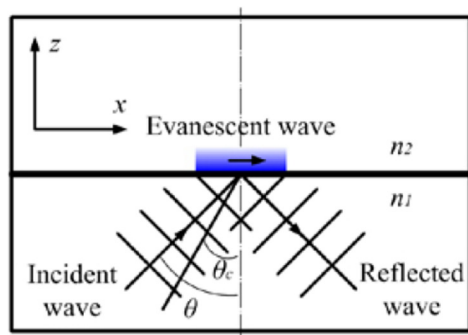
Figure 1. 1   **Total internal reflection of an incident wave between two dielectrics media. Where θ_c is the critical angle, θ the angle of incidence ($\theta > \theta_c$) and $n_1 > n_2$. The evanescent wave propagates in the x direction but decays in the z direction. Adapted from Fig.1 of [12].**

1.1.1 Evanescent wave excitation at a dielectric–sample interface

Fluorescence from fluorophores in the vicinity of a dielectric surface excited by TIR is called total internal reflection fluorescence (TIRF). TIRF is mostly used in microscopy for its benefit in imaging labeled cells [13]. Indeed, since the excitation light is confined to a region of around 100 nm due to the exponential decay of the evanescent wave, fluorophores outside this region won't contribute to blurring the image by emitting unwanted fluorescence light.

Välimäki *et al.* [14] made good use of this light confinement above the dielectric-sample interface provided by TIRF to restrict the fluorescence detection to only the molecules of interests near the vicinity of the surface. Specifically, they have developed a surface-sensitive fluorescence measurement platform based on a parabolic polystyrene lens that enabled simultaneous total internal reflection excitation and supercritical angle fluorescence (SAF) collection. SAF is a method by which fluorescence of surface-bound fluorophores is collected at angles greater than the critical angle [15]. Unlike TIRF, for which it is technically challenging to reach such high angles of illumination, collection of SAF by confocal microscopy shows excellent surface-restricted detection at angles around 62–75° (for glass/water interface; above the critical angle) [15]. Indeed, in TIRF, fluorophores located at the dielectric–sample interface can emit into the dielectric, with a maximum intensity directed at the critical angle. A more selective sampling of

fluorescence in close proximity to the surface is therefore possible in SAF microscopy by collecting the radiant fluorescence at angles above the critical angle, without the need for grazing incident light (as in the case for TIRF). In this system, a standard flat bottom polystyrene micro titer plate containing 96 sample wells is placed on the parabolic polystyrene lens, which both excites the bottom of the plate and collects SAF from its surface, Figure 1.2. This set-up permitted real-time monitoring of antibody–antigen binding [14] and sandwich ELISA detection of morphine directly in the well. This system permitted the detection of 2.7 ng·mL^{-1} morphine in 20 seconds while until then the fastest detection time was 2 min for a 5 ng·mL^{-1} [16].
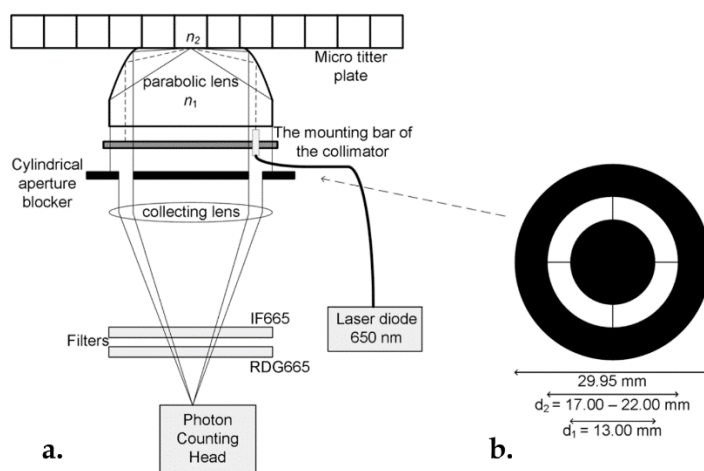
Figure 1. 2   **a) Experimental arrangement for simultaneous TIR excitation and SAF detection. b) The cylindrical aperture blocker used to select an appropriate range of super critical angles for surface generated fluorescence detection. Adapted from Fig.2 of [14].**

1.1.2 Evanescent wave excitation at a dielectric–metal-sample interface

1.1.2.1 Surface plasmon fluorescence excitation

An evanescent wave generated at the interface between dielectric and metal can, under appropriate conditions, excite a surface plasmon. When the wavevector of the incident light perfectly matches that of the surface plasmon, resonance can occur (*i.e.*, surface plasmon resonance, SPR) [17]. This resonance causes a significant absorbance of the reflected light at angles near the SPR critical angle, thus causing a considerable dip in

the reflectance sensorgram. Small changes in the refractive index of the media of interest will translate into a shift in the resonance dip, Figure 1.3.
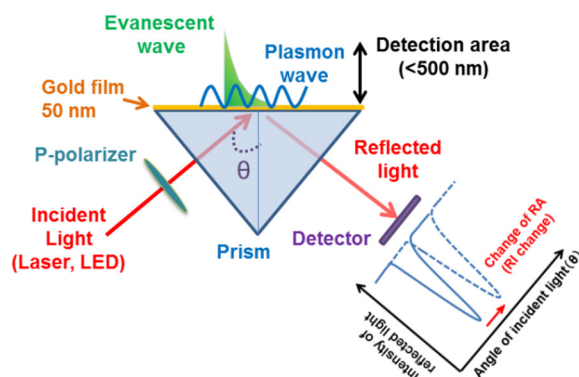
Figure 1. 3   Schematic diagram showing the principles of SPR detection. RI: refractive index, RA: resonance angle. Adapted from Fig.1 of [18].

Hence, the monitoring of this shift, which can occur upon binding of a target to an immobilized recognition species such as antibodies [19, 20] or aptamers [21], can be used as a sensing mechanism. This form of detection has found many applications in bio-sensing [5, 22-24]. However, fluorescent molecules near the metallic surface also can couple with the latter's surface plasmon and consequently transmit their emission to the dielectric layer [25]. Using the SPR platform for fluorescence bio-sensing is known as surface plasmon coupled emission [26]. SPR bio-sensing is a well-known technique and has been used extensively to detect numerous biological and chemical species including pathogens, hormones, drugs, pesticides, proteins, and nucleic acids [6, 7]. This section sequentially discusses surface plasmon couple emission and long-range surface plasmon coupled emission.

1.1.2.2 Surface plasmon coupled emission (SPCE)

SPCE is an attractive technique due to the particularity of SPR to enhance fluorescence excitation and as a consequence, sensitivity. For SPCE, a prism is used to couple the incident light to a glass substrate coated with a thick (*ca.* 50 nm) layer of noble metal (gold

or silver). At the proper angle, wavelength, and polarization (which must be p-polarized) the wave vector of the light matches the wave vector of the surface plasmon and resonance is achieved. The resulting evanescent wave (*ca.* 200 nm) can excite fluorophores present near the metallic layer. A highly directional emission from the fluorophore will occur in the glass substrate at its corresponding SPR angle. This set-up is commonly known as the Kreschtmann configuration. However, unlike SPR, SPCE can occur even if the fluorophores are excited from free space (*i.e.*, reverse Kretschmann configuration). This can be understood as being inverse to SPR: the light emitted by the fluorophore couples with the surface plasmon of the metallic surface and then re-radiates within the glass slide at an angle that fulfills the resonance criteria. This highly directional emission suggests that fluorophores with different fluorescence wavelengths will emit at different angles due to the different resonance conditions [27]. This particularity of SPCE makes it attractive for multi-analyte detection because it provides a way to distinguish emission from different fluorophores without any dispersive optics (other than the coupling lens), Figure 1.4.
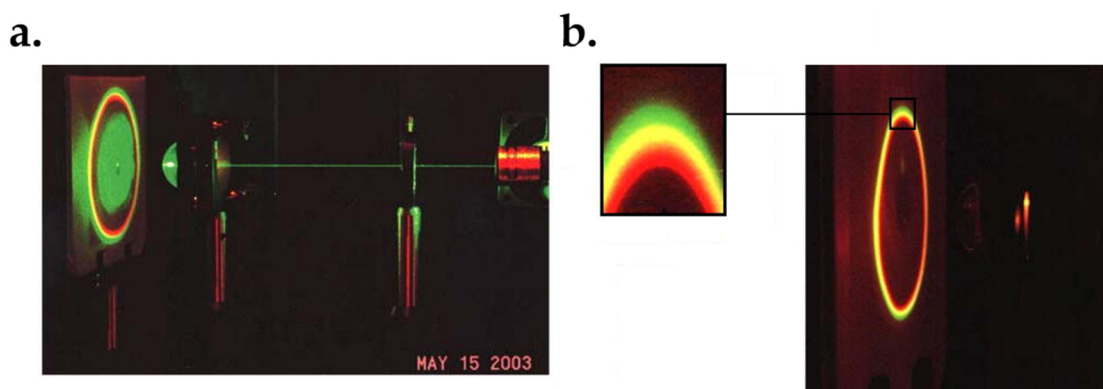
Figure 1. 4   Photograph of the optical setup with reverse Krestchmann configuration and hemi-spherical prism for SPCE of a mixture of fluorophores excited with green light (λ = 532 nm) with a) no emission filter and b) long pass filter. Adapted from Fig.9 of [27].

One of the particularities of all evanescent wave sensors is to reduce the signal-to-background ratio. SPCE, used with the Kretschmann configuration, effectively rejects background noise beyond *ca.* 200 nm from the metal layer, and has strong coupling with the fluorophores within its range. In addition, the evanescent field is increased by 20-fold

when the conditions for SPR are fulfilled, resulting in a stronger excitation of the fluorophores compared to the reverse Kretschmann configuration [28]. Another interesting property of SPCE is that the metallic layer promotes de-excitation of the fluorophores, thereby increasing photostability and quantum yield [29]. Unfortunately, the metallic layer also strongly dissipates the emission energy passing through it, leading to lower coupling into the glass substrate [30].

Field enhancement is already known to result from deposition of metallic nanoparticle or other small metallic structures onto the waveguide from the extensive study of localised surface plasmon [31]. Indeed, Chowdhury *et al.* [32] have shown that the sensitivity of SPCE can be increased by 6 fold with the attachment of *e.g.* silver nanoparticles on a thin silica layer (5 nm) coated on a continuous silver layer. In addition, Yuk *et al.* have demonstrated a similar effect with metallic gratings, for example, for use in a gold grating-based chip [33, 34] (Figure 1.5c). This property of SPCE can be used in the reverse Kretschmann configuration, thus enabling the use of cheap LED excitation sources rather than lasers [35]. In addition, solution-phase electrochemical luminescence [36] and, more recently, solid-state electrochemical luminescence [37] have been used as compact light sources for SPCE, leading the way to cheaper and more portable sensors.

Original combinations of SPCE with other methods, such as SAF (Section 1.1.1.2), can result in adding the advantages of the SPCE with the high light-collection efficiency of SAF. This approach has been applied for human immunoglobulin G assays [38, 39]. In addition, combining SPCE with quantum dots, for *e.g.* Hg(II) ion detection, has been achieved by exploiting the quenching effect of the latter on cadmium telluride (CdTe) quantum dots, making this another interesting avenue for future sensing [40].

It was shown recently that a gold grating-based SPCE biosensor (gold grating exposed to p-polarized light where SPCE emission is formed) with additional polyelectrolyte spacer layers (Figure 1.5ab) was a highly sensitive method for immunoassay [33]. Indeed, the quenching effect of the metal layer can be reduced with increasing number of polyelectrolyte spacer layers as long as it doesn't exceed the dominant quenching range of 10 nm. A limit of detection as low as 1 pg·mL^{-1} was achieved with the model mouse

immunoglobulin G (IgG) sandwich immunoassay with an Alexa fluor 647 labeled anti-mouse IgG as a fluorescent secondary antibody.

Figure 1. 5   **a) Multilayer polyelectrolyte surfaces prepared with the layer-by-layer technique. b) Structure of the sandwich immunoassay for mouse IgG. c) Scheme of gold grating chip for SPCE with corresponding excitation/emission light. Adapted from Fig.1 of [33].**

1.1.2.3 Long range surface plasmon coupled emission (LRSP)

Exciting surface plasmon modes in a thick noble metal film sandwiched in between two dielectric media with the same or nearly the same index of refraction generates two independent surface plasma waves. If the thickness of the noble metal film is sufficiently decreased, two bound coupled surface plasmon modes can be excited, namely a symmetric and an asymmetric mode [41]. For a decreasing metal film thickness, the asymmetric mode gets more confined inside the metal film. Consequently, increasing the attenuation considering that much of the power dissipation occurs in the metal. On the contrary, for a decreasing metal thickness, the symmetric mode has a smaller fraction of its field inside the metal. Therefore, the evanescent field will penetrate more into the claddings. The later symmetric mode is also called long range surface plasmon. Compared to the surface plasmons on a single interface, the long range surface plasmons are characterized by a lower damping and a larger evanescent mode field. This yields a narrower resonance since the angle for optimum excitation is close to the critical angle. Long-range surface plasmons are usually obtained using a configuration similar to that used for SPR, but with the addition of spacing, or buffer (e.g., oil or polymers) between the coupling prism and the thin metallic film. An excellent review [42], shows numerous

potential configurations for obtaining long-range surface plasmons. Kasry *et al.* [43] showed a narrower resonance for the long range surface plasmon compared to the single interface surface plasmon for the Krestchmann configuration (Figure 1.6ad) and with simulated angular reflectivity spectra (Figure 1.6be).
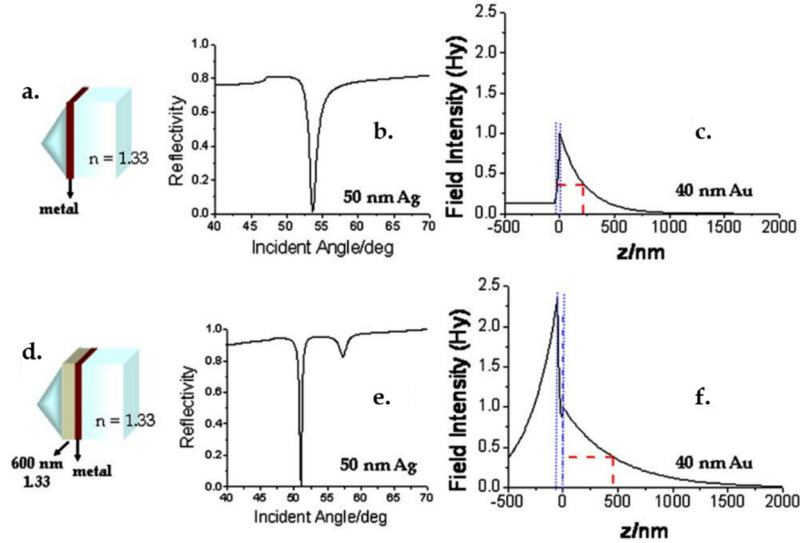
Figure 1. 6   **a) Kretschmann configuration for SPR. b) Simulation of a SPR curve for a high refractive index prism ($n_{\lambda=633nm}$ = 1.85) nm and 50 nm Ag with ε = –17 + 0.7i, in contact with water of n = 1.33. c) Normalized optical field distribution, Hy vs z, normal to the interface for the architecture given in (a) but calculated for 40 nm (cf the broken blue lines) of Au ε = –12.3 + 1.29i as the metal layer. d) Kretschmann configuration for LRSP. e) Simulation of a LRSP curve for a high index prism with a first a layer of a low index cladding layer assumed to be n = 1.33, followed by the metal coating Ag with d = 50 nm. f) Normalized optical field distribution, Hy vs z, normal to the interface for the architecture given in (d) but calculated for 40 nm (cf the broken blue lines) of Au ε = –12.3 + 1.29i as the metal layer and cladding layer of n = 1.29 (to be closer to the experimental conditions, see below). Adapted from Fig.1 of [43].**

The SPR Krestchmann configuration, Figure 1.6a, consists of a high index prism with a 50 nm thick Ag film deposition. The same configuration is used to excite LRSP to the exception that a 600 nm Teflon layer (n = 1.33) is deposited on the prism before the 50 nm Ag film deposition, Figure 1.6d. The simulated angular reflectivity spectrum of the LRSP shows two dips at different angles. The deepest dips corresponds to the symmetric mode (LRSP) and the more shallow dip corresponds to the asymmetric mode (short range surface plasmon, SRSP) mentioned previously, Figure 1.6e. Compared to the surface plasmon resonance, Figure 1.6b, the LRSP resonance is definitely narrower and appear

at a lower angle, Figure 1.6e. This sharp resonance can contribute to a high resolution of detection as demonstrated by Homola *et al.* [44]. A simulation of the optical field distribution of the Hy magnetic field vs z (normal to the metal slab) was performed with a 40 nm thick Au film and a Teflon film with an index of 1.29 (to match a further experiment, Figure 1.7). Both Hy magnetic fields were scaled at the water/metal interface. Comparing Figure 1.7c & f, it is again obvious that the decay of the evanescent field of the LRSP is weaker than the normal SP extending it to a greater extent in the buffer solution. It was also reported that the optical field intensity from the LRSP is significantly enhanced compared to the normal SP [45]. Both of these properties would also suggest an enhancement of sensitivity for fluorescence spectroscopy detection with LRSP compared to SPCE, since the fluorophores would benefit from a greater and deeper excitation. Kasry *et al.* [43] also demonstrated the increased sensitivity for LRSP fluorescence spectroscopy compared to SPCE with the architecture given in Figure 1.7a for the LRSP.
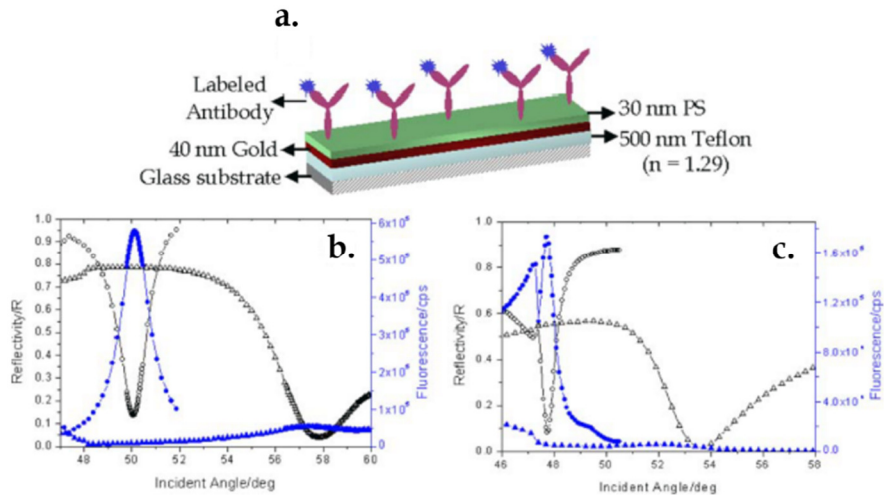
Figure 1. 7   **a) Scheme of the test sample for the LRSP excitation with a 40 nm Au metal layer evaporated onto a 500 nm thick Teflon cladding layer, on a high index glass substrate. The 30 nm of polystyrene prevents in both cases the fluorophores from being quenched by the proximity of the metal substrate. Same configuration for the SP excitation, except for the Teflon layer and a 50 nm Au metal layer instead of 40 nm. b) Angular reflectivity curves for LRSP (open circles) and SPR (open triangles) with angular fluorescence intensity curves for LRSP (full circles) and SPCE (full triangles) based on configuration in (a). c) Angular reflectivity curves for LRSP (open circles) and SPR (open triangles) with angular fluorescence intensity curves for LRSP (full circles) and SPCE (full triangles) for configuration with 500 nm Teflon (embedded with labeled antibodies) coated on 40 nm Au for LRSP and 50 nm for SPCE. Adapted from Fig.3 of [43].**

The configuration consists of a glass substrate a 500 nm thick Teflon slab (n = 1.29) a 40 nm Au thick film and a 30 nm polystyrene film to prevent quenching of the fluorophores. The analyte consists of Alexa 647 fluor labeled antibodies that would attach to the polystyrene film. For the SPCE, the same amount of antibodies was attached and the architecture is identical to the exception of the Teflon coating and of 50 nm instead of 40 nm Au film for optimum yield. The experimental results are shown in Figure 1.7b, the narrower resonance of the LRSP is still apparent and appears at lower angles as predicted theoretically. An increase of 22 fold is observed for the LRSP excitation if the fluorescence peaks are compared at the resonance. Now, to demonstrate the weaker decay of the LRSP field, the same configurations for SP and LRSP excitation than previously will be used except that the labeled antibodies will be adsorbed on a 500 nm Teflon coated on top of both of the Au films. Needless to say, the fluorescence is almost vanished for the SPCE detection method, showing that the fluorophores where significantly distanced from the penetration depth of the evanescent field of the surface plasmons. On the other hand, the fluorescence from the LRSP excitation was measured to be 33 times higher than with the SPCE detection confirming the extended range of the LRSP, Figure 1.7c.

These properties of the LRSP excitation was made of good use by Wang *et al.* [46] for the detection with fluorescence spectroscopy of aflatoxin M1 in milk with a Cytop-Au structure. The setup for the LRSP excitation and fluorescence detection with the sensor chip with the added chemicals for functionalization is shown in Figure 1.8a. An inhibition immunoassay was used for the detection of the AFM1. Consequently, the free a-AFM1 were attached to the BSA-AFM1 conjugate and a solution of Cy5-Gar was pumped so that they bind to the captured a-AFM1. The fluorescence emission excited by the LRSP was detected for different AFM1 concentrations as seen in the calibration curves for the buffer and milk solutions, Figure 1.8b. The limit of detection of a concentration of AFM1 as low as 0.6 pg·mL^{-1} was determined for the milk solution.
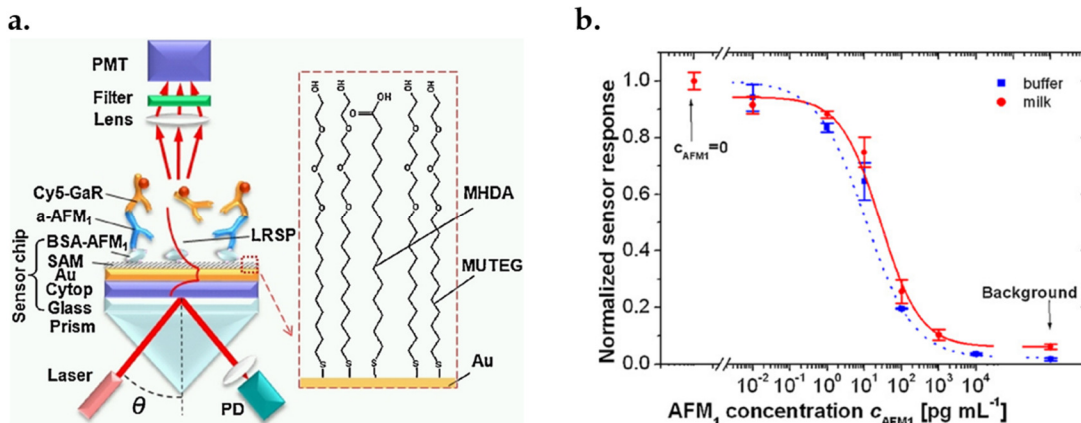
Figure 1. 8   a) Scheme of the LRSP-enhanced fluorescence spectroscopy setup with the biolayers necessary for the detection of AFM$_1$ by an inhibition immunoassay. b) Calibration curves for the detection of AFM$_1$ in buffer (red squares) and milk (blue circles) samples. Adapted from Fig.1 of [46].

1.1.2.4 Metal clad leaky waveguides (MCLW)

Metal clad leaky waveguides (MCLWs) are an extension of TIRF within an unclad waveguide, in which a thin metallic film is placed between the two dielectric layers (*i.e.*, the core and substrate; Figure 1.9a). In this configuration, light that undergoes total internal reflection at the dielectric–sample interface is directed towards the metallic film, which acts like a semi-transparent mirror that partially reflects the incident light, thereby allowing it to undergo additional reflections. For each reflection at the metal layer, TIR light will lose part of its energy through the metallic film which can be collected, hence the denomination "leaky". While referred to as a waveguide, the high attenuation loss of the leaky mode makes fluorescence collection through the dielectric difficult. Rather, collection through the substrate or from the top of the MCLW, using *e.g.*, a microscope, is most often employed. In fact, collection under appropriate conditions using a microscope is expected to result in a substantial (~70-fold) increase of sensitivity [47]. One particularity of MCLWs is that they generate a deep evanescent field suitable for the detection of large biological entities, such as bacteria [48]. For instance, while the evanescent field of SPR or SPCE is limited to a few hundred nanometers, the evanescent

12

field of MCLW can extend up to 1 µm, which is convenient for the detection of *e.g.*, bacterial spores of this approximate dimension [49]. Indeed, the size of the evanescent field can be adjusted by varying the angle of the incident light.

MCLWs are more sensitive than SPR (Section 1.1.1.2) or traditional TIRF (Section 1.1.1) for the detection of fluorescence originating micrometers away from the dielectric–sample interface [50]. This sensitivity in part arises from the very efficient excitation of a fluorophores in close proximity to the dielectric–sample interface, and to the larger volume of sample analyzed due to the deep evanescent field. However, the high directionality of the emission coupled with the leaky mode of the MCLW leads to a loss of collection efficiency compared to traditional fluorescence detection carried out on a bare glass–water interface [47]. Nevertheless, despite this reduced collection efficiency of the MCLW-coupled emission, a stronger fluorescence signal is ultimately detected for molecules near the dielectric–sample interface due high excitation efficiency.

To date, only few experiments involving MCLWs for fluorescence excitation/detection have been reported [48, 51]. Goddard and co-workers have developed a MCLW-based system for the detection of *Bacillus subtilis variant niger* bacterial spores (Figure 1.9b) labelled with fluorescent antibodies by means of refractive index changes, light scattering, and fluorescence. In this system, fluorescence was excited from the glass substrate and collected in the form of a 2D image by means of a CCD camera positioned to detect light from the top [51]. The number of pixels in which a fluorescent signal was detected, rather than the absolute fluorescence intensity, was correlated to the number of bacterial spores in the solution. In another example, the same group has developed a planar sol–gel film based biosensor for the analysis of glucose on a MCLW [49]. This system was based on the incorporation of a fluorescent, pH-sensitive ruthenium ligand complex along with glucose oxidase within a thick sol–gel matrix that acts as the dielectric layer directly in contact with the sample solution (Figure 1.9c). Sensing is based on the quenching of fluorescence of the complex due to the acidification accompanying the conversion of glucose to gluconic acid by the entrapped enzyme. The limit of detection of this system was 3 µM and there was no diffusion limitation of the glucose analyte or product, resulting in excellent reproducibility. One advantage of using a MCLW was that an electrical potential could be applied to accelerate the diffusion of larger charged analytes within the

sol–gel matrix, resulting in a shortened analysis time and reduction of non-specific binding.
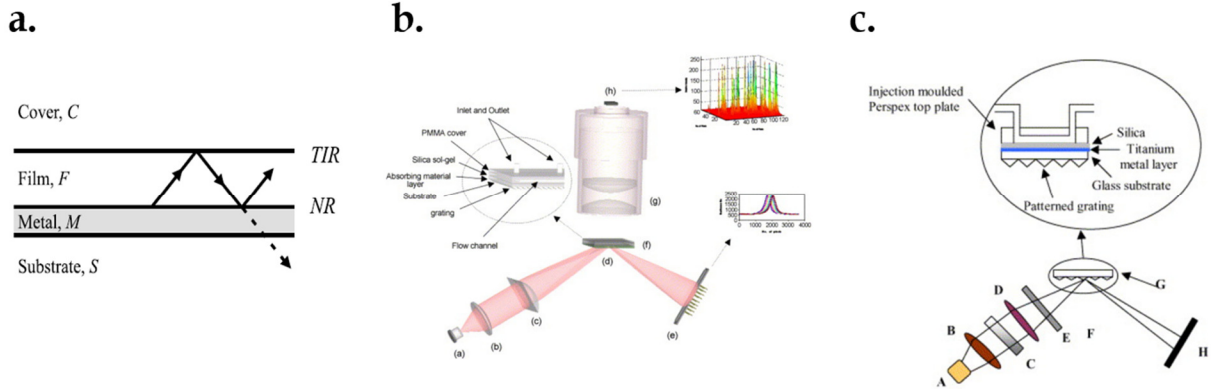
Figure 1. 9   a) Basic MCLW configuration with illustration of light guided in the waveguide film by total internal reflection (TIR) at the core/cladding boundary and normal metallic reflection (NR) at the core/metal boundary. b) [49] & c) [51] experimental setup with MCLW for refractive index and fluorescence based detection.

1.2   Fluorescence sensing by excitation from evanescent wave from guided light

1.2.1   Fluorescence detection by evanescent wave excitation from light guided in planar waveguides

Unlike conventional TIRF (Section 1.1.1) for which the evanescent field is generated directly at the interface of a dielectric and the sample, the evanescent field generated at each reflection within a waveguide can be used to excite fluorophores in proximity to its outer, cladding layer. In practice, an optical planar waveguide consists of three layers of dielectrics: the substrate, the core, and the cladding (Figure 1.10a). The refractive index of the core is always higher than the two other layers which makes it the preferable path for light propagation [8].
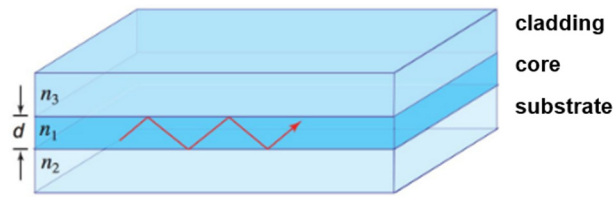
Figure 1. 10   Schematic drawing of an asymmetric planar waveguide with $n_1 > n_2 > n_3$.

In general, higher sensitivity is obtained with single mode planar waveguide rather than a multimode planar waveguide. A single mode waveguide is characterized by a core thinner than the light wavelength and usually corresponds to the cut-off wavelength (i.e., the longest wavelength to propagate in the waveguide). By simple geometry, it is understandable that more reflections will occur in within thin cores, compared to the thicker cores used in multimode waveguides. In addition, higher evanescent field intensity can be obtained by increasing the refractive index difference between the substrate and the core (ratio >0.3) [52], an effect that has been used in the early days of optical planar waveguide sensors with SiO_2–TiO_2 cores [53]. A higher intensity of the evanescent field in the sensing region along with a faster decay of the evanescent field outside the sensing region will result in a greater sensitivity. A conventional planar dielectric waveguide has a substrate refractive index greater than that of the cladding, which ensures that most of the mode power will be in the substrate. Waveguide excitation fluorescence microscopy was first introduced as a novel biosensing and imaging technique in 2006 [54]. The sensitivity of the system was demonstrated by monitoring in real time the streptavidin–biotin binding event to below 20 pM concentrations, an improvement of more than 10 fold was observed in the signal to noise ratio for fluorescence detection of streptavidin-633 and high surface sensitivity was found for cell imaging [54]. Usually, high refractive index film made of Ta_2O_5 or SiO_2–TiO_2 on glass or polymer were used to ensure higher ratio between the substrate and film refractive index for higher sensitivity, many applications were reported in this extensive review [55].

Thin films made with TiO_2 or Ta_2O_5 were proven to be sensitive but still needed complex technology such as plasma enhanced chemical vapor deposition (PECVD) or sputtering to be fabricated. An alternative to these inorganic materials deposited by PECVD (for thin

15

film) was proposed by Martinez *et al.* [56] by developing a sol-gel core planar single mode optical waveguide by dip-coating and with a grating coupler for fluorescence biosensing. The same waveguide structure was also used with a silicon oxynitride ($SiON_x$) core for comparison. The sol-gel waveguide fabricated with the dip coating method [57] resulted in a 200 nm thick titanium doped silica core with a refractive index of 1.60–1.70. The second waveguide was a 120 nm thick $SiON_x$ deposited with the PECVD process with a refractive index of 1.76. A thin layer (40 nm) of SiO_2 was deposited on the $SiON_x$ core to facilitate the attachment of recognition ligands, Figure 1.11.
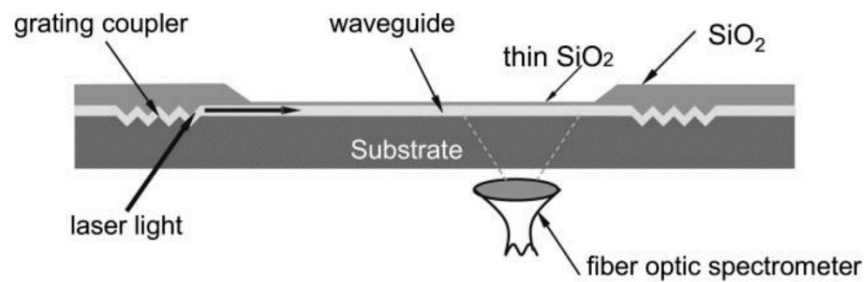
Figure 1. 11 **Configuration of the SiON$_x$ planar optical waveguide with grating coupler and the fiber positioned perpendicularly for fluorescence collection. Picture taken from Fig.1 of [56].**

The parameters for both waveguides were chosen so their optical field intensity and penetration depth are similar, as seen on Figure 1.12. The optical field decays of 150 nm Ta_2O_5 cores with and without SiO_2 cladding were also represented for comparison.
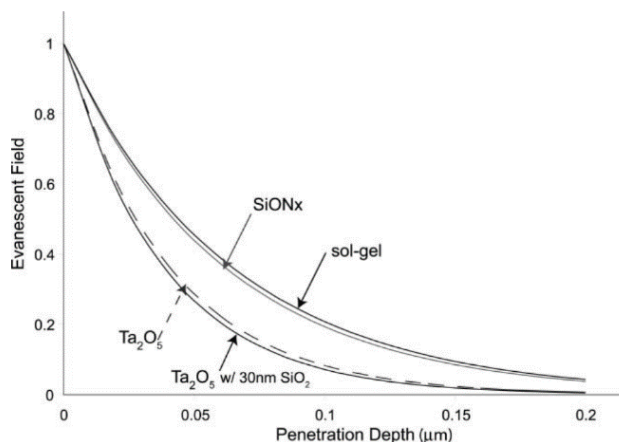
Figure 1. 12   Evanescent field profiles at the surface of planar waveguide with different materials. Picture taken from Fig.2 of [56].

Since in this work the sensing platforms are presented as an alternative to enzyme-linked immunosorbent assays (ELISA), sandwich assays that utilize capture and detection antibodies are used as an immobilization method to mimic ELISA procedures to ensure that any marker protein detected by ELISA could also be detected by the sol-gel or $SiON_x$ waveguide. For both protective antigen (PA) and *Bacillus anthracis* cell detection, the target analyte was sandwiched between a labelled antibody with Alexa Fluor 532 or 647 and a biotinylated capture antibody which was attached to an avidin-biotin conjugation immobilized on the bioactive membrane, Figure 1.13.
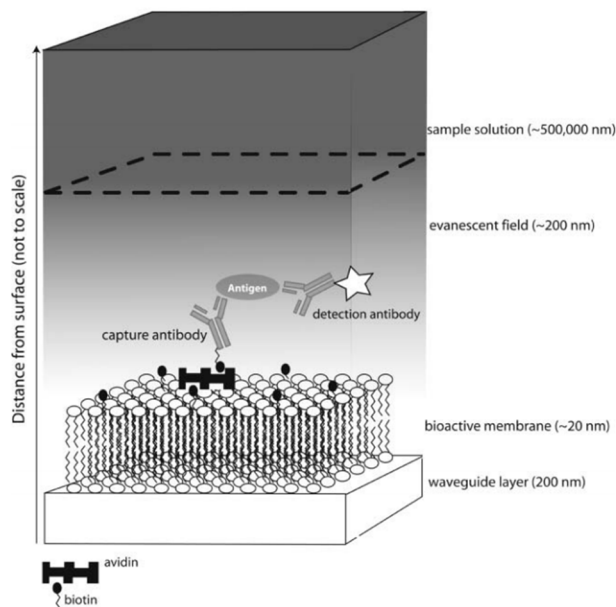
Figure 1. 13   Diagram of the sandwich immunoassay with the representation of the evanescent field. Picture taken from Fig.3 of [56].

Detection as low as 1 pM of PA (0.083 ng·mL^{-1}) in a complex medium (sugars, proteins, and cellular debris) was obtained for the sol-gel waveguide. The response of the sensor for 1pM PA is seen in Figure 1.14a, the smaller spectrum corresponds to the non-specific binding i.e. the signal of the detection antibodies without the presence of PA. A calibration curve was also obtained for the SiON$_x$ waveguide for different concentration of PA, Figure 1.14b. Interestingly, the signal from the 1 pM PA was detected in 10 minutes. That contrast greatly with the ELISA detection which took 5 hours to detect the same analyte concentration.
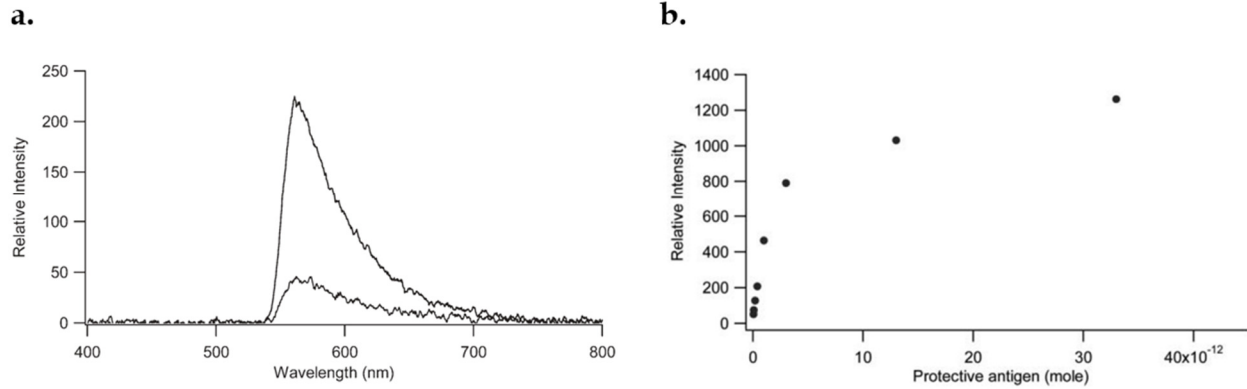
Figure 1. 14 **a) Spectral response of the sol-gel waveguide from a spiked complex medium with 1 pM of PA (top curve) and a complex medium without PA (bottom curve). b) Calibration curve of different PA concentrations for the SiON$_x$ waveguide. Adapted from Fig.4 & Fig.5 B of [56].**

Other than the detection of pathogenic antigens, the sensing platforms were also able to detect B. anthracis cells or even cell detritus since the penetration depth of the evanescent field can only cover a small part of the cell. The spectra on Figure 1.15, show the performance of the sol-gel and SiON$_x$ waveguides for the detection of B. anthracis cellular components. The lower spectrum corresponds to the background fluorescence (532 nm excitation source) coming from the waveguide material and the middle spectrum is the signal from the non-specific binding.
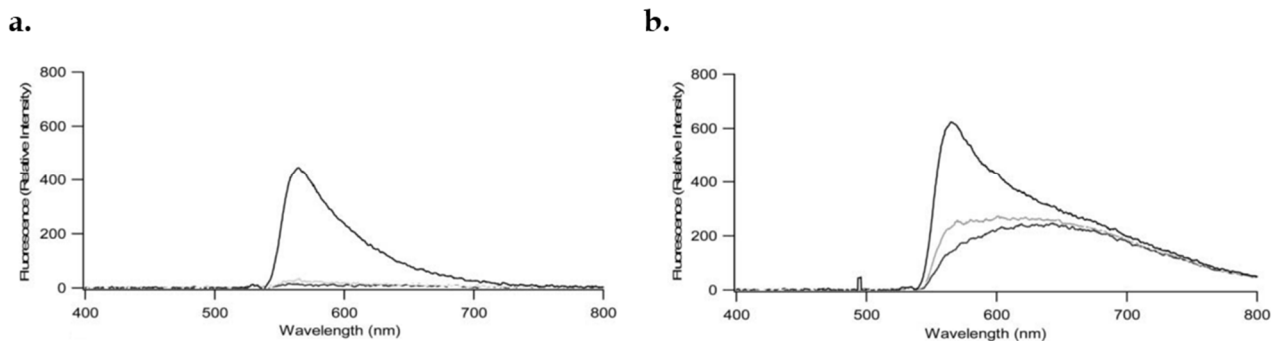
Figure 1. 15 **Spectral responses of labeled cellular components for a) the sol-gel waveguide b) SiON$_x$. Top curve: specific binding response, Middle curve: non-specific response, Lower curve: background fluorescence. Adapted from Fig.8 A& B of [56].**

19

As observed from these spectra, the sol-gel waveguide shows a very low background fluorescence compared to the $SiON_x$ waveguide. A higher background fluorescence would results in a lower sensitivity, since it will be harder to distinguish small signals. Nonetheless, It was presented that $SiON_x$ waveguide could benefit from an excitation source with a longer wavelength (635 nm, for Alexa 647 label) to diminish the background fluorescence. Although the sol-gel waveguide seems to offer higher sensitivity, Martinez *et al*. [56] reported that the fabrication process of the $SiON_x$ waveguide allowed for better reproducibility thus making the comparison between repeated measurements with different waveguides more reliable. Also, the light coupling angle with respect to the grating coupler was conserved making it a better candidate for commercial use. In brief, Martinez *et al*. [56] were able to fabricate a single mode waveguide based sensor with a polymeric and $SiON_x$ core that outperform ELISA in detection time and sensitivity for PA detection and possibly to other protein marker also detectable with ELISA. They also showed that the sensing platforms were able to detect cellular components of B. anthracis.

As presented previously, thin films as waveguide cores can offer high sensitivity and quick detection but still need sophisticated equipment to be deposited and a complex coupling system necessitating high index prisms or grating with an opto-mechanical arrangement directing the incident light at specific angles.

Huang *et al.* [58] proposed to overcome these challenges with the use of thicker planar waveguides and an integrated light coupling and collection system. Indeed, by employing the glycerol-compensated oblique-exposure technique [59] they were able to fabricate microprisms from SU-8 resist to couple the light from an optical fiber in a SU-8 layer and a quartz substrate. As seen in Figure 1.16, an emitting optical fiber is inserted at the upper right where its light is first collimated by an integrated cylindrical lens and refracted by the microprism at angles satisfying the condition for TIR in the SU-8 layer or the quartz substrate. The light is then guided inside the SU-8 layer or quartz substrate creating different spots for the excitation of the labeled analytes at the top of the guiding layer.
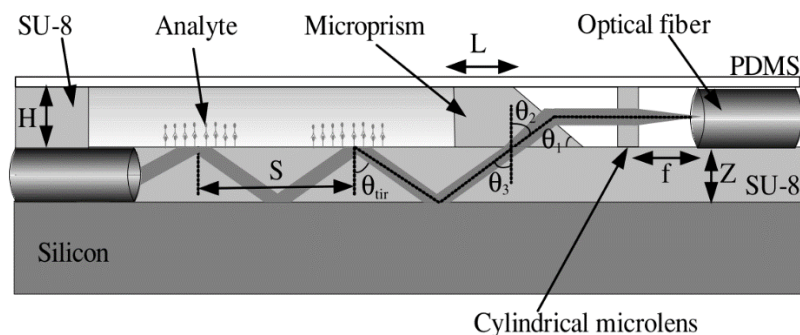
Figure 1. 16 Schematic drawing of the monolithically fabricated TIR-based biosensor for fluorescence sensing. Picture taken from Fig.1b of [58].

The fluorescence light evanescently couples into the SU-8 layer and is guided to the collection fiber to be then filtered by a bandpass filter and detected by a photomultiplier tube. A CCD camera paired with a filter was used to measure the fluorescent light from the spots on the top of the quartz substrate. Photo of the SU-8/silicon monolithically fabricated chip with SEM photos (in caption) of the integrated optical coupling system can be seen on Figure 1.17a. Also, the SU-8/quartz chip with the microfluidic chamber can be seen on Figure 1.17b.
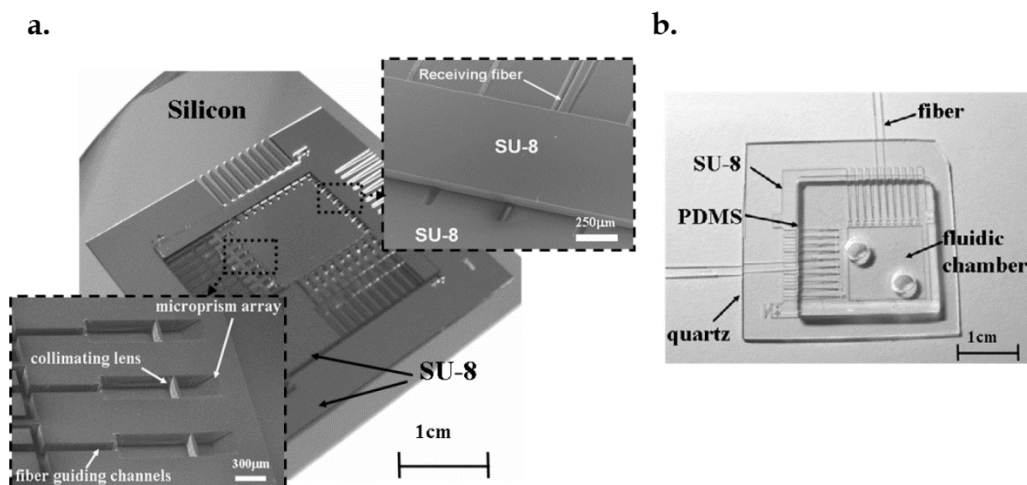
Figure 1. 17 Photograph of the monolithic TIR-based a) SU-8/silicon chip with the SEM photos (in captions) of the microprism array (left) and the receiving fiber in its respective groove (right). b) SU-8/quartz chip with the microfluidic chamber. Adapted from Fig.1c & d of [58].

Fluorescence sensing was performed for both of the SU-8 layer and quartz with different concentrations of Cy3-conjugated anti-mouse IgG solutions with their respective measurement systems, Figure 1.18. Limit of detections as low as 125 ng·mL^{-1} and 206 ng·mL^{-1} were measured for the quartz and SU-8 as waveguides respectively. Autofluorescence from SU-8 [60] added to the background noise decreasing the signal-to-noise ratio of the detection system. Hence, affecting negatively the sensitivity of the sensor.
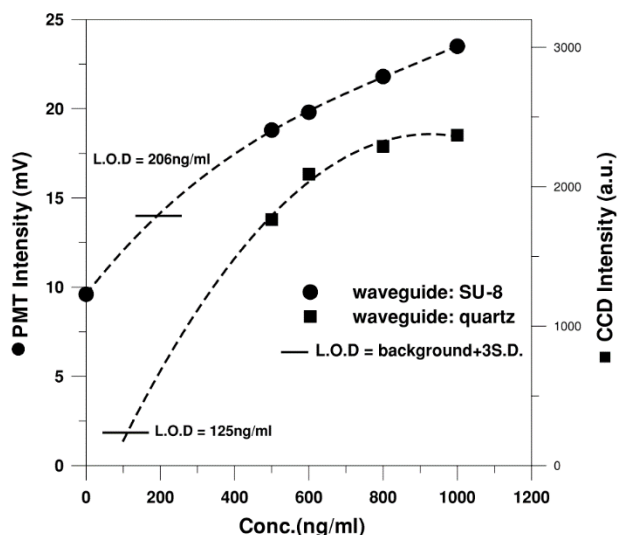
Figure 1. 18   **Calibration curves of the average fluorescence intensities of different concentrations of Cy3-conjugated anti-mouse IgG solutions for the SU-8/silicon and SU-8/quartz biochip. Picture taken from Fig.7 of [58].**

The monolithic fabrication of this biosensor including integrated micro optics proved that it was possible to get rid of the complex opto mechanical system needed for the alignment which arises from the light coupling and collection to the optical arrangement. Making this unique monolithic fabrication a great candidate for integration in a lab-on-a-chip microsystem.

The use of a beveled angle coupling light into a planar waveguide was also used by other groups, namely Liu *et al.* [61]*,* who which also used a multimode waveguide to create different reflections spots as sensing regions. Moreover, they used a multi-channel flow cell to allow for multi-analyte detection of water contaminants. As seen in Figure 1.19, a

diode laser (λ = 635 nm) was used as the excitation light which was fanned out by a line generator. The fanned laser light is coupled in a 1.5 mm K9 glass slide with one extremity polished at a 45º angle to facilitate the light coupling and with the other extremity painted with black ink to absorb the output light. Air at the bottom of the glass slide and the sample at the top acted as the substrate and cladding of the waveguide. A PDMS flow cell with 8 different linear channels was sealed on the waveguide chip to allow for detection of different concentrations of various contaminants simultaneously. Each linear channels confined the samples on 3 spots where hapten-protein conjugates (MC-LR-OVA, 2,4- d-OVA, and BPA-OVA, used as the recognition elements) could be immobilized for indirect competitive immunoassay detection with their respective antibodies labeled with Cy5.5 dye. Optical fibers of 1 mm core diameter were positioned perpendicularly to the sensing spots to collect the emitted fluorescence light.
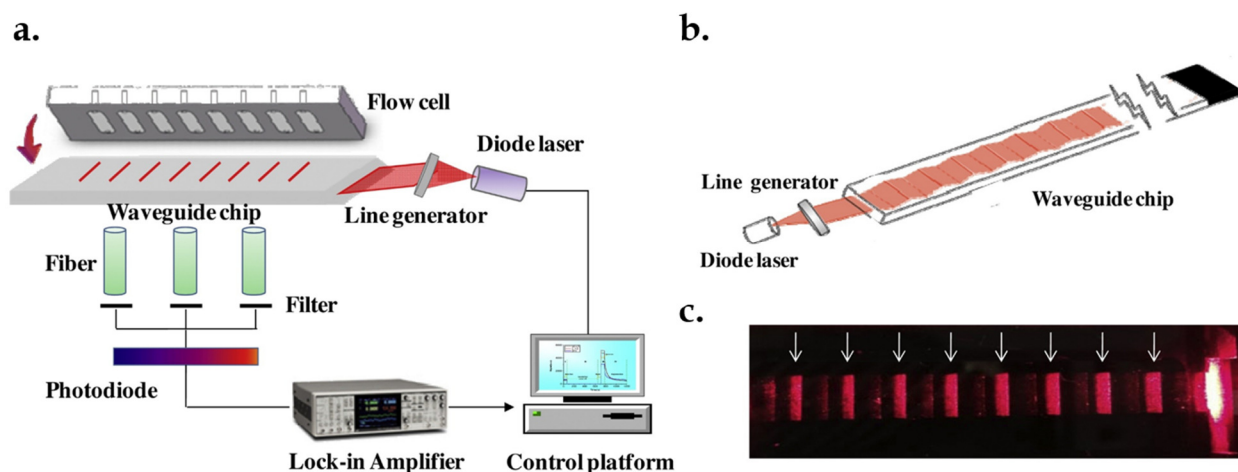
Figure 1. 19 **Schematic drawings of a) the complete setup for the multi analyte detection of water contaminants with the planar waveguide-based array immunosensor with its multi-channel PDMS flow cell b) the light path through the planar waveguide c) photo of the light spots (pointed by the white arrows) created from the TIR of the guided light. Adapted from Fig.1 of [61].**

Since an indirect competitive immunoassay approach was used for detection, the fluorescence signal was inversely proportional to the amount of analyte detected. On Figure 1.20, the calibration curves are presented for the three contaminants.
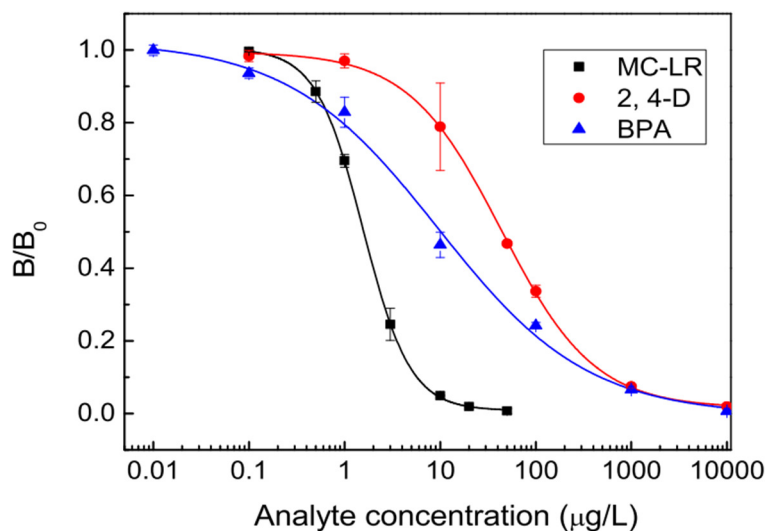
Figure 1. 20 **Calibration curves for the indirect competitive fluorescence immunoassays of the MC-LR, 2, 4-D and BPA contaminants with the planar waveguide-based array immunosensor. Picture taken from Fig.5 of [61].**

No more than 25 minutes were necessary to complete the entire multi-analyte detection including the washing steps. Detection limits as low as 0.67 µg·L^{-1} for MC-LR, 7.53 µg·L^{-1} for 2,4-D and 0.03 µg·L^{-1} with linear dynamic ranges going from 0.98 µg·L^{-1} to 5.89 µg·L^{-1} for MC-LR, 18.17 µg·L^{-1} to 406.52 µg·L^{-1} for 2,4-D and 0.10 µg·L^{-1} to 5.37 µg·L^{-1} for BPA were measured. This simple system proved to be a promising device for water monitoring since the detection limits met the requirements for Chinese drinking water standard (GB 5749–2005). Although this optical device was also successfully used for the detection of various analyte [62-64], the complete system with the laser source, the optical sensing device with the collecting fibers, the pumping system assuring the delivery of the sample, and the washing and the signal processing instruments makes it bulky and inadequate for a portable point of care device.

A handheld optical sensor, the portMD-113, also with the ability to perform simultaneous detection of multiple sensing spots was proposed by Kozma *et al.* [65] as an alternative to cumbersome bench top instruments for fluorescence micro array detection.

The main principle of their design was to develop a compact, low energy consumption, and light device with no moving parts, with simple but reliable optical coupling and the

use of a microlens array to image the sensing spots excited by the evanescent field of a planar waveguide into a CCD image sensor. The planar waveguide was cut out from a 188 µm thick cyclic olefin copolymer film where a square area of 14 mm^2 contains a grid of 113 spots where the labeled analyte will be distributed. As seen on Figure 1.21, the light is coupled directly to the edge of the planar waveguide. The light from a laser diode (λ = 635 nm) was shaped into a line with the help of a Powell lens line generator prism and a half-cylinder lens to be then focused at the edge of the planar waveguide where an aperture was used to block the stray light. The fluorescence light emitted from the fluorescence spots would be then imaged by the microlens on the CCD image sensor. However, if it wasn't for the pinhole array in between the fluorescence spots and the microlens array the imaged spots would overlap and the stray light would increase the background noise. For a cleaner signal, a single-band bandpass interference filter was inserted before the CCD image sensor to prevent the residual excitation light to distort the results.
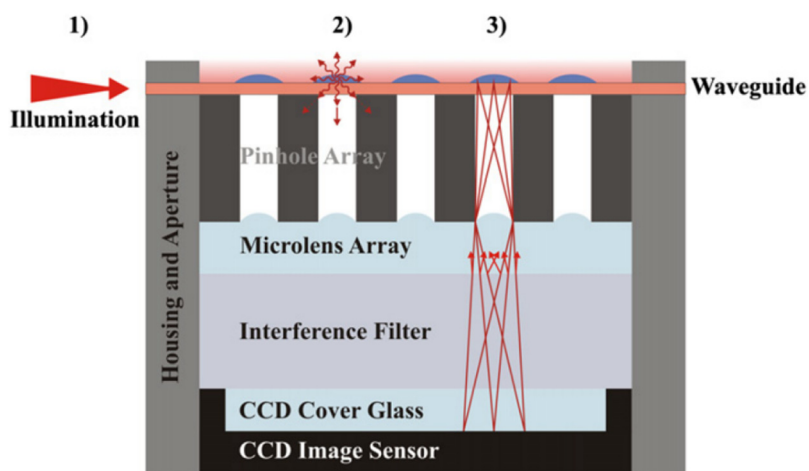
Figure 1. 21 **Scheme of the handheld microarray reader with the light path of the excitation and emission light. 1) Excitation light coupling 2) fluorescence emission from the sensing spots 3) imaging of the sensing spots into the CCD sensor. Picture taken from Fig.1 of [65].**

The device was designed so that there is no need to do any alignment between the source and the planar waveguide. To this effect, guiding edges on top of the pinhole array were used so that the glass slide containing the waveguide could be slid inside the housing of

the device (Figure 1.22) for alignment with the pinhole array and microlens array without effort.
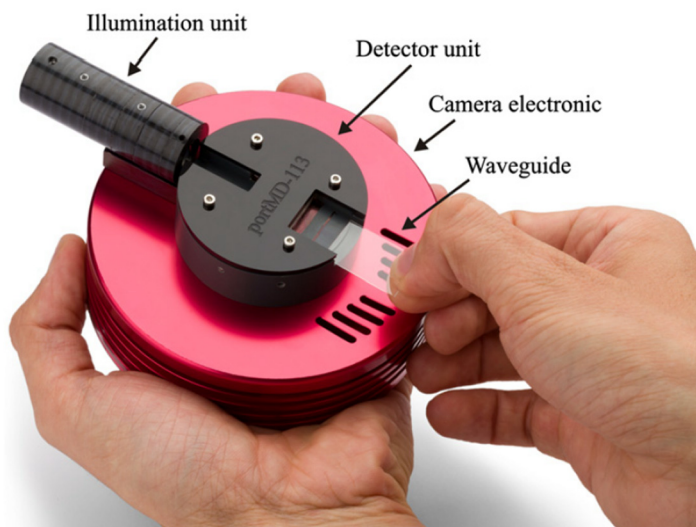
Figure 1. 22   **Photograph of the PortMD-113 with the glass slide (containing the waveguide) being inserted within the housing of the device. Picture taken from Fig.3 of [65].**

To demonstrate the capabilities of the device it was compared with the commercial gold standard, the Tescan LS Reloaded, for fluorescence measurements. To this effect, 8 concentrations of Alexa Fluor 647-conjugated mouse anti-goat IgG antibodies diluted in a pure solvent (Tween 20 0.05%-MilliQ water) were prepared. The solutions went from 1 $\mu g \cdot mL^{-1}$ to 8 $\mu g \cdot mL^{-1}$ in increment of 1 $\mu g \cdot mL^{-1}$ and were distributed as 1 nL droplets on the designed spots. The droplets were spotted successively in ascending and descending concentrations for the line 1-3 and 5-7 respectively, Figure 1.23a. The line 4 and 8 were spotted with antibody-free solutions. A blank spot was left at the center of a formation of 4 adjacent activated spots to investigate the crosstalk between the adjacent fluorescence sensing spots.
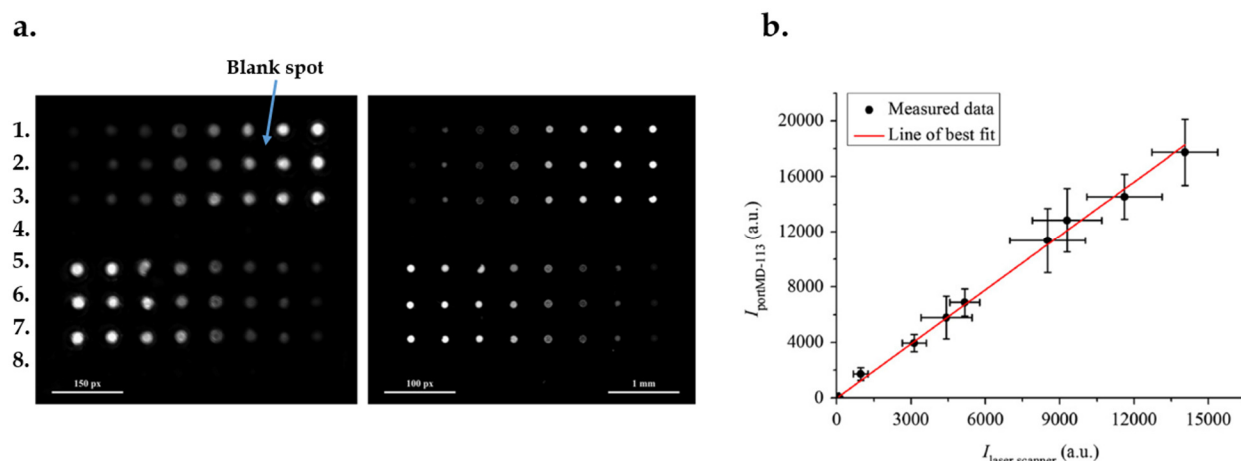
Figure 1. 23   Images of the sensing spots of the a) PortMD-113 b) reference laser scanner (Tescan LS Reloaded) c) correlation of fluorescence intensity values between the mean intensity values of the different concentrations measured with the portMD-113 and the reference laser scanner. Adapted from Fig.4 & 5 of [65].

As seen on Figure 1.23a, the images of the fluorescence spots for the portMD-113 are 2 fold bigger than the spots from the Tescan LS Reloaded. This effect is due to the magnification resulting from the arrangement and dimensions of the components of the optical system. To evaluate the dependability of the portMD-113 the mean values of the different concentrations (0 to 8 $\mu g \cdot mL^{-1}$) were plotted in function of the mean values of the reference laser scanner (error = standard deviation), Figure 1.23b. The coefficient of determination (R^2) of the fitted curve with respect to the linear regression of the data points was found to be 0.995, which corresponds to an excellent agreement. It was also reported that from the blank spots array the cross talk between the adjacent fluorescence spots revealed to be very weak. The limit of detection was found to be 1 fluorophore·μm^{-2} for the reference laser scanner and 10 times more for the portMD-113. Although the sensitivity of the proposed optical device is lesser than the "gold standard", its characteristics and capabilities as a handheld optical sensor makes it an advantageous choice for point of care analysis. Indeed, its smaller size, lower weight (400 g), quick detection (less than 20 sec) and the plug-and-play system makes it a better choice for a point of care device that could be used by untrained users.

1.2.2 Fluorescence detection by evanescent wave excitation from light guided in channel waveguides

As opposed to planar waveguides that have an optical confinement in only one transverse direction, channel waveguides confine the light transversally in 2 dimensions. Many kinds of channel waveguides have been developed, such as the buried waveguides (Figure 1.24a), strip-loaded waveguides (Figure 1.24b), rib waveguides (Figure 1.24d), diffused waveguide (Figure 1.24e), etc. However, to our knowledge, none or very few of these waveguides have been used for fluorescence biosensing except for the ridge waveguide, Figure 1.24c. The advantages of the ridge waveguide for fluorescence detection is that the core is surrounded on all sides by the cladding except for the bottom side which rest on the substrate.
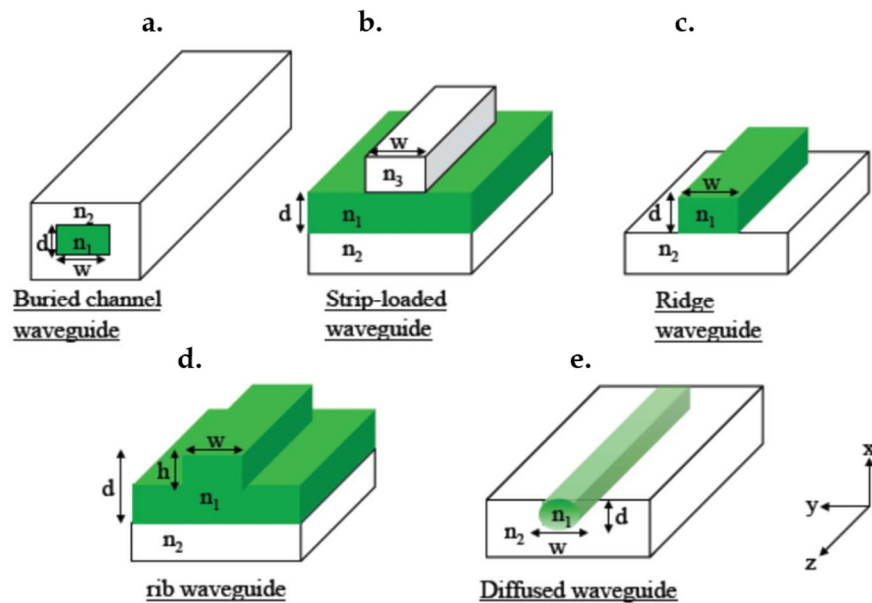
Figure 1. 24   Schematic representations of different channel waveguide configurations.

Aparicio *et al.* [66], exploited the guiding capability of channel waveguides to split a waveguide in two branches for the benefit to have a waveguide where a bioreactor was used for fluorescence sensing and another waveguide to monitor the stability of the excitation light ($\lambda = 473$ nm) to assure the reliability of the measurements. The Y-junction

separating the input waveguide into the reference waveguide and the waveguide with the integrated bioreactor well with the associated microfluidics can be seen on Figure 1.25a. The substrate and core of the waveguide were both deposited by plasma-enhanced chemical vapour deposition (PECVD) forming layers of 2 μm of silica (SiO$_2$, n = 1.45) and 950 nm of silicon oxynitride (SiO$_x$N$_y$, n = 1.85)), respectively, Figure 1.25b. Also, a 550 nm borophosphosilicate glass (BPSG, n = 1.45) layer was grown by low-pressure chemical vapour (LPCVD) as a cladding to improve the surface planarity of the core after the reactive ion etching (RIE). RIE combined with photolithography were used to shape the bioreactor and to thin out the core layer to increase the penetration depth of the evanescent field to favor the interaction with the labeled sample. Finally, a 50 nm layer of SiN$_x$ was coated by a chemical process to facilitate the immobilization of carboxyl moieties which would be marked with 5-(aminomethyl) fluorescein (AMF, a xanthene derivative) for fluorescence detection. The dimensions of the micro bioreactor were chosen to be large enough to make sure it could accommodate the functionalization of the sensing surface by means of a spotter. For this reason, the bioreactor was patterned to have an area of 50 × 50 μm^2.
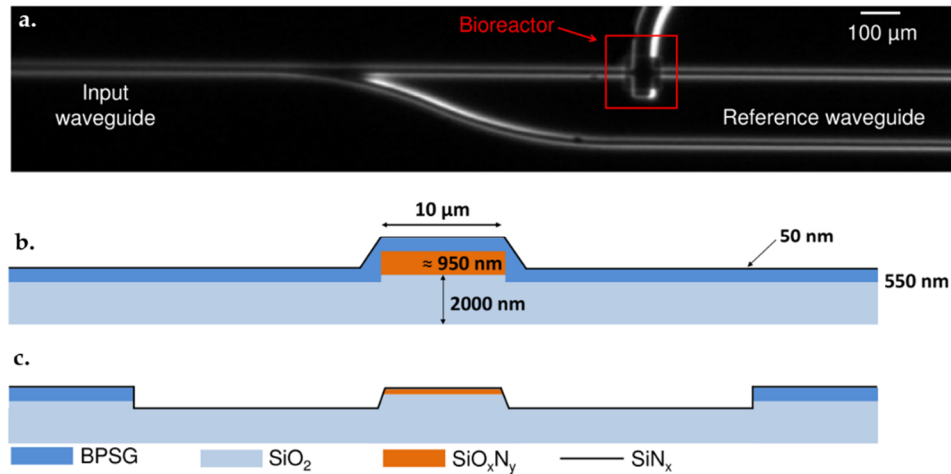
Figure 1. 25   **a) Photograph of the top view of the photonic layer b) Scheme of the cross section of the waveguide b) before and c) after the bioreactor. Adapted from Fig.1 of [66].**

To investigate the performance of the device for fluorescence detection, two experiments were conducted. The experimental setup used can be observed on Figure 1.26, where

the excitaion light is carried by an optical fiber to the waguide chip. The fluorescence emission is collected by an objective lens (20X) positionned perpendicularly to the bioreactor and carried by an optical arrangement to a spectrometer (SOPRA DMS2) to be spectrally analyzed.

a.   b.
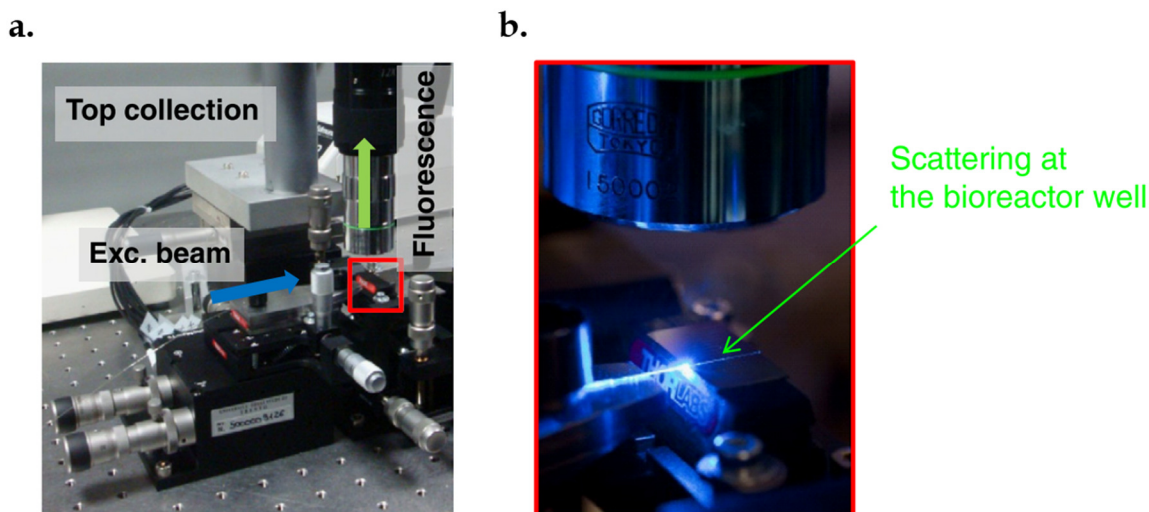
Figure 1. 26   a) Photograph of the experimental setup for the fluorescence detection b) Enlarged view of the chip with the scattering of the excitation light (λ = 432 nm) guided through the waveguide. Adapted from Fig.2 of [66].

The first experiment consisted in detecting the emitted fluorescence from the micro bioreactor filled with AMF-water solutions of different concentration. As seen in Figure 1.27a, the fluorescence emission of 4 different concentrations of AMF-water solutions were measured with a limit of detection of 10^{-8} M. The spectra peaks have a tendency to shift to longer wavelength for greater concentrations of AMF molecule. This is understandable, since the emission band of xanthene derivatives is known to red-shift when the species starts to aggregate [67]. The second experiment was the detection of the fluorescence emission after the immobilization of the AMF molecules dye on the functionnalized SiN_x layer (functionnalization protocol details in [66]). After the last washing step, the measurements revealed that a surface concentration of 10^{-11} mol·cm^{-2} of AMF molecules remained attached to the SiN_x layer on the sensing surface. The spectrum resulting from this detection is shown in Figure 1.27b. The emission band

extend from a wavelength of 500 to 550 nm, which confirms the presence of AMF dye molecules.
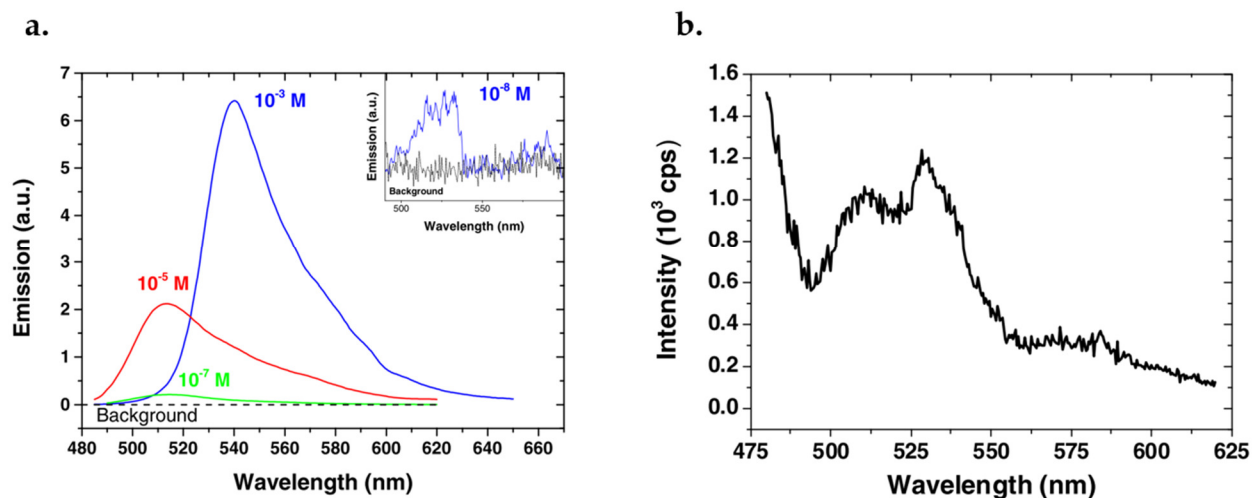
Figure 1. 27 **a) Fluorescence spectra of different concentrations of AMF-water solutions delivered in the bioreactor. b) Fluorescence spectrum of the bioreactor functionalized with a surface concentration of 10^{-11} mol cm^{-2} of AMF. Adapted from Fig.3 & 5 of [66].**

Potentially, this system could be used as a multi-analyte detection device if different bioreactors could contain different bio-recognition layers. Also, the penetration depth of the evanescent field could be easily modified to accommodate larger analytes by tuning the proportion of SiO_2 and Si_3N_4 in the fabrication of the silicon oxynitride core to modify its refractive index [68] or by increasing the solvent index of refraction that fills the bioreactor [69].

This ability of the channel waveguides to split was also taken advantage by Ozhikandathil *et al.* [70], but this time it was used to increase the area of detection and to increase the sensitivity of the fluorescence spectroscopy. On a planar platform, Ozhikandathil and Packirisamy have extended this principle to design a cascaded waveguide coupler, monolithically integrated on a silica-on-silicon platform [70]. The waveguide pattern was composed of a single waveguide split into multiple paths using *s*-bend couplers and subsequently combined into a single waveguide (Figure 1.28c). By splitting the waveguide into multiple paths, more area is available for detection. In addition, the

penetration depth of the evanescent wave was increased with the use of the s-bend and taper. The increased intensity of the evanescent field at the vicinity of the convex side of an s-bend waveguide, where an emitting point source is located, favors the fluorescence collection efficiency as shown by a finite difference time domain (FDTD) simulation on Figure 1.28ab. Several approaches to enhance both the intensity and penetration depth of the evanescent field produced by planar optical waveguides have been adapted from work on fiber optics. Indeed, it has been shown that by bending or tapering an unclad section of a fiber optic, it is possible to enhance the evanescent field by directing the light ray closer to the critical angle and increasing the number of reflections, respectively [71, 72].
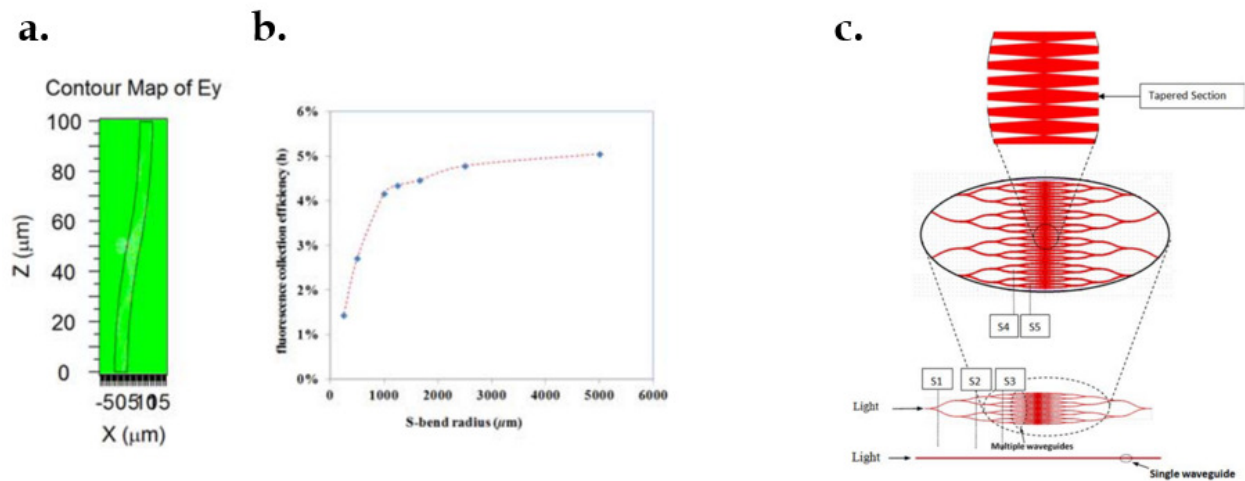
Figure 1. 28   **a) FDTD simulation of fluorescence coupling of light by *s*-bend and b) the estimated fluorescence collection efficiency against the radius. c) Schematic of evanescent wave sensor using cascaded waveguide coupler in comparison with a straight waveguide. Adapted from Fig.4 & 5 of [70].**

The fabrication process consisted in the deposition of two SiO_2 layers on a silicon wafer to form the bottom cladding (or susbstrate) and core of the waveguide. The first deposition resulted in a 14 µm layer of silica. For the second deposition session, the process parameters were changed to increase the index of refraction and resulted in a 6 µm layer of silica. Refractives indices of 1.445 and 1.457 for a wavelength of 635 nm were obtained for the bottom cladding and the core, respectively. The cascaded waveguide design was

patterned with the combination of the direct lithography and RIE methods. SEM photos of the top and facets view of the cascaded coupler can be seen in Figure 1.29.
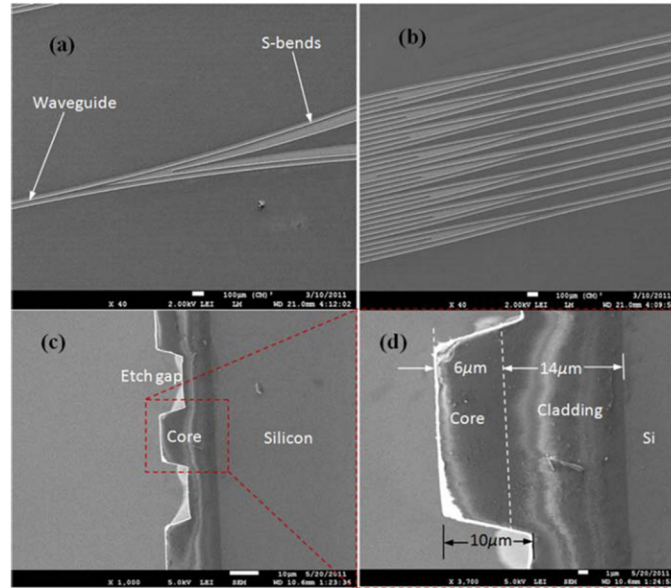
Figure 1. 29 **SEM photograph of the cascaded coupler showing a) the first s-bend coupler in stage S1 (top view), b) the multiple waveguides in stage S3 (top view), c) the etch gap profile and d) the dimensions of the facet. Picture taken from Fig.8 of [70].**

The experimental setup for fluorescence spectroscopy, Figure 1.30, made first use of an optical fiber (single mode) which was butt-coupled to the cascaded/single waveguide to couple the excitation light unto the system. Then, the excitation light and the evanescently coupled fluorescence light from the labeled target were collected by a spectrometer using another optical fiber (multimode) at the output of the waveguides.
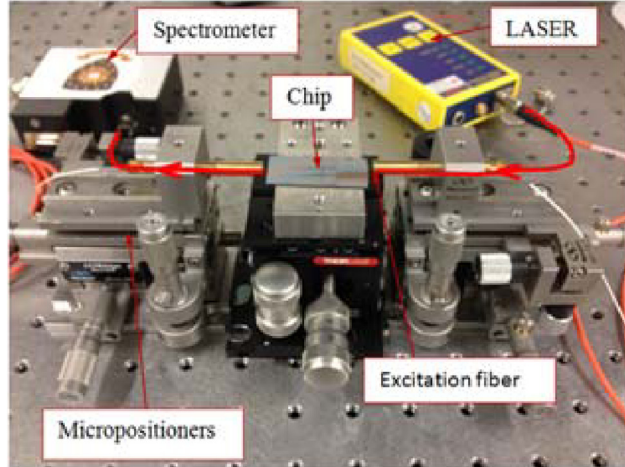
Figure 1. 30   Experimental setup for the fluorescence spectroscopy of Alexa 647 labeled rbST with the cascaded waveguide coupler. Picture taken from Fig.9 of [70].

To validate the cascaded waveguide design it was compared to a single waveguide for the fluorescence detection of recombinant growth somatotropin (rbST), an artificial hormone found in cow milk, tagged with Alexa 647 fluor dye. The calibration curves, Figure 1.31, revealed that the limit of detection of the fluorescently-tagged recombinant growth hormone was as low as 25 ng·mL^{-1}, and the sensitivity of the waveguide coupler system was more than 5 times higher than that of a single waveguide. These results indicate the possibility of developing sensitive integrated optical detections systems for lab-on-a-chip applications.
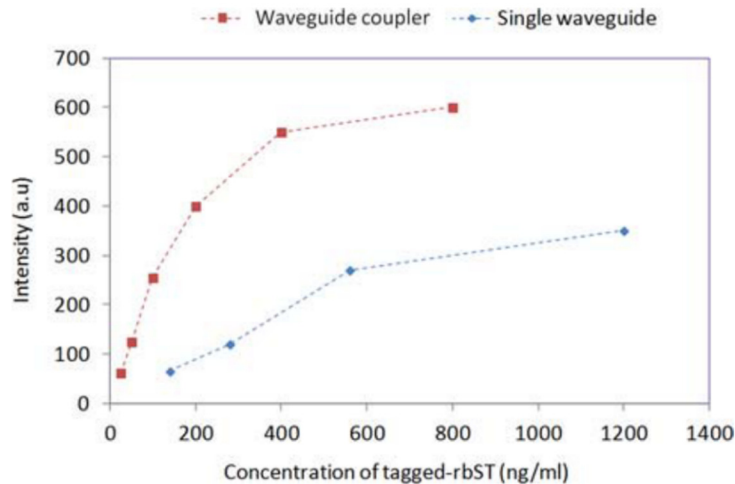
Figure 1. 31   Calibration curves from the detection of Alexa 647 labeled rbST with a) the single waveguide (blue diamonds) b) the cascaded waveguide coupler (red squares). Picture taken from Fig.15 of [70].

This asset of channel waveguides to be multiplied from only a single waveguide was also adopted by Liu *et al.* [73], but instead of using this property to increase the sensitivity of the detection it was used in a manner to increase the number of sensing spots to allow for the detection of 32 contaminants simultaneously. A scheme and a photo of the sensing system is illustrated on Figure 1.32ac. The waveguides were fabricated with a potassium ion-exchange process in BK7 glass substrates to better match the numerical aperture of the input fiber. As seen on Figure 1.32a, a 2.5 µm wide single mode waveguide splits in 2 steps with the help of Y-junction splitters to form 4 waveguides. These four waveguides expand in width by being tapered over 10 mm of length until reaching a width of 30 µm. Following the end of the tapers, 4 straight waveguides also of 30 µm of width have 8 sensing windows of 1500 µm × 300 µm each along their entire length. These sensing windows were etched from a silica coating of 1 µm of thickness deposited previously. A fully automated fluid system delivered the necessary solutions into the exposed waveguide area confined in the flow cell, Figure 1.33. A fiber coupled diode laser (λ = 635 nm) was used as the excitation light which was also pigtailed at the input of the chip as seen in Figure 1.32c. The emitted fluorescence light was collected by 32 polymer fibers (diameter: 1 mm) positioned perpendicularly to the 32 sensing windows. Subsequently, the fluorescence light was filtered by a long pass filter to block the scattered excitation light. The light was then transformed in a current by the photodiode, which was processed by a lock-in-amplifier. Since the system was conceived for the on-line and semi continuous detection of microcystin-LR (MC-LR) in lakes, an indirect competitive immunoassay was chosen as the method of immobilization due to its attribute to regenerate the chip surface for reuse. To this matter, a monolayer of BSA-MC-LR conjugate was first immobilized on the chip surface. Followed, by the delivery of a preincubated solution consisting of MC-LR and Cy5.5-labelled anti-MC-LR antibody.
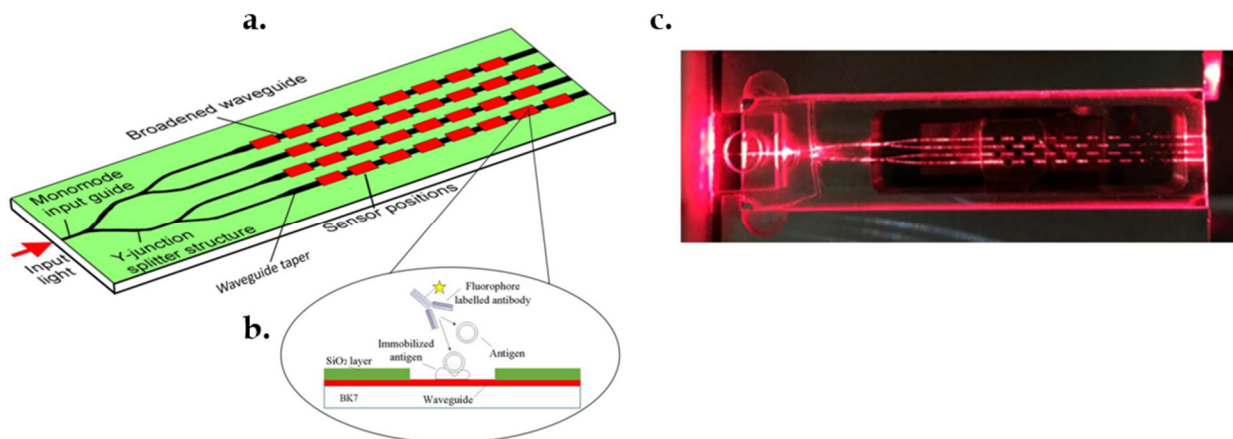
Figure 1. 32 Schematic drawings of a) the sensor layout b) the cross section of the sensing window with the surface chemistry. c) Photograph of the sensor showing the excitation light propagation and scattering. Adapted from Fig.1 of [73].
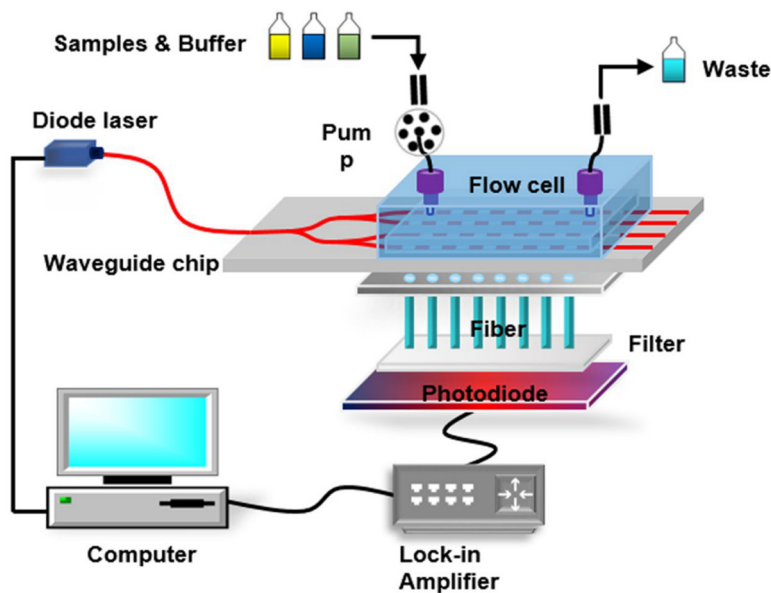
Figure 1. 33 Scheme of the entire setup for the multichannel biosensor. Picture taken from Fig.3 of [73].

The purpose of tapering the waveguide was to diminish the rate of photobleaching by lowering the optical density of the the excitation light at the surface of the chip. Indeed, the larger surface of the taper will allow for more fluorophores to be excited, keeping the same peak fluorescence emission, but at the same lowering the rate photobleaching. This allows for a longer acquisition time and a consequent increase of the signal to noise ratio

and lowering the limit of detection (LOD). The taper was parabolic in width, which favors a better adiabatic transition i.e not allowing for the excitation of higher modes when the width of the taper increases. The 3D beam propagation method was used to design the adiabatic parabolic tapers. As seen in Figure 1.34a, the optical surface & emitted intensity were estimated from the start of the taper (2.5 µm waveguide) to the end of the tapers width (30 – 60 µm). As the tapers widen, higher order modes are more susceptible to be excited. However, as seen on the simulation of the propagation of the excitation light through the 60 µm taper, Figure 1.34b, the single mode was preserved until the end of the taper. Assuring a uniform illumination of the fluorophores on the sensing surface.
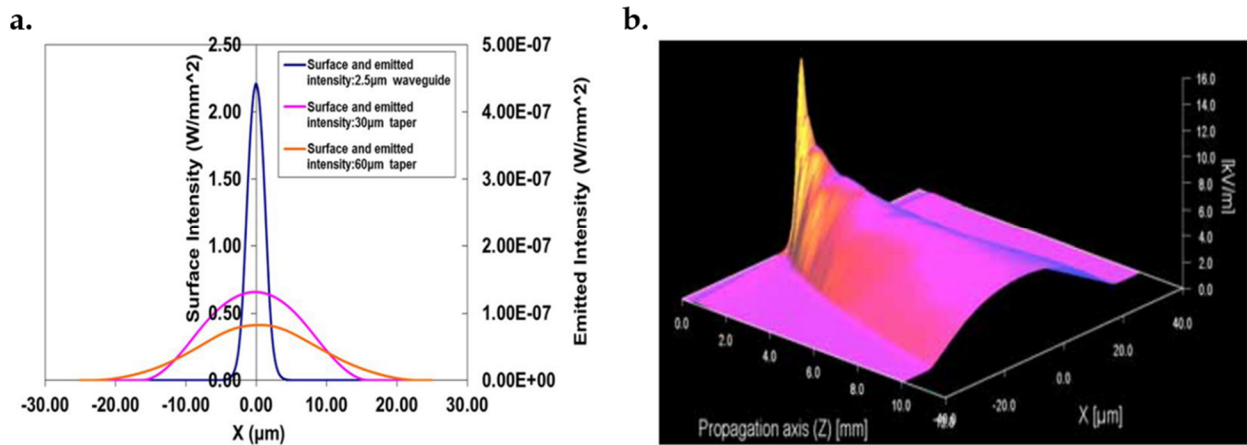
Figure 1. 34   **a) Surface intensity at the start (2.5 µm width) and at the end of the 30 µm and 60 µm tapers. b) Electric field strength from the start (2.5 µm width) to the end of the 60 µm taper over a length of 10mm. Pictures taken from Fig. 2 of [73].**

To determine which taper width will result in higher sensitivity, different concentrations of Cy5.5-labelled anti-MC-LR antibody solutions were administrated to the corresponding waveguides. On Figure 1.35, the results of the fluorescence signal are seen for the untapered, 30 µm and 60 µm waveguides. As expected, the tapered waveguides offered a higher emitted fluorescence due to, as explained above, the greater area of immobilization for the labeled antibodies and the lower rate of photobleaching. The fluorescence signal for the 60 µm taper was lower than the 30 µm taper due to less efficient collection into the fibers. For this reason, the 30 µm taper was preferred as it promotes a higher fluorescence emission for the same excitation power.
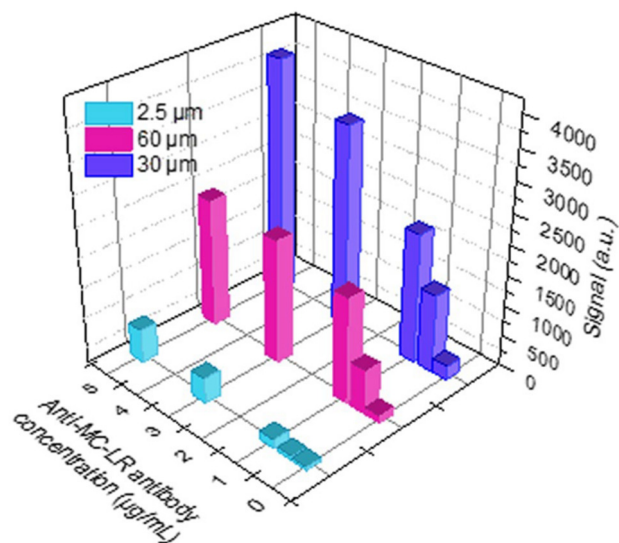
Figure 1. 35 **Fluorescence signals from different concentrations of Cy5.5-labelled anti-MC-LR antibody solution detected from the 2.5 μm waveguide, the 30 μm and the 60 μm taper. Picture taken from Fig.4 of [73].**

With the optimized design, the sensor was finally tested with an indirect competitive immunoassay for the detection of a series of different concentrations of MC-LR. The linear dynamic range was of 0.36 – 2.50 μg·L^{-1} and the LOD of 0.21 μg·L^{-1} as illustrated on the calibration curve on Figure 1.36. These results were satisfying, since the World Health Organization (WHO) recommended a limit of 1 μg·L^{-1} of MC-LR in drinking water.
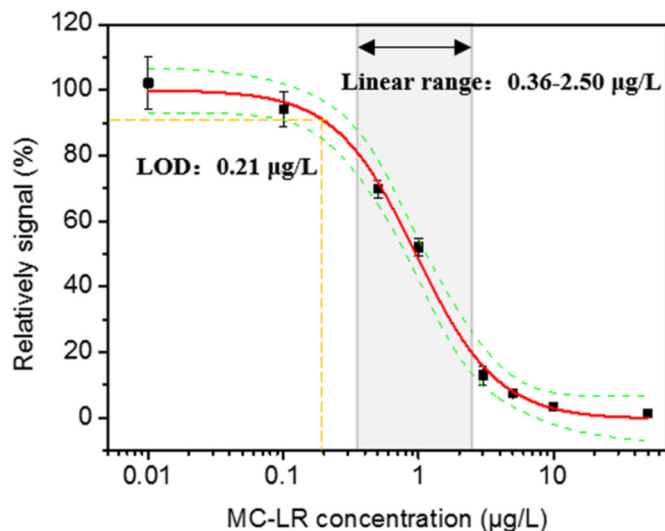
Figure 1. 36   Calibration curve from the detection of MC-LR with the multichannel immunosensor. (Green lines represents 95% confidence range). Picture taken from Fig.6d of [73].

A regeneration process was also put in place for multiple uses. Indeed, with the help of a solution of 0.5% sodium dodecyl sulfate (SDS), the regeneration of the chip surface was performed up to a 100 times with less than 10% of signal decrease using lake water samples. As such, this sensor is a good candidate for on-line, semi-continuous, and cheap water monitoring. Also, a recovery study was performed with spiked water from two different lakes (Fuhai lake/Beihai lake, Beijing) with 3 different concentrations (0, 0.5, 1 µg·L^{-1}) of MC-LR. The average recoveries went from 84 ±7 % to 108 ± 6 %, indicating good accuracy of the biosensor.

Most of the channel waveguides used for fluorescence spectroscopy are made with inorganic materials, as shown above. However, Jiang *et al.* [74] fabricated a polymer waveguide on a silica substrate for this purpose and tested it with fluorescence detection of Cy3-conjugated antimouse IgG. More precisely, the waveguide was made of a core of cross-linked SU-8 photoresist ($n_{532\ nm}$ = 1.59) on a substrate made of a 5 µm thick silica layer ($n_{532\ nm}$ = 1.46) oxidized from a silicon wafer and the liquid buffer ($n_{532\ nm}$ = 1.33) was used as the cladding, Figure 1.37a. Both ends of the waveguide are tapered on a distance of 1 mm from the edge of the chip with a width of 120 µm to the waveguide with a cross section of 40 × 40 µm and 30 mm of length, Figure 1.37b. Tapering of the extremities of the waveguide promoted better coupling efficiency with the input/output optical fibers,

39

0.27 NA graded-index 62.5-µm multimode fibers. The method of fabrication was to spin coat the SU-8 photoresist on the oxidized silicon wafer and to pattern it with UV lithography while following the corresponding baking steps from the manufacturer's protocol.

a.

b.
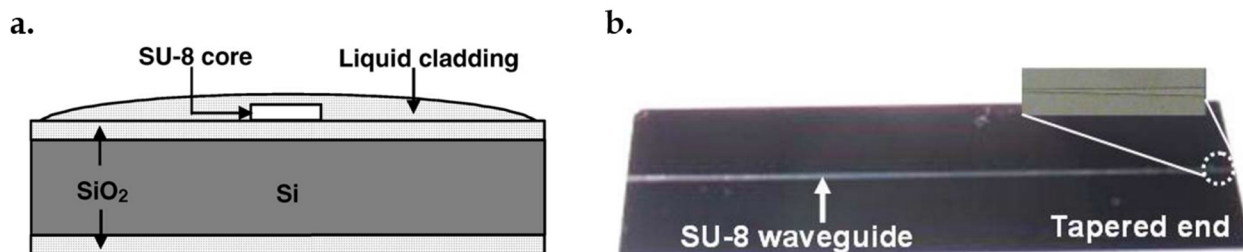
Figure 1. 37   a) Scheme of the cross section of the waveguide. b) Photograph of the chip with the microscopic image of the tapered end. Adapted from Fig.2 of [74].

A 532 nm diode pumped solid-state laser was used as the excitation light and was coupled into the optical fiber with the help of a lens after passing through an attenuator to prevent saturation of the signal, Figure 1.38a. Then, the input optical fiber carrying the excitation light was butt-coupled to the waveguide, Figure 1.38a. The evanescent wave resulting from the propagation of the excitation light within the waveguide excites the labeled antigen at the surface on the waveguide, Figure 1.38b. The emitted fluorescence light was then coupled into the waveguide and guided together with the excitation light to the output of the waveguide. Subsequently, before being collected by the multimode output fiber the signal passed through a bandpass filter with a 570-nm central wavelength and a 10 nm FWHM which prevented the excitation light to go through but allowed the fluorescence light from the Cy3 dye to be guided to the spectrometer for spectral analysis, Figure 1.38a.
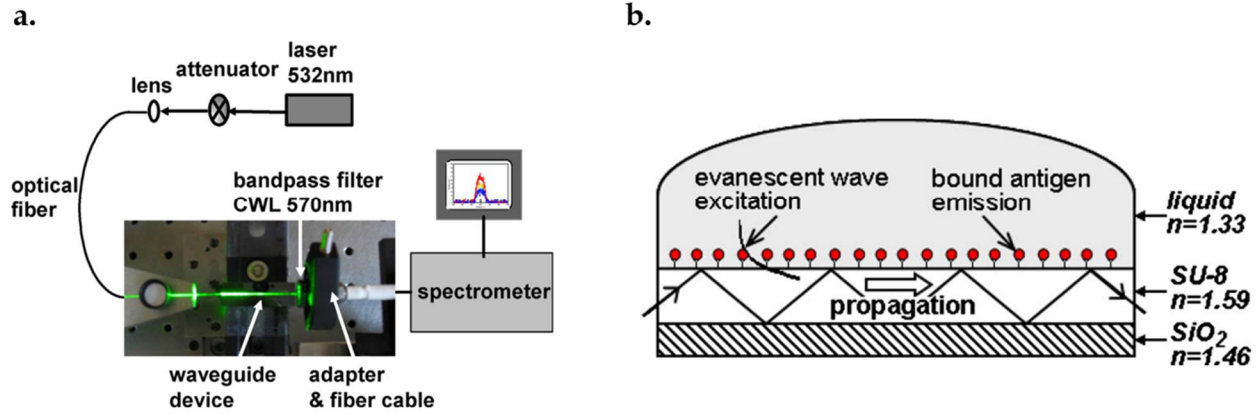
Figure 1. 38   a) Experimental setup for fluorescence spectroscopy based analysis with the SU-8 waveguide b) Schematic of the biosensor showing the light path propagation and surface chemistry. Adapted from Fig.1 & 6 of [74].

To test the waveguide for biosensing, a fluorescence spectroscopy experiment with the setup shown above was performed with different concentrations of Cy3-antimouse-IgG which were delivered on the waveguide where mouse IgG antibodies were previously immobilized. The Cy3-antimouse-IgG concentrations ranged from 0 to 150 µg·mL^{-1}, Figure 1.39a. As seen in Figure 1.39a, the spectrum for 0 µg·mL^{-1} is not nil, this is due to the autofluorescence from the SU-8 photoresist resulting from the 532 nm excitation light. It was reported that the spectrum with bare SU-8 or with the biolayers before Cy3-antimouse-IgG binding were similar, hence the spectrum for 0 µg·mL^{-1} was taken as the reference spectrum. To investigate the binding activity of the labeled antigen with the antibodies, the waveguide emission output power in relation to the labeled antigen concentration was derived with the help of the Langmuir isotherm, giving the following equation:

$$\frac{P_{o-em} - P_0}{P_{sat} - P_0} = \frac{Kc}{1 + Kc} \qquad (1.1)$$

P_{o-em} being the waveguide output power of the labeled antigen emission, P_0 the output power of the reference spectrum, P_{sat} the power at the saturation concentration, K the binding constant and c the concentration of the Cy3-antimouse-IgG. The fitting of the experimental data based on the equation (1.1) was possible with a $K = 53 \, mL \cdot mg^{-1}$

as seen on Figure 1.39b. Denoting that the labeled antigens binding activity with the antibodies could be quantified following the Langmuir model. Also, the curve responded linearly for concentration lower than 30 µg·mL^{-1}, hence the sensitivity was determined from the linear slope. Which revealed a change of 2% for the optical power for each 1 µg·mL^{-1} of change in the Cy3-antimouse-IgG concentration. This work showed that rectangular polymer waveguides could be used for biosensing by means of evanescent wave fluorescence spectroscopy.
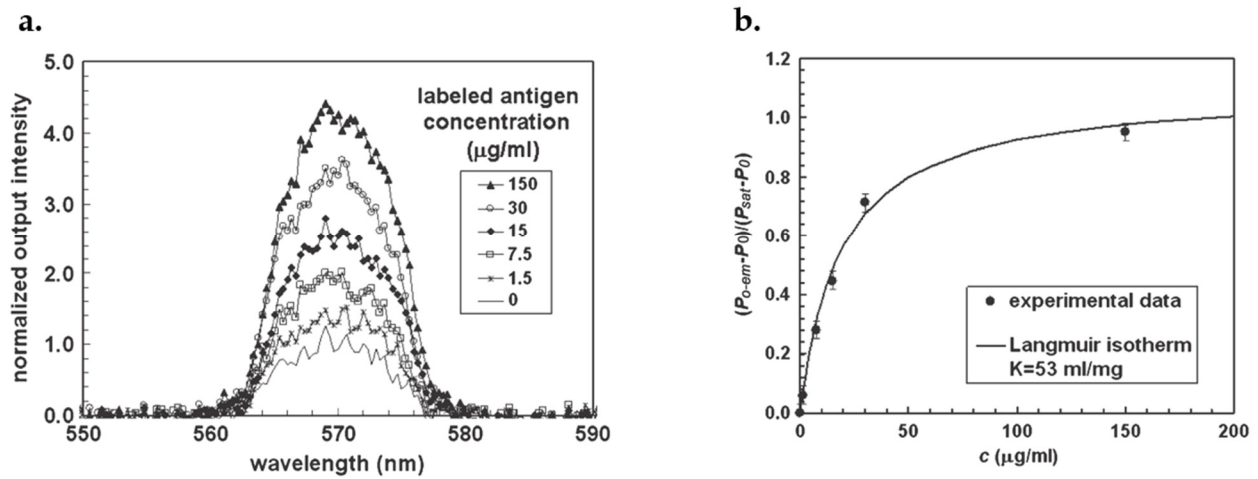
Figure 1. 39   a) Fluorescence spectra from the detection of the Cy3-antimouse-IgG. b) Experimental data fitted with eq. (1.1). Adapted from Fig.8 & 9 of [74].

To our knowledge very few groups have used polymer rectangular waveguides for fluorescence spectroscopy. Yet, polymer rectangular waveguides could be advantageous in many senses for this purpose compared to inorganic materials. Indeed, polymers as a material for waveguide structures, allows for easy, cheap, and quick fabrication processes with relatively simple equipment such as a spin coater and UV mask aligner. In contrast, silicon/silica based waveguides require long oxidation sessions, or deposition with PECVD and RIE etching, with also the addition of spin coating and UV lithography for design patterning. Industrially speaking, polymer materials offer simple manufacturing processes for microfabrication purposes at large scale such as embossing [75], molding [76], and even by printing [77].

1.3 Structure of the thesis

Optical technologies for biosensing by fluorescence detection means that were presented above offer, for the most part, great sensitivity and useful applications. However, in terms of miniaturization, mass production, and point-of-care analysis, only the planar and channel waveguides stand out. One of the drawbacks of planar waveguides is that the optical coupling for the input/output light is somehow complex and doesn't allow for total planar integration of all the optical components. Also, its intrinsic structure doesn't allow for much flexibility in terms of geometrical shaping. On the contrary, channel waveguides or more particularly rectangular waveguides are ideal for monolithic planar fabrication including the integration of other optical components, for optical coupling without alignment and for the design of elaborate microstructures for optical manipulation. These characteristics are favorable for lab-on-a-chip systems, which can be integrated with microfluidics for delivery of the biochemical solutions to the sensing platforms. The polymer material chosen for the core of the waveguides for this thesis was polymerized SU-8 photoresist for its advantageous properties for our applications. Indeed, our work deals with visible light and SU-8 has very good transparency for wavelengths ranging from ~400 to 800 nm [78]. Also, SU-8 allows for high resolution of fabrication [79, 80] which is crucial for low propagation losses. And since the waveguides were subjected to harsh rinsing and manipulation the remarkable structural solidity of SU-8 [81] was essential to perform the experimental tasks. Moreover, the biocompatibility of SU-8 allowed to use biological samples for biosensing [82]. For all these reasons, SU-8 rectangular waveguides were preferred to perform this work which focus on enhancing the performance of the evanescent wave fluorescence spectroscopy with polymer waveguides for biosensing purposes.

Before testing SU-8 waveguides for evanescent wave fluorescence spectroscopy, the fabrication and characterization of the SU-8 waveguides were performed for silica and quartz substrates in **Chapter 2**. For the first time, a novel fabrication for SU-8 and eventually for other polymer waveguides was developed and optimized for quartz substrates. Lower propagation losses, an increase in refractive index, and better reproducibility was found for SU-8 waveguides fabricated with the novel fabrication

method than using the standard protocol used for the SU-8 on silica waveguides. The optimized fabrication protocols described in this chapter for the SU-8/quartz and SU-8/silica waveguides are used for all the remaining chapters.

As understood from the previous section, the optical characterization of the SU-8/quartz waveguides revealed lower optical propagation losses and an increase in refractive index compared to the SU-8/silica waveguides. Also, the quartz substrate was measured to have a lower refractive index than the silica layer. Different refractive indices for the cores and substrates will result in different asymmetry. It will be the purpose of the **Chapter 3** to study the performance of both waveguides taking into account the different characteristics of each. Indeed, different propagation losses and asymmetries between the SU-8/quartz and SU-8/silica waveguides will affect the fluorescence output of the aforementioned properties. To this effect, 3D FDTD simulations were used for analyzing the impact of the different asymmetries on the fluorescence collection efficiency of the SU-8/quartz and SU-8/silica waveguides for point sources located at their vicinities. Also, an evanescent wave fluorescence spectroscopy experiment with different concentrations of Alexa 647 Fluor labeled BSA molecules was performed on both of the waveguides to compare the performance of both waveguides in terms of sensitivity and limit of detection.

The 3D FDTD simulations and the fluorescence spectroscopy experiment showed that the novel fabrication method for the SU-8/quartz waveguide showed greater potential for fluorescence detection than the SU-8/silica fabricated with the standard protocol. However, the 3D FDTD simulations were very lengthy in time. Consequently, an analysis on the variation of the different waveguide parameters (index of refraction, dimensions, asymmetry) on the fluorescence collection efficiency will be even more time consuming. For this reason, the **Chapter 4** will be combine a modal propagation approach to calculate the fluorescence collection efficiency of planar waveguides with point sources at their vicinity with the effective index method to perform the aforementioned analysis in a quick manner. Also, this new calculation method was used to make an analysis of the fluorescence collection efficiency of both waveguides for varying parameters (core & substrate index, dimensions). The experimental data from the previous chapter are used to compare the fluorescence collection efficiency calculated for both the SU-8/quartz and SU-8/silica waveguides.

The previous two chapters prove that it was possible to increase the fluorescence output of the waveguides by diminishing the optical propagation losses and increasing the core refractive index by adjusting the fabrication process parameters. Although the fluorescence output could be further increased with more control over the fabrication parameters and further optimization, it would reach a threshold if, hypothetically, the waveguide's walls were free from roughness and the core index of SU-8 will probably not exceed 1.6 for the fluorescence light ($\lambda = 671$nm). Thus, to better the performance of the sensor, another path was taken in **Chapter 5** by increasing the sensing area which subsequently increased the fluorescence yield. The chosen design was the cascade waveguide for its ability to keep simple direct coupling for the input/output fiber while increasing the area of immobilization for the labeled targets.

The cascaded waveguide design successfully increased the sensitivity comparatively to the straight waveguide. However, optical losses from the multiple junctions and the modal restriction of the output waveguide to guide fluorescence signals with modes that it couldn't support hindered the fluorescence yield expected from the increased area of immobilization. To address these issues, novel designs as the doubled and tripled waveguides were developed in **Chapter 6**. The particularities of these designs compared to the cascaded waveguide were that instead of having multiple ramifications only 2 or 3 straight waveguides were used as a mean to increase the area of immobilization of the labeled targets and also only 2 junctions were needed to support the straight waveguides. Hence, less waveguides recombining into the output waveguide lowered the mode order of the fluorescence signal allowing more evanescently coupled modes to be guided through the output waveguide. Also, less junctions prevented excessive optical propagation losses.

1.4 Contributions

Published articles (Chapters 2 & 3):

1. A.-H. Jalal, G. Marc Andre, and P. Muthukumaran, "Silicon-free, low-loss and high contrast polymer multimode waveguides," Journal of Micromechanics and Microengineering, vol. 27, no. 10, p. 105006, 2017.

2. J. Abdul-Hadi, M. A. Gauthier, and M. Packirisamy, "Polymer on quartz waveguide sensing platform for enhanced evanescent fluorescence spectroscopy," IEEE Photonics Journal, pp. 1-1, 2018.

Submitted articles (Chapters 4, 5 & 6):

1. J. Abdul-Hadi, M. A. Gauthier, and M. Packirisamy, "Polymer waveguide biosensor for enhanced evanescent wave fluorescence detection," Optics Letters, December 12, 2018.

2. J. Abdul-Hadi, M. A. Gauthier, and M. Packirisamy, "Cascaded optical polymer waveguide for enhanced fluorescence evanescent wave spectroscopy," Journal of Biophotonics, December 12, 2018.

3. J. Abdul-Hadi, M. A. Gauthier, and M. Packirisamy, "Doubled and tripled optical polymer waveguides for enhanced fluorescence evanescent wave spectroscopy," Photonics Research, December 12, 2018.

Conference:

1. J. Abdul-Hadi *(Oral)*, Gauthier MA, Packirisamy M, "Air-cladded Optical Waveguide Array for Enhanced Fluorescence Detection," in 98th Canadian Chemistry Conference and Exhibition, CSC 2015, Ottawa June 2015.

Standard operational procedures (SOPS):

1. J. Abdul-Hadi, Gauthier MA, Packirisamy M, SOP for the fabrication of SU-8 waveguides on a quartz substrate, December 2018.
2. J. Abdul-Hadi, Gauthier MA, Packirisamy M, SOP for the fabrication of SU-8 waveguides on a silica substrate, December 2018.

CHAPTER 2

SILICON-FREE, LOW-LOSS AND HIGH CONTRAST POLYMER MULTIMODE WAVEGUIDES

2.1　Introduction

In the early ages of microfabrication, silicon was the preferred structural material and was used almost exclusively. While silicon-based microfabrication remains very popular, fabrication costs are high and silicon is frangible, optically opaque (to visible light), and poorly biocompatible (important for implantable devices). In response to these shortcomings, polymers have emerged as alternatives to silicon, due to their simpler fabrication processes, low cost, scalability, optical transparence in the visible range, and biocompatibility. For these reasons, optical polymer waveguides are regarded as attractive replacements for optical silica waveguides used for sensing and telecommunication applications. In 1989, IBM developed the SU-8 photoresist [83], which could reach high degrees of crosslinking during polymerization due to its eight reactive epoxy groups (on average) per monomer. This property of SU-8 gives it high mechanical strength [84] and fast polymerization kinetics, which contribute to high resolution [85]. These characteristics of SU-8 also make it a good candidate for micro and nanofabrication. Indeed, its optical transparency over a wide bandwidth [86] and ability to produce high-resolution structures, make it a material of choice for many integrated optical devices [87-90]. The fabrication and characterization of single and multimode optical SU-8 waveguides has been performed by several groups [86, 91-95]; though most of these studies employ substrates made of silicon dioxide, glass, or polymers. However, alternative substrates such as fused quartz offer other advantages. Since fused quartz, compared to other glasses, is made solely out of silica, it represents an interesting alternative substrate for optical waveguides. In contrast to the thick layer of silicon oxide on a silicon wafer it simplifies the process and avoids optical absorption by the underlying silicon substrate. In addition, it provides better confinement since its index of refraction is

slightly lower than silicon oxide, provides a sturdier platform, and is completely transparent (possibility to illuminate the optical waveguides from the base in case of fluorescence microscopy or bio sensing). Moreover, a substrate with a lower index of refraction contribute in increasing the penetration depth of the evanescent field in the cladding, this property is used in a greater extent for the reverse symmetry waveguide to detect bacteria and living cells [96]. This contribution presents the protocol to fabricate 10 × 5 µm SU-8 waveguides with air as cladding on a fused quartz substrate by UV photolithography. The optical propagation losses at 635 nm are reported and compared to equivalent waveguides fabricated using the standard protocol on a silicon dioxide substrate.
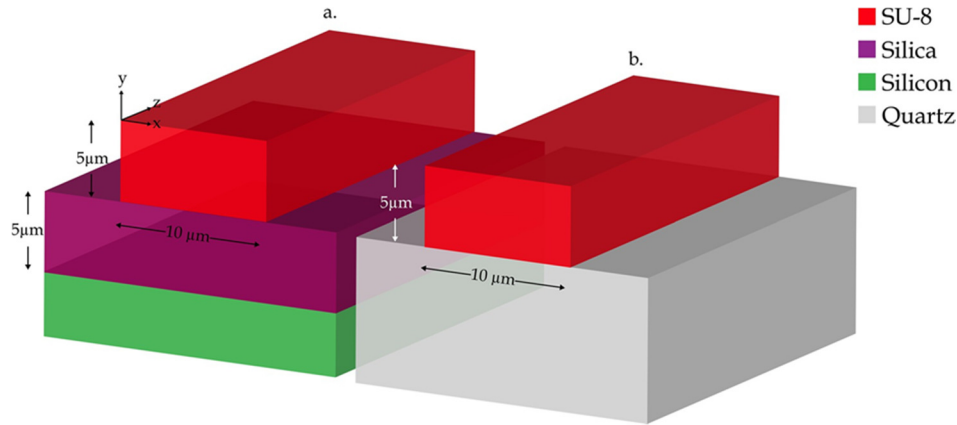
Figure 2. 1   SU-8 waveguides on (a) silica-on-silicon and (b) quartz.
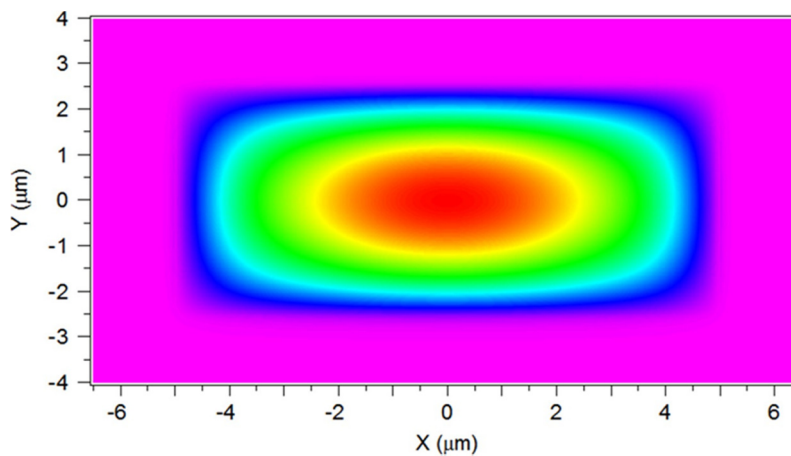
Figure 2. 2   Electromagnetic field distribution of the fundamental quasi-TE mode at the output of the SU-8 waveguide on quartz.

2.2   Design

The chosen dimensions for the SU-8 cores were 10 µm for the width and 5 µm as thickness. These SU-8 cores were fabricated with different protocols according to their substrates. The first substrate is a 5 µm grown silicon dioxide layer on silicon, and the second a 1 mm thick fused quartz wafer. The indices of refraction of the substrates and cores were measured by ellipsometry and are 1.4597 and 1.4567 for the silicon dioxide and the fused quartz and 1.5826 and 1.5896 for the SU-8 cores on silica and fused quartz respectively. The different processes involved in the fabrication of the SU-8 cores affected their refractive indexes. This phenomenon will be addressed later in the characterization section. A scheme of the two SU-8 waveguides on their respective substrates can be seen in Figure 2.1.

Although the dimensions and characteristics of the SU-8 waveguides described above allow them to excite many modes, a simulation was performed with the beam propagation method with the software Beam Prop of Synopsis, to show the electromagnetic field distribution of the quasi-TE fundamental mode at the output of the SU-8 waveguide on quartz Figure 2.2. The wavelength chosen for the simulation was the central wavelength of the laser (λ = 635 nm) and the indices of refraction were 1.5896 and 1.4567 for the SU-8 core and the quartz substrate respectively.

2.3   Fabrication

2.3.1 SU-8 waveguides on a silicon dioxide substrate

A four inch diameter silicon wafer with a thickness of 500 µm (Rogue Valley Micro Devices, Medford, USA) and possessing a 5 µm thick silica cladding grown by wet thermal oxidation was used as substrate. SU-8 5 photoresist (Microchem, Newton, USA) was used because of the desired thickness of the waveguide. The oxidized silicon wafer was carefully rinsed with acetone and isopropanol, dried with a stream of nitrogen, and spin coated with SU-8 5 (8 ml) in two steps: 500 rpm for 10 s then 3000 rpm for 30 s as shown in Figure 2.3(i(a)). Solvent was evaporated by a soft bake (SB) on a hot plate at

65 °C for 2 min and then at 95 °C for 5 min as presented in Figure 2.3(i(b)). Using a mask aligner, the SU-8 5 photoresist was exposed for 18 s under a 365 nm I-line UV light at a 9 mW cm^{-2} intensity to transfer the photomask (chrome on soda lime, 3 µm resolution) to the resist as in Figure 2.3(i)c)). Then, a post-exposure bake (PEB) at 65 °C for 1 min and at 95 °C for 2 min was performed, Figure 2.3(i(d)). Development of the pattern was accomplished by immersing the wafer for 2 min in SU-8 developer solution (Microchem, Newton, USA) followed by a dip of a few seconds in isopropanol to stop the reaction, Figure 2.3(i(e)). After rinsing the wafer with the developed pattern using water and gently drying with a stream of nitrogen, a hard bake at 150 °C for 1 h was carried out to stabilize the properties of the polymer, Figure 2.3(i(f)). Scheme of the SU-8 waveguide on silica is shown in Figure 2.1(a). This process will be called Process SU-8/SiO$_2$ in the remainder of the document.
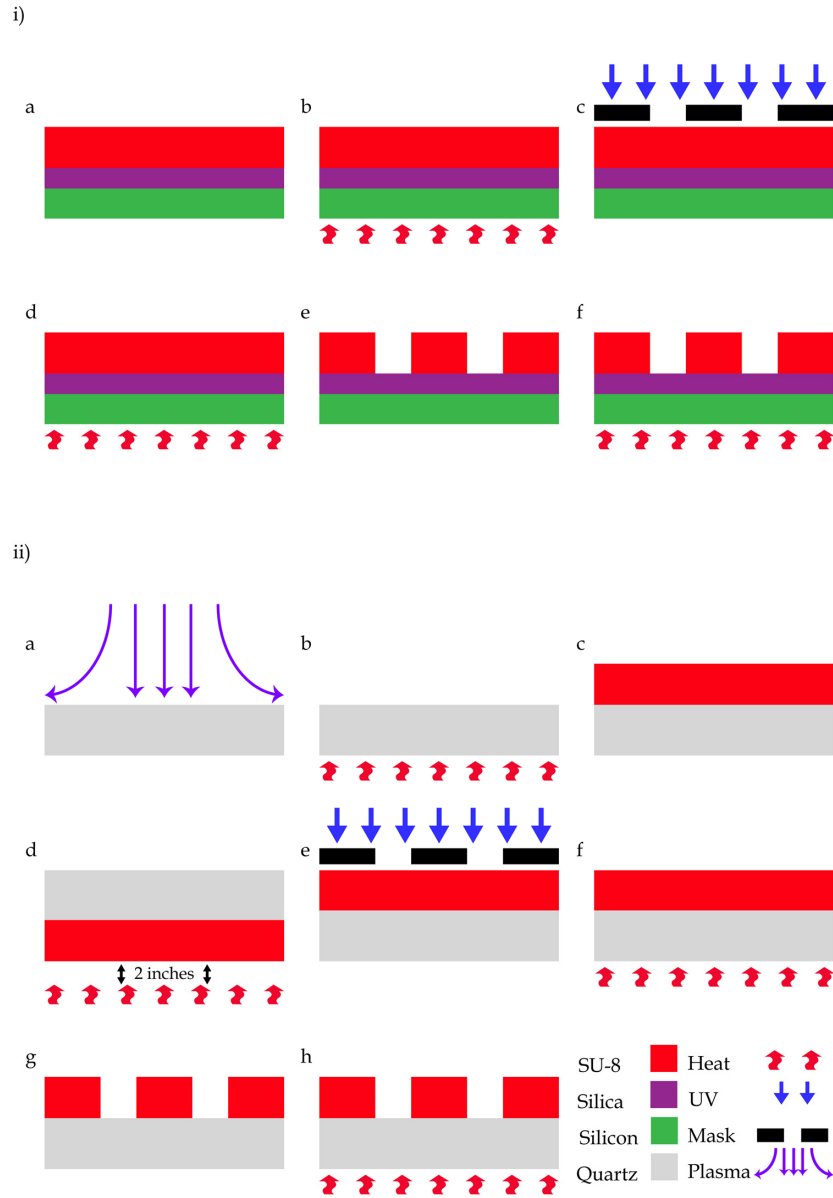
Figure 2. 3   **(i) Illustration of the main fabrication steps for SU-8 waveguides on an oxidized silicon wafer and (ii) on a fused quartz wafer. Details are given in the fabrication section.**

2.3.2 SU-8 waveguides on a fused quartz substrate

To our knowledge, this is the first study that investigates the preparation of SU-8 waveguides on a fused quartz substrate. A four inch fused quartz wafer with a thickness of 1 mm (Semiconductor Wafer, Hsinchu, Taiwan) was selected as substrate, and SU-8 5 photoresist was selected as the core material for the waveguides, as above. The substrate was rinsed with acetone and isopropanol, and dried with a stream of nitrogen.

To assure optimal adhesion and uniformity of the photoresist, the surface of the quartz needed to be further modified. Indeed, a fused quartz surface has a lower OH group content than silica, making it more hydrophobic. This resulted in greater shrinking of the photoresist after spin coating. To increase the wettability of the surface, the fused quartz wafer was hydroxylated by exposure to oxygen plasma for 1 min, Figure 2.3(ii(a)), which also removed organic impurities. While making the fused quartz surface more hydrophilic, treatment with oxygen plasma decreased adhesion of the photoresist due to adsorbed water, resulting in holes in the photoresist after spin coating, and loosening of the waveguides after development. In order to reduce hydrophilicity, the surface was heated at 150 °C for 2 ½ min on a hotplate, Figure 2.3(ii(b)), after the oxygen plasma treatment. Using the same spin coating conditions as for the silicon oxide substrate, the photoresist spread uniformly over the surface. After the spin coating, Figure 2.3(ii(c)), the photoresist was developed as for the silicon dioxide substrate, though delamination of the waveguides was observed along cracking. Because fused quartz and silicon dioxide have almost the same coefficients of thermal expansion, this phenomenon was not expected to be the cause of the cracking. This suggested adhesion between the polymer and the fused quartz surface was the cause of this phenomenon. Indeed, a similar problem was reported by Keller *et al.* [97] for thin SU-8 films on silicon wafers. The authors' approach to avoid cracking was to promote higher cross linking density of the resist by increasing the solvent concentration. One way to achieve this is to reduce the temperature of the SB from 65°C to room temperature, and to perform it over a longer period of time. Delamination, which is mainly caused by polymerization stress, can also be diminished by lowering the PEB temperature (T_{PEB}) and increasing its time. All of these parameters, including exposure conditions, have to be balanced out to maintain good resolution, and were optimized empirically. The optimized procedure, Figure 2.3(ii), for our desired waveguide thickness is as follows: after spin coating, Figure 2.3(ii(c)), the SU-8 5-coated substrate was left at room temperature (23 °C) for 225 min. To prevent the resist from sticking to the mask, it was dried for 30 s by holding the wafer with the resist side facing down at a distance of 2 inches from the hotplate (65 °C), so that only the surface dries up, Figure 2.3(ii(d)). Thereafter, the photomask was fixed in the mask aligner, the resist was exposed to UV light for 15 s, Figure 2.3(ii(e)), and was followed by a PEB consisting

of heating up the wafer from room temp to 55 °C at a rate of 5 °C min^{-1} and maintaining this temperature for 65 min, Figure 2.3(ii(f)). To prevent thermal stress, the wafer was cooled directly on the hotplate for 15 min, after turning off the hot plate. The pattern was developed for 2 min in SU-8 developer solution, and rinsed with isopropanol, Figure 2.3(ii(g)). It was followed by a hard bake at 150 °C for 1 h as for the protocol of SU-8 waveguides on silica, Figure 2.3(ii(h)). Consistent results were obtained with this protocol, which will be referred to as Process SU-8/quartz in the remainder of the document. Scheme of the SU-8 waveguide on quartz is shown in Figure 2.1(b).

2.3.3 Fabrication results

Scanning electron microscopy images of the fabricated waveguides taken from the top are shown in Figures 2.4(a)–(d), and of the facets are shown in Figures 2.4(e) and (f). As can be seen from these images, the resolution of the waveguides obtained with Process SU-8/quartz is better than the resolution obtained using the standard protocol (Process SU-8/SiO$_2$). This result is probably due to an increase of the photoacid diffusion into the non-exposed resist in Process SU-8/SiO$_2$, because of the higher post-exposure bake temperature [97]. Indeed, temperature has been shown to have a greater effect on this phenomena compared to time [97]. Only small protuberances are observed on Figure 2.4(c). Moreover, a longer PEB can contribute to smoothing the side walls of the waveguides. Further, the width of the waveguides produced on the silicon dioxide substrate was around 10% smaller, probably due to a partial development. The measured width and height of both waveguides are shown in Figures 2.4(g) and (h). This could be caused by the lower amounts of residual solvent expected after a SB at high temperature. Indeed, lower residual solvent is known to limit the degree of cross-linking attained in the exposed resist [97]. Also, solvent evaporation during the PEB and hard bake contributes to shrinking of the structures [98, 99]. The shrinkage will be greater for a higher solvent content but will lead to a greater tensile intrinsic stress for a lower solvent content for a same T$_{PEB}$ [97]. From the facet images in Figures 2.4(e) and (f), it can be seen that waveguides produced by both processes display round edges due to the long hard bake, though they both possess vertical walls. The facets result from cleaving the substrates by scratching the edge of the wafer and applying pressure on both sides of the scratch line

for the silica on silicon wafer, and by dicing from the back of the quartz wafer while leaving 50 μm thick of material to subsequently cleaving it by applying pressure on both sides on the dicing lines, which produces a relatively sharp edge that is critical for direct light coupling. Atomic force microscopy (AFM) was used to observe the topography of structures produced by both processes as given in Figure 2.5. Analysis of a 5 × 5 μm^2 area on the middle of the top of the waveguides revealed RMS roughness of 0.924 nm and 1.68 nm for SU-8 on silicon dioxide and quartz, respectively. An elevation of around 55 nm is measured at the middle of the SU-8 on silica waveguide, compared the SU-8 on quartz waveguide that is almost perfectly flat. It is suspected that the flatness of the waveguide prepared with the Process SU-8/quartz is due to a better structural stability due to the higher cross linking density as opposed to the lower cross linking density due to the parameters of process SU-8/ SiO$_2$. The lesser structural stability of the waveguide on silica may have allowed the formation of a rounded top due to the shrinking from the PEB or hard bake.

SU-8 waveguides on silica substrate

SU-8 waveguides on quartz substrate

SU-8 waveguides on silica substrate

SU-8 waveguides on quartz substrate
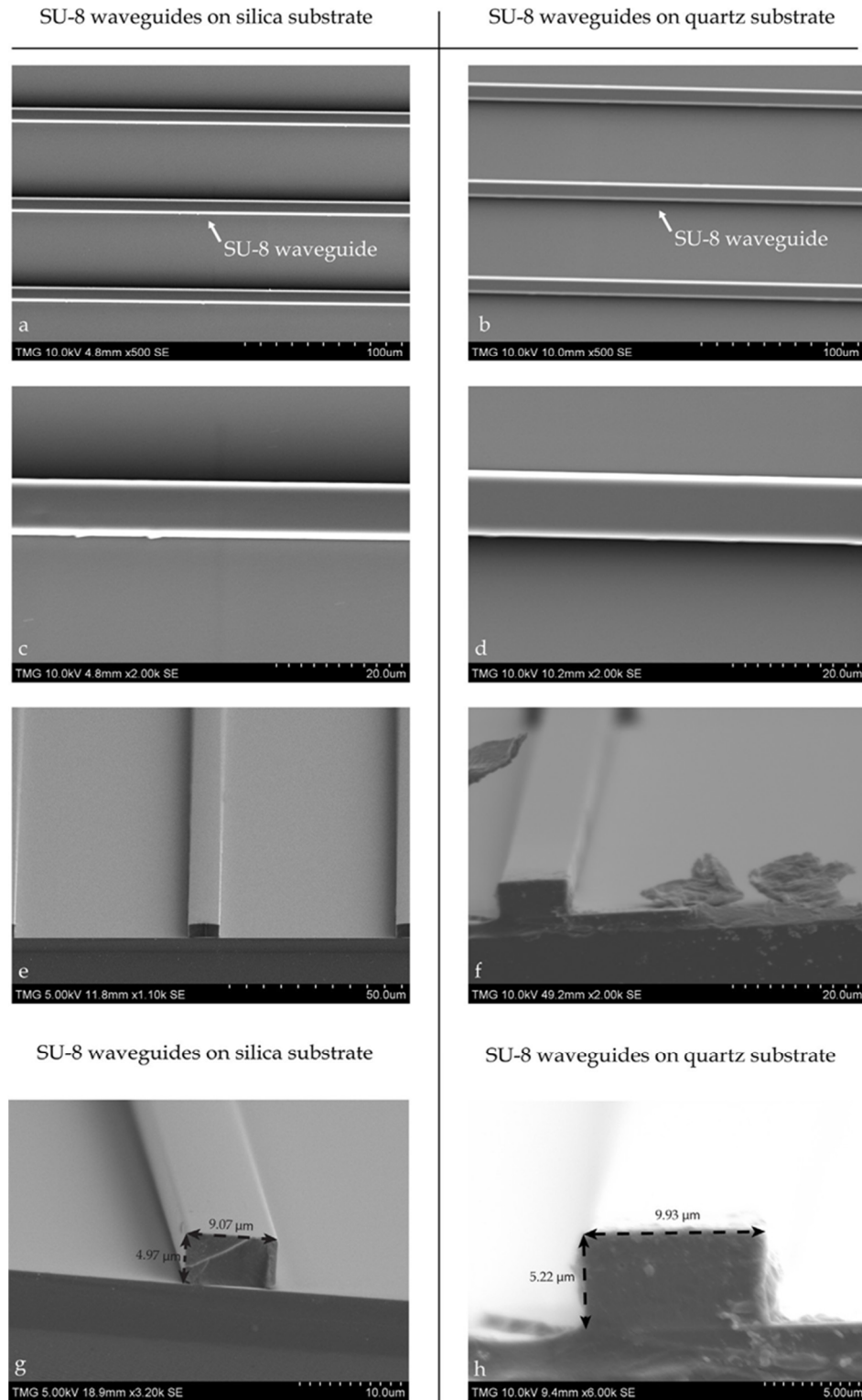
Figure 2. 4 **SEM pictures of SU-8 waveguides on oxidized silicon and fused quartz wafer respectively: (a) and (b) waveguide array (c) and (d) single waveguide (e) and (f) facet (g) and (h) measured width and height. Smallest scale division indicates 1/10 of the scale value (bottom right of images).**
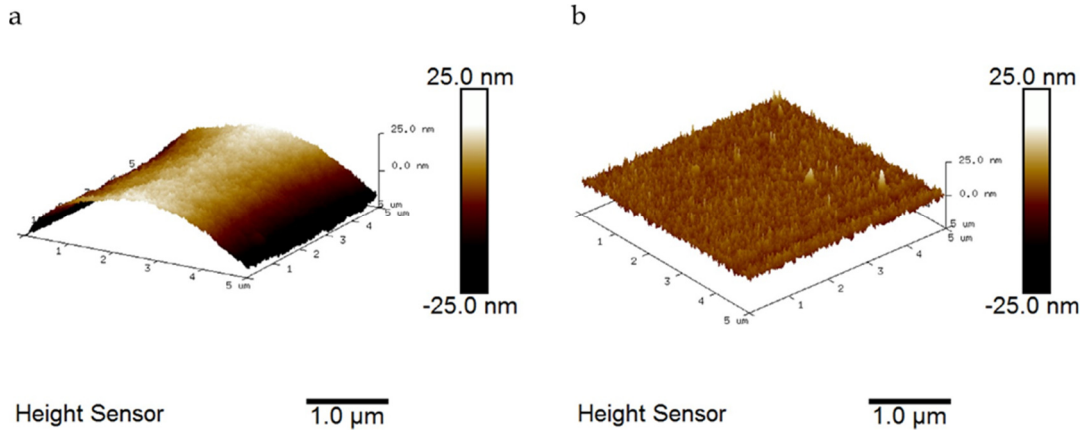
Figure 2. 5   AFM images of a 5 × 5 µm2 area in the middle of the top of the SU-8 waveguides obtained by (a) process SU-8/SiO2 and (b) process SU-8/quartz

2.4   Characterization

The propagation losses and the refractive indexes of the waveguides produced by the different processes were determined. A fiber-coupled laser diode of 1 mW of power (OZ Optics, Westbrook, Canada) was used as a light source with a 635 nm center wavelength guided through a 4.2 µm mode field diameter (at 630 nm) polarization maintaining (PM) fiber (Thorlabs, Newton, USA) inserted in a rotator to switch from TE to TM polarization. To determine the optical propagation losses, the cutback method was used for four different waveguide lengths. The output power was measured with a 62.5 µm core fiber connected to a power meter. The power meter consisted of a fiber-coupled Si photodetector (Thorlabs, Newton, USA) connected to an oscilloscope for signal processing. A scheme of the set-up for the cutback method is shown in Figure 2.6.
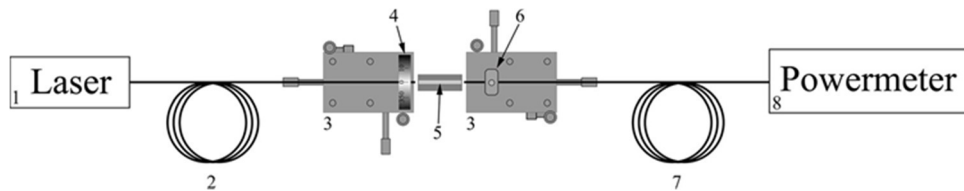
Figure 2. 6   Cutback method setup: (1) laser, (2) polarization maintaining fiber, (3) five-axis stages micro positioners, (4) rotator, (5) SU-8 waveguide on silica or quartz substrate, (6) fiber holder, (7) output fiber (62.5 µm core), (8) power meter.

56

The input power (P_{in}) from the PM fiber output and the output power (P_{out}) from the   end of the waveguide were used to determine their ratio in dB. Each point on the graph, Figure 2.7, is an average of four ratios (– P_{out}/P_{in}) for four different waveguides of same lengths (1.042 cm, 1.557 cm, 1.905 cm, 2.37 cm for SU-8 on silica and 0.993 cm, 1.493 cm, 1.995 cm, 2.461 cm for SU-8 on quartz). The optical propagation loss and coupling loss were determined from the slope and ordinate of the linear fit, respectively. Ellipsometry measurements were also performed for both substrates and both SU-8 films and results are presented in Figure 2.8.
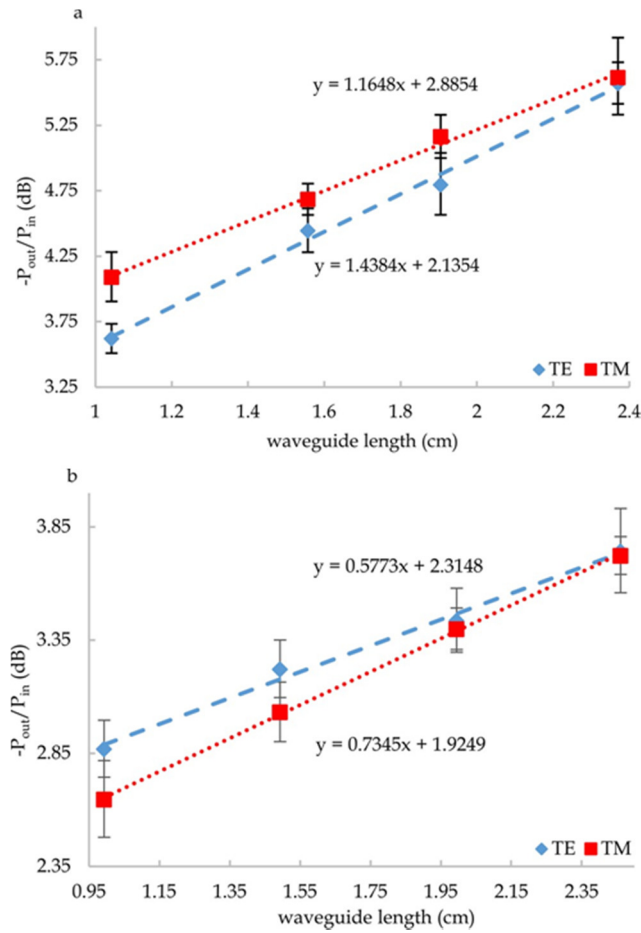
Figure 2. 7   **Propagation losses for SU-8 waveguides produced by (a) process SU-8/SiO₂ or (b) process SU-8/quartz. Data presented as mean ± SD (n = 4).**
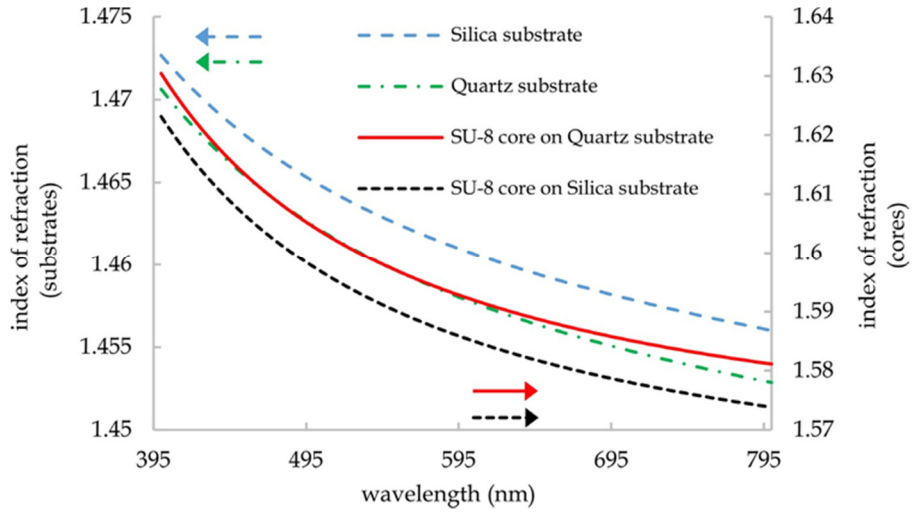
Figure 2. 8 **Refractive indices of the substrates and SU-8 waveguides cores (process SU-8/SiO₂ and process SU-8/quartz) by ellipsometry.**

2.4.1 Characterization results

Based on the propagation losses measured in Figures 2.7(a) and (b), the absolute TE propagation loss of the waveguides produced by Process SU-8/quartz is almost 2.5-fold lower than that of waveguides produced by Process SU-8/SiO$_2$. This observation is consistent with electron microscopy images Figure 2.4, where smoother edges are obtained with Process SU-8/quartz used for production of the waveguides. Further, the TM propagation loss measured for waveguides produced by Process SU-8/quartz is also lower than for those produced by Process SU-8/SiO$_2$. While data for the RMS roughness of the side walls of the waveguides are not available, one possible explanation is that higher loss is due to greater roughness, and also certainly (partially) due to the protuberances observed in Figures 2.4(a) and (c). Further, the thinner silicon dioxide substrate could contribute to the losses by absorption from the silicon base. From Figure 2.7(b), it can be observed that the propagation loss for TM is higher than for TE, for waveguides produced by Process SU-8/quartz. Several studies have already shown that greater waveguide widths reduce scattering loss due to sidewalls roughness [100, 101]. Indeed, numerical calculations predict that surface scattering loss is inversely proportional to the cube of the thickness or width [102]. Keeping this in mind, for a same RMS

roughness, the relative propagation loss, for TE, should be 1.87-fold less for the waveguides produced by Process SU-8/quartz, since they are ~10% wider. Furthermore, TE polarization is more affected by the width than the thickness of the waveguide, as opposed to TM polarization [103], though to a lesser extent for multimode waveguides (since the mode overlaps to a lesser extent at the waveguide boundaries). For waveguides produced by process SU-8/SiO_2, Figure 2.7(a), the propagation loss for TM polarization is lower than for TE, probably due to the sidewalls roughness and smaller width/thickness ratio. Different cleaving techniques and substrates could affect the Fresnel reflections, which would explain the different coupling losses. Ellipsometry measurements were conducted to determine the index of refraction of the substrates and cores of the waveguides fabricated with the different protocols, Figure 2.8. The SU-8 polymer on quartz possessed a higher refractive index as shown in (1.5896) than on silicon dioxide (1.5826). Higher processing temperatures are expected to lower the index of refraction of SU-8 [93]. A longer SB was also shown to increase the refractive index of SU-8 [104]. Process SU-8/quartz removes less solvent during the soft bake and in addition we kept the PEB temperature (55 °C) in the optimal range to reduce stress [97]. As a result, the refractive index of SU-8 in SU-8/quartz process was higher than that of SU-8 in SU-8/silica process due to its more relaxed state [105]. So, we see a small difference between the two indices of refraction. Overall, a small difference in refractive index is unlikely to affect significantly the propagation losses for a thick waveguide [102]. The propagation losses of both SU-8 waveguides for the TE and TM polarization are compiled in Table 2.1.

Table 2. 1   Optical losses for SU-8 waveguides on silica and quartz substrates.

SU-8 waveguides propagation losses (dB cm^{-1})		
Polarization	Silica substrate	Quartz substrate
TE	1.44	0.58
TM	1.16	0.73

2.5   Conclusion

In this study, SU-8 waveguides produced on oxidized silicon and fused quartz wafers were compared. A new protocol to fabricate 10 × 10 µm SU-8 waveguides on fused quartz is described. The waveguide adhered firmly to the quartz substrate, preserved the dimensions expected from the photomask, and possessed lower optical losses compared to waveguides produced on silicon dioxide, using the manufacturer-recommended protocol. This new procedure could be adapted for the fabrication of other SU-8 waveguides on other substrate materials with proper surface treatment. This study demonstrated that fused quartz is suitable to be used as a substrate for SU-8 waveguides. This is interesting because fused quartz is optically transparent, a property that could be exploited to illuminate or detect light output through integrated optical structures for bio sensing or microscopy. Also, the SU-8/quartz process resulted in a SU-8 core with a higher index of refraction, which was proven to be more efficient for evanescent fluorescence sensing [106]. The same process resulted also in smoother sidewalls which could improve the flow for SU-8 micro channels. Furthermore, cleaving proved to be an acceptable method for achieving sharp facets, but adding a polishing step for the facets could improve further the light transmission.

CHAPTER 3

POLYMER ON QUARTZ WAVEGUIDE SENSING PLATFORM FOR ENHANCED EVANESCENT FLUORESCENCE SPECTROSCOPY

3.1   Introduction

Optical sensing by means of fluorescence labeling is widely used to determine the concentration of analytes with different platforms and techniques [107], [108]. Although sensing using evanescent waves is also used for absorbance measurements, a higher sensitivity and specificity could be achieved by combining the technique with fluorescent labeling. Indeed, fluorescence evanescent wave spectroscopy exploits the evanescent wave of the guided light to excite fluorophore-labeled analytes in close proximity to the waveguide surface. Optical fibers are popular platforms to be used for fluorescence evanescent wave spectroscopy for remote or on-site sensing [109], [1]. However to use optical fibers for evanescent wave sensing has some drawbacks. The cladding of the fiber has to be etched to expose the core of the fiber to the sample so that the evanescent wave can reach the labeled analyte. This renders the fiber structurally fragile and hard to manipulate. Micro-structured fibers are an alternative to common step index optical fibers for evanescent wave sensing where the sample could be flowed inside the hollow core, offering a more robust structure [110]. Although optical fibers offer a long interaction length and are useful for remote sensing, they do not allow for multiplexing. On the other hand, planar waveguides allow for easy fabrication, multiple analyte detection for a unique sample, microfluidic integration, and are structurally more robust than optical fibers. Planar waveguides are usually single mode waveguides where a thin layer of material is deposited on a substrate of lower refractive index, thus acting as the waveguide core. The coupling of light to the waveguide is usually accomplished with a prism or grating, where the incoming light has to be directed to a specific angle for wave vector matching. The components required for light coupling and signal analysis required to fabricate a

functional biosensor with planar waveguides make the system quite bulky [111]. Miniaturization and integration of optical and microfluidics components in a single platform is key to develop an integrated optical biosensor that could fit on a chip, hence the name lab-on-a-chip [112]. Rectangular waveguides, are so far the best candidates for this function. Indeed, rectangular waveguides have the advantage to be modeled in different designs and can be matched with more sophisticated integrated optical components for signal processing, such as Bragg filters, spectrophotometers, interferometers, micro resonators, etc. Light coupling can also be facilitated with larger rectangular multimode waveguides by direct coupling. Silicon based materials are the most popular for the fabrication of integrated optics [113] and have also been used for the fabrication of rectangular waveguides in integrated optical evanescent wave sensors [114-116]. Although inorganic materials make the most of the integrated optical components, particular properties from polymer materials make them an interesting medium for integrated optics [117]. Their simpler fabrication process and ease of integration over mineral materials make them an attractive choice especially for the optical telecommunication industry [118]. Indeed, polymers can be fabricated with embossing [119] and stamping [120], which offers the possibility for cheap and high volume manufacturing. Other fabrication methods were also used for polymers as direct photolithography [86], laser ablation [121], reactive ion etching (RIE) [122], dip-floating [123], electron- beam writing [124], etc. Also, compared to silica and silicon, polymers have a low thermal conductivity but a high thermo-optic coefficient, which is ideal for thermal actuation [125]. This property allows for high performance thermo-optical devices to be developed [126-128]. Another interesting property is that polymeric waveguides have the ability to be flexible. This unique characteristic was justifiably used to develop flexible optical interconnects [129, 130] or strain sensors [131, 132] with polymeric materials. Moreover, polymers were used for optical biosensors as the medium to fabricate different kind of sensing platforms as planar waveguides [133], inverted rib waveguides [134], micro resonators [135], interferometers [136], rectangular waveguides [74], etc. As for bio sensing assays, the analytes contaminate the sensing platform after binding and would alter the response of future examinations. Hence, since polymers are cheap and easy to fabricate, they are ideal for disposable biosensors [137]. A great variety

of polymer materials were suitable for integrated optical devices such as acrylates [138], polyimides [139], polycarbonates [140], olefins [141] and epoxide [142]. SU-8, an epoxy based negative photo resist developed in 1989 by IBM, has demonstrated great potential for being a material of choice for integrated optical waveguides due to its transparency to a wide range of wavelengths [86], high resolution [143], mechanical resistance [144], and biocompatibility [145, 146] for bio sensing purposes. For this reason SU-8 will be used in this work as the core material of the waveguides. Various methods have been developed to increase the sensitivity of evanescent wave fluorescent spectroscopy of planar or rectangular waveguide such as, gratings [147], micro cavities [148], surface plasmon-enhanced fluorescence [149], etc. A novel fabrication process for SU-8 waveguides on quartz developed by Abdul-Hadi *et al.* [150] has demonstrated lower optical propagation losses and an increased index of refraction of the SU-8 core, which were exploited to increase the sensitivity of evanescent wave fluorescence spectroscopy.

Our previous work focused on developing polymer waveguides for low optical losses. This paper aims to evaluate the effect of the novel fabrication process for SU-8/quartz waveguide [150] on evanescent fluorescence spectroscopy and to compare it with a SU-8/silica waveguide fabricated with the standard protocol. 3D FDTD simulations with randomly oriented and phased dimensionless emitting current dipoles for the SU-8 waveguides on quartz and silica substrates were used to compare the fluorescence coupling of both sensing platforms. Finally, in this work, the SU-8 waveguides on quartz fabricated with our optimized process [150] are compared with SU-8 waveguides on silica fabricated with the standard protocol for evanescent fluorescence spectroscopy with Bovine Serum Albumin labelled with Alexa 647 (BSA-Alexa 647) as the analyte of interest.

3.2   Design

SU-8 5 photoresist (Microchem, Newton, U.S.A) was the preferred material for the waveguides cores. An oxidized silicon wafer with a 5-μm thick silica layer (Rogue Valley Micro Devices, Medford, U.S.A) and a 1 mm thick fused quartz wafer (Semiconductor Wafer, Hsinchu, Taiwan) were chosen as substrates. The width, the thickness, and the

length of the waveguides were 10 µm, 5 µm, and 2.5 cm respectively (Figures 1(a) and (b)) following the same dimensions as the structures in [150].

The indices of refraction of the SU-8 cores and substrates were previously measured by ellipsometry (also in [150]) and presented in Table 3.1 for the fluorescence light wavelength (λ=671 nm). Water is used as the cladding for the purpose of this work. The asymmetry parameters (along the y axis) [151] were calculated accordingly to the waveguides respective indices of refraction.

The indices of refractions of the cores and substrates of the waveguides for the fluorescence collection efficiency calculations in the remainder of the document are taken from Table 3.1. The dimensions and indices of refraction for the SU-8/quartz and SU-8/silica configurations allows for highly multimodal waveguides for λ=671 nm. With the help of the effective index method it was numerically solved that for λ=671 nm the SU-8/quartz and SU-8/silica waveguides allows for approximately 137 and 126 guided (TE or TM) modes respectively.
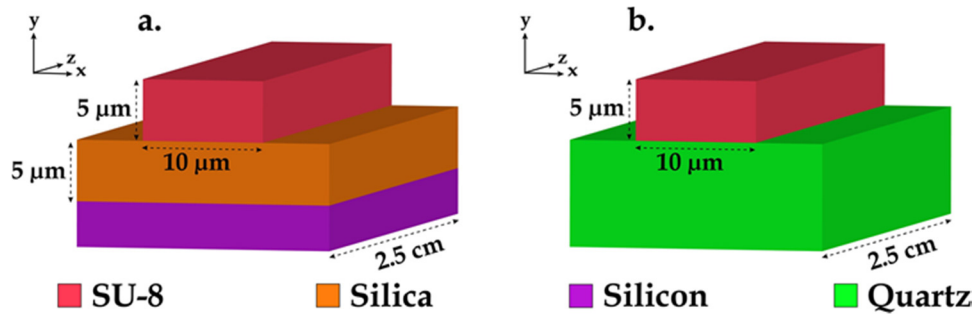
Figure 3. 1   **SU-8 waveguides on (a) silica-on-silicon and (b) quartz substrates.**

Table 3. 1   **Indices of Refractions of the Cores, Substrates, Cladding and Asymmetry Parameters (Along Y Axis) of the SU-8/Quartz and SU-8/Silica Waveguides for a Fluorescence Light Wavelength of λ = 671 nm.**

Waveguides	Index of refraction (λ= 671 nm)			Asymmetry parameters	
	Cores	Substrates	Cladding	TE	TM
SU-8/quartz	1.587	1.456	1.330	0.88	1.78
SU-8/silica	1.580	1.459	1.330	0.98	1.94

64

3.3   Fabrication and Characterization

The fabrication of the SU-8 waveguides on the silica-on-silicon and quartz substrate was done by way of UV lithography. However, the processes for each substrates differed. The fabrication protocol for the SU-8 waveguides on the silica-on-silicon substrate followed the basic guidelines of the standard protocol. However, the standard fabrication protocol was not suitable for the SU-8 waveguides on quartz. A comparative study performed by Abdul-Hadi *et al.* [150], gives detailed explanations about the fabrication process of SU-8 waveguides on a silica-on-silicon and quartz substrates and the resulting characteristics of both waveguides. The same fabrication steps used in [150] were used in this work for the fabrication of the SU-8 waveguides on silica-on-silicon and quartz. Scanning electron microscopy (SEM) images of the SU-8/Quartz and SU-8/Silica are shown on Figure 3.2.
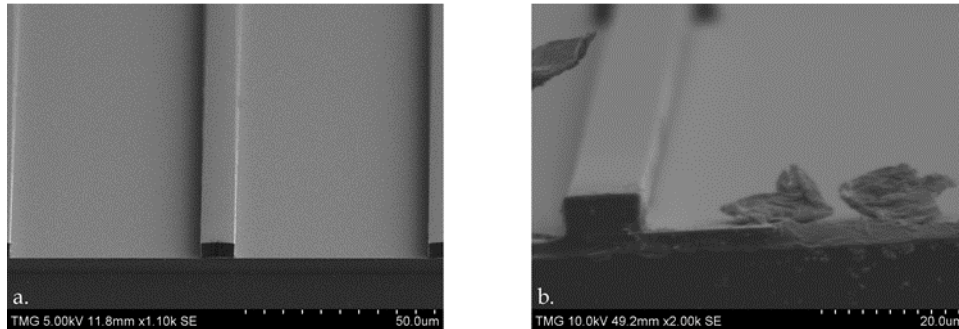
Figure 3. 2   SEM pictures of the (a) SU-8/silica and (b) SU-8/quartz waveguides.

The most important results from [150] are the lower optical propagation losses of the SU-8/Quartz waveguides compared to the SU-8/Silica waveguides obtained from the optimized fabrication process as shown on Figure 3.3.
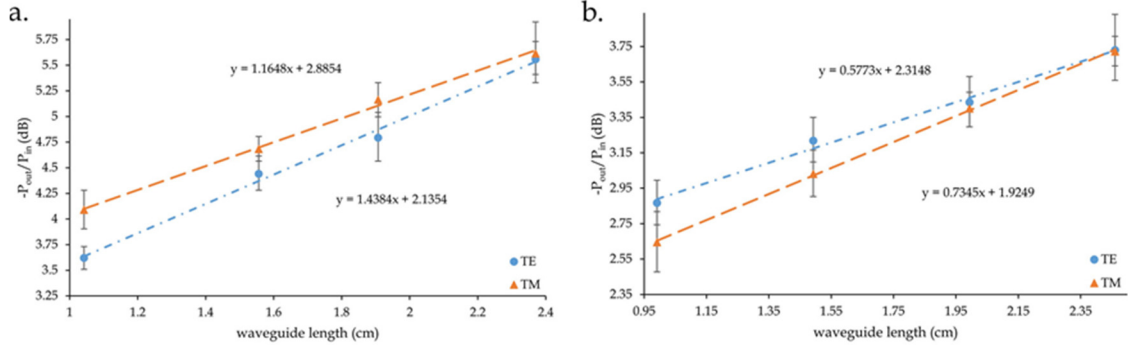
Figure 3. 3 Optical propagation losses for the TE and TM polarizations evaluated with the cutback method for (a) SU-8/silica and (b) SU-8/quartz waveguides.

3.4 Theory

3.4.1 Evanescent Fluorescence Coupling Near a Dielectric Waveguide

A dielectric surface near a radiating dipole, in our case a fluorophore, modifies the angular distribution of the emitted light [152] and at the same time provokes a back-coupling of the fluorescence in the dielectric medium [153]. The light propagating in the dielectric is partly under the critical angle, termed 'allowed' light [154], and partly above the critical angle, termed 'forbidden' light [154]. The light propagating above the critical angle, can be guided if another layer is added as a substrate if its index of refraction is lower than the dielectric layer, understanding that the dipole is also located in a medium of lower index than the dielectric layer. This arrangement is called a waveguide (Figure. 3.4), where the dielectric layer is acting as the guiding layer for the light. In this work, the fluorophores are attached to a BSA protein and diluted in a buffer solution (PBS). The buffer solution is mainly composed of water, hence its index of refraction is around 1.33. Alexa Fluor 647 was chosen as the fluorescent dye which can be excited with a 635 nm light and has a peak emission at a wavelength of around $\lambda=671$ nm. The BSA molecule, in this work, can be seen as a prolate ellipsoid with diameters of 14 nm and 4 nm of size [155] with a labeling degree of 4. Therefore, the distance between the fluorophore and the PBS-SU-8 interface is approximated to be 10 nm. The light in the forbidden region is guided through, for instance, the SU-8/quartz waveguide formed by the buffer solution,

66

the SU-8 core and the quartz substrate, Figure. 3.4. It has been demonstrated that when a fluorophore is excited near a higher refractive index medium it emits evanescent waves that are transformed into propagating plane waves by the medium [153].

The emission of the fluorophore couples to the evanescent field of the guided mode(s) (Figure. 3.4). This phenomenon is called evanescent coupling and is used to detect labeled biological entities immobilized on the waveguide by measuring the guided fluorescence light at the output of the waveguide.
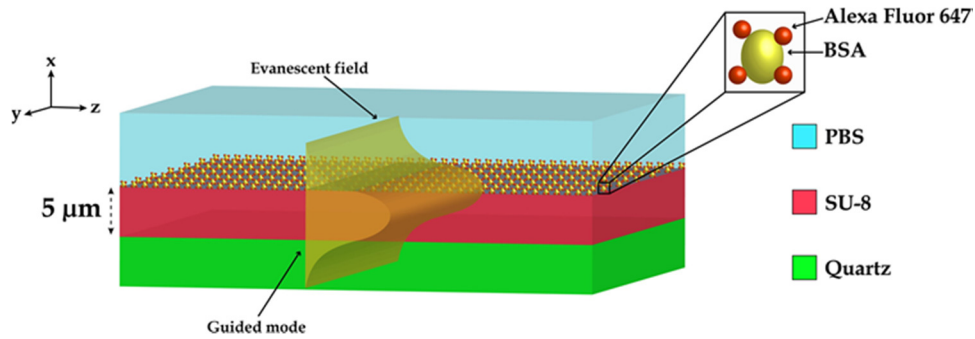
Figure 3. 4   Schematic representation of the fundamental mode propagating through a planar waveguide with a SU-8 core layer, a PBS cladding, and quartz substrate with BSA-Alexa 647 immobilized on the SU-8 surface.

The fluorescence collection efficiency gives the proportion of the light from the sources captured and guided by the waveguide. A more extensive definition of the fluorescence collection efficiency can be found in [156, 157]. Although, in this work, the waveguides are rectangular in shape the same principle applies for the fluorescence evanescent coupling but the modes will be confined in a 2D geometry instead. The calculation of the fluorescence collection efficiency for sources near a planar dielectric planar waveguide was already developed by Srivastava *et al.* [157] with the modal propagation approach. However, to calculate the fluorescence collection efficiency with the modal propagation approach for rectangular waveguides will require the use of the effective index method. The effective index method works better for high width/thickness ratio and low index contrast. Since the dimensions of the SU-8/quartz and SU-8/silica waveguides are 10×5 µm and the index contrast is moderately high. A relative study may be acceptable using this method, but for a more accurate calculation the FDTD method would be more appropriate.

3.5 3D FDTD Modeling of Simulated Fluorophores in the Vicinity of the SU-8/Quartz and SU-8/Silica Waveguides

The 3D FDTD numerical method was used for an accurate evaluation of the relative difference of the fluorescence collection efficiencies between the waveguides with a 10-nm Alexa-647 fluorescent layer located on the top or on the sides of the waveguides. Firstly, a study with a 3D FDTD model of the SU-8/quartz and SU-8/silica waveguides with simulated fluorophores close to the waveguide surface was performed to evaluate the collection efficiency at the output of the waveguide. Emitting dimensionless dipoles were used to simulate the Alexa-647 fluorophores. As mentioned above, the BSA molecule was approximated to a size of 10 nm. The dipoles were then located at a 10 nm distance from the waveguides and also spaced from one another at a distance of 10 nm. The simulated fluorophores were uniformly distributed from one extremity to the other for the top and side part of the waveguides. The simulation was performed with the FDTD software *Fullwave* from *Synopsis*. Covering with simulated fluorophores from the left extremity to the right extremity along the top and from bottom to the top for the sides of the waveguide would require 1001 and 1002 simulated fluorophores respectively, if spaced from one another at a distance of 10 nm. That amount of simulated fluorophores exceeded the limits of the software. Only 32 simulated fluorophores are allowed at once. A series of simulations with each simulation having the maximum number of simulated fluorophores was performed until fully covering a 10 µm line along the top or two 5 µm lines on the sides of the waveguides. For each simulation, the monitor was placed at 60 nm from the fluorophores and the resulting field was recorded (Figure. 3.5(a), (d)). Each of the successive resulting fields from each simulation were then combined as a single source (Figure. 3.5(b), (e)). The simulation of this source was then performed and the resulting field was also recorded at a distance of 60 nm (Figure. 3.5(b), (e)). The last simulation was then performed, for which the resulting field propagated along the remainder of the 39 µm long waveguide (Figure. 3.5(c), (f)). The resulting fields from the top and sides of the waveguides were combined and the resulting field was recorded at 60 nm from its initial position (120 nm; Figure. 3.5(g)). A monitor was placed at 39 µm distance from the start of the waveguide to measure the averaged power at the output

68

(Figure. 3.5(c), (f), (h)). The ratio between the measured averaged power between the SU-8/quartz and SU-8/silica waveguides gives the increase in fluorescence collection efficiency between both waveguides. The dipoles were randomly oriented only along the x, y or z axis as depicted on the inset of Figure. 3.5. Also, the phase of each dipole was randomly generated from 0° to 360°. The total electric field E_y, with a view from the waveguide facet, is shown on Figure. 3.6(a), (c) for a simulation of 32 simultaneously emitting dimensionless dipoles at the top and sides of the waveguide. The results of the simulations in Figure. 3.6(a), (c) displays the electric field emissions from the configurations (1st image) of Figure. 3.5(a), (d) respectively. The combined fields of the series of simulations resulting in 1001 (top), 1002 (2 x 501) (sides) and 2003 (top/sides) emitting dipoles are shown on Figure. 3.6(b), (d), (e). The results of the simulations in Figure. 3.6(b), (d), (e) displays the electric field emissions from the configurations of Figure. 3.5(b), (e), (g) respectively.
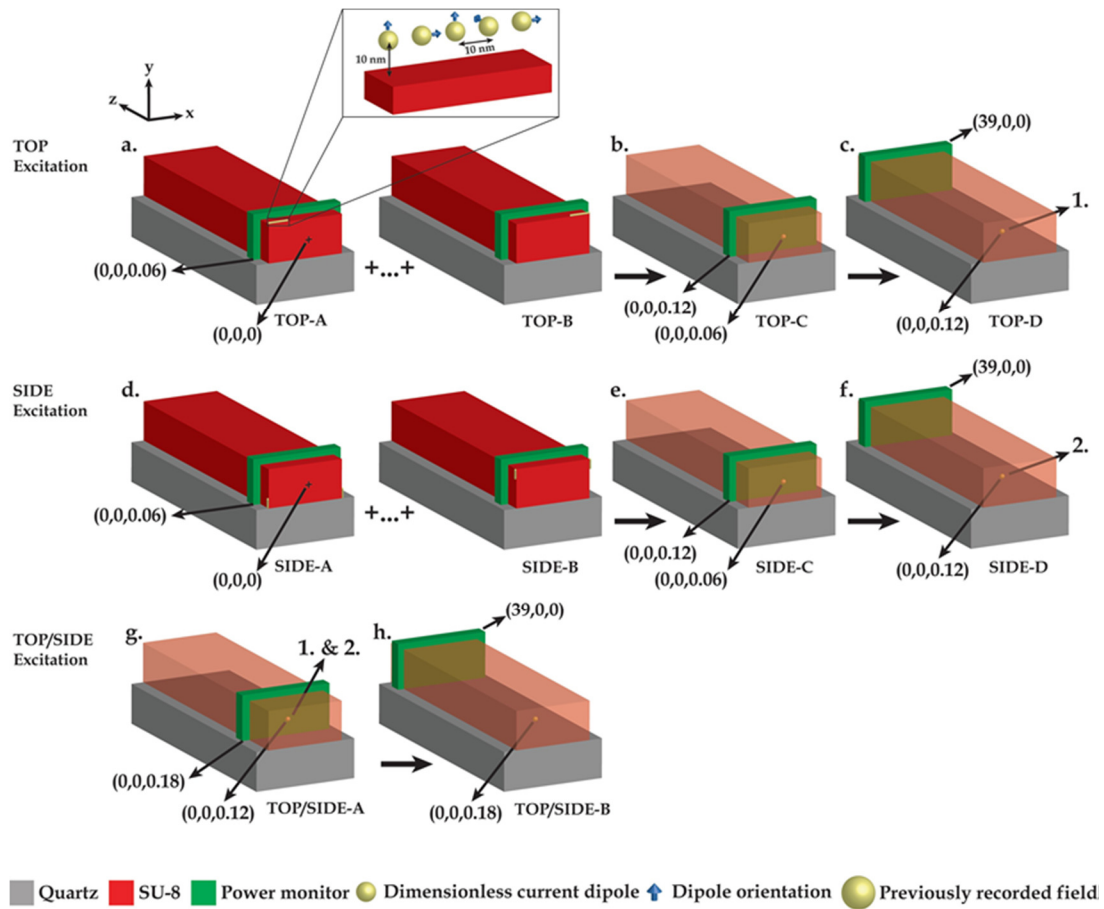
Figure 3. 5   **Successive steps for the 3D FDTD simulation of a line(s) of dimensionless, randomly oriented and phased emitting current dipoles on the (a) top, (d) sides and (g) combined fields of the top and sides of a SU-8/quartz or SU-8 silica waveguide for the evaluation of the guided coupled light propagating through the waveguide.**
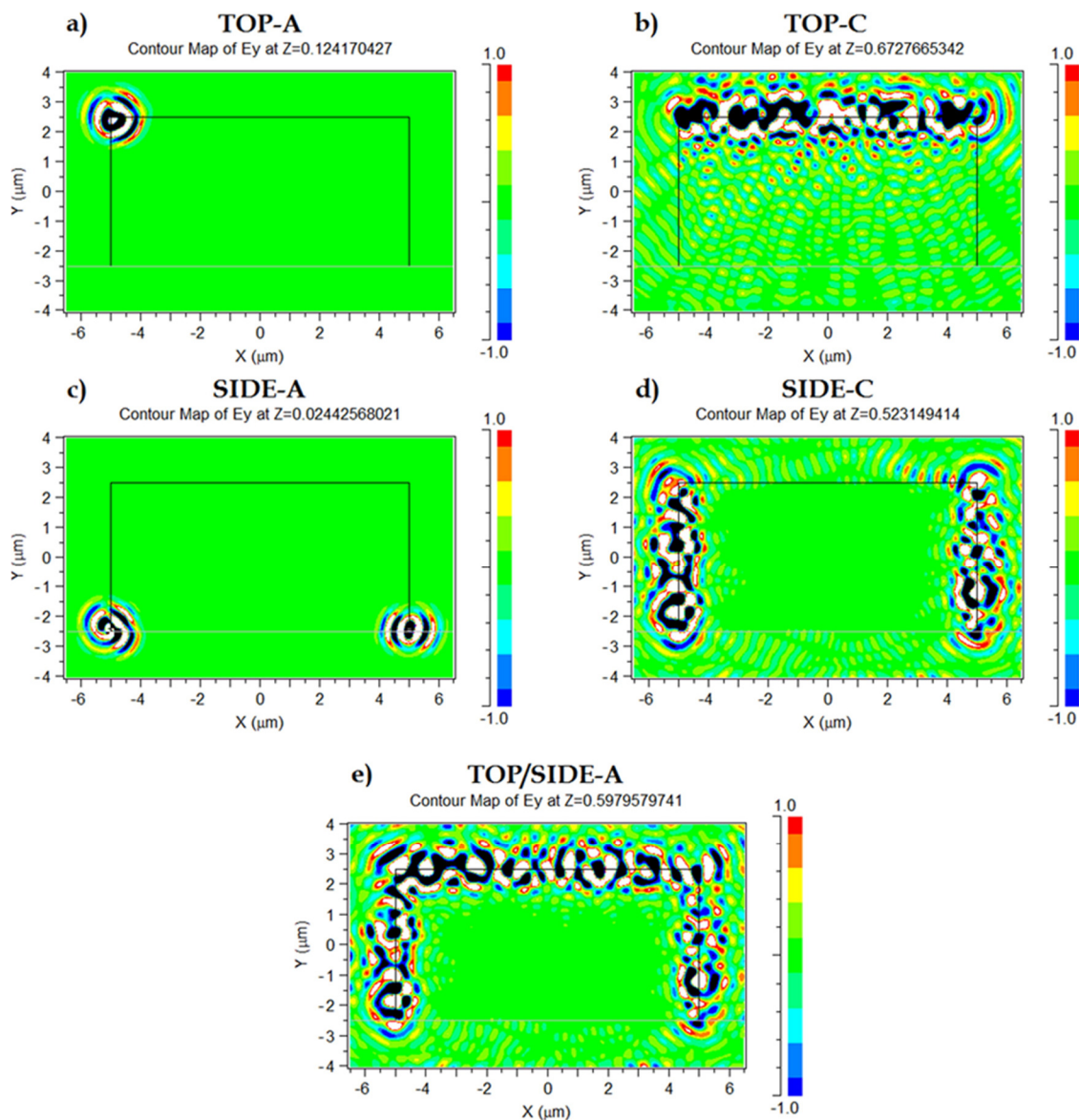
Figure 3. 6   **Total electric field Ey for 32 emitting dimensionless, randomly oriented and phased current dipoles (a)on the top left and (c) both sides (2 × 16) of the SU-8/quartz or SU-8/silica waveguide facets. Total resulting field Ey from the emitted light from 1001,1002 and 2003 simulated fluorophores on the (b) top, (d) sides (2 × 501) and (e) top/sides of a 10 × 5 μm SU-8/quartz or SU-8/silica waveguide.**

The ratios between the averaged powers from four different distributions of randomly oriented dipoles and phases for the top, sides and top/sides of the SU-8/quartz and SU-8/silica waveguides are shown on Table 3.2.

Table 3. 2   **Average Values of the Ratios of the Fluorescence Collection Efficiencies (F.C.E) for the Different Distributions of Randomly Oriented and Phased Dimensionless Current Dipoles for the Top, Sides and Top/Sides between the SU-8/Quartz and SU-8/Silica Waveguides.**

		Distribution number	SU-8/Quartz	SU-8/Silica	F.C.E Ratio (%)	Average of F.C.E ratios (%)	Standard deviation (%)
Fluorescence Collection efficiency	Top	1	4.04	3.64	10.88	10.3	1.2
		2	3.01	2.71	11.11		
		3	4.42	4.07	8.48		
		4	3.20	2.90	10.51		
	Side	1	5.92	5.72	3.44	3.4	1.3
		2	6.86	6.52	5.14		
		3	7.97	7.74	2.95		
		4	7.51	7.36	2.08		
	Top/Side	1	3.98	3.74	6.32	5.4	1.4
		2	3.64	3.41	6.54		
		3	4.98	4.73	5.30		
		4	4.20	4.06	3.42		

It is seen from results from Table 3.2 that the SU-8/quartz waveguide presents a higher fluorescence collection efficiency than the SU-8/silica waveguide for any sides of the waveguides. If the rectangular waveguide is approximated as 2 planar waveguides, the planar waveguide varying in index along the y axis will have a TE/TM asymmetry parameters [151] of 0.88/1.78 for SU-8/quartz waveguide and 0.98/1.94 for SU-8/silica waveguide. The asymmetry parameters of the planar waveguides varying in index along the x axis will be nil. It was shown in [157] that a lower asymmetry increases the fluorescence collection efficiency. Hence, the higher collection efficiency from the top of the waveguide. Although, the asymmetry parameters are nil for the sides of the waveguides, the core index of the SU-8/quartz waveguide is higher than the core of the SU-8/silica waveguide. It was also shown from [158] that a higher index core increases the fluorescence collection efficiency. Indeed, a higher core index increases the coupling of the light of the emitting fluorophores by increasing the confinement of the light near the core cladding interface. While a higher substrate index will drag more of the power of the modes in the substrate resulting in less power in the cladding, resulting in lower fluorescence collection efficiency. The SU-8/quartz waveguide fabricated with the novel

process from [150] have both a higher core index and a lower substrate index than the SU-8/silica making it a better choice for evanescent fluorescence spectroscopy.

3.6 Fluorescence Evanescent Wave Spectroscopy

3.6.1 Experimental Setup

The experimental setup used for the detection of the Alexa-647 labeled BSA by fluorescence evanescent wave spectroscopy is illustrated on Figure 3.7. The excitation light source used was a fiber-coupled laser diode with a 635 nm central wavelength (OZ optics, Westbrook, Canada). A single mode fiber with a 3.6-5 µm mode field diameter (Thorlabs, Newton, USA) was connected to the fiber-coupled laser diode and to the input of a single mode fiber coupler (Thorlabs, Newton, USA) containing a 650 nm shortpass filter (Thorlabs, Newton, USA). This light source was butt- coupled to the input of the SU-8/quartz or SU-8/silica waveguide. The excitation light guided through the waveguide was collected simultaneously with the guided fluorescence light coupled to the waveguide from the BSA-Alexa-647 by a 62.5 µm core multimode fiber (Thorlabs, Newton, USA) at the output of the waveguide. The 62.5 µm core multimode fiber was also connected to a multimode fiber coupler (Ocean Optics, Largo, USA) holding a 676/29 nm bandpass filter (Semrock, Rochester, USA). Finally, the light was guided through a 600 µm multimode fiber (Ocean Optics, Largo, USA) to a spectrometer (USB-2000 Ocean optics) to be spectrally analyzed. The two interference filters were essential to discriminate the guided fluorescence light from the Alexa-647 fluorophores. The 676/29 nm bandpass filter (Figure 3.8(a)-8) was mainly used to prevent the stray light from the excitation source (635 nm) from entering the spectrometer. Indeed, without any filters, the stray light caused the excitation of pixels that are not attributed to the specific wavelength diffracted by the grating. Therefore, the spectrum was saturated and the fluorescence signal indiscernible. Even only with the 676/29 nm bandpass filter (Figure 3.8(a)-8), the fluorescence signal was not discernible from the spectrum. Hence the addition of a 650 nm shortpass filter (Figure 3.8(a)-1), to the 676/29 nm bandpass filter (Figure 3.8(a)-8), which will let through the excitation light (635 nm) but block the light with a higher wavelength than 650 nm to

allow the fluorescence light (671 nm peak) to be apparent (Figure 3.8(b)). The polarization of the light at the output of the input fiber (Figure 3.8-3), was measured to be 41˚ from the plane of the substrate surface
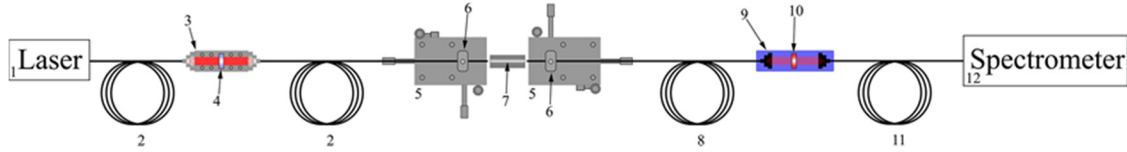
Figure 3. 7   **Fluorescence evanescent wave spectroscopy experimental setup. 1) Fiber-coupled laser (λ=635 nm). 2) Single mode fiber. 3) Single mode fiber-to-fiber coupler. 4) 650 nm shortpass filter. 5) Five-axis stage micro positioners. 6) Fiber holders. 7) SU-8/quartz or SU-8/silica waveguide. 8) Mutlimode fiber (62,5 μm core). 9) Multimode fiber-to-fiber coupler. 10) 676-29 nm bandpass filter. 11) Multimode fiber (600 μm core). 12) Spectrometer.**
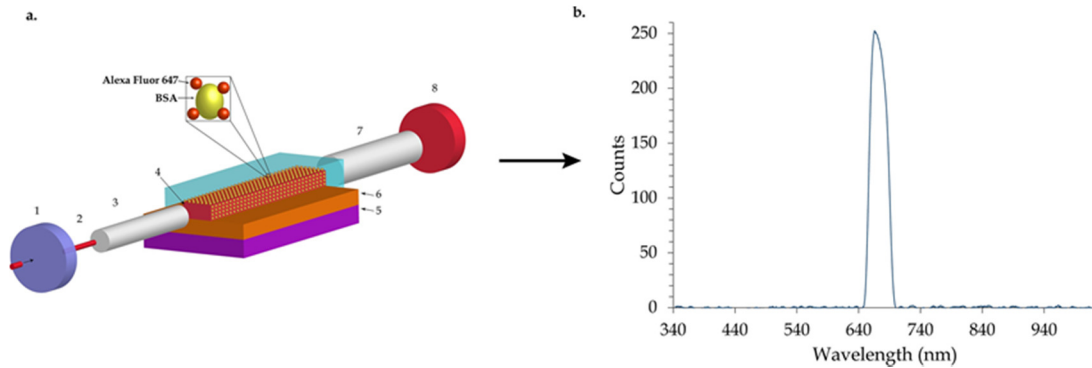
Figure 3. 8   **Arrangements of the SU-8/silica waveguide with the immobilized BSA-Alexa 647 (a) with the 650 nm shortpass filter and the 676/29 nm bandpass filter, (b) the resulting spectrum. The components on a) are 1) 650 nm shortpass filter, 2) laser (λ=635 nm), 3) single mode fiber, 4) SU-8 core, 5) silicon wafer, 6) silica substrate, 7) multimode fiber, 8) 676/29 nm bandpass filter.**

3.6.2 SU-8 Autofluorescence

It was already shown that SU-8 shows a strong fluorescence at visible wavelengths [159]. Bleaching of the SU-8 autofluorescence can be achieved with a long illumination [160]. Before proceeding with the evanescent wave spectroscopy, a complete photobleaching of the SU-8 waveguides was done to get rid of the fluorescence background with the help of the 1 mW laser light (λ=635 nm) guided through the waveguide. The spectrum of the output signal of a SU-8 waveguide on a silica-on-silicon substrate was taken at different

time, Figure 3.9, with continuous illumination until no change was visible in the intensity of the spectrum.
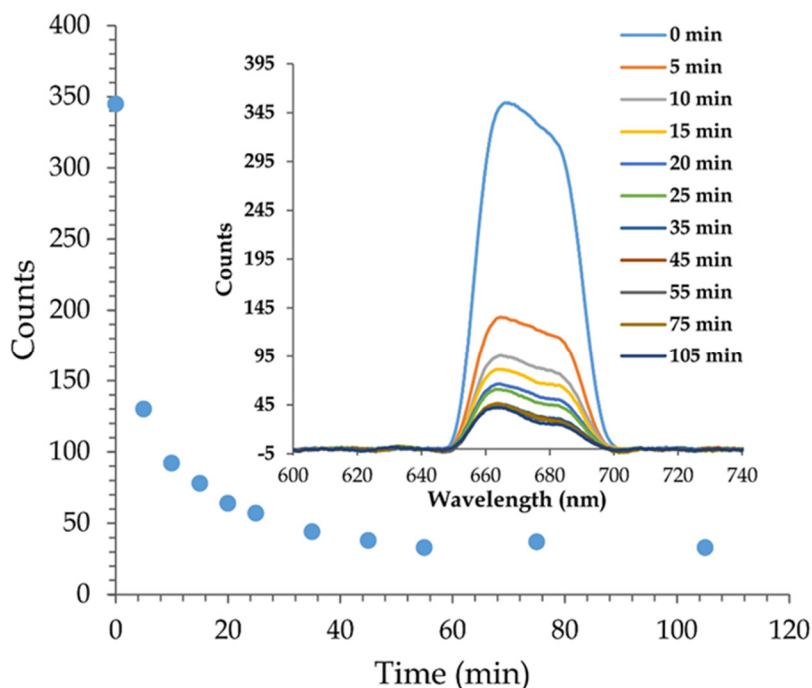
Figure 3. 9   **Intensity (counts) of the SU-8 autofluorescence in function of time from a 635 nm laser light guided through the SU-8 core of a SU-8/silica waveguide. Inset: spectra of the SU-8 autofluorescence signals (after smoothing).**

The photobleaching of the SU-8 cores for both the SU-8/silica and SU-8/quartz waveguides was complete after around 55 min of illumination, Figure 3.9. Fading of the fluorescence was permanent. Indeed, the photobleaching was effective even weeks after the illumination session.

3.6.3 Immobilization of BSA-Alexa 647 on SU-8/Quartz and SU-8/Silica Waveguides

The immobilization procedures were identical for both SU-8 waveguides on silica-on-silicon and quartz substrates. Firstly, the chips were rinsed with acetone and isopropanol. After drying with a nitrogen jet, the chips were exposed to oxygen plasma for 20 seconds to functionalize the surface with OH groups (Figure 3.10(a)). After, the chips were silanized by immediate immersion in 1% (v/v) APTES-ethanol solution for 1 hour at room

temperature (Figure 3.10(b)). The chips were then rinsed with ethanol and DI water, dried with a gentle nitrogen flow and kept in oven at 100°C for 10 min. After cooling down to room temperature, drops of 1, 2% (v/v) glutaraldehyde-PBS (glutaraldehyde- Phosphate buffered saline) solution were placed on the SU-8 waveguides until the entire waveguide was submerged by the solution (Figure 3.10(c)), and kept at room temperature for 2 hours in a sealed petri box with a water-soaked paper to prevent the drying of the solution. The waveguide was then flushed with PBS and DI water. After drying with a nitrogen jet, the SU-8 waveguides were exposed to different concentrations of ready-to-use Alexa 647 labeled BSA (Thermofisher Scientific) with PBS as solvent (Figure 3.10(d)). The chips were kept at room temperature in a sealed petri box with a water soaked tissue overnight. The waveguide was finally rinsed with PBS and was always kept wet (with PBS over the entire length of the waveguides).
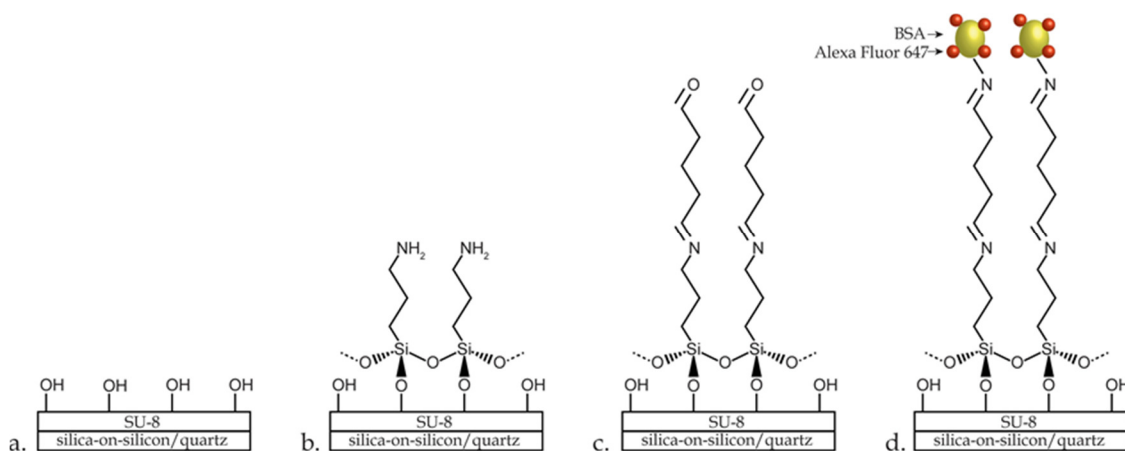
Figure 3. 10   Schematic of the immobilization steps. (a) Functionalization. (b) Silanization. (c) Glutaraldehyde treatment. (d) BSA-Alexa 647 immobilization.

3.6.4 Fluorescence Detection From BSA-Alexa 647 Immobilization

After complete photobleaching of the SU-8 cores for both the SU-8/silica and SU-8/quartz waveguides, a comparative study was performed to evaluate the fluorescence output of each waveguide with different concentrations of BSA-Alexa 647 immobilized following the steps on Figure 3.10. All the waveguides were cleaved so that they were 2.5 cm long. The cleaving techniques were similar to those described in [150], i.e., scratching the edge

of the silica-on-silicon wafer and applying pressure on both sides of the scratch to obtain a sharp fissure. For the SU-8/quartz waveguide, the quartz wafer was diced from the back while leaving 50 µm of material and cleaved by applying pressure on both sides of the dicing line.

Fluorescence evanescent spectroscopy was performed with concentrations of BSA-Alexa 647 varying from 0.15 nmol·L^{-1} to 15 nmol·L^{-1}. The responses of the waveguides are expressed as the normalized fluorescence power output, Γ. Which is defined as $\Gamma = \frac{P_{wg}^*}{P_{wg}^* max}$ with P_{wg}^* referring to P_{wg} from [157], but including optical losses and $P_{wg}^* max$ the measured fluorescence output for SU-8/Quartz at saturation (75.20 nmol·L^{-1}). Since the experiment is a ligand binding assay, the experimental data for the SU-8/quartz and SU-8/silica waveguides were fitted with the commonly used 4 parameters logistic regression model [161]:

$$Y = D + \frac{(A-D)}{\left(1+\left(\frac{x}{C}\right)^B\right)} \tag{3.1}$$

Where Y is the response, A the lower asymptote, D the upper asymptote, B the slope factor, C the analyte concentration at the inflection point of the calibration curve, and x the analyte concentration. This led to the following equations:

$\Gamma = \left((3.68 - 105.20)/1 + \left(\frac{x}{11.96}\right)^{1.106}\right) + 105.20, R^2 = 0.9889$ and

$\Gamma = \left((2.73 - 79.22)/1 + \left(\frac{x}{13.46}\right)^{1.275}\right) + 79.22, R^2 = 0.9953$. The linear dynamic ranges for each waveguides were evaluated as an interval going from 20 % to 80 % of the value of $D - A$ [73]. The linear ranges corresponds then to 2.85–40.45 nmol·L^{-1} and 3.76–37.90 nmol·L^{-1} for SU- 8/Quartz and SU-8/Silica waveguides respectively. The linear regression equations were adjusted to $\Gamma = 25.92 \ln x - 9.63, R^2 = 0.9985, \Gamma = 22.15 \ln x - 16.45, R^2 = 0.9982$ .The limits of detection were determined as the analyte concentrations at the blank+3σ (where σ is the standard deviation of the blank signal) [162], which were 0.24 and 0.69 nmol·L^{-1} for SU-8/Quartz and SU-8/Silica waveguides, respectively.
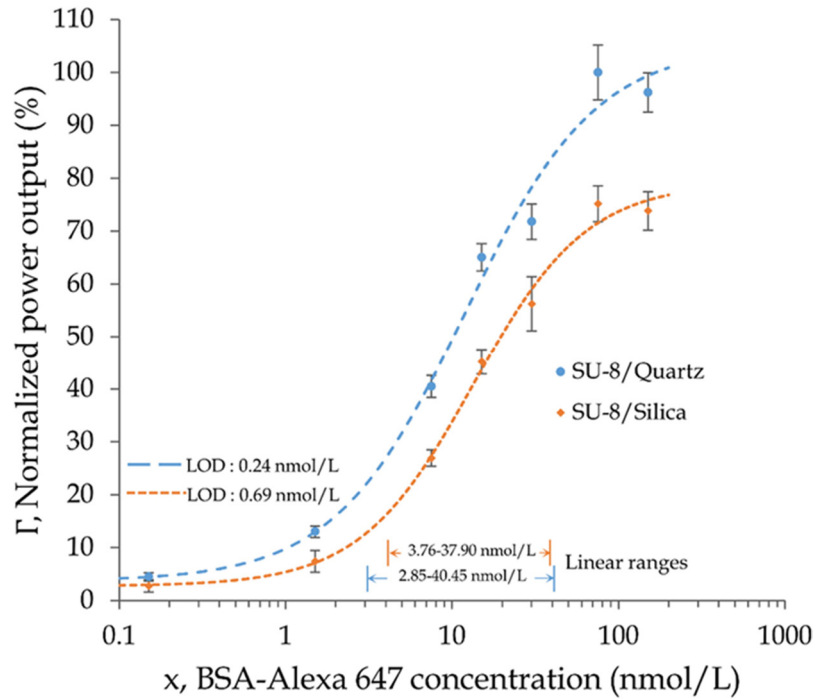
Figure 3. 11   Calibration curves for the fluorescence evanescent spectroscopy of BSA-Alexa 647 fluor immobilized on SU-8/Quartz and SU-8/Silica waveguides.

3.7   Discussion

Many parameters can affect the fluorescence evanescent coupling spectroscopy between the SU-8/Quartz and SU-8/Silica waveguides. The dimensions of the waveguides can be affected by the fabrication process. As shown from [150], the width of the SU-8/Quartz waveguide (~10 μm) is around 10% greater than the SU-8/Silica waveguide (~9 μm) due to the different fabrication protocols. Although the fluorescence collection efficiency is not affected by the width difference for highly multimode waveguide [158], the larger width offers a greater area that would accommodate more labeled analyte leading to a higher fluorescence coupling. This characteristic will result in an increase in the fluorescence light output that should be taken into account when comparing the calibration curves of both waveguides. The thicknesses of the waveguides should not affect the fluorescence output since they are similar, as seen in [150]. It was seen from the calibration curves, Figure 3.11, that the sensitivity of the SU-8/Quartz waveguides was greater than the SU-8/silica waveguides. The enhancement in sensitivity can be determined by the ratio of the slope of the linear regression equations, which gives 17% enhancement in sensitivity. Also, the limits of detection were evaluated as the

analyte concentrations of the blank signal + 3σ (where σ is the standard deviation of the blank signal) [162], which were 0.24 and 0.69 nmol·L^{-1} for the SU-8/Quartz and SU-8/Silica waveguides, respectively. As explained above, the lower asymmetry and optical losses due to the choice of substrates and the particularities of the fabrication processes that led to different indices of refraction resulted in a greater fluorescence evanescent coupling and less optical losses from the guided fluorescence light. This led to a higher fluorescence output for the SU-8/Quartz waveguide for a similar labeled analyte concentration. Although the linear ranges should be similar since the immobilization protocols were similar for both waveguides, the small difference observed in the linear ranges of both waveguides was probably due to experimental errors. According to [150], the optical propagation losses, for both waveguides, determined for the TE polarization, differed from the ones evaluated with the TM polarization. Taking this into consideration, and the fact that the light polarization at the input of the waveguides was measured to be 41° from the plane of the substrate surface, the guided light output should be 48% higher for the SU-8/quartz waveguide by calculating the optical losses for both waveguides with the values from Figure 3.3 with respect to the measured input light polarization. Also, from the 3D FDTD simulations the average value of the ratio of the 4 distributions (with randomly phased and oriented simulated fluorophores) for the total fluorescence collection efficiency for both waveguides was evaluated to be 5.39 ±1.42% (error =standard deviation), Table 3.2.

Taking into consideration the values from above, the fluorescence light output for the SU-8/Quartz waveguides should be around 63% greater than the SU-8/silica waveguides if, as mentioned above, 10% of its surface is larger, its lower asymmetry contribute to 5.4 ± 1.4% (Table 3.2) increase, and the optical propagation losses are 48% lower. For comparison, the average of the ratios of the averaged values of the relative signal (%) (Figure 3.11) between both waveguides gives an average fluorescence output enhancement of 46 ± 18% (error = standard deviation). In brief, the lower asymmetry parameters (Table 3.1) of the SU-8/quartz waveguide compared to the SU-8/silica waveguide contribute to a higher fluorescence output of 5.4 ± 1.4% as demonstrated by the 3D FDTD simulations. Also, if the asymmetry contribution for the fluorescence output is about 5.4 ± 1.4% and the average fluorescence output enhancement is 46 ± 18% it could be understood that the enhancement from the lower optical propagation losses of the SU-8/quartz waveguide (Figure 3.3) should be of 41 ±18%

or 31 ± 18% taking into account the 10% greater area of the SU- 8/quartz waveguide. Interestingly, it is the first time that fluorescence spectroscopy was done with direct coupling on a SU-8 on quartz rectangular waveguide. The SU-8 core and quartz substrate being both transparent to visible light could offer the possibility to perform fluorescence microscopy from the bottom of the substrate at the same time than fluorescence spectroscopy. This could be convenient if microfluidics are bonded on the top of the chip. Also, the fabrication process used for the SU-8/quartz waveguide [150] conveniently increases the core index of refraction and smoothen the side walls of the waveguide, which is favorable for evanescent wave fluorescence spectroscopy as shown is this work. This fabrication process could also be applied to other photo resist materials for rectangular waveguides for evanescent wave fluorescence spectroscopy. That being said, the fabrication process could be greatly improved if other parameters, such as temperature and humidity were controlled. These parameters could particularly influence the solvent concentration within the photo resist during the long soft bake specific to the SU-8/quartz waveguide fabrication process which is a crucial factor to obtain smoother waveguide walls as stated in [150]. Therefore it could modify the optical propagation losses from time to time. Hence, also the guided fluorescence light output.

3.8   Conclusion

A comparative study was done to evaluate the performance of a SU-8 rectangular waveguide on a quartz substrate fabricated with a novel process with a SU-8 waveguide on a silica-on-silicon substrate fabricated with the standard protocol for fluorescence evanescent spectroscopy. A 3D FDTD analysis was performed to evaluate the difference between the fluorescence collection efficiencies between both waveguides by simulating randomly oriented and phased dimensionless current dipoles acting as fluorophores along the top and sides of the waveguides. Fluorescence evanescent wave spectroscopy with different concentrations of BSA-Alexa 647 was experimented on the SU-8/Quartz and SU-8/silica waveguides. The fluorescence bio detection calibration curves revealed that the SU-8/Quartz waveguides showed a 17% enhancement in sensitivity compared to the SU-8/Silica waveguide fabricated with the standard protocol. Also, the limits of detection went as low as 0.24 nmol·L^{-1} and 0.69 nmol·L^{-1} for the SU-8/Quartz and SU-

8/Silica waveguides respectively. A higher sensitivity could probably be attained if control over the temperature and humidity was available during the fabrication processes. An optimization of these parameters could results in smoother waveguide sidewalls. Also, the 3D FDTD analysis to evaluate the fluorescence collection efficiency for fluorophores in the vicinity of a rectangular waveguide could be extended to different fluorophores and rectangular waveguides with different dimensions and indices of refraction.

CHAPTER 4

POLYMER WAVEGUIDE BIOSENSOR FOR ENHANCED EVANESCENT WAVE FLUORESCENCE DETECTION

4.1   Introduction

Optical sensors have known to be excellent candidates for chemical and biological sensing due to their ability to probe different analytes at the vicinity of surfaces with high sensitivity, speed, real time measurements, and immunity from electromagnetic interferences [163]. Most optical sensing devices exploit the evanescent wave as sensing mechanism. Evanescent waves appear when incident light is subjected to total internal reflection. Optical fibers sensors were the first to make use of this property of light for evanescent spectroscopy [164]. Optical fibers with stripped cladding expose the core to the analyte of interest and have been widely used for absorption and fluorescence measurements [165, 166]. Although optical fibers permit remote sensing [167] and geometrical flexibility, they lack structural strength and don't allow for multiplexing. Planar waveguides, on the contrary, offer a platform that is sturdier and allows for multiplexed analysis [168]. Moreover, patterning of sensing platforms with standard microfabrication techniques is possible with planar waveguides. However, patterning of microstructures are usually limited to simple geometries such as microarrays [169] or gratings [170]. Rectangular waveguides offer the possibility for multiple configurations and are best suited for miniaturization [117]. Indeed, rectangular waveguides allow for multi-analyte detection and multiple functionalities by patterning different integrated optical components, such as semiconductor lasers [171], Bragg gratings [172], interferometers [173], spectrometers [174], etc. on a single chip. Until now, silicon based materials were the most popular in the fabrication of integrated optics [113] and also in evanescent wave-based waveguides sensors [114-116]. Nevertheless, complex, costly, and extended fabrication processes of silicon-based waveguides led to the popularity of polymer based waveguides. Indeed, polymer materials offer sensibly the same optical properties but are

cheaper and can be deposited by a simple spin coating process. Many polymers materials were proven suitable for integrated optics [175]. Amongst these, SU-8, a photo resist developed in 1989 by IBM [83], has shown great potential. Many properties of the SU-8 polymer such as transparency to a wide range of wavelengths [86], mechanical resistance [84], high resolution [85], and biocompatibility [145, 146] for bio sensing purposes make it suitable for optical waveguides applications. An interesting fabrication process for SU-8/quartz waveguides optimized by Abdul-Hadi *et al.* [150], showed that the optical losses were diminished compared to SU-8/silica waveguides fabricated with the standard protocol. In addition, the core index of refraction of the SU-8 core on quartz was higher due to the particularities of the fabrication process. Also, with a substrate of lower index of refraction, the SU-8/quartz waveguide shows a lower asymmetry parameter than the SU-8/silica waveguide. These characteristics of the SU-8/quartz waveguide obtained from the optimized fabrication process of our previous work will be used to increase fluorescence yield from fluorescence evanescent wave spectroscopy. This Chapter aims to understand the mechanism of enhanced fluorescence coupling for effective sensing with rectangular waveguides. In order to study the effect of the selected design parameters on the sensitivity of the sensing platforms, the effective index method was combined with the modal propagation approach developed by Srivastava *et al.* [157] to calculate the fluorescence collection efficiency for sources near a planar waveguide surface. Furthermore, a fluorescence evanescent wave spectroscopy experiment with Bovine Serum Albumin labelled with Alexa 647 (BSA-Alexa 647) as model analyte was performed to compare the fluorescence output of the SU-8 waveguides on quartz fabricated with our optimized process [150] with SU-8 waveguides on silica fabricated with the standard protocol.

4.2   Design

The waveguides cores were fabricated with SU-8 5 photoresist (Microchem, Newton, U.S.A). The substrates were a 5 µm thick silica layer oxidized from a silicon wafer (Rogue Valley Micro Devices, Medford, U.S.A) and a 1-mm thick fused quartz wafer

(Semiconductor Wafer, Hsinchu, Taiwan). The width, the thickness, and the length of the waveguides were 10 µm, 5 µm, and 2.5 cm respectively (Figure 4.1ab).
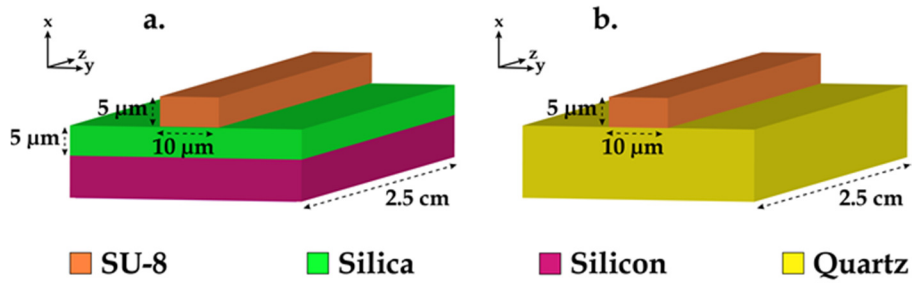
Figure 4. 1 **SU-8 waveguides on (a) silica-on-silicon (b) quartz.**

4.3 Fabrication & Characterization

UV lithography was used for the fabrication of the SU-8 waveguides on the silica-on-silicon and quartz substrates. The processes used for each substrate were different. The basic guidelines of the standard protocol was followed for the SU-8 waveguides on the silica-on-silicon substrate. The standard fabrication protocol was performed for the SU-8 waveguides on silica, but was inappropriate for the quartz substrate. A novel fabrication process was developed by Abdul-Hadi *et al.* [150] and was successful for preparing SU-8 cores on a quartz substrate. The same fabrication protocol used in [150] was used in this work for the fabrication of the SU-8 waveguides on silica-on-silicon and quartz. Also, the same group [150] performed a study comparing the SU-8/silica and SU-8/quartz waveguides optical characteristics. SU-8 on quartz waveguides outperformed the SU-8/silica waveguides with regards of optical losses. Moreover, the core indices of the SU-8/quartz waveguides were higher due to the specifics of the fabrication process. The higher core index and the lower substrate index of the SU-8/quartz waveguide compared to the SU-8/silica waveguide also make its asymmetry parameter lower. Lower optical propagation losses and asymmetry parameter of the SU-8/quartz waveguide should favor it for evanescent wave fluorescence spectroscopy. To establish this, the fluorescence collection efficiencies of the SU-8/quartz and SU-8/silica waveguides will be calculated with the effective index method combined with a modal propagation method and verified

with an evanescent wave fluorescence spectroscopy experiment with BSA-Alexa 647 fluor as model analyte.

4.4 Effective index method with modal propagation approach for fluorescence collection efficiency calculation

4.4.1 Fluorescence collection efficiency for a planar waveguide (modal propagation approach)

It was shown that when a fluorophore is excited close to a dielectric of a higher refractive index a portion of its emitted fluorescence is coupled back into the medium [153]. The coupling, known as evanescent coupling, is done with the help of the exponentially decaying evanescent field of the waveguide mode(s) (Figure 4.2).
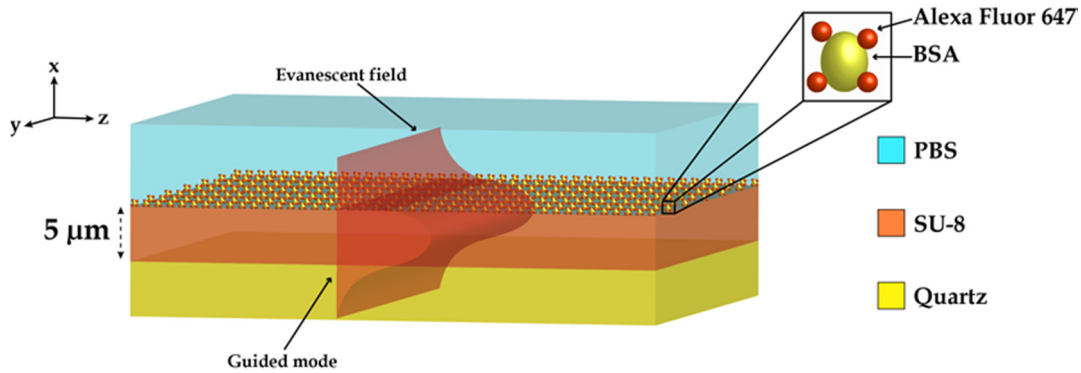
Figure 4. 2   **Scheme of a planar waveguide with a SU-8 core, a quartz substrate, and a PBS cladding with BSA-Alexa 647 immobilized on the SU-8 surface**

Table 4. 1   **Indices of refraction of the cores, substrates and claddings of the SU-8/quartz & SU-8/silica waveguides for the excitation light (λ= 635 nm) and the fluorescence light (λ = 671 nm). Data taken from [150].**

Waveguides	Index of refraction (λ = 635 nm)			Index of refraction (λ = 671 nm)		
	Cores	Substrates	Cladding	Cores	Substrates	Cladding
SU-8/quartz	1.590	1.457	1.330	1.587	1.456	1.330
SU-8/silica	1.583	1.460	1.330	1.580	1.459	1.330

The fluorescence collection efficiency η is defined as the ratio between the ensemble average of the total power coupled to the waveguide P_{wg} (measured at the output for a lossless waveguide) on the total power radiated by the sources P_{rad} [156, 157]

$$\eta = P_{wg}/P_{rad} \tag{4.1}$$

Where P_{wg} can be described as the sum over the ratios between the power of the mode in the region where the sources are located on the power carried by each mode P_ν for each waveguide mode [157]

$$P_{wg} = \sum_\nu \frac{\int_V S|\vec{E}_\nu|^2 dV}{16P_\nu} \tag{4.2}$$

$$\text{where } P_\nu = \frac{\beta W}{2\omega\mu_0} \int_{-\infty}^{\infty} |\vec{E}_\nu|^2 dx \tag{4.3}$$

With V the volume occupied by the sources, $\vec{E}_\nu$ the transverse electric field of the related TE mode with index ν where the mode function of the electric field in the y direction is taken from [176] for the three regions of the waveguide as seen in Figure 4.2, W the waveguide width of the planar waveguide, β the propagation constant, ω the angular frequency, μ_0 the magnetic permeability of vacuum, and S the source strength [177]

$$S = \frac{16\pi^2 R}{\omega\mu_0 n k_0} \tag{4.4}$$

Where R is the power radiated by a unit volume of the layer of fluorophores to a unit solid angle and where as in [157] it is approximated that $n \approx n_f \approx n_c$. The total power radiated by the sources P_{rad} for a planar waveguide is defined in [157] as

$$P_{rad} = 4\pi W t_c L R \tag{4.5}$$

With L as the length of the planar waveguide, and t_c the thickness of the layer of fluorophores. By substitution of Eq.4.3 & 4.4 into Eq.4.2 and subsequently Eq.4.2 & 4.5 into Eq.4.1, the fluorescence collection efficiency for the TE mode for a specific fluorescent layer thickness t_c becomes [157]

86

$$\eta = \frac{\pi}{2Wt_c n_c{}^2 k_0{}^2} \sum_v \frac{\int_0^{t_c} |\vec{E}_v|^2 \, dx}{\int_{-\infty}^{\infty} |\vec{E}_v|^2 \, dx} \tag{4.6}$$

By substituting the transverse electric field $\vec{E}_v$ by the transverse magnetic field $\vec{H}_v$ and the mode function of the magnetic field in the the y direction for the three regions of the waveguide taken from [176], the fluorescence collection efficiency for the TM mode for a specific fluorescent layer thickness t_c is

$$\eta = \frac{\pi}{2Wt_c n_c{}^2 k_0{}^2} \sum_v \frac{\int_0^{t_c} \left| \vec{H}_v \Big/ n^2(x) \right|^2 \, dx}{\int_{-\infty}^{\infty} \left| \vec{H}_v \Big/ n^2(x) \right|^2 \, dx} \tag{4.7}$$

From the decay constant in the cladding γ_c [178], the penetration depth is obtained

$$1/\gamma_c = (\beta^2 - k_0{}^2 n_c{}^2)^{-1/2} \tag{4.8}$$

As a first approach to understand the general behavior of the fluorescence collection efficiency, the rectangular SU-8 on quartz waveguide will be modelled as a simple asymmetric planar waveguide as depicted in Figure 4.2, with the respective indices for the substrate, core, and cladding. The plot of the penetration depths for an excitation light at $\lambda = 635 \, nm$ for each mode of the planar waveguide described in Figure 4.2 is shown in Figure 4.3.
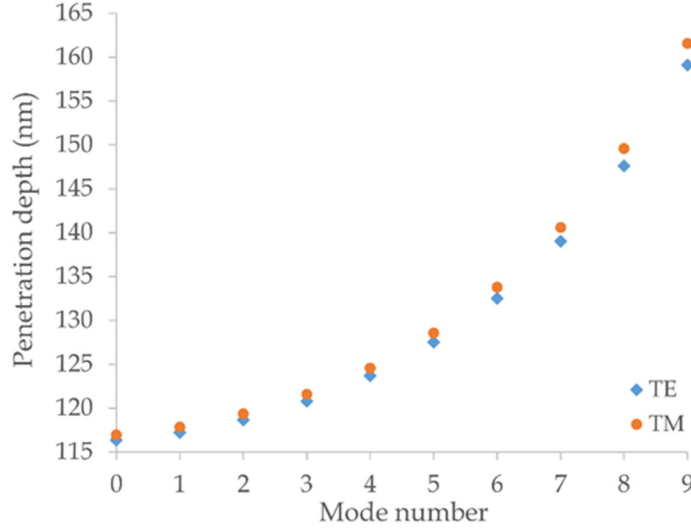
Figure 4. 3   Variation of the penetration depth of each mode of a planar waveguide for an excitation wavelength of λ=635 nm for both TE and TM polarizations.

The penetration depths are around 11 – 16 times greater than the fluorescent layer, which is around 10 nm thick. This indicates that the fluorescence layer is largely within the evanescent field of the excitation light. To calculate the fluorescence collection efficiency for the TE and TM modes for a 10 nm fluorescent layer, equations (4.6) and (4.7) are evaluated for $t_c = 10\,nm$. Various parameters such as the core thickness, core and substrate index of refraction, and the asymmetry parameter were varied to understand their impact on the fluorescence collection efficiency for a planar waveguide. The following Figures are all evaluated for a fluorescence emission at λ = 671 nm, a fluorescent layer thickness of 10 nm, and a cladding refractive index $n_c = 1.33$. On Figure 4.4, the substrate refractive index is n_s =1.45568 and the core thickness of the planar waveguide was varied from 50 nm to 20 μm. It is seen, as in [158], that the collection efficiency is more sensitive to variation to the core dimension for smaller cores sizes. For highly multimode waveguides, the collection efficiency is almost constant even for small core size variation. Each period corresponds to a specific number of modes where the peaks appears when the overlap of the evanescent field with the fluorescent layer in the cladding is optimal. The dips, however, appear when the core dimension is just thick enough to support a new guided mode.
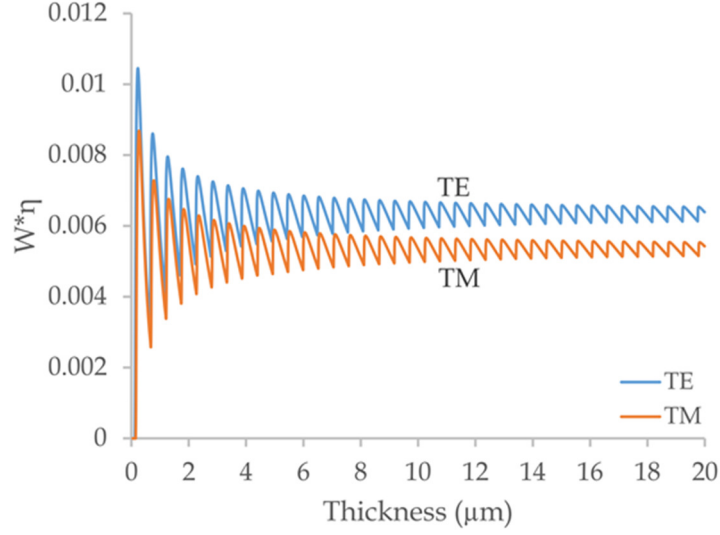
Figure 4. 4 Fluorescence collection efficiencies for a varying core thickness of a planar waveguide (Figure 4.2) for a fluorescence light wavelength of λ = 671 nm.

On Figure 4.5, the refractive index of the core n_f was varied from 1.46 to 3, the substrate refractive index is $n_s = 1.45568$, and the core thickness was kept at 5 μm. It is also observable on Figure 4.5, as in [158] that the collection efficiency increases with a higher n_f. The curve shows also a saw-like shape as in Figure 4.4, for similar reasons. The collection efficiency was also plotted as a function of the asymmetry parameter for the TE mode aTE and the TM mode aTM [151].

$$aTE = \frac{n_s{}^2 - n_c{}^2}{n_f{}^2 - n_s{}^2} \tag{4.9}$$

$$aTM = \frac{n_s{}^2 - n_c{}^2}{n_f{}^2 - n_s{}^2}\left(\frac{n_f{}^4}{n_c{}^4}\right) \tag{4.10}$$
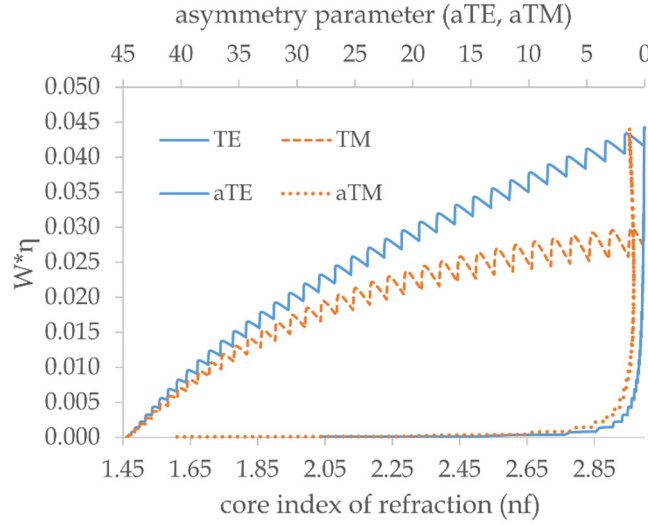
Figure 4. 5   Fluorescence collection efficiencies for a varying core refractive index of a planar waveguide (Figure 4.2) for a fluorescence light for a wavelength of λ = 671 nm.

The collection efficiency increases for a higher core index of refraction, as seen on Figure 4.5. Indeed, a higher core index confine more of the modal power in the fluorophore region (core-cladding interface). Hence, increases the coupling of the emitted fluorescence light.

On Figure 4.6, the core refractive index n_f was kept at 1.58716 and core thickness at 5 µm. The substrate refractive indices were varied from 1.33 to 1.586.
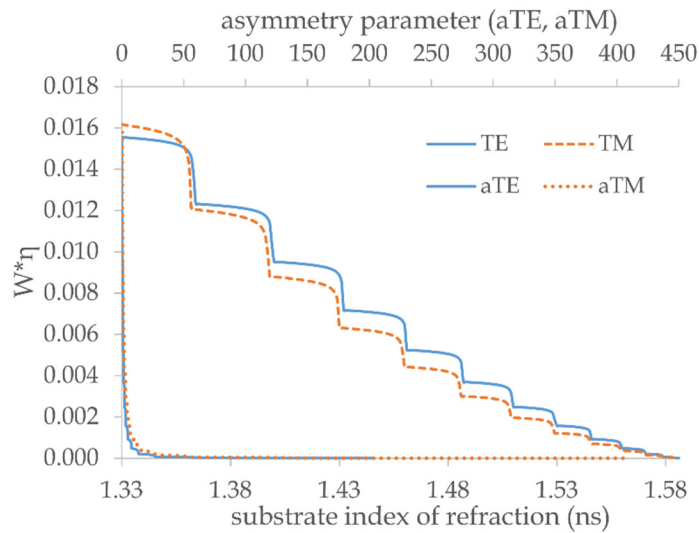
Figure 4. 6   Fluorescence collection efficiencies for a varying substrate refractive index of a planar waveguide (Figure 4.2) for a fluorescence light for a wavelength of λ=671 nm.

90

A greater proportion of the modal power will be located in the substrate if its index of refraction is increased. Hence, lower power located in the cladding resulting in a lower fluorescence collection efficiency. It is observable that in both Figures 4.5 and 4.6 the asymmetry parameters for TE and TM polarization correspond to a higher collection efficiency when their values are lower. This has also been reported in [157]. Comparing Figures 4.4–4.6, it is obvious that the more a planar waveguide is multimodal the more the core and substrate index of refraction have a impact on the collection efficiency than the thickness of the planar waveguide.

4.4.2 Fluorescence collection efficiency for a rectangular waveguide (effective index method with modal propagation approach)

The impact of the different parameters of the waveguide on the fluorescence collection efficiency was also investigated. Since strip waveguides are used in this work, the calculation of the fluorescence collection efficiency was done with the help of the effective index method. The effective index method [179] assumes that the electromagnetic field, with the use of the separation of variable, can be expressed as

$$\psi(x,y) = X(x)Y(y) \tag{4.11}$$

By inserting Eq.4.11 in the scalar Helmhotz equation and by introducing the y-dependent variable $k_0{}^2 n_{eff}^2(y)$ to it, the resulting equation can be separated into two independent equations that ressemble the equations of two 1 dimensional slab waveguides.

$$\left[\frac{\partial^2}{\partial y} + \left(k_0{}^2 n_i^2 - k_0{}^2 n_{eff}^2(y)\right)\right] Y(y) = 0 , \quad n_1 = n_c, \ n_2 = n_f, \ n_3 = n_c \tag{4.12}$$

$$\left[\frac{\partial^2}{\partial x} + \left(k_0{}^2 n_{x,i}^2 - k_0{}^2 N_{eff}^2(y)\right)\right] X(x) = 0 , \quad n_{x,1} = n_c, \ n_{x,2} = n_{eff}(y), \ n_{x,3} = n_s \tag{4.13}$$

The rectangular waveguide will be then treated as two separate slab waveguides for which the effective index of the first slab waveguide will be used as the core refractive index of the second slab waveguide. For example, to evaluate the collection efficiency for

the fluorescent layer at the top of the waveguide, Figure 4.7a,b (ii), for the TE polarization, the effective indices of each mode are calculated for the TM polarization for a slab waveguide as illustrated on Figure 4.7a,b (i). In the latter case, the slab waveguide is invariant in the x direction but finite in the y direction where the core corresponds to the SU-8 layer and the buffer solution is taken as the claddings, Figure 4.7a,b (i). Then, the effective index $n_{eff}(y)$ was used as the core refractive index $n_{x,2}$ of the slab waveguide evaluated with the TE polarization. The same procedure was applied for a fluorescent layer on the sides of the waveguide, Figure 4.7(a,b)(iv), instead the effective indices of each mode are calculated for the TM polarization for a slab waveguide as illustrated on Figure 4.7a,b (iii). In the latter case, the slab waveguide is invariant in the y direction but finite in the x direction where the core corresponds to the SU-8 layer and the buffer solution is taken as the cladding and the silica or quartz as the substrate, Figure 4.7(a,b)(iii). For a fluorescent layer on the top of the waveguide, the same process was applied except that the modes were first calculated for the TE polarization and finally with the TM polarization. The fluorescence collection efficiency for TE or TM modes for a fluorescent layer on the top or on the side of the waveguide is similar to Eq.4.6 & Eq.4.7 but with the mode functions from Eq.4.13 with the x or y variable with respect to the fluorescent layer being at the top or side of the waveguide. The effective index method was preferred to the FDTD numerical method for this three dimensional analysis of the fluorescence collection efficiency with variation of the waveguide parameters because the FDTD numerical method would be extremely time consuming for this matter. Nonetheless, the absolute values of the collection efficiencies obtained with this method are not to be considered very accurate since it does not consider the nodes and antinodes of the modes for a three dimensional analysis that render the evanescent field discontinuous at the core-cladding interface. Also, since the width/height ratio is 2 (10 × 5 µm) the calculation for the fluorescence collection efficiency is not highly accurate but meant to be used as a quicker approach compared to FDTD simulations to evaluate qualitatively the impact of different parameters on the fluorescence collection efficiency of a rectangular waveguide. For a more precise calculation of the fluorescence collection efficiency using 3D FDTD simulations for the SU-8/quartz and SU-8/silica waveguides with the same parameters than this work, refer to our previously published work [180].
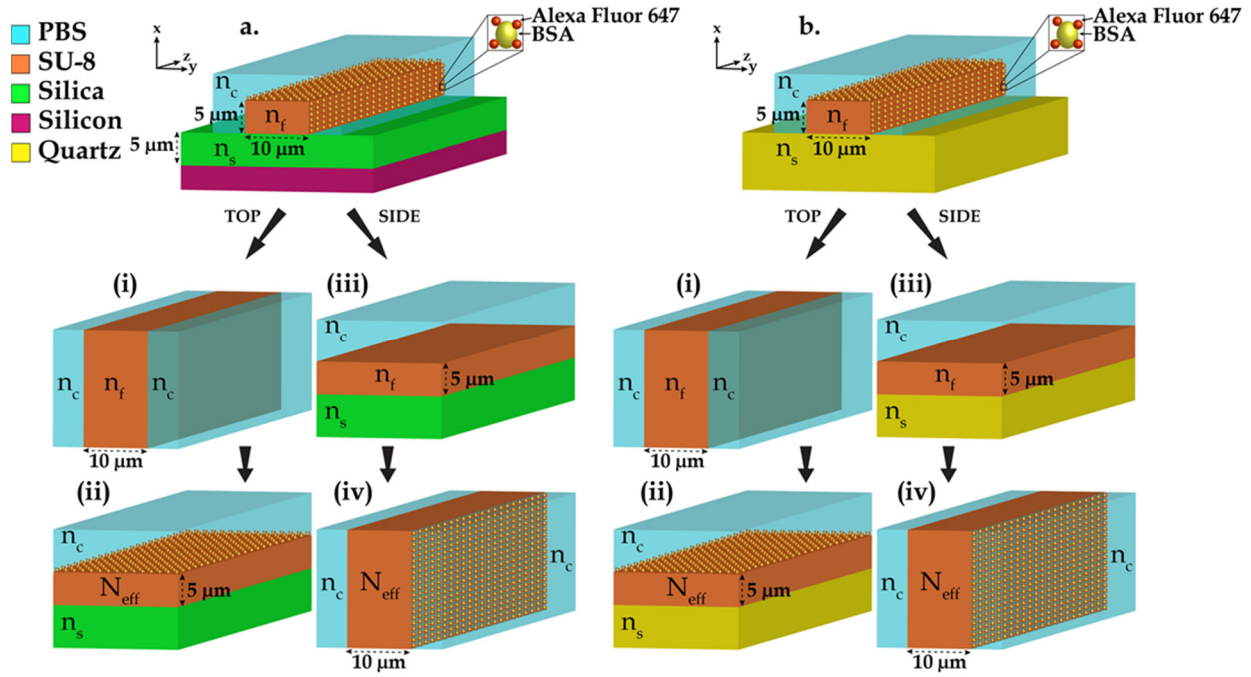
Figure 4. 7   Schematic showing the reduction of the 3D rectangular waveguides into 2D planar waveguides following the steps according to the effective index method for the calculation of the fluorescence collection efficiency for fluorophores on the top and side of the rectangular waveguides.

Fluorescence collection efficiency as a function of the core thickness, core index of refraction, and substrate index of refraction with their respective asymmetry parameters are shown from Figures 4.8-4.10.

4.4.2.1 Fluorescence collection efficiency for SU-8/Quartz and SU-8/Silica waveguides with varying core thickness

Below are shown the collection efficiencies for the TE and TM polarization of the top and sides of the SU-8/quartz and SU-8/silica waveguides that were calculated for a core thickness that was varied from 10 nm to 10 μm. The width of both waveguides was kept at 10 μm, the wavelength at $\lambda = 671\,nm$ and the indices of refraction of the cores, substrates and claddings are identical as identified on Figure 4.2.
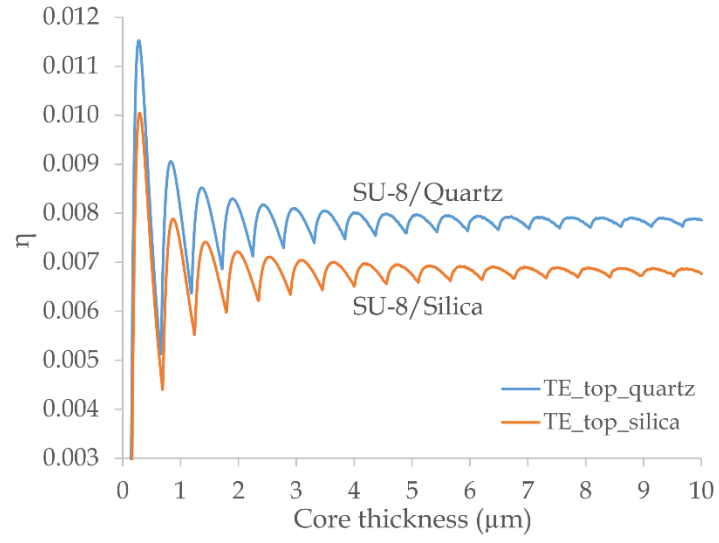
Figure 4. 8   **Effect of the core thickness on the fluorescence collection efficiency for a 10 nm fluorescent layer on top of a SU-8/Quartz and SU-8/Silica waveguides with a 50 μm width for the TE polarization.**
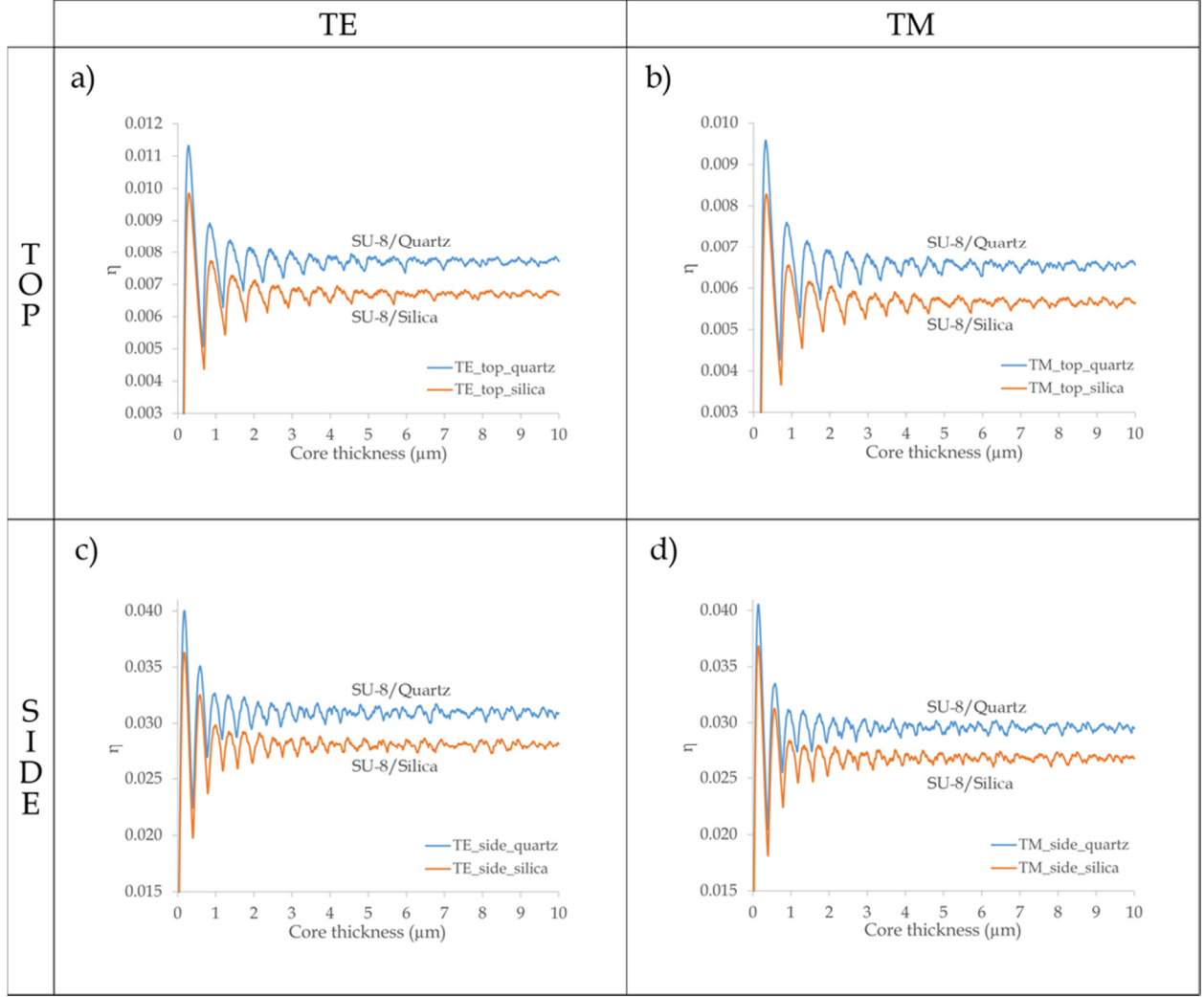
Figure 4. 9 Effect of the core thickness on the fluorescence collection efficiency for a 10 nm fluorescent layer on top of a SU-8/Quartz and SU-8/Silica waveguides for the a) TE and b) TM polarizations and at the side for the c) TE and d) TM polarizations.

It is observable that the fluorescence collection efficiencies for the TE and TM polarization from the top and side of the waveguide in Figures 4.9 a-d look similar to those of a planar waveguide (Figure 4.4). The roughness on the periods appears when the ratio between width/height or height/width decreases. For example, for a waveguide width fixed at 50 μm, the irregularities disappear and the periods are smoother (Figure 4.8). Indeed, a smaller width reveals the discrete nature of the modes with these irregularities. A greater difference is observable between the collection efficiencies from the top of the waveguide compared to the collection efficiencies from the side of the waveguide. Indeed, for a core of 5 μm thickness, the ratio between the collection efficiencies of the SU-8/quartz

waveguide and the SU-8/silica waveguide for the TE and TM polarization are, respectively, 1.180 & 1.171 from the top of the waveguide and 1.099 & 1.103 from the side of the waveguide. Although the penetration depth is mostly greater for the TM polarization, the confinement for the TE polarization is greater than for the TM polarization. This concentrates more power near the core/cladding interface. Also, the collection efficiencies from the side of the waveguide are higher in comparison to the top, due to a greater coupling of the light resulting from the lower asymmetry of the configuration. Although the asymmetry for the configuration of the side of the waveguide is nil for both the SU-8/quartz and SU-8/silica, the core index of refraction of the SU-8/quartz waveguide is greater than the SU-8/silica waveguide. This also increases the evanescent coupling resulting in a higher collection efficiency as seen on Figures 4.9 cd.

4.4.2.2 Fluorescence collection efficiency for SU-8/Quartz and SU-8/Silica waveguides with varying core index

The impact of the variation of the core index of refraction on the collection efficiency for the TE and TM polarization from the top and side of the waveguides with respect to the quartz and silica substrates was investigated by varying the core index from 1.46 to 2. The cladding index was kept at 1.33 and the fluorescence wavelength at $\lambda = 671 \ nm$. The corresponding asymmetry parameters were also calculated (Figure 4.10).
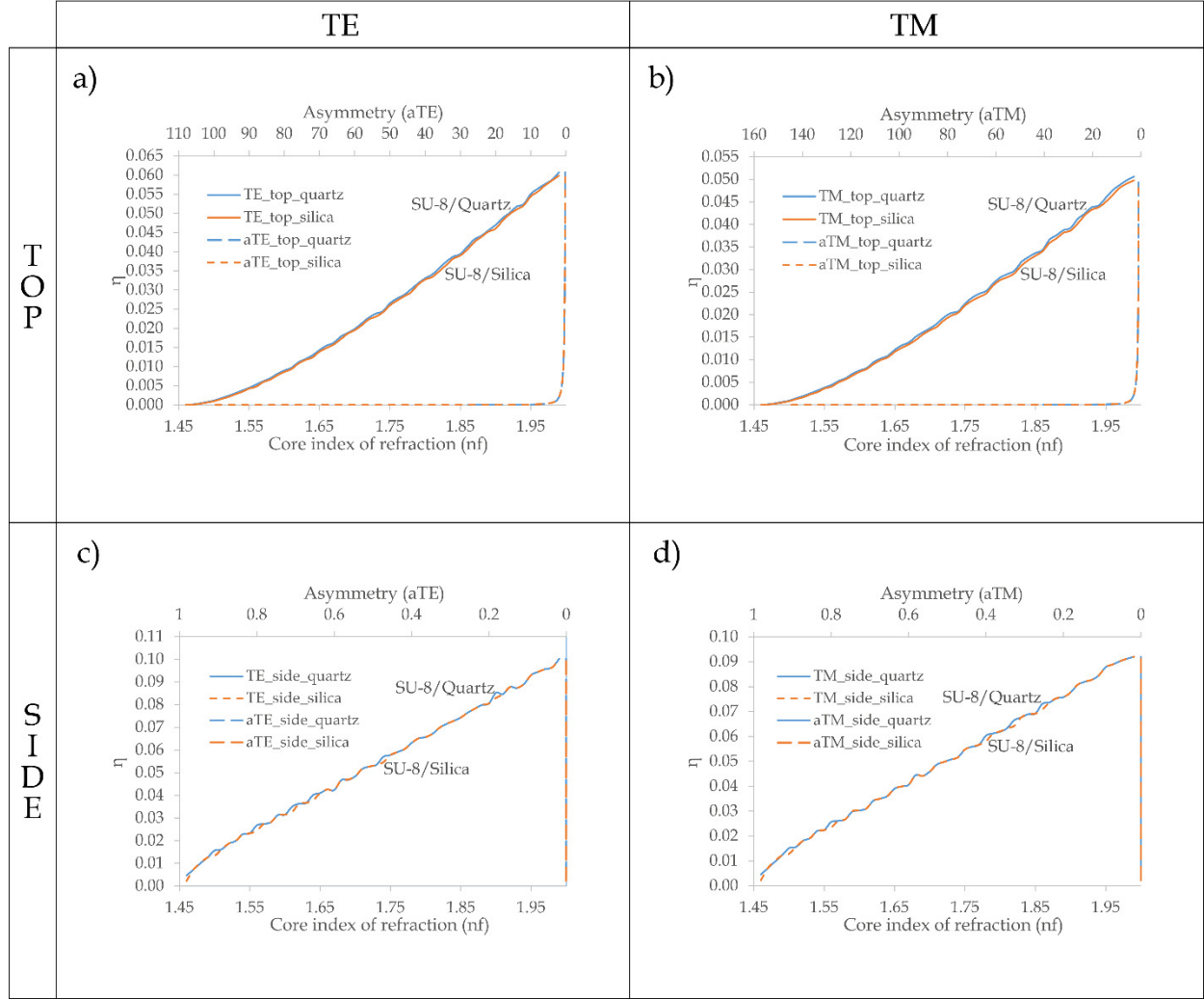
Figure 4. 10   Effect of the core index on the fluorescence collection efficiency for a 10 nm fluorescent layer on top of a SU-8/Quartz and SU-8/Silica waveguides for the a) TE and b) TM polarizations and at the side for the c) TE and d) TM polarizations.

As for the planar waveguide, the fluorescence collection efficiency increased with a higher index of refraction for a fluorescent layer on the top and on the side of the rectangular waveguide (Figure 4.10). Interestingly, the fluorescence collection efficiencies for the fluorescent layer on the side of both SU-8/quartz and SU-8/silica waveguides (Figures 4.10 cd) are almost identical for an increasing core index of refraction. The asymmetry parameters for the final side waveguide (Figure 4.7ab (iv)) are nil, $n_s = n_c$, for both substrates. The fluorescence collection efficiencies of two waveguides having the same asymmetry parameters will vary accordingly to their $\Delta n = n_f - n_s$. The final side waveguides (Figure 4.7ab (iv)), having the same asymmetry parameters and also the

same Δn, will be influenced by the effective index of the first calculated slab waveguide. Since the substrate refractive indices are almost similar, the effective indices are also approximatively the same and, from Figures 4.10 cd, it is seen that a small variation in the substrate index of refraction does not affect the collection efficiency significantly. Similar to the graphs for the collection efficiencies vs the core thickness, the collection efficiencies for the fluorescent layer on the side of the waveguide are also higher than the ones for the top of the waveguide.

4.4.2.3 Fluorescence collection efficiency for SU-8/Quartz and SU-8/Silica waveguides with varying substrate index

Finally, the fluorescence collection efficiencies for the TE and TM polarizations for the top and side of the waveguide were calculated by keeping the same parameters as identified in Figure 4.2 except for the substrate refractive index that was varied from 1.33 to 1.586 for the SU-8/quartz waveguide and from 1.33 to 1.579 for the SU-8/silica waveguide. The resulting graphs for a wavelength of λ = 671 nm are shown below.
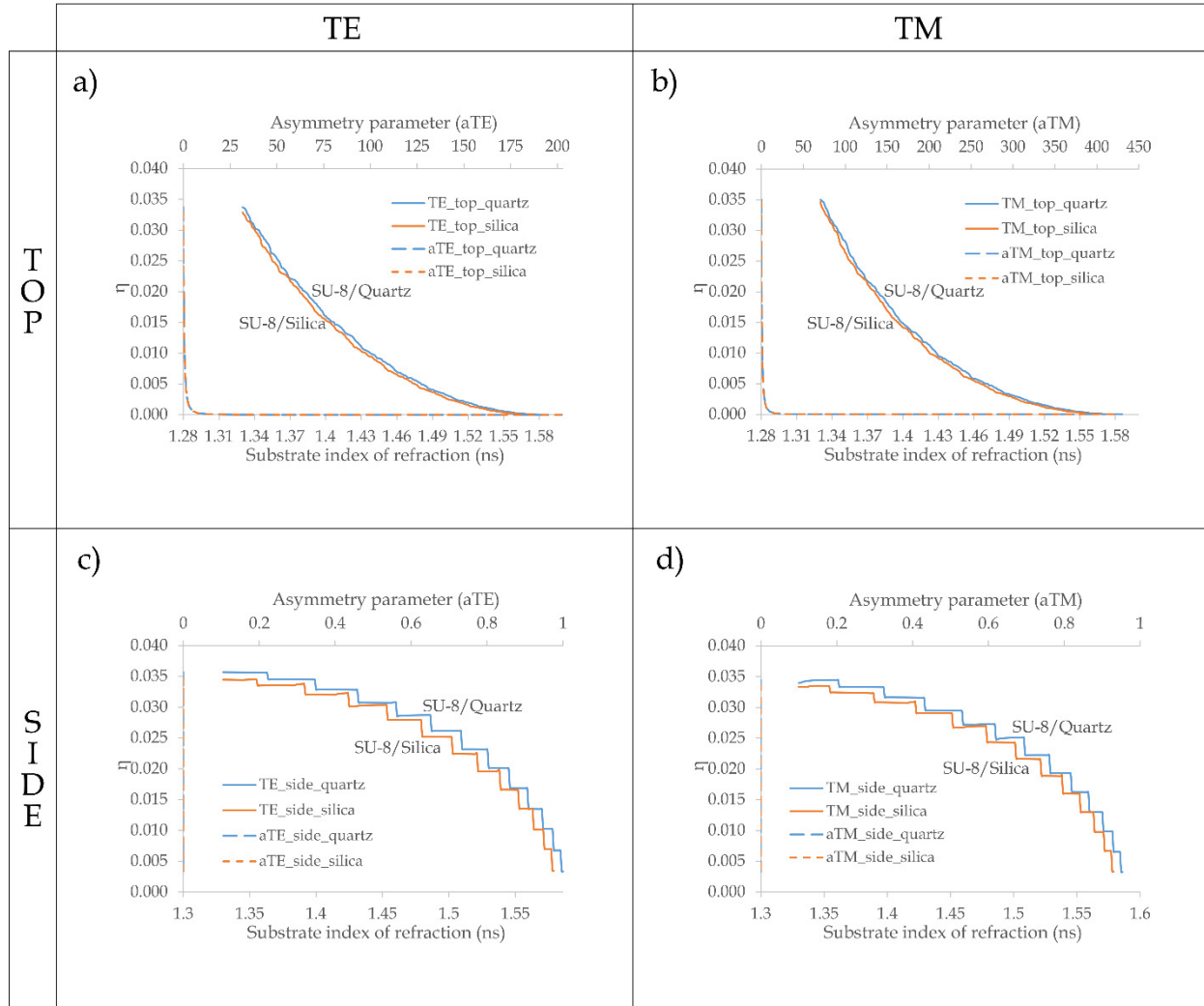
Figure 4. 11 **Effect of the substrate index on the fluorescence collection efficiency for a 10 nm fluorescent layer on top of a SU-8/Quartz and SU-8/Silica waveguides for the a) TE and b) TM polarizations and at the side for the c) TE and d) TM polarizations.**

As for the planar waveguide, a greater substrate index will drag more of the mode power into the substrate region, therefore diminishing the fluorescence collection efficiency as seen for an increasing substrate index of refraction (Figure 4.11). Since the SU-8 core has a higher index with the process SU-8/quartz, its collection efficiency will be higher than for the waveguide prepared via the SU-8/silica process for a varying substrate index of refraction.The modal periods are seen again in Figures 4.11 cd, ressembling the ones on Figure 4.6 because it was the substrate refractive index of the first calculated waveguide (Figure 4.7ab (iii)) that was varied.

From the previous results it is observable that the fluorescence collection efficiency for an increasing core thickness tends to get constant (Figure 4.9). The same behavior is seen for a larger width (Figure 4.8). From Figures 4.8-4.9, it can be seen that in the case of a small variation (~0.5 µm to 1 µm) around the values of the selected dimensions (10 × 5 µm) the fluorescence collection efficiency varies insignificantly. This renders the selected dimensions from our previous work valid for a comparative study between the SU-8/Quartz and SU-8/Silica waveguide since the fabrication results showed that the core thicknesses of both waveguides were almost identical. On the other hand, the width of the SU-8/Silica waveguide was 10% smaller. As explained before, a 10% change in the width will not affect the fluorescence collection efficiency significantly. Nonetheless, it will be taken into consideration for the experimental analysis since a greater number of immobilized fluorophores will affect the total fluorescence yield. Also, the greater core index and the smaller substrate index for the SU-8/Quartz waveguide showed to be advantageous for the fluorescence coupling compared to the SU-8/Silica waveguide (Figures 4.10-4.11). Consequently, the design parameters were validated for a comparative study and will be used for the fluorescence evanescent wave spectroscopy experiment.

4.5   Penetration depths for SU-8/Quartz and SU-8/Silica waveguides

In order to see the reach of the excitation light, the penetration depths for a 635 nm wavelength excitation light were calculated for each mode, for both the top and side of the two waveguides (for the TE polarization) (Figure 4.12).
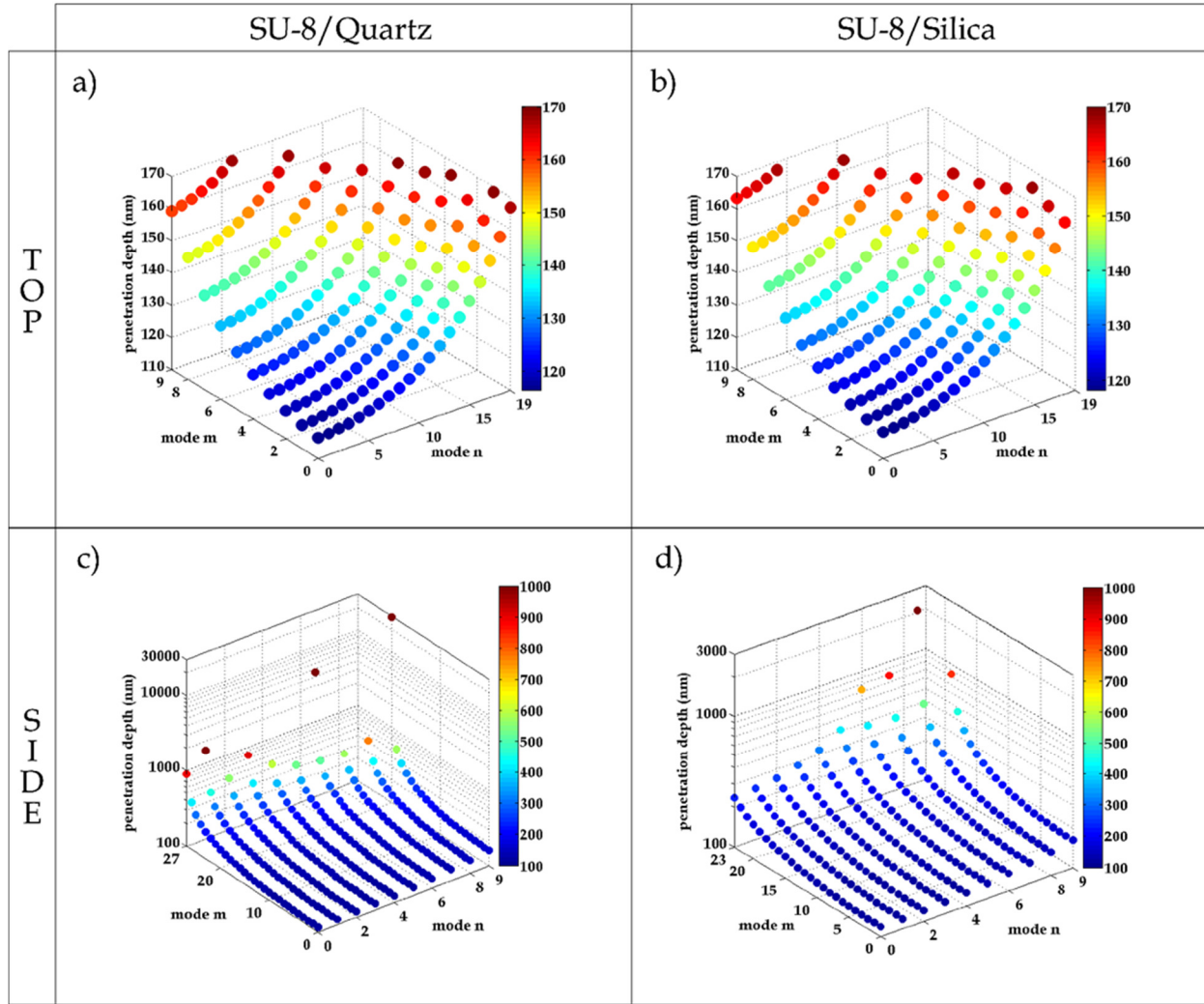
Figure 4. 12   Penetration depths at the top of the SU-8/quartz waveguide for a λ = 635 nm excitation wavelength (TE).

It can be seen that the penetration depth of the different modes from the top of the waveguide are lower in value than the penetration depths from the sides of the waveguide. Indeed, the lower asymmetry for the sides of the waveguide allows for deeper penetration of the evanescent field than for the top of the waveguide. However, a higher asymmetry as for the top of the waveguide enables a smaller variation of penetration depth [157]. It is noticeable for the penetration depths from the sides of the waveguide that a couple values seems to be overestimated. Indeed, when calculating the effective indices for the sides of the waveguide, some modes have a lower effective index than the substrates. Hence, these modes could potentially be leaky.

4.6　Fluorescence evanescent wave spectroscopy

4.6.1　Experimental setup

The experimental setup shown on Figure 4.13 served to detect the selected target (BSA-Alexa 647 Fluor) by fluorescence evanescent wave spectroscopy. A fiber-coupled laser diode with a 635 nm central wavelength (OZ optics,Westbrook,Canada) was used as the excitation light. A single mode fiber coupler (Thorlabs,Newton,USA) containing a 650 nm shortpass filter (Thorlabs,Newton,USA) was connected from its input with a single mode fiber with a $3.6 - 5$ µm mode field diameter (Thorlabs,Newton,USA), which was connected to the fiber-coupled laser diode. A similar fiber was connected to the output of the single mode fiber coupler and coupled directly to the input of the SU-8/quartz or SU-8/silica waveguide. The purpose of the 650 nm short-pass filter was to prevent saturation of the signal by blocking lower frequency light but still let through the excitation light. The excitation light was guided through the waveguide exciting the fluorescent dye where its fluorescence emission was evanescently-coupled and guided through the same waveguide. Both guided lights were collected simultaneously by a 62.5 µm core multimode fiber (Thorlabs,Newton,USA) at the output of the waveguide. This same fiber was connected to a multimode fiber coupler (Ocean Optics,Largo,USA) holding a 676/29 nm bandpass filter (Semrock,Rochester,USA), which was necessary to block the remaining excitation light. Lastly, the light guided through a 600 µm multimode fiber (Ocean Optics,Largo,USA) was spectrally analyzed with a spectrometer (USB-2000 Ocean optics). The polarization of the light at the output of the fiber butt-coupled to the input of the waveguide, was measured to be 41° from the plane of the substrate surface.
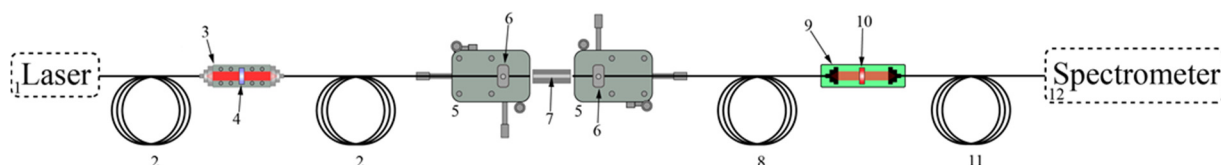
Figure 4. 13   **Fluorescence evanescent wave spectroscopy experimental setup.1) Fiber-coupled laser (λ = 635 nm) 2) single mode fiber 3) single mode fiber-to-fiber coupler 4) 650 nm shortpass filter 5) five-axis stage micro positioners 6) fiber holders 7) SU-8/quartz or SU-8/silica waveguide 8) mutlimode fiber (62,5 µm core) 9) multimode fiber-to-fiber coupler 10) 676-29 nm bandpass filter 11) multimode fiber (600 µm core) 12) spectrometer.**

4.6.2 Immobilization of BSA-Alexa 647 on SU-8/Quartz and SU-8/Silica waveguides

The same protocol was applied for immobilizing the BSA-Alexa 647 on both SU-8 waveguides on silica-on-silicon and quartz substrates. To prevent any trace of orgnic impurities from the fabrication process, the chips were rinsed with acetone and isopropanol. Following that, they were dried with a nitrogen jet and exposed to oxygen plasma for 20 seconds to functionnalize the surface with OH groups (Figure 4.14a). Then, the chips were immediately immersed in an 1% (v/v) APTES-ethanol solution for 1 hour at room temperature for silanization (Figure 4.14b). The chips were then placed in an oven at 100 ˚C for 10 min following after being rinsed with ethanol and DI water and dried with a gentle nitrogen flow. Thereafter, the chips were cooled down to room temperature and drops of a 1,2 % (v/v) glutaraldehyde-PBS (glutaraldehyde-Phosphate buffered saline) solution were placed on the SU-8 waveguides until the entire waveguide was covered by the solution (Figure 4.14c). To prevent the solution to dry, the chips were kept in a sealed petri box with a water-soaked paper for 2 hours at room temperature. Ensuingly, the chips were flushed with PBS and DI water and dried with a nitrogen jet. Solutions (~0.5 mL) of different concentrations of Alexa-647 labeled BSA (Thermofisher Scientific) with PBS as solvent were administrated to the SU-8 waveguides (Figure 4.14d). Again, the chips were kept in a sealed petri box with a water-soaked tissue at room temperature overnight. Finally, the waveguides were rinsed with PBS and was always kept wet by being submerged with PBS over the entire length of the waveguides.

Figure 4. 14 Schematic of the immobilization steps. a) functionalization b) silanization c) glutaraldehyde treatment, and d) BSA-Alexa 647 immobilization. Scheme not drawn to scale.

4.6.3 Fluorescence detection from BSA-Alexa 647 immobilization
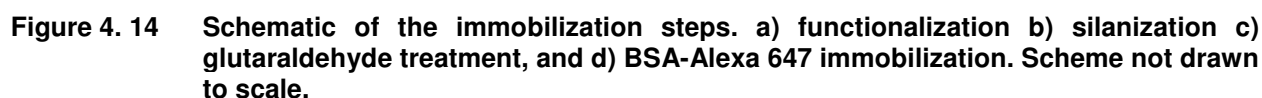
Firstly, an hour of illumination with the excitation light (λ = 635 nm) guided from the input to the output of the SU-8/silica and SU-8/quartz waveguides was enough to photobleach completely the SU-8 autofluorescence.

The fluorescence evanescent spectroscopy was conducted with varying concentrations of BSA-Alexa 647 ranging from 0.15 nmol·L^{-1} to 15 nmol·L^{-1}. The fluorescence output from the waveguides are expressed as the normalized fluorescence power output, Ω. This is defined as $\Omega = \frac{P^*_{wg}}{P^*_{wg}max}$ with P^*_{wg} referring to P_{wg} of Eq.4.1, but including optical losses and $P^*_{wg}max$ the measured fluorescence output for SU-8/Quartz at saturation (75.20 nmol·L^{-1}). The experimental data for the SU-8/quartz and SU-8/silica waveguides were fitted with the 4 parameters logistic regression model [161]:

$$\Omega = \frac{(A-D)}{\left(1+\left(\frac{x}{c}\right)^B\right)} + D \tag{4.14}$$

Where Ω is the response, A the lower asymptote, D the upper asymptote, B the slope factor,

C the analyte concentration at the inflection point of the calibration curve, and x the analyte concentration. This led to the following equations:

$$\Omega = \left((3.68 - 105.20)/1 + \left(\frac{x}{11.96}\right)^{1.106}\right) + 105.20, R^2 = 0.98894 \text{ and}$$

$$\Omega = \left((2.73 - 79.22)/1 + \left(\frac{x}{13.46}\right)^{1.275}\right) + 79.22, R^2 = 0.9953.$$ The evaluation of the linear ranges, 20% to 80% of $D - A$ [73], for the SU-8/Quartz and SU-8/Silica waveguides coincided with intervals of 2.85-40.45 nmol·L^{-1} and 3.76-37.90 nmol·L^{-1} respectively. The linear equations were evaluated within the linear ranges and led to these subsequent equations: $\Omega = 25.92 \ln x - 9.63, \ R^2 = 0.9985$ and $\Omega = 22.15 \ln x - 16.45, \ R^2 = 0.9982$ for the SU-8/Quartz and SU-8/Silica waveguides respectively. The limits of detection were determined as the analyte concentrations at the blank + 3σ (where σ is the standard deviation of the blank signal) [162], which were 0.24 and 0.69 nmol·L^{-1} for SU-8/Quartz and SU-8/Silica waveguides, respectively.
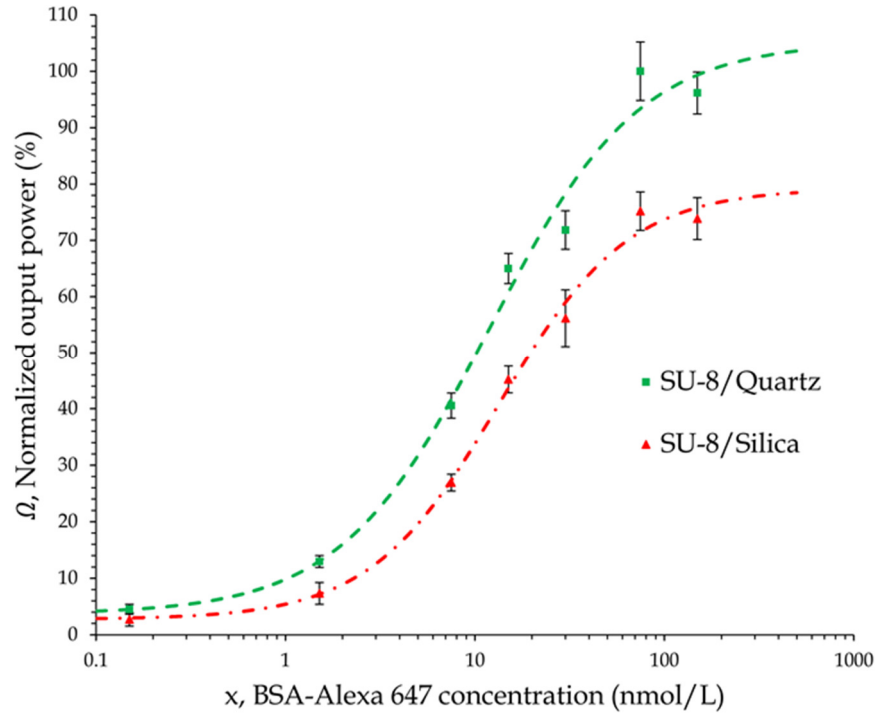
Figure 4. 15   Standard calibration curves of the SU-8/Quartz and SU-8/Silica waveguides for BSA-Alexa 647 fluor detection.

4.7   Discussion

As shown by the calculations, the fluorescence collection efficiency could be affected by many parameters. Indeed, the dimensions of the waveguides were affected by the fabrication process as shown from [150]. Further, the width of the SU-8/Quartz waveguide (~10 µm) was approximately 10% greater than the SU-8/Silica waveguide (~9 µm), due to the different fabrication procedure. As seen on Figure 4.8, the difference between the fluorescence collection efficiency of both waveguides was relatively constant for a larger width and for highly multimode waveguides. The larger width provides a greater area that would allow more labeled analyte to attach to the waveguide, leading to a higher fluorescence coupling. This characteristic should be taken into account when comparing the calibration curves of both waveguides. In contrast, as seen in [150] the thicknesses of the waveguides are similar and shouldn't affect the fluorescence output. The variation of the fluorescence collection efficiency due to the core or substrate index change was sensibly the same for both waveguides (Figures 4.9-4.10). The ratio of the slopes of the linear regression equations of both waveguides reveals an increase in sensitivity of 17% from the SU-8/Quartz waveguide compared to the SU-8/Silica waveguide. Furthermore, concentrations of BSA-Alexa 647 as low as 0.24 and 0.69 nmol·L^{-1} were found as the limits of detection for the SU-8/Quartz and SU-8/Silica waveguides, respectively. These results are consistent with our previous arguments about the greater fluorescence evanescent coupling due to the lower asymmetry of the SU-8/quartz waveguide compared to SU-8/silica waveguide because of the choice of substrates and the particular parameters of the fabrication processes that led to different core indices of refraction. Also, the lower optical propagation losses showed by the SU-8/quartz waveguide in [150] as opposed to the SU-8/silica waveguide increases even more the fluorescence output SU-8/Quartz waveguide for a similar BSA-Alexa 647 concentration. As stated previously, the light polarization at the input of the waveguides was measured to be 41º from the plane of the substrate surface. Considering also that the optical propagation losses differed for the TE and TM polarization for both waveguides and the light polarization at the waveguides input, a 48% increase in the light output should be observed for the SU-8/quartz waveguide by evaluating the ratio between the optical losses [150]. Previous

calculations showed that the ratios of the fluorescence collection efficiency between SU-8/quartz and SU-8/silica waveguides were evaluated to be around 18% for the top and 10% for the sides of the waveguides. Therefore, the average will be approximately 15% of total enhancement for the SU-8/quartz waveguide. It is understandable that around 73% more guided light will reach the output of the SU-8/Quartz waveguide since its area of immobilization if 10% greater. Its lower asymmetry increases by 15% the fluorescence collection efficiency and the optical propagation losses are reduced by 48%. In contrast, an average fluorescence output enhancement of 46 ± 18 % was obtained from the average of the ratios between the measured data of the SU-8/quartz and SU-8/silica waveguides from Figure 4.15. In view of these values, the enhancement of the measured fluorescence output is lower than predicted. However, the waveguide fabrication process was subjected to an environment where humidity and temperature were not controlled. Since, the SU-8/quartz waveguides are put through a very long soft bake [150] these parameters could influence the roughness of the waveguides. Hence, more optical losses will lead to lower guided fluorescence output. Nonetheless, the principles of the novel fabrication process from [150] were proven to be favorable for evanescent fluorescence spectroscopy and could be applied to other polymer waveguides and could also be improved by humidity and temperature control. As claimed previously, the method used for the calculation of the fluorescence collection efficiency may not be highly accurate for the chosen waveguides parameters but still predicted an enhancement in the fluorescence output as verified experimentally and was useful for a quick analysis of the impact of the waveguides parameters on the fluorescence collection efficiency. However, the same method could be more accurate for the calculation of the fluorescence collection efficiency for waveguides with greater width/height aspect ratios and lower index contrast.

4.8 Conclusion

A fluorescence evanescent wave spectroscopy experiment was performed to assess the fluorescence output of SU-8 rectangular waveguides on quartz substrates fabricated with a novel process in comparison to SU-8 waveguides on silica-on-silicon substrates fabricated with the standard protocol. The impact of the variation of different parameters

such as the core width, the core, and substrate indices for the TE and TM polarization on the fluorescence collection efficiency on both waveguides was calculated with the effective index method combined with a modal propagation approach. Solutions containing different concentrations of BSA-Alexa 647 were applied to the SU-8/Quartz and SU-8/silica waveguides to construct their respective calibration curves, which revealed a 17% enhancement in sensitivity for the SU-8/Quartz compared to the SU-8/silica waveguides for fluorescence evanescent wave spectroscopy assays. Furthermore, limits of detection of 0.24 nmol·L^{-1} and 0.69 nmol·L^{-1} were attained for the SU-8/Quartz and SU-8/Silica waveguides respectively. Control and optimization over parameters such as temperature and humidity during the fabrication processes could have resulted in smoothing furthermore the waveguide sidewalls. Hence, resulting in a higher sensitivity by diminishing the optical losses. Also, the study on the impact of the variation of different parameters inherent to a rectangular waveguide on its fluorescence collection efficiency could be used with fluorophores with different emission wavelengths and waveguides with different aspect ratio and refractive indices.

CHAPTER 5

CASCADED OPTICAL POLYMER WAVEGUIDE FOR ENHANCED FLUORESCENCE EVANESCENT WAVE SPECTROSCOPY

5.1 Introduction

The detection and monitoring of biological analytes are essential for the fields of biology, biochemistry, and the biomedical field in general. Fortunately, biosensors have been developed to respond to this need. Biosensors are analytical devices that turn a biological response to an electric signal. They are mainly composed of a biological or chemical receptor that recognize the analyte of interest and produce a signal, which a transduction component converts into an electrical signal that can be analyzed by a reading device. A multitude of biosensors have been developed with different transducing approaches such as electrochemical, gravimetric, mechanical, electronic, acoustic, optical, etc. Interestingly, compared to other biosensors, optical biosensors compared offer high sensitivity, fast detection, immunity to electromagnetic interference, suitability for miniaturization, multiplexing, as well as label and label-free detection capabilities [3, 181-184]. The sensing mechanism of most optical biosensors arise from a property of light when it is confined in an optical waveguide, called the evanescent wave. Indeed, first described by Hirschfeld [185], the evanescent wave appears after total reflection of an incident light at the boundary between two dielectric media, where the incident light propagates from a high index dielectric medium and is totally reflected at the boundary with a lower index dielectric medium. The evanescent wave is a field that exponentially decays inside the lower index medium and is used to probe changes in the vicinity at the surface of the platform. Optical fibers were the first and still widely used sensing platforms for optical bio sensing [1]. Indeed, their ability to perform remote sensing with good geometrical flexibility is attractive for many biomedical applications [186]. However, the main drawback about optical fibers is their fragility. Especially when their cladding is

removed or subjected to extreme tapering to allow the core to be exposed to a sample for example for absorption [165, 187] or fluorescence detection [188, 189]. Planar waveguides arose as alternative to optical fibers since they provide a more robust platform. Most importantly, they allow for miniaturization and patterning of biological materials such as antibodies or antigens for real time multi-analyte assays. Different optical methods were employed with the planar waveguide platform for bio detection such as surface plasmon resonance (SPR) [190], localized surface plasmon resonance (LSPR) [191], surface plasmon-coupled emission (SPCE) [192], reverse symmetry [193], fluorescence evanescent wave spectroscopy [194], etc. Among others, fluorescence evanescent wave spectroscopy combines the surface restricted probing of the evanescent field and the high sensitivity and specificity provided by fluorophores. Although planar waveguides have been shown to be suitable for optical bio-sensing and allow for miniaturization, they are usually incorporated into a bulky setup [195]. To fully miniaturize the optical components and analysis, as well as to incorporate a microfluidic system, rectangular waveguides (two-dimensional waveguides) are more suitable. Indeed, rectangular waveguides can be designed in a wide range of optical structures for bio-sensing applications such as micro-ring resonators [196], Bragg-grating resonator [197], directional couplers[198], interferometers [87], etc. Amongst others, the cascaded waveguide design by Ozhikandathil *et al.* [70] has been proposed to increase the sensitivity of fluorescence evanescent wave spectroscopy. The cascaded waveguide, fabricated with silica core and substrates, was tested for the detection of tagged recombinant growth hormones (RBST), reportedly at a concentration as low as 25 ng·mL^{-1}. In this Chapter, the cascaded waveguide design will be fabricated with SU-8 polymer on silica waveguides and tested for fluorescence evanescent wave spectroscopy with different concentrations of Alexa 647-labeled biotin. Also, simulations with the beam propagation method will be used to analyze the excitation and guided fluorescence light through the sensors.

5.2   Design

The chosen design relies on increasing the area of immobilization of the labeled targets to increase the fluorescence output. To attain this, an initial waveguide is split into two, creating two branches that are then split again into two, creating four branches that are finally split into two once again, thus creating eight branches. From these eight branches, the same process is done in reverse. Hence, the branches recombine successively until a single output waveguide is obtained, Figure 5.1b. A single waveguide is fabricated next to the cascaded waveguide to compare its sensitivity to fluorescence evanescent wave spectroscopy, Figure 5.1a. The substrate used is a 5 µm silica layer oxidized from a silicon wafer. The cores of the waveguides (10 × 5 µm) were fabricated with SU-8 photoresist, Figure 5.1. The dimensions of the cascaded waveguide configuration are shown in Figure 5.2.
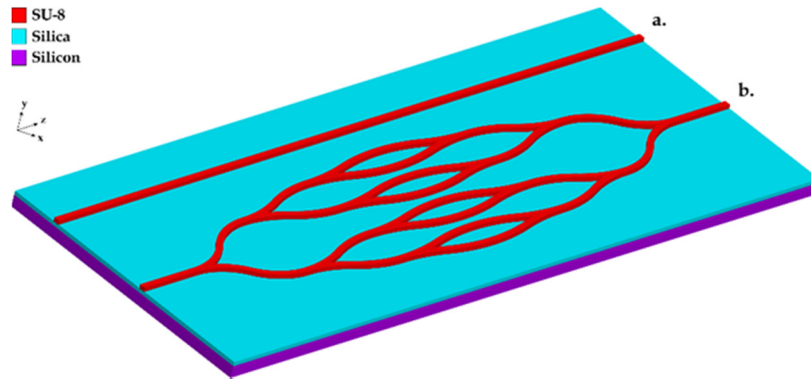
Figure 5. 1   **Scheme of the a) single and b) cascaded waveguides for enhanced fluorescence evanescent wave spectroscopy.**
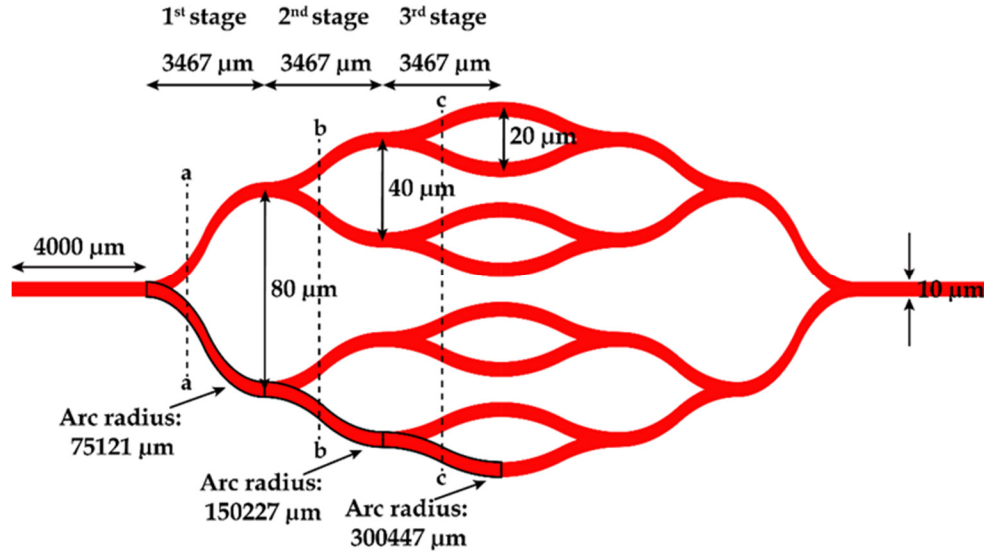
Figure 5. 2   Scheme of the cascaded waveguide design with dimensions for enhanced fluorescence evanescent wave spectroscopy. Drawings are not to scale.

The splitting junctions shown in Figure 5.2 are made of two S-bend waveguides. S-bends are made of two arcs of same radius configured as an S shape. The arcs radii of the different splitting junctions of the cascaded waveguide were chosen to be very large to minimize the optical losses that are usually attributed to bent waveguides. Also, the branches of the splitting junctions are very long compared to the width between the branches. This configuration was chosen to expand the space between the branches of the splitting junctions very gradually so as to minimize the optical losses from light division.

5.3   Fabrication

The chosen substrate was a 5 µm wet thermally-oxidized silica film on a silicon wafer (Rogue Valley Micro Devices, Medford, U.S.A). The wafer was rinsed with acetone and isopropanol to remove contaminants. After being dried with a nitrogen jet, SU-8 photoresist was spin coated onto the wafer at 500 rpm for 10 s and then at 3000 rpm for 30 s, Figure 5.3a. The preferred photoresist was SU-8 5 (Microchem, Newton, USA) for its property to form film as thin as 5 µm. After spin coating, the wafer was placed onto a

hotplate heated at 65 ºC for 2 min and then at 95 ºC for 5 min, Figure 5.3b. After cooling the wafer to room temperature, the wafer was exposed to a 365 i-line UV light (9 mW·cm^{-2}) through a photomask, Figure 5.3c. After 18 s of exposition, the UV light transferred the desired pattern to the photoresist. Thereafter, the wafer was placed again on the hotplate at a temperature of 65 ºC but for 1 min and then at 95 ºC for 2 min, Figure 5.3d. After cooling the wafer to room temperature, the wafer was immersed in a SU-8 developer (Microchem, Newton, USA) for 2 min, Figure 5.3e. Immediately after the developing session, the wafer was dipped in isopropanol to stop the reaction. Subsequently, the wafer was rinsed with isopropanol and deionized water. After being dried with a nitrogen jet, the wafer was heated at 150 ºC on the hotplate for 1 hour to stabilize the properties of the resist, Figure 5.3f.
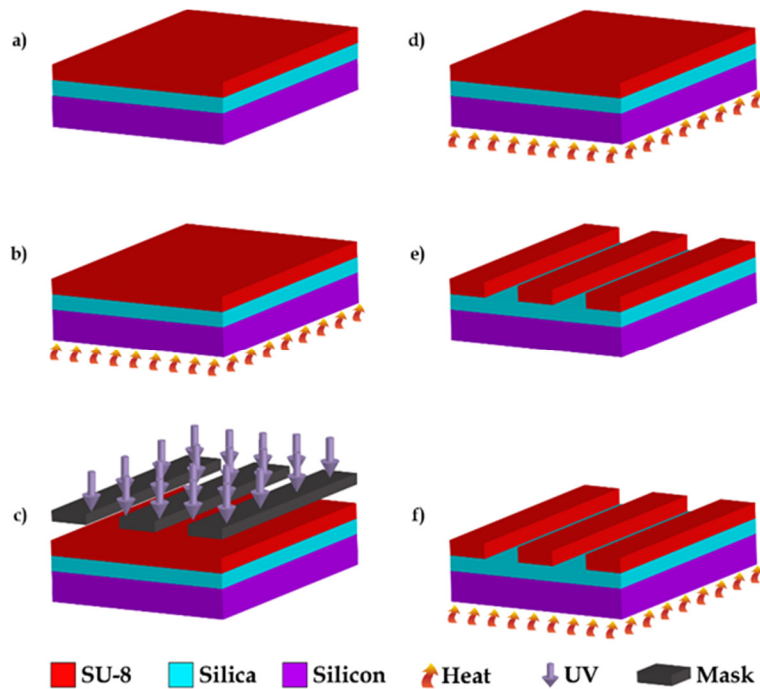
Figure 5. 3   **Illustration of the main steps of the fabrication process for the cascaded waveguides. Details are given in Fabrication.**

Images of the fabricated design were taken by scanning electron microscopy (SEM), to assess the quality of the fabrication. The splitting junctions of the cascaded waveguides are shown altogether with the single waveguide in Figure 5.4abc. The first splitting

junction in which the initial waveguide splits into two branches is shown in Figure 5.4a. The second stage of 2 splitting junctions is shown in Figure 5.4b. Finally, the third stage with 4 splitting junctions is shown in Figure 5.4c.

TMG 5.00kV 6.6mm x500 SE   100um

TMG 5.00kV 6.6mm x370 SE   100um

114
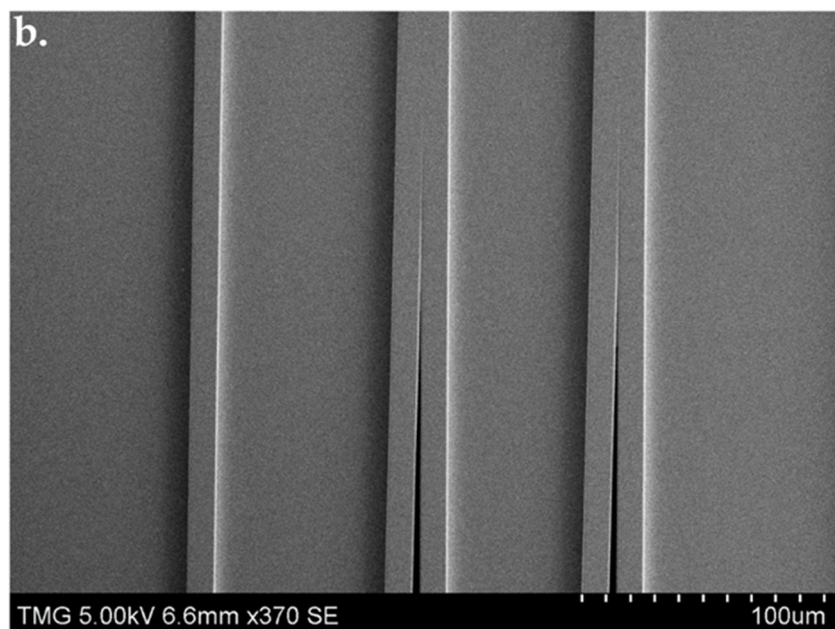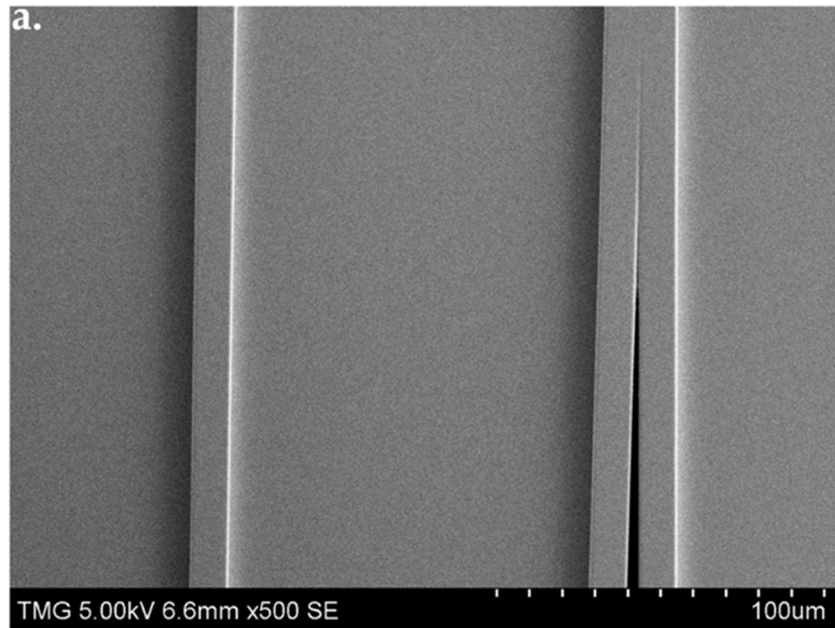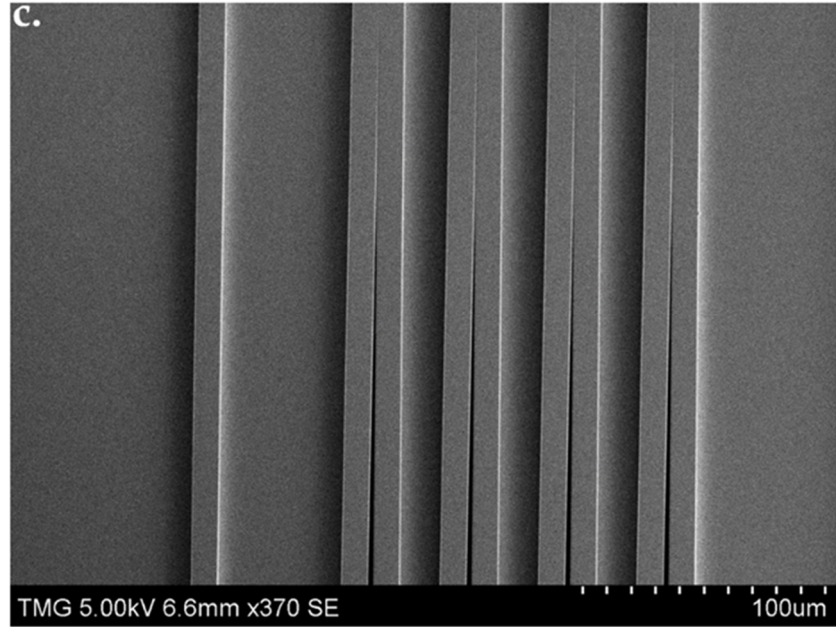
Figure 5. 4   **SEM pictures from the top of the sensing platform showing the single waveguide and the splitting junction(s) of the a) first stage (line aa), b) second stage (line bb) and c) third stage (line cc).**

From the SEM images, the spacing between the branches of the junction appear to gradually grow, as expected. Also, the resist is fully developped and no underdeveloped resist appears to be left between the branches. Although the splitting junctions have sharp edges, the beginning of the junctions do not appear to have been etched completely. This is expected from the resolution limit of photolithography. It is seen in Figure 5.4abc, that the etching between the branches fade gradually. This extra resist could affect the propagation of the excitation and fluorescence light guided through the waveguides. Numerical simulations were then performed next to analyze the effect of this extra resist on the original design.

5.4   Optical power characterization

Since the excitation light comes through a single mode fiber, the output light from the fiber must be simulated with the fiber characteristics. The fiber used was a single mode fiber (Thorlabs, Newton, USA) with a 3.5 µm core diameter, a cladding of refractive index 1.45709 and a core of index difference 0.00603. The beam propagation method was used to simulate the light through the fiber facet. As seen in Figure 5.5a, the scheme of the

115

core of the fiber in 3D is shown on the left of the image and on the right the resulting electromagnetic field at the output of the fiber. A light with a Gaussian profile was injected in the 3D fiber until convergence was attained. The resulting effective index n_{eff} reached a value of 1.460124. Now that the effective index was determined, the mode profile in a 2D configuration was calculated. Translating the simulated light from a 3D to a 2D configuration is necessary for further simulations implicating the whole cascaded waveguide design. To proceed with this, a slab waveguide confined in the x direction and infinite in the y direction with a width similar to the fiber core (3.5 µm) was used, Figure 5.5b. Also, the cladding index was set with the same value of the fiber cladding index (1.45709). However, the slab core index was varied until the effective index of the fundamental mode matched the effective index of the fundamental mode of the 3D fiber. The index difference resulted in a value of 0.004212.
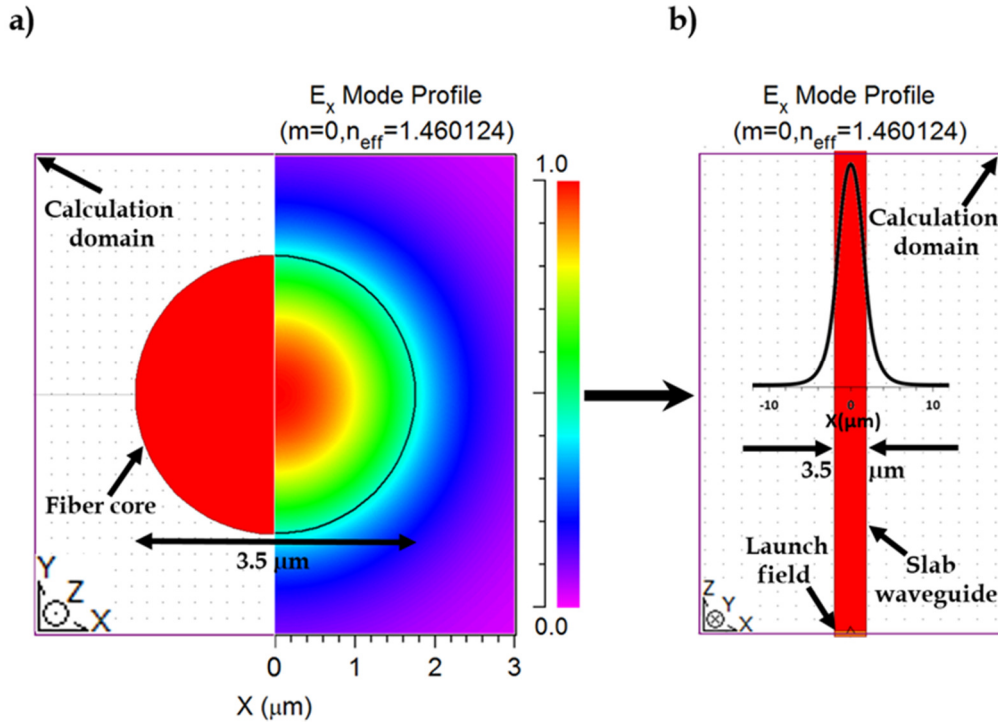
Figure 5. 5   a) scheme of the fiber facet with the calculation domain and electromagnetic field distribution of the fundamental quasi-TE mode at the output of the fiber b) scheme of the slab waveguide mimicking the fiber in a 2D configuration inside the calculation domain with its respective fundamental mode profile.

Now that the light output from the fiber was determined for a 2D configuration, the simulated source was used at the input of the 2D scheme of the cascaded waveguide for

beam propagation method simulations, Figure 5.6.
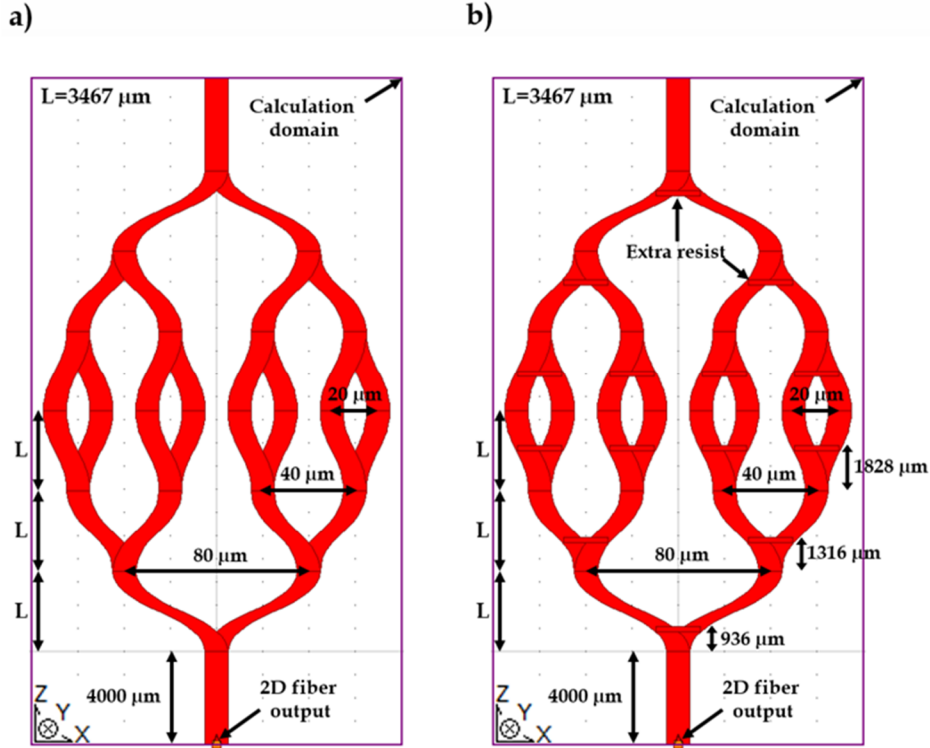
Figure 5. 6   Scheme of the a) original design and b) configuration after fabrication of the cascaded waveguide with the simulated fiber source (Aspect ratio 100:1).

The beam propagation method was used to evaluate the remaining amount of the excitation power at the output of the original design, Figure 5.6a, and the design after fabrication (with the extra resist), Figure 5.6b. The configurations have the same dimensions as in the scheme on Figure 5.2, with the exception of the design after fabrication containing the added resist at the opening of the splitting (or recombining) junctions. The addition of the extra resist starts at the beginning of the opening of the splitting junctions and end at the same width where it ends on the SEM images. The results from the simulations are presented in Figure 5.7.
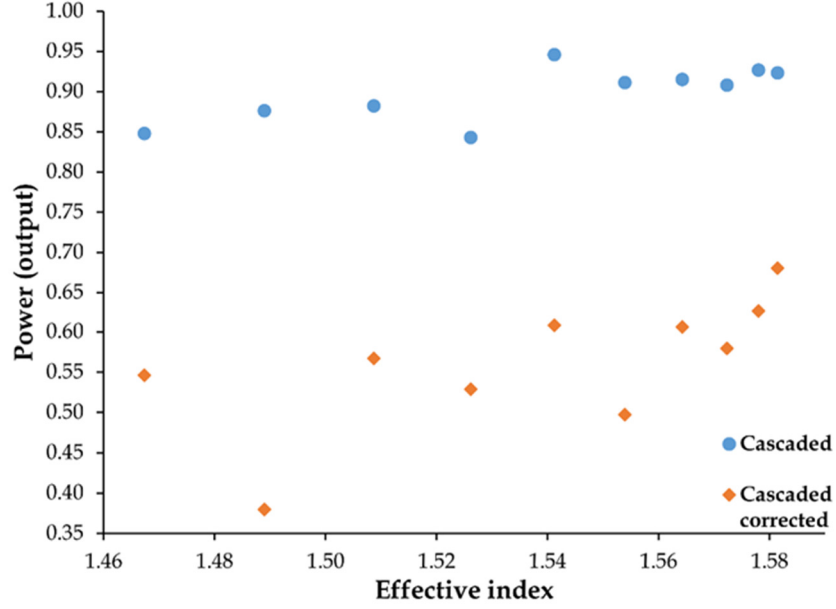
Figure 5. 7 **Power at the output of the cascaded waveguides for the effective indices related to their respective mode confined in the y direction for the original and corrected design.**

Since the waveguides are multimodal, the simulations were performed for each effective indices related to their respective mode confined in the y direction. Ten guided modes are allowed for a 5 μm-thick slab waveguide with silica as substrate ($n_{SiO_2} = 1.4597$), the SU-8 as core ($n_{SU8} = 1.5826$) and phosphate buffered saline (PBS) as the cladding ($n_{PBS} = 1.33$). Hence, the ten power outputs for each design. The average of the power outputs values for the original cascaded design is 90% and 56% for the corrected design. These results indicate that the extra resist due to the fabrication has a significant impact on the guided excitation light.

To find out the optical losses of the excitation light at the output of the cascaded waveguides and also to verify the distribution of light within the branches, the outcoming light through the waveguides facets was imaged with the optical setup shown in Figure 5.8. The light from the fiber-coupled laser diode with a 635 nm central wavelength (Thorlabs, Newton, USA) passes through a single mode fiber coupler containing a variable neutral density and a 650 nm shortpass filter. The light is then inserted at the input of the cascaded waveguide with the help of a 3.5 μm core diameter single mode

fiber (Thorlabs, Newton, USA). The light at the output of the cascaded waveguide design is then imaged with the ccd camera (JAI, Copenhagen, Denmark) paired with a 40X microscope objective (Nikon, Minato, Japan).
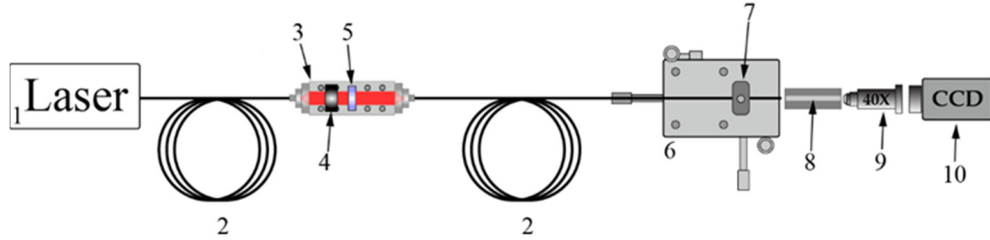
Figure 5. 8   **Optical characterization experimental setup. 1) Fiber-coupled laser (λ=635 nm) 2) single mode fiber 3) single mode fiber-to-fiber coupler 4) variable neutral density filter 5) 650 nm shortpass filter 6) five-axis stage micro positioners 7) fiber holder 8) single & cascaded waveguides 9) 40X microscope objective 10) ccd camera.**

The variable neutral density filter was necessary to prevent the ccd camera from saturating and the 650 nm shortpass filter blocked higher wavelengths, which will be of importance for the future fluorescence evanescent wave spectroscopy experiments. Imaging of the light at the output of the single and cascaded waveguide is shown in Figure 5.9ac. The chip was cleaved in the middle to image the light at the output of the middle of the single and cascaded waveguide, Figure 5.9bd.
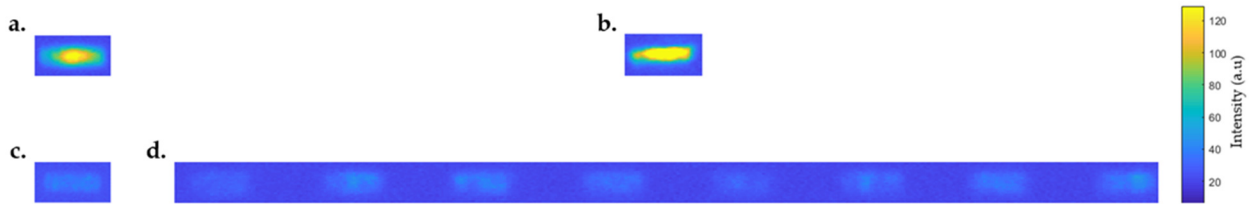
Figure 5. 9   **Images of the excitation light at the end output of the a) single and c) cascaded waveguide. Images of the excitation light from the branches output at the middle of the b) single and d) cascaded waveguide (the contrast was increased for better visualization).**

The intensity of light from the outputs at the end and the middle of the waveguides were evaluated by summing their pixel intensities for a similar area. The average of the intensities for three measurements were made for each output where their standard

deviation were taken as error as shown in Figure 5.10 for the waveguides end outputs (Figure 5.9ac) and Figure 5.11 for the middle outputs (Figure 5.9bd).
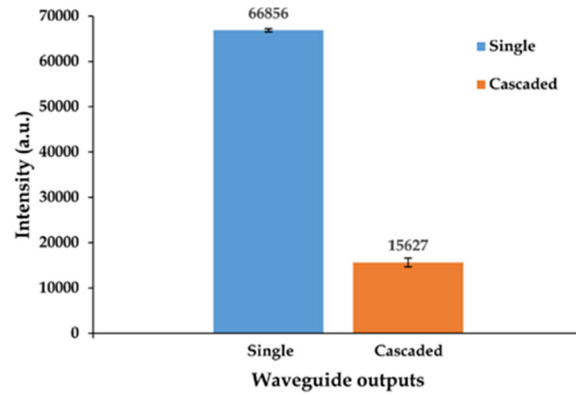
Figure 5. 10   Average intensities of the waveguides end outputs. Data presented as Mean ± SD (n = 3).
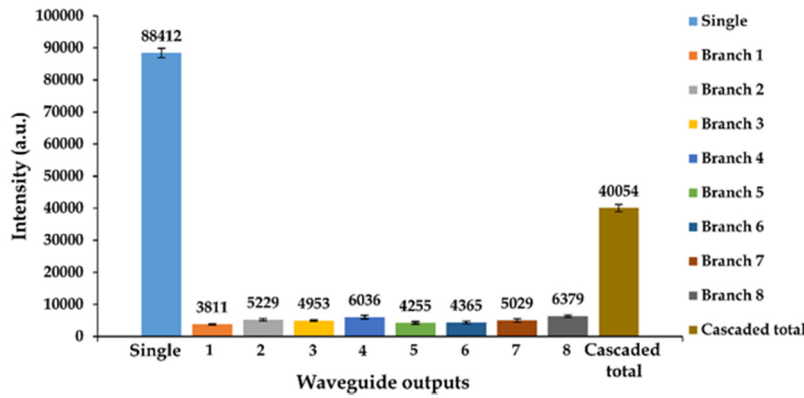
Figure 5. 11   Average intensities of the waveguides middle outputs. Data presented as Mean ± SD (n = 3).

As seen in Figure 5.10, the optical losses of the excitation light from the cascaded waveguides are 75% greater than the single waveguide. Comparing this value to the simulation results (Figure 5.7), it is almost double the value found with the numerical simulation, which is 44% of optical losses. Many factors could explain this discrepancy, including that the numerical simulations do not take into account the propagation losses in the y-z plane, since it is a 2D configuration. As the splitting junctions are numerous, it could have a significant impact on the optical losses. Nonetheless, from Figure 5.11, it is seen that the light is relatively well distributed between the eight branches of the cascaded waveguide, which is expected since the configuration is symmetric. Differences could

120

appear due to fabrication defects or input fiber misalignement. However, from the simulation results of Figure 5.7, the original design shows only 10% of optical losses at the output of the sensor. Hence, the patterned resist could benefit from a fabrication method that could offer a higher resolution as e-beam lithography for lower excitation light losses. It is important to note that although the losses are significant for the excitation light, the power could always be increased to satisfy the needs of the experiment if the optical arrangement allows it.

5.5   Fluorescence immunoassay

It is assumed from the larger area of immobilization that the fluorescence output of labeled analytes from the cascaded waveguide would be greater than that from a single waveguide. To verify this claim, the sensitivity from the different sensors will be studied by a fluorescence evanescent wave coupling spectroscopy experiment. The experimental setup used to this effect is shown in Figure 5.12.
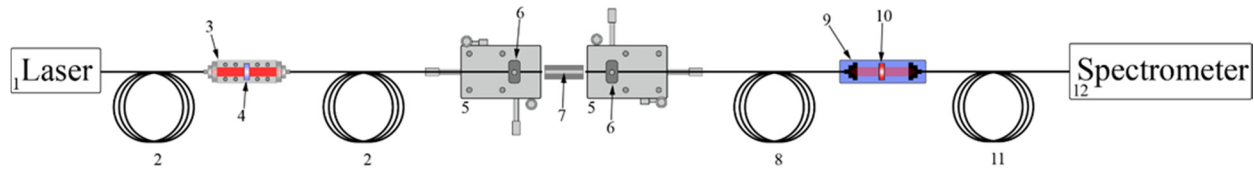
**Figure 5. 12   Fluorescence evanescent wave spectroscopy experimental setup.1) Fiber-coupled laser (λ = 635 nm) 2) single mode fiber 3) single mode fiber-to-fiber coupler 4) 650 nm shortpass filter 5) five-axis stage micro positioners 6) fiber holders 7) single & cascaded waveguides 8) mutlimode fiber (62,5 μm core) 9) multimode fiber-to-fiber coupler 10) 676-29 nm bandpass filter 11) multimode fiber (600 μm core) 12) spectrometer.**

The excitation light (λ = 635 nm) go through the 650 nm shortpass filter which is inserted in the single mode fiber coupler and block the higher wavelength that could saturate the ccd sensor. After going through the short pass filter, the light is guided through the waveguides and excite the labeled targets. The resulting light at the output of the waveguide includes the filtered excitation light and the guided fluorescence coupled to the waveguide. Subsequently, the light is filtered by the 676-29 nm bandpass filter inserted in the multimode fiber coupler restricting the light to the spectrum of the

fluorescence light analyzed by the spectrometer.

To proceed to the fluorescence evanescent wave spectroscopy experiment, the waveguides have to be treated to capture labeled analytes. To do so, the chips, after being rinsed with acetone and isopropanol, were first hydroxylated with an oxygen plasma treatment for 20 s to create OH groups on the waveguide surfaces, Figure 5.13a. Immediately after, the chips were immersed in a solution of 1% (v/v) APTES-ethanol for silanization, Figure 5.13b. After 1 h, the chips were rinsed with ethanol, deionized (DI) water, dried with a nitrogen jet, and placed in an oven at 100 ℃ for 10 min. Then, after the chips were cooled to room temperature, a solution of 1,2% (v/v) glutaraldehyde-PBS was administrated on the entirety of the waveguides, Figure 5.13c. After 2 h, the chips were rinsed with PBS and administrated with a solution of 200 µg·mL^{-1} of streptavidin-PBS for 8 hours, Figure 5.13d. After rinsing the chips with PBS, different concentrations of biotin-Alexa 647 Fluor-PBS were placed on the chips, covering wholly the waveguides, and kept overnight in a sealed petri dish with a wet tissue to prevent dehydration, Figure 5.13e. Lastly, the chips were rinsed thoroughly with DI water and PBS. The chips were always kept covered with PBS during the whole experiment.
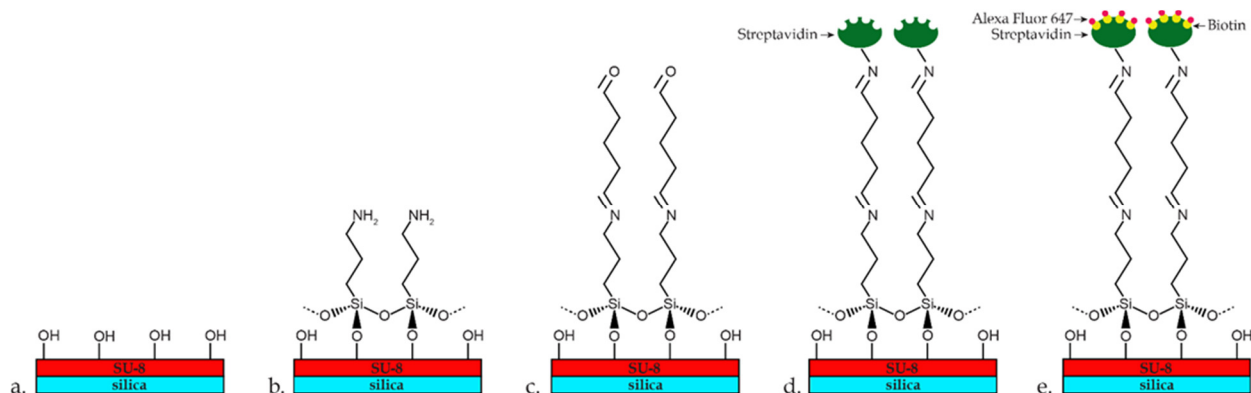
Figure 5. 13   **Schematic of the immobilization steps. a) functionalization b) silanization c) glutaraldehyde treatment d) streptavidin immobilization and e) biotin-Alexa 647 immobilization.**

It was demonstrated that SU-8 polymer shows autofluorescence to certain wavelengths [199]. Eliminating autofluorescence emission is necessary to evaluate with certitude the

fluorescence output. To this effect, it was shown that the SU-8 autofluorescence could be bleached by irradiating it with visible light for a long period [160]. Consequently, before the biotin-Alexa 647 immobilization, the SU-8 waveguides were coupled with the laser excitation light (λ = 635 nm). The light was kept guided through the waveguides for 15 min for a laser power of 4 mW, which resulted in the complete photobleaching of the SU-8 autofluorescence.

Now that the SU-8 waveguides are free from the autofluorescence, concentrations varying from 0.1 to 250 pg·mL^{-1} of biotin-Alexa 647-PBS solution were placed on the single and cascaded waveguides. A total of 4 measurements of the fluorescence output were performed for each concentration. Each point in Figure 5.14 is presented as the average of these 4 measurements with the standard deviation as error. Calibration curves were constructed by fitting the data with the help of the 4 parameters logistic regression model [161]:

$$\psi = D + \frac{(A-D)}{\left(1+\left(\frac{x}{C}\right)^B\right)} \tag{5.1}$$

Where ψ is the fluorescence intensity, A the lower asymptote, D the upper asymptote, B the slope factor, C the analyte concentration at the inflection point of the calibration curve, and x the analyte concentration. Fitting of the data led to the following equations:

$\psi = \left((6.66 - 24.09)/1 + \left(\frac{x}{44.48}\right)^{1.978}\right) + 24.09, R^2 = 0.9599$ and

$\psi = \left((11.23 - 42.91)/1 + \left(\frac{x}{38}\right)^{1.513}\right) + 42.91, R^2 = 0.9943$ representing the calibration curves for the single and cascaded waveguides respectively.

As observed in Figure 5.14, the calibration curves do not pass through zero, but are shifted to higher fluorescence intensities due to non-specific binding. For this reason, the value of the lower asymptote A is added to the linear dynamic range which is evaluated from 20% to 80% of the value of $D - A$ [200]. This resulted in linear ranges of 22 − 90 pg·mL^{-1} and 15 − 95 pg·mL^{-1} for the single and cascaded waveguides respectively. Fitting the data in the linear

ranges to a linear equation results in the following linear regression equations: $\psi = 7.84 \ln x - 14.38, \; R^2 = 0.9983$ and $\psi = 10.89 \ln x - 12.72, \; R^2 = 0.9984$ for the single and cascaded waveguides respectively. Again, since the calibration curves don't go through zero, the lower asymptote A is taken as the blank signal and with the addition of three fold of its standard deviation it was possible to determine the limits of detection. Consequently, limit of detections of 15 pg·mL⁻¹ and 9 pg·mL⁻¹ were calculated for the single and cascaded waveguides respectively.
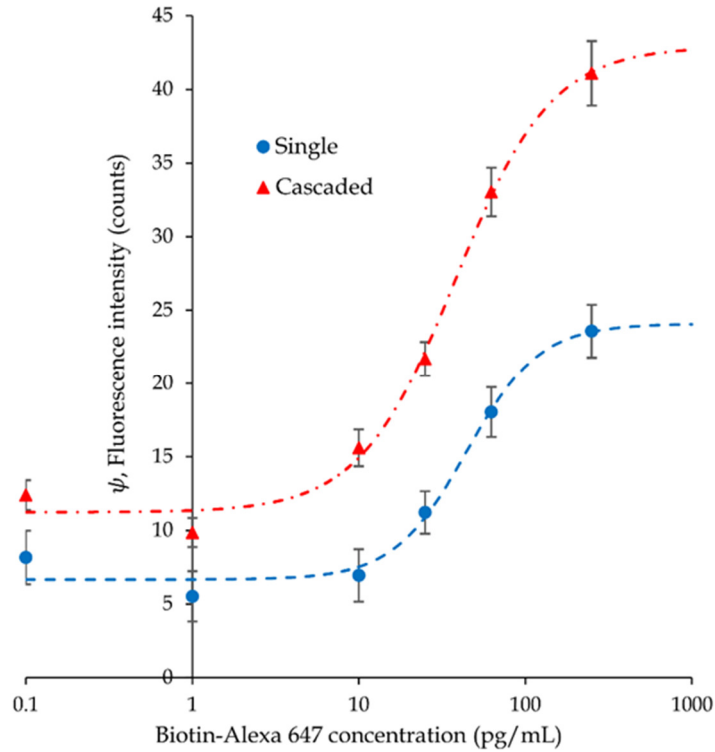
Figure 5. 14   **Calibration curves for the fluorescence evanescent wave spectroscopy of biotin-Alexa 647 immobilized on the single and cascaded waveguides.**

Further, the slopes of the linear regression equations give the sensitivities of the sensors. Hence, the ratio between the slopes gives the increase in sensitivity. Consequently, the cascaded waveguides resulted in 1.39 fold increase in sensitivity compared to the single waveguide. Surprisingly, the area available for immobilization of the cascaded waveguides is around 1900000 µm² and 576000 µm² for the single waveguide, which should result in 3.30 fold in increase in sensitivity if only the area of immobilization was

taken into account. To investigate the difference between the expected increase in sensitivity if only the area of immobilization is taken into account and the experimental results, an analysis of the guided fluorescence coupled to the waveguides was performed.

5.6 Simulations of the evanescently coupled fluorescence guided through the cascaded waveguide

Since the fluorescence emission comes from the Alexa 647 fluorophores attached to the biotin molecules, it is expected that the coupling of the fluorescence light appears on the entirety of the surface of the waveguides where the biotin-Alexa 647 fluor are immobilized. However, the number of fluorophores is immense and simulating each fluorophore will be impossible. For this reason, sources strategically positioned into the sensor configuration will launch the guided modes allowed by the waveguides. Indeed, the fluorescence light couples into all the guided modes of the waveguides. As seen in Figure 5.15, eleven sources are positioned to simulate the fluorescence light coupled into different sections of the sensor for the original and the corrected design.
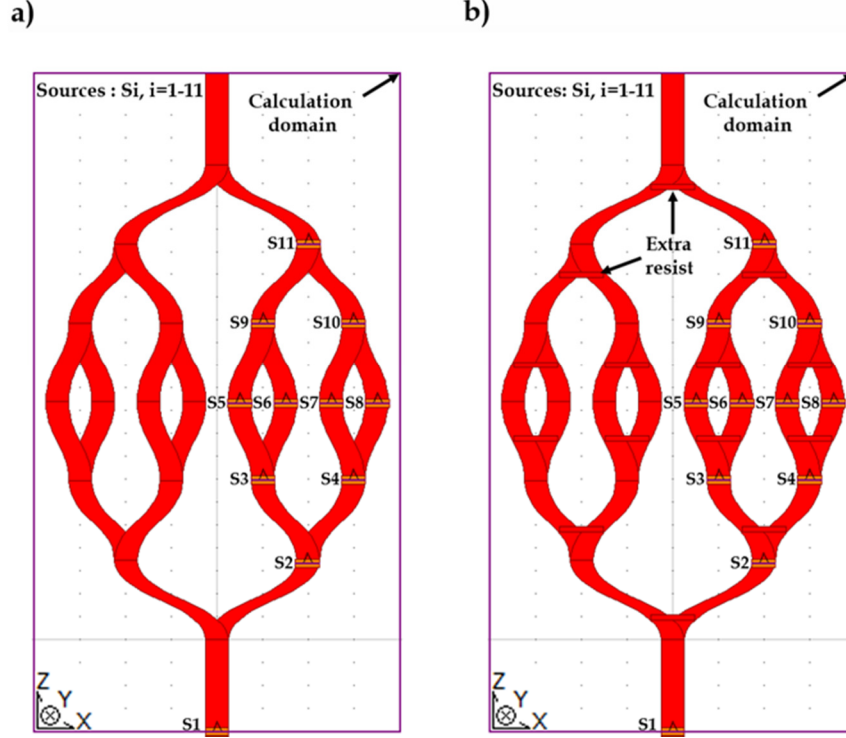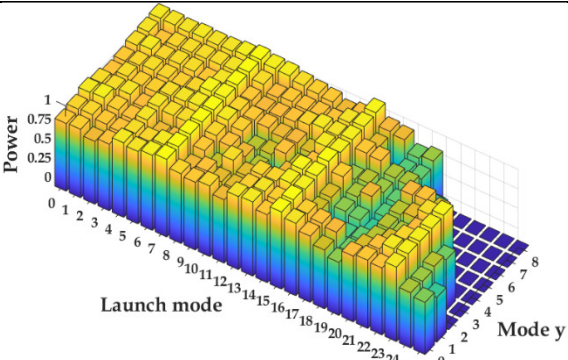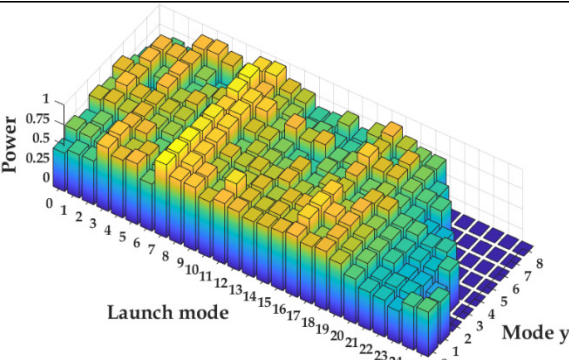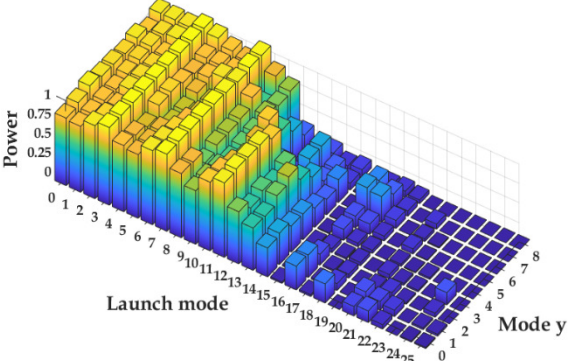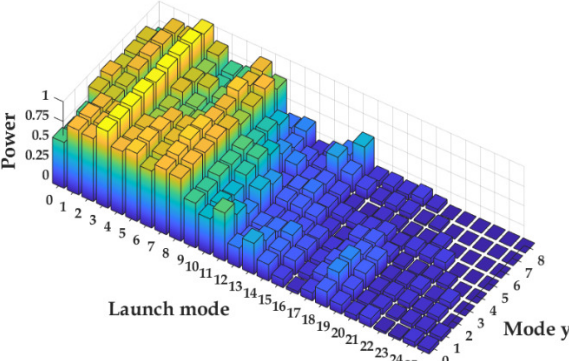
Figure 5. 15 Scheme of the eleven sources where the fluorescence light coupled modes are launched for the a) original and b) corrected cascaded waveguide design (aspect ratio 100:1).

The S1 source was used to simulate the fluorescence light coupled in the initial waveguide (4000 μm long). The S2 source simulates the fluorescence light coupled in the branch of the first splitting junction, the S3 and S4 for the second splitting junction and so on. It is important to note that since the bending radius is very large, the branches are approximated as straight waveguides. Each source in Figure 5.15 is activated individually during a simulation, the sources are displayed all together in the scheme only for sake of simplicity. Also, each simulation corresponds to the power at the output of the sensor for one of the guided modes allowed by the waveguide parameters. Since the Alexa 647 emits a fluorescence light peaking at around λ = 671 nm, this wavelength was used for the light sources. Considering the effective index method, two slab waveguides are taken into account, one slab waveguide confined in the y direction and another one confined in the x direction. At this wavelength (λ = 671 nm), nine guided modes (Mode y) are allowed in the slab waveguide confined in the y direction represented as a planar waveguide with the silica as substrate ($n_{SiO_2} = 1.45876$), the SU-8 (5 μm thick) as the core ($n_{SU-8} =$

1.58012) and with PBS as the cladding ($n_{PBS} = 1.33$). Also, at λ = 671 nm there are up to 26 modes (Launch mode) that are allowed in the slab waveguide confined in the x direction represented by the SU-8 (10 µm of width) with an index related to the effective index for each mode of the slab waveguide confined in the y direction and the PBS as substrate and cladding. Hence, for each effective index of the nine "Mode y" a series of simulations was conducted with each of the allowed guided modes of the slab waveguide confined in the x direction (up to 26 modes). The power of the sources was always 1 at the initial launch of the mode. The results consist of the power at the output of the sensor for each of these guided modes launched by the sources corresponding to their respective effective index calculated from the slab waveguide confined in the y direction. The results of the simulations are presented in Table 5.1 for each sources for the original and corrected design.

Table 5. 1 **Output power of the cascaded waveguide for modal sources located at different positions.**

Source No.	Original design	After fabrication
S1		
S2		

127
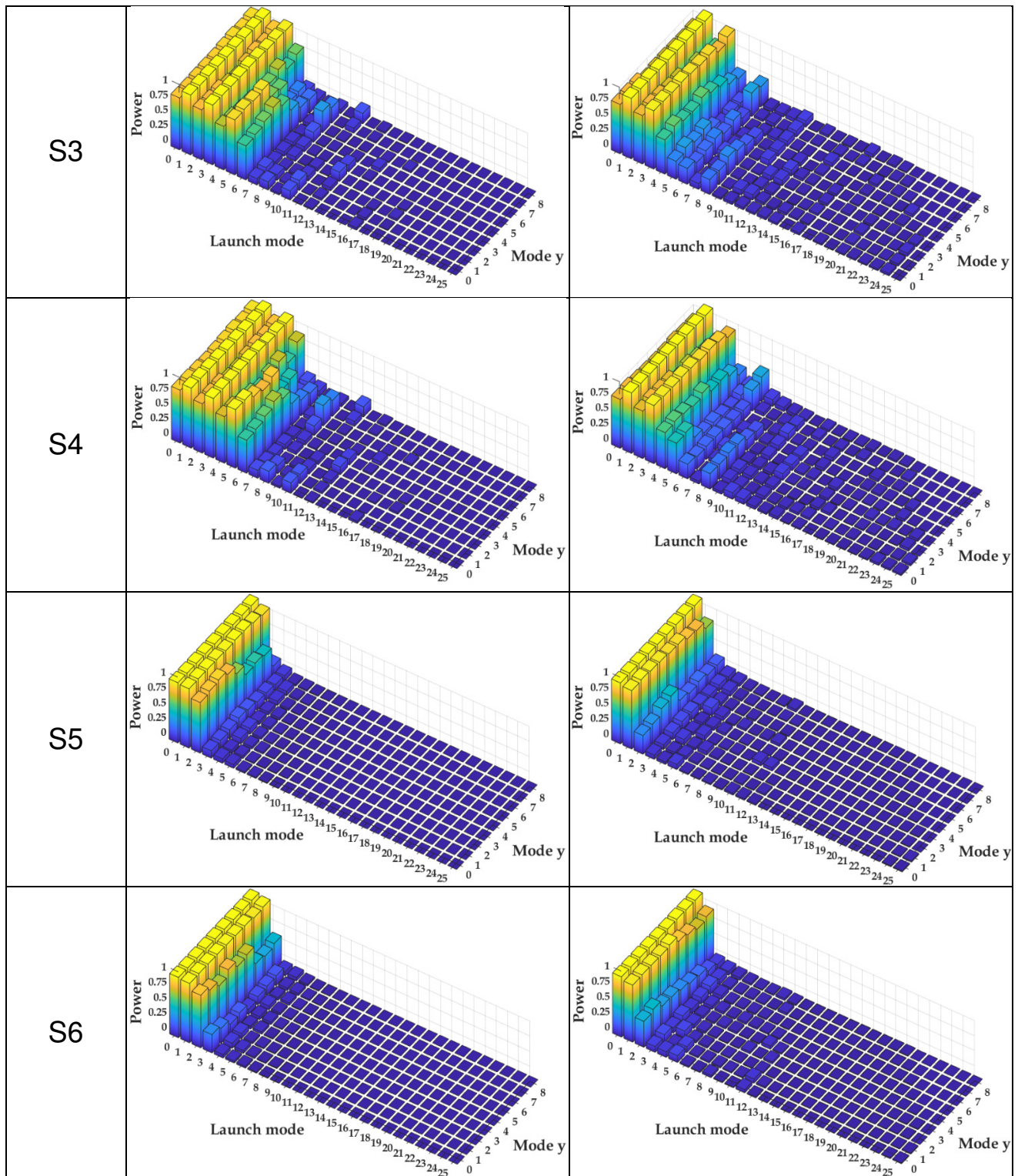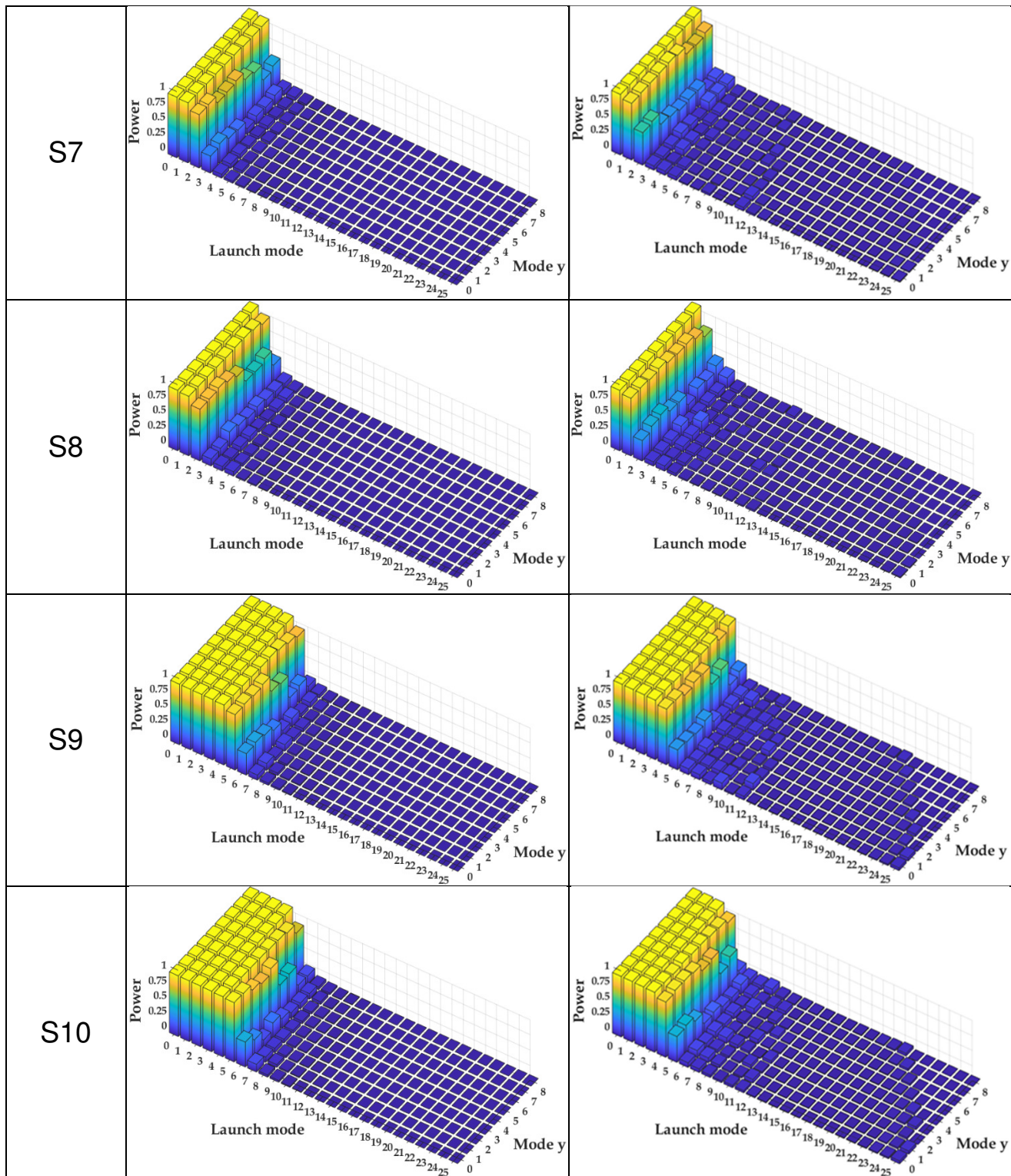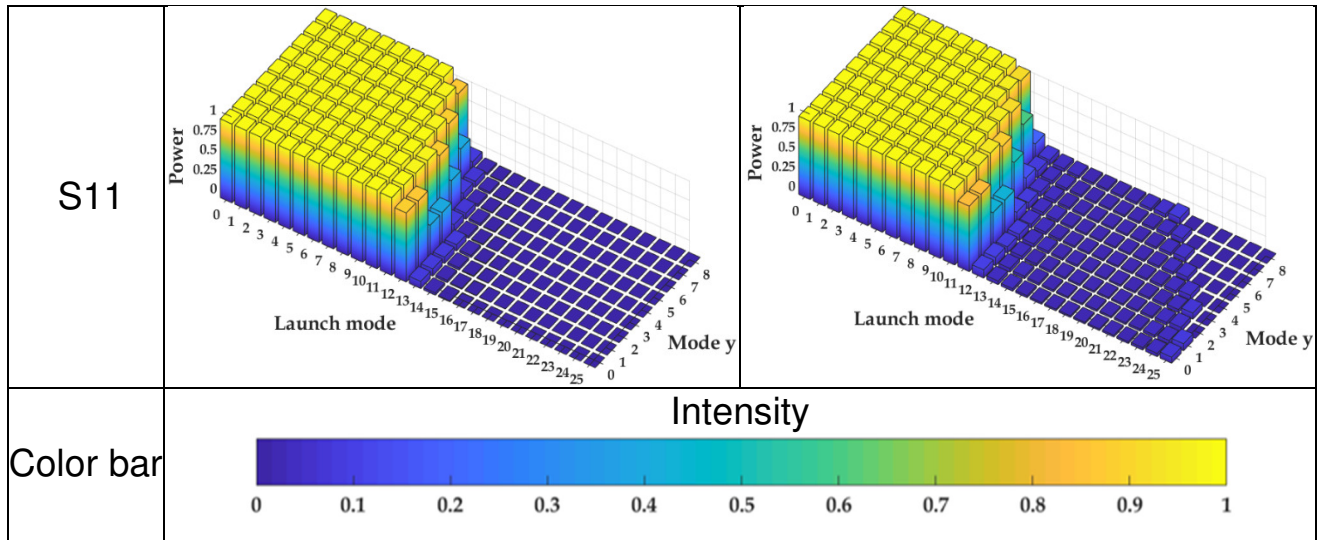
Table 5. 2   Comparison between the optical losses of the original and after-fabrication design for modal sources located at different positions.

Source no.	S1	S2	S3	S4	S5	S6	S7	S8	S9	S10	S11
Optical losses original/after fabrication (%)	29.40	23.20	16.71	16.40	12.54	13.60	12.30	12.51	11.31	10.00	5.73

As seen for the original design in Table 5.1, all the modes launched by S1 from the initial waveguide were preserved at the output of the sensor. This was expected since the modes will be divided by the splitting junctions but recombined to the same modal order at the output of the sensor. For the S2 and S11 sources, the highest mode order preserved at the output of the sensor could only be half (to the nearest integer) of the highest mode allowed for the specific effective index related to the Mode y. The same reasoning applied for the S3-S4 sources and the S9-S10 sources, which are placed at the branches of two splitting or recombining junctions but the highest order preserved at the output of the sensor will be this time the quarter (to the nearest integer) of the highest mode allowed for the specific effective index related to the Mode y. Finally the S5-S6-S7-S8 sources were positioned in between the four splitting and recombining junctions resulting in the preservation at the output of the sensor of only the eighth (to the nearest integer) of the highest mode order allowed for the specific effective index related to the

130

Mode y. As for the sources for the design after fabrication, it was observed that the power of the modes diminished compared to the original design due to the extra resist at the opening of the splitting and recombining junctions. In light of the simulation results in Table 5.1, the light from the fluorophores coupled to the waveguides cannot all be guided through the output waveguide due to the restriction from their mode order and this could alter significantly the fluorescence output. This phenomenon could explain in part the discrepancy between the area of immobilization ratio (3.30) and the sensitivity ratio (1.39). Also, the splitting and recombining junctions with added resist causes optical losses that adds to the difference between these ratios. The simulation results show the limitation of the cascaded design as presented in this work. Indeed, the number of splitting stages is limited by the number of modes allowed in the output waveguide. Hence, only a part of the fluorescence light power coupled to the waveguides will reach the output of the sensor. It is understandable that for each time there is a splitting around half of the power is lost since half of the modes won't be guided into the output waveguide. If only this phenomenon is taken into account, it won't be any difference between the single and cascaded waveguide in terms of sensitivity. However, in reality the higher modes are a lot more affected by the roughness on the waveguide sidewalls. Indeed, it was demonstrated by Tien *et al.* [201] that from the 4th mode the optical power reduces 14 times compared to the fundamental mode. In view of this, it is understandable that the lower modes have more chance to reach the output waveguide. Further studies should be performed to evaluate to which extent the modal losses affect the fluorescence output. Nonetheless, the cascaded waveguide still showed an increase in sensitivity compared to the single waveguide. As seen in Figure 5.7 and in Table 5.2 the cascaded waveguide design is affected significantly from the optical losses from the extra resist in between the splitting or recombining junctions. To this effect, it would be beneficial for the cascaded waveguides to be fabricated with a fabrication method that could allow a higher resolution as e beam lithography.

5.7   Conclusion

The cascaded waveguides design was realized and tested for fluorescence evanescent wave spectroscopy. It was also compared to a single waveguide for fluorescence evanescent wave spectroscopy and showed a 1.39 fold increase in sensitivity. The limit of detections of 15 pg·mL^{-1} and 9 pg·mL^{-1} of biotin-Alexa 647 for the single and cascaded waveguides, respectively, were found experimentally. The fluorescence light coupled from the fluorophores and guided through the waveguides was simulated with the beam propagation method and demonstrated the limitation of the cascaded waveguides design for increasing the fluorescence output. However, further optimization could be done by finding to which extent the coupled mode order affects the evanescent coupling efficiency and the optical propagation losses from the waveguide sidewalls roughness.

CHAPTER 6

DOUBLED AND TRIPLED OPTICAL POLYMER WAVEGUIDES FOR ENHANCED FLUORESCENCE EVANESCENT WAVE SPECTROSCOPY

6.1   Introduction

Bio-assays have greatly benefited from the development of optical biosensors as they offer high specificity, quick analysis, the possibility of miniaturization, immunity to electromagnetic interference, and in-situ/real-time measurements [163, 202]. When the light is coming from a high index to lower index medium it displays a powerful property used by most of the optical biosensors. Indeed, for a certain angle of incidence (critical angle) the light gets completely reflected. This phenomenon is called total internal reflection. In these conditions, an evanescent wave is created between the two media to satisfy the boundary conditions, since all the light is reflected. The evanescent wave is used as the sensing mechanism to probe the phenomena happening on the surface of the sensing platform. Many popular optical sensing methods such as surface plasmon resonance (SPR) [190], total internal reflection fluorescence (TIRF) [203], surface plasmon-coupled emission (SPCE) [204], absorption spectroscopy [205] etc., use the evanescent field to probe analytes. While label-free methods are usually quicker and cheaper, labeled methods surpass them due to higher sensitivity and specificity. Evanescent spectroscopy combines the principles of evanescent waves and fluorescent labeling. This makes this method highly sensitive, since the evanescent field limits detection to the region of interest and the fluorescent label offers a second level of specificity beyond analyte capture by an antibody or aptamer. Optical fibers were the first platforms to be used for optical biosensing. Fibers are advantageous for remote sensing [206] and offer geometrical flexibility. On the other hand, they are fragile when their claddings are etched to expose their cores to analytes and don't offer the possibility for miniaturization and multiplexing. On the contrary, planar waveguides are sturdier platforms. Planar waveguides have been proven to be effective for evanescent wave

fluorescence spectroscopy but are quite bulky [207, 208]. Rectangular waveguides allows for easy on chip integration, thus are ideal for miniaturization [209]. For this reason, in this work, rectangular waveguides will be used as the sensing platforms. Many approaches have been explored to increase the sensitivity of the evanescent wave fluorescence spectroscopy, including plasmon enhanced fluorescence [210], numerical aperture increase [211], grating coupled-surface plasmon-field enhanced fluorescence [212], etc. In this work an increase in the sensitivity of the fluorescence detection is proposed by increasing the area of immobilization, by multiplying the number of waveguides with the help of double and triple junction splitters. Double junction splitters evenly the incoming light power distribute into the two branches (or waveguides), but light loss still happens depending on the junction design. Many designs have been proposed to lower light losses [213-215]. If the application allows it, the easiest way to lower the optical losses would be to restrict the angle of separation between the two branches (to start very narrow and then slowly increase separation). Unlike the double junction splitters, the triple junction splitters suffer from an asymmetrical geometry. Indeed, most of the power of the incoming light is directed in the central branch of the junction. Banba *et al.*[216] proposed to insert a triangular spacing between the input waveguide and the central branch of the junction to reduce the transmission coefficient. Therefore, by controlling the spacing area it is possible to achieve equal distribution of light power in each of the three branches. Another way to distribute the power with a spacing was proposed by Yabu *et al.*[217]. The structure is a fork-type three-branch optical power divider consisting of only two dielectric materials. The design is composed of a symmetrical Y-junction distanced from the central branch by a coupling gap, with the Y-junction acting as a phase front retarder. This configuration allows for wider branching angles, especially when the index difference increases as shown by numerical simulations. Larger branching angles can also be achieved by the use of micro prisms as proposed by Lin *et al.*[218]. The micro prisms were strategically located at the junction to correct the phase mismatch occurring by the side branches. It was shown by numerical simulations that by increasing the index of refraction of the micro prisms it was possible to evenly distribute the incoming light power. It was also demonstrated by Wang *et al.*[219] that a three branched optical power splitter, consisting of a substrate micro prism combined with two waveguide expanders made by

134

nickel diffusion into LiNbO$_3$ single-crystalline substrate, was efficient in wide branching angle and power tuning. Another method to distribute the incoming light into different channels other than with directional couplers is to use multimode interference (MMI) couplers [220, 221]. All the above, and most double and triple junction splitters, are designed for single mode waveguides. However, few groups such as Prajzler *et al.* demonstrated multimode 1X2 and 1X3 large core rectangular planar polymer power splitters [222, 223]. In this Chapter, double and triple junction splitters were designed for 10 × 5 µm SU-8 on silica multimode waveguides to multiply the number of waveguides as a mean to increase the area of immobilization for labeled analytes. Moreover, the waveguides not only split but recombine at the output to benefit from the increased fluorescence coupling. This work presents the optimization of the double and triple junction to assure an even distribution of the excitation light by numerical simulations and experimentation. Also, an evanescent wave fluorescence spectroscopy experiment with biotin-Alexa 647 (as model analyte) was performed to evaluate the enhancement in fluorescence detection of the doubled and tripled waveguides compared to a single waveguide. Finally, a modal study was done with numerical simulations to address the optical losses of the different modes at the splitting junctions.

6.2   Design

The approach taken to design the configuration of the sensor was to increase the area of immobilization of the labeled targets, to increase the amount of guided fluorescence light coming from fluorescence evanescent coupling to the waveguide. The doubled waveguide, Figure 6.1 b, starts with a straight waveguide that splits into two straight waveguides with the help of a Y-junction, and recombines again to form a straight waveguide at the output. The tripled waveguide, Figure 6.1c, has the same configuration as the doubled waveguide, except that an additional straight waveguide goes from the input to the output. The single waveguide, Figure 6.1a, was added to compare sensitivity of fluorescence evanescent wave spectroscopy to that of the doubled and tripled waveguides. The waveguides cores were made of SU-8 photoresist and the substrate was a 5 µm silica layer oxidized from a silicon wafer, Figure 6.1.
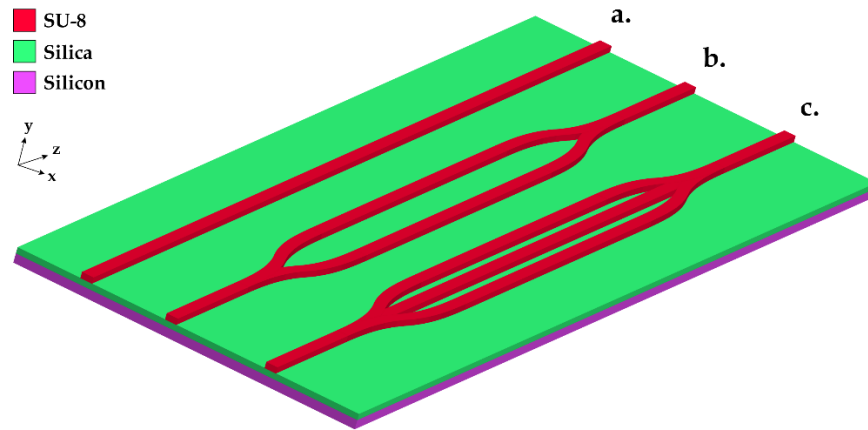
Figure 6. 1   Scheme of the a) single, b) doubled and c) tripled waveguides for enhanced fluorescence evanescent wave spectroscopy.

The splitting junctions could cause optical losses for the incoming excitation light. For this reason, numerical simulations with the beam propagation method were performed with the software Beam Prop of Synopsis to optimize the splitting junction configuration for lower optical losses. Direct coupling with an optical fiber to the input facets of the waveguides was used to guide the excitation light into the waveguides. The fiber used was a single mode fiber (Thorlabs, Newton, USA) with a 3.5 µm core diameter, a cladding with a refractive index of 1.45709, and a core with an index difference of 0.00603. A 3D beam propagation simulation was performed with a 635 nm wavelength Gaussian profile light at the input of the fiber. The scheme of the fiber facet and the simulation with the electric field are shown in Figure 6.2. The resulting effective index was equal to 1.460124.
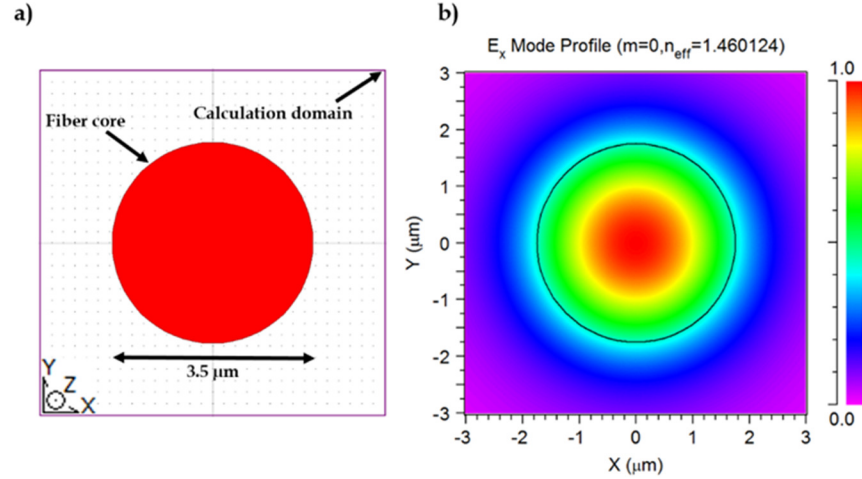
Figure 6. 2   **a) scheme of the fiber facet with the calculation domain and b) electromagnetic field distribution of the fundamental quasi-TE mode at the output of the fiber.**

Since the simulations will be performed in 2D instead of 3D to save time, the mode profile found from the 3D simulation (Figure 6.2b) will be translated into a 2D mode profile. To obtain the same effective index for a mode profile in 2D, the fiber was depicted as a slab waveguide with the same width (3.5 µm) and the same cladding index (1.45709). The index difference between the core and the cladding was diminished until the effective index matched the one obtained for the 3D fiber (1.460124). The resulting index difference was equal to 0.004212.
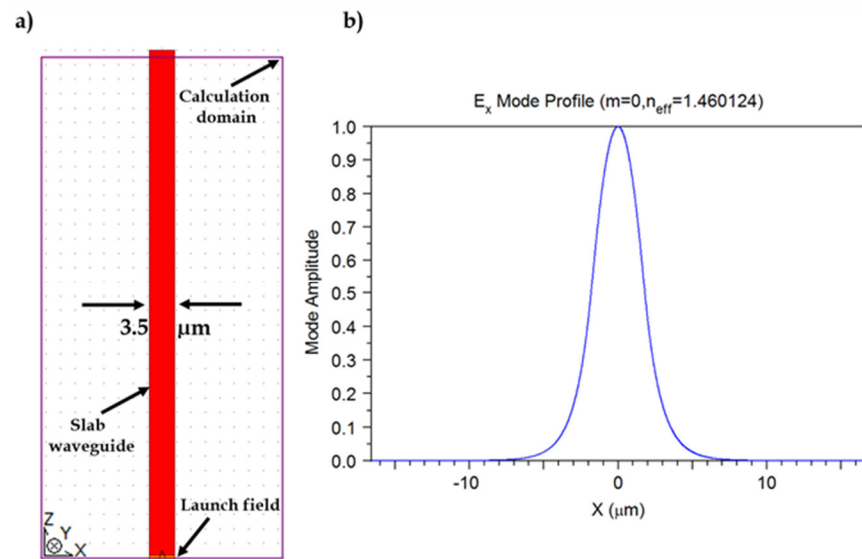
Figure 6. 3   **a) scheme of the slab waveguide mimicking a fiber in 2D with the calculation domain and b) the resulting mode profile for a 635 nm wavelength light.**

The resulting 2D signal, Figure 6.3b, was then used as the input light source for the next simulations, Figure 6.4ab, in which the splitting junction length was varied from 50 to 5000 µm for both the doubled and tripled waveguides, Figure 6.4 cd. The two side branches of the double and triple splitters were distanced by 60 µm from each other and the length of the input waveguides were fixed at 4000 µm as shown in Figure 6.4ab. The effective index of the fundamental mode with respect to the y direction was evaluated from the slab waveguide formed by the substrate ($n_{SiO_2} = 1.4597$), core ($n_{SU8} = 1.5826$), and cladding ($n_{PBS} = 1.33$), and was chosen as the index of the core (in red), $n_{eff} = 1.5815$. An index of 1.33 was chosen for the background index to act as the buffer solution (phosphate-buffered saline, PBS). The power indicated in Figure 6.4ab represents the fraction of light in the left or right branch for both designs compared to the input light (power = 1). As observed in Figure 6.4 c, from around 1000 µm of junction length the power in the doubled splitting junction branch stays constant at around 50%. The light is evenly distributed between the two branches, which is consistent with their symmetry. As for the light power distribution in the tripled waveguide splitter branch, the power varies periodically as seen on Figure 6.4d. For an even light distribution in the branches of the tripled waveguide splitter, the power in the branch should reach 33%. Different splitting junction lengths of the tripled waveguide could allow a 33% power distribution in the branches due to the periodic nature of the function. Since one definitive length has to be chosen for the waveguide fabrication, a length of 2377 µm was chosen for the tripled waveguide splitting junction, Figure 6.4d.
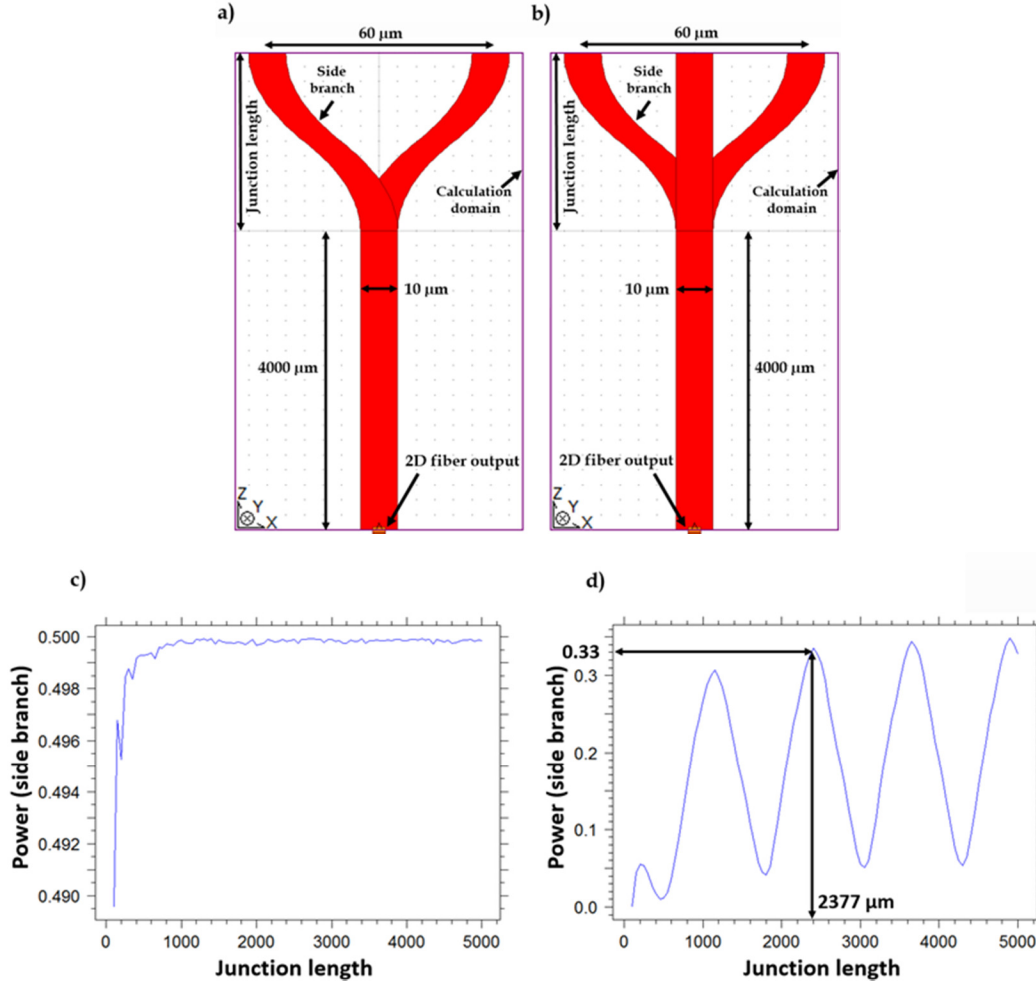
Figure 6. 4   Scheme of the input waveguide and the splitting junction of the a) doubled and b) tripled waveguide (Aspect ratio 50:1). Power in the side branch in function of the length of the splitting junction of the c) doubled and d) tripled waveguide.

The resulting electric field of the beam propagation simulations of the doubled and tripled waveguides for a fixed junction length of 2377 µm is shown in Figure 6.5 ac. As predicted, the power in both of the doubled waveguides is similar (50%), Figure 6.5b. The power from the side and middle branches of the tripled waveguide are also similar, at 33% of the value of the input light indicating no optical losses, Figure 6.5d.
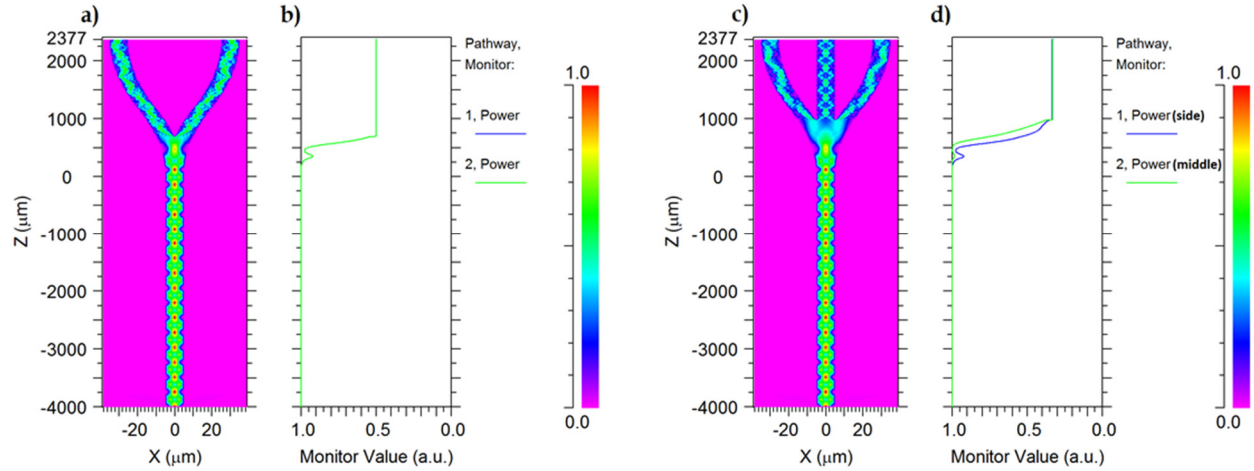
Figure 6. 5 **Resulting electromagnetic field of the beam propagation simulation for the a) doubled and c) tripled waveguide for a 2377 µm junction length. Results of beam propagation simulations for a junction length of 2377 µm for the power in the side branch of the b) doubled and in the side and middle branch of the d) tripled waveguide.**

However, the waveguides are multimodal for an excitation light of 635 nm wavelength. If the waveguides are seen as slab waveguides with respect to the y direction, they can support 10 modes. A study of the impact of the different effective indices related to each of the 10 modes confined in the y direction on the power distribution in the side branches (splitting junction length: 2377 µm) was performed with the beam propagation method, Figure 6.7. It is important to mention that after the fabrication, the design changed a bit due to the limitations of UV lithography. Indeed, as seen in Figure 6.9ab additional resist fills the junction at the start of the splitting junction. For this reason, the original design will be corrected with this extra resist in mind. Therefore the simulations for the remainder of the document will include both the original design and the design after fabrication. The original designs of the doubled and tripled waveguide as depicted in Figure 6.4ab and the corrected designs as shown in Figure 6.6ab will be used for the modal study as seen in Figure 6.7.
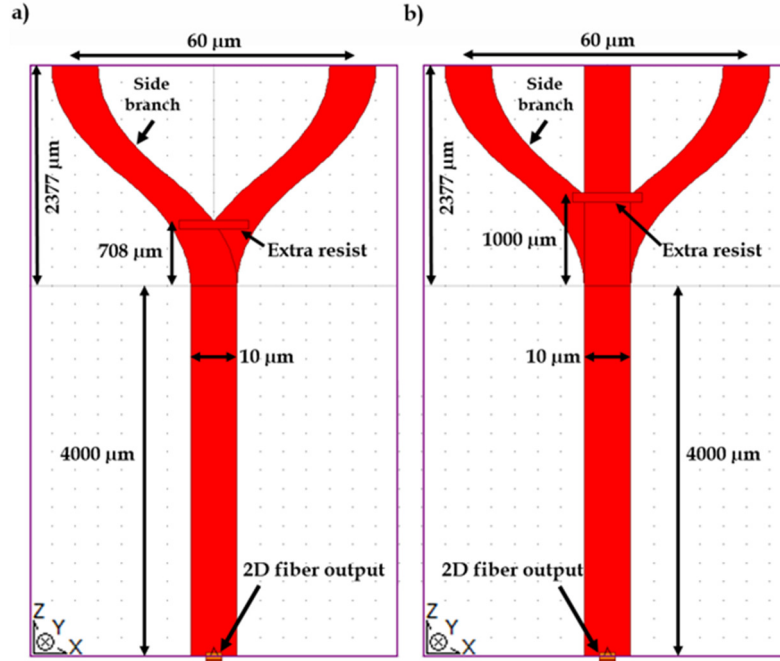
Figure 6. 6   Scheme of the input waveguide and the splitting junction of the design after fabrication of the a) doubled and b) tripled waveguide (Aspect ratio 50:1)
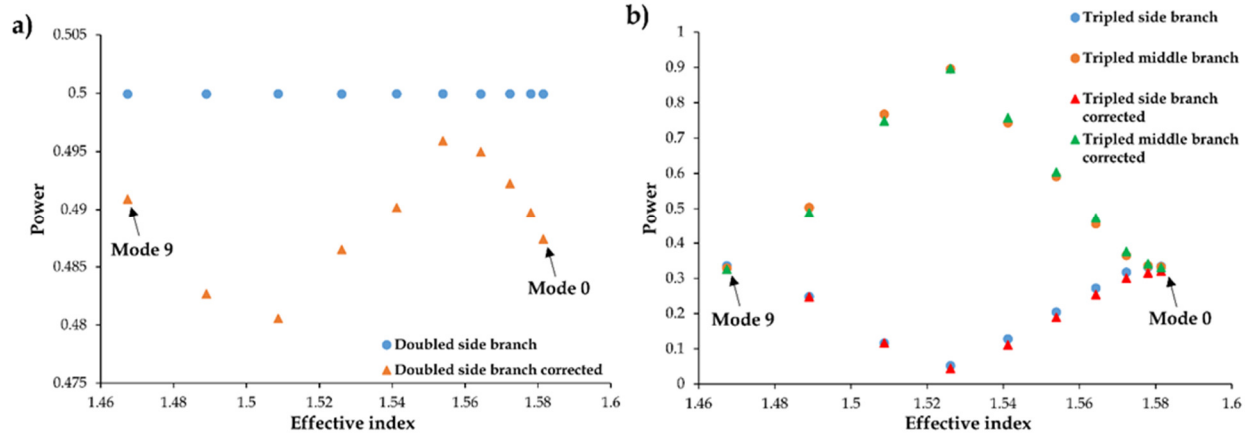
Figure 6. 7   Power in the a) double and b) triple splitter branches for the effective indices related to their respective mode confined in the y direction for the original and corrected design.

As seen in Figure 6.7a, the power in the doubled waveguide branch (original design) was stable at 50%. The corrected doubled design is lightly different due to the tampering of the smooth transition of the opening of the junction from the extra material. Nevertheless,

the averaged power is 49%, which is an insignificant change. For the tripled waveguide original design (Figure 6.7b), the power in the side branch diminished from the effective indices of the lower order modes and raised up after the effective index of the 7th mode. The power values in the triple splitter side branch for the effective indices of the first four and last modes are ~33%. The power values in the tripled waveguide branch for the effective indices of the 5–8th modes are moderately to greatly lower from the desired value of 33%. On average, the power in the triple splitter side branch is 23%, accounting for the effective indices of all the modes. As for the corrected doubled design, the corrected tripled waveguide design doesn't show a significant change in the power as compared to the original design. As expected, the power in the middle branch is complementary to the power in the side branches. In view of this, it will be reasonable to keep the length of the splitting junction at 2377 µm. However, the power distribution in the double and triple splitters will be verified experimentally in section 6.4. The length of the splitting junctions for the doubled and tripled waveguide were then kept at 2377 µm and the straight waveguides after the splitting junctions had a length fixed at 16046 µm. For a junction length of 2377, the bending radii of the side branches (S-bends) was of 47 000 µm, which can be approximated to being straight waveguide. A large bending radius will be beneficial to reduce optical losses.

6.3 Fabrication

A silicon wafer with a 5 µm silica layer obtained by wet thermal oxidation (Rogue Valley Micro Devices, Medford, U.S.A) was used as a substrate for the waveguides. The silica-on-silicon wafer was thoroughly rinsed with acetone and isopropanol then dried with a nitrogen stream before being spin coated with SU-8 photoresist. SU-8 5 (Microchem, Newton, USA) was chosen as the photoresist for the 5 µm core layer. The wafer was spin coated at 500 rpm for 10 s and then at 3000 rpm for 30 s, Figure 6.8a. Afterwards, a soft bake on a hotplate was done at 65 ℃ for 2 min and then at 95 ℃ for 5 min, Figure 6.8b. After the wafer was cooled down to room temperature, an exposition of 18 s was performed under a 365 i-line UV light (9 mW·cm^{-2}) through the patterned photo mask to transfer the waveguide design to the SU-8 5 layer, Figure 6.8c. Following UV exposure,

a post-exposure bake was done by heating the wafer on a hotplate at 65 ℃ for 1 min and then at 95 ℃ for 2 min, Figure 6.8d. Again, after cooling the wafer to room temperature the wafer was completely immersed in the SU-8 developer (Microchem, Newton, USA) for 2 min, Figure 6.8e. The wafer was then quickly dipped in isopropanol to stop the reaction. It was also rinsed with isopropanol and deionized water before being dried with a nitrogen stream. Finally, the wafer was heated to 150 ℃ for an hour, to stabilize the properties of the photoresist, Figure 6.8f.
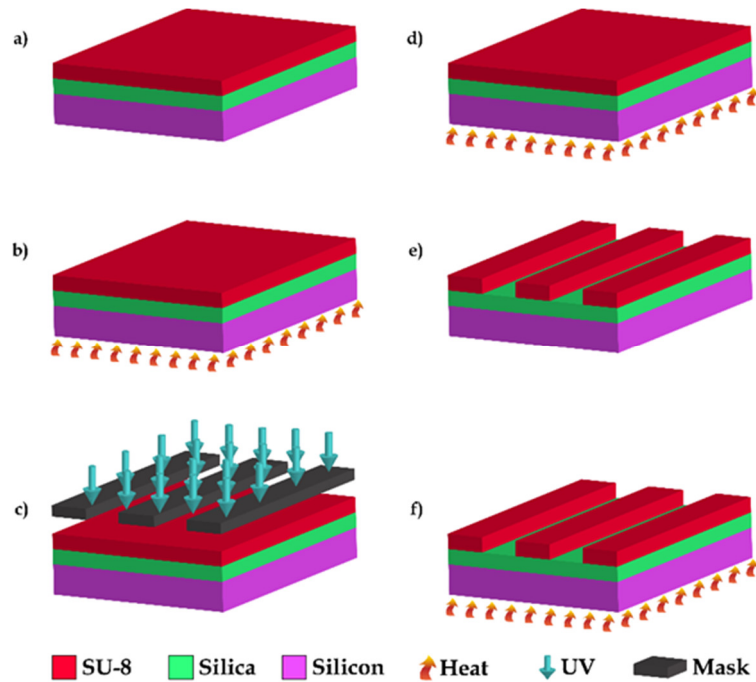
Figure 6. 8   **Illustration of the main steps of the fabrication process for the single, doubled and tripled waveguides. Details are given in Fabrication.**

Images of the fabricated waveguide were acquired by scanning electron microscopy (SEM) to assess the quality of the fabrication. The single, doubled, and tripled waveguides are all shown in Figure 6.9a. The doubled and tripled waveguide junctions are clearly seen in Figure 6.9b. The junctions appear sharp with no under-developed resist. However, the limit of resolution from the photolithography is apparent with what seems like an engraved line, as seen clearly at the start of the doubled and tripled junctions in Figure 6.9b. By evaluating the width of the junction where the "extra resist" ends, it was possible to do the correction on the original design, Figure 6.6, by adding the

143

material at the same junction width.
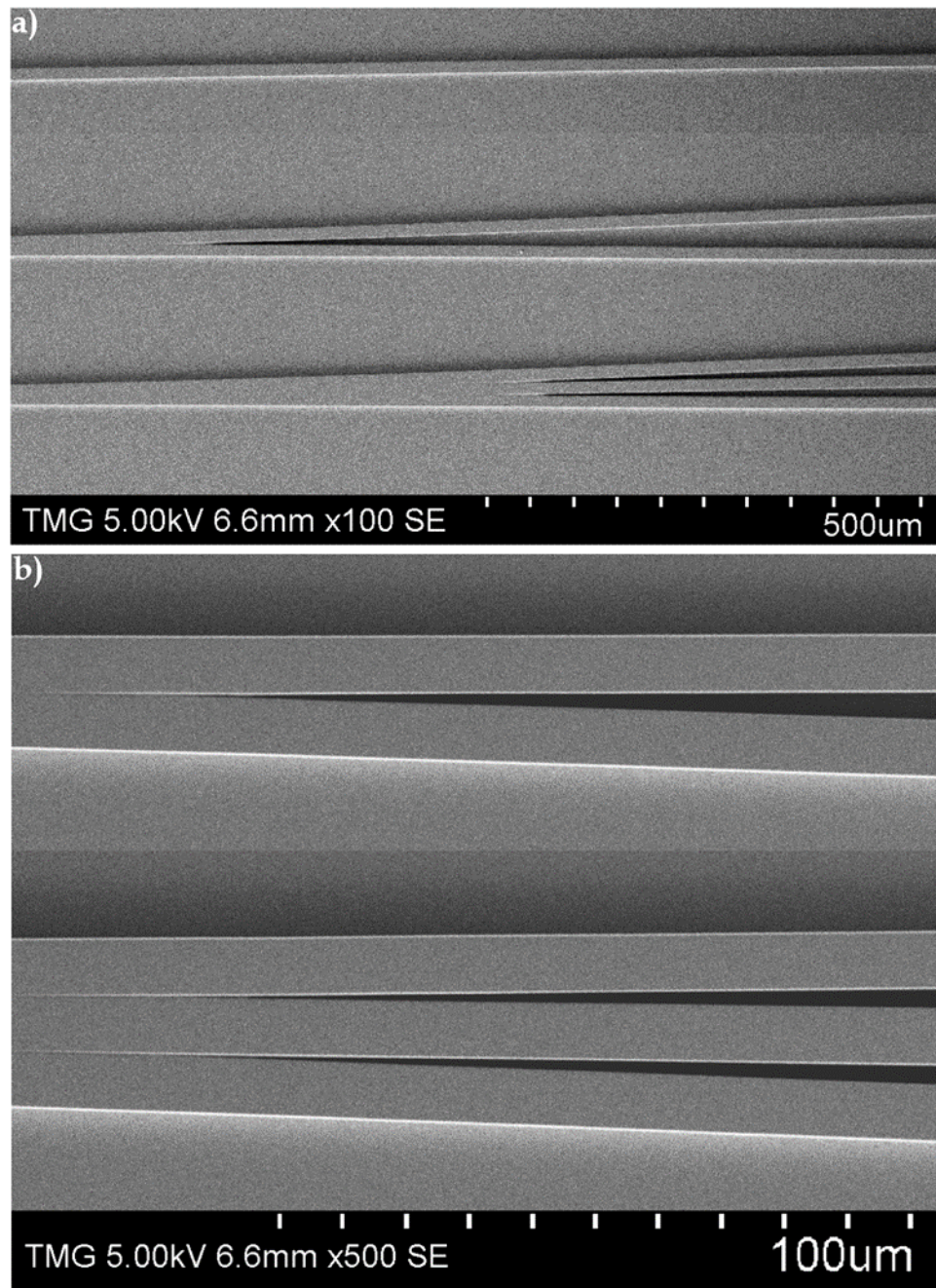
Figure 6. 9 **SEM pictures from the top of the sensing platform showing the a) single, doubled, and tripled waveguides with a 100X magnification and the doubled and tripled waveguides splitting junction at a b) 500X magnification.**

6.4   Optical power characterization

To verify the distribution of the excitation light in the branches of the doubled and tripled waveguides, and also to compare the optical losses at the output of both designs, the outcoming light of the facets was imaged with the optical setup depicted in Figure 6.10. The excitation light source used was a fiber-coupled laser diode with a 635 nm central wavelength (Thorlabs, Newton, USA). The input of a single mode fiber with a 3.6 – 5 µm mode field diameter (Thorlabs, Newton, USA) was coupled to the light source and the output was connected to a single mode fiber coupler (Thorlabs, Newton, USA). Inside the single mode fiber coupler was inserted a variable neutral density and a 650 nm shortpass filter, (Thorlabs, Newton, USA). Another single mode fiber with a 3.5 µm core diameter (Thorlabs, Newton, USA) was connected to the output of the single mode fiber coupler and inserted in a fiber holder fixed on a 5-axis stage micro-positioner (Newport, Irvine, USA). The end of the fiber was cleaved and butt-coupled to the input facets of the different waveguide designs. The outcoming light from the output facets was imaged with the help of a 40X microscope objective (Nikon, Minato, Japan) paired with a ccd camera (JAI, Copenhagen, Denmark).
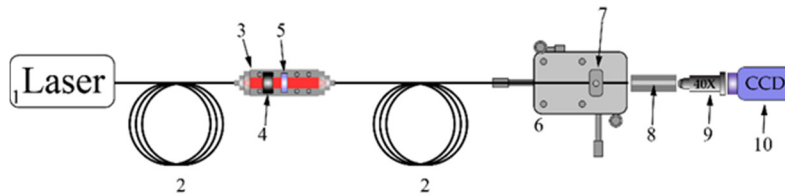
Figure 6. 10   Optical characterization experimental setup. 1) Fiber-coupled laser (λ = 635 nm) 2) single mode fiber 3) single mode fiber-to-fiber coupler 4) variable neutral density filter 5) 650 nm shortpass filter 6) five-axis stage micro positioners 7) fiber holder 8) SU-8/silica waveguides 9) 40X microscope objective 10) ccd camera.

The variable neutral density filter was used to not saturate the light on the CCD camera and the 650 nm shortpass filter was necessary to block the higher wavelengths, which will be of importance for the future fluorescence evanescent wave spectroscopy experiment. The images of the end outputs of the single, doubled, and the tripled waveguides are shown in Figures 6.11ace. Then, the chip was cleaved in the middle to be able to image the light output of each branch individually, Figures 6.11bdf.

145
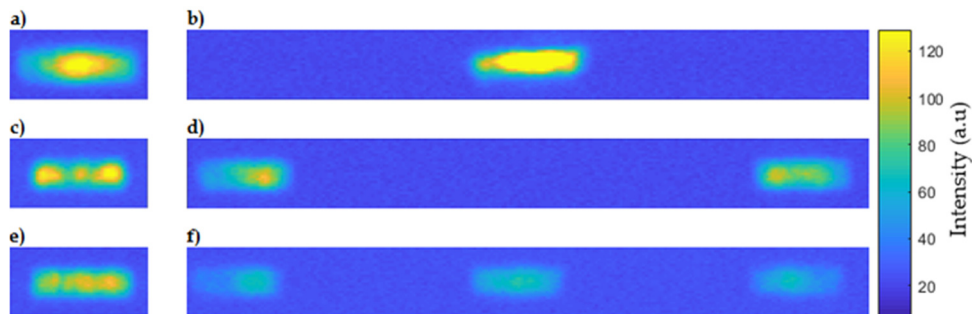
Figure 6. 11   Images of the excitation light at the end output of the a) single, c) doubled and e) tripled waveguides. Images of the excitation light from the branches output at the middle of the b) single, d) doubled and f) tripled waveguides.

The intensities of the light from the outputs at the end and the middle of the waveguides were evaluated by summing their pixel intensities for a similar area. The average of three measurements were made for each output where their standard deviation which were taken as error as shown in Figure 6.12 for the waveguides end outputs (Figure 6.11ace) and Figure 6.13 for the middle outputs (Figure 6.11bdf).
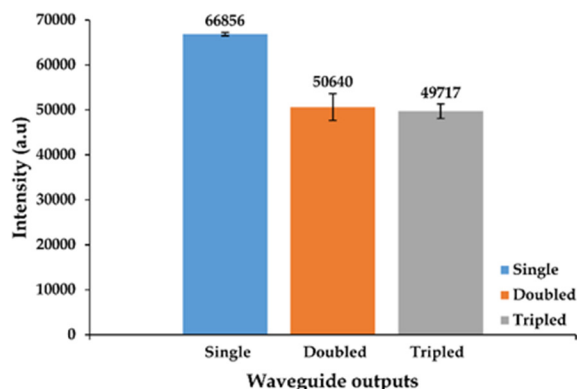
Figure 6. 12   Average intensities of the waveguides end outputs. Data presented as Mean ± SD (n = 3).

146
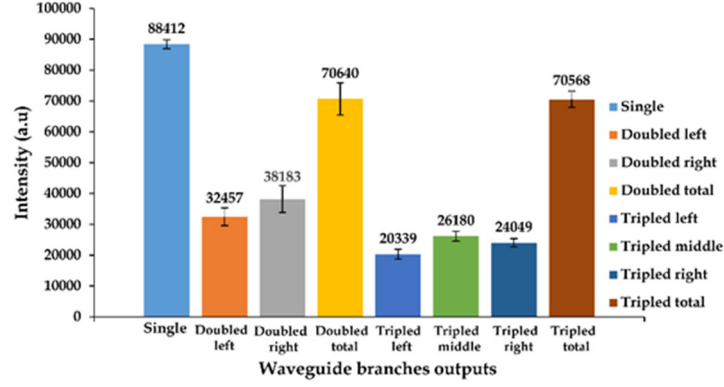
Figure 6. 13   Average intensities of the waveguides middle outputs. Data presented as Mean ± SD (n = 3).

From Figure 6.12, it can be seen that the optical propagation loss of the single waveguide is around 33% lower than for the doubled and tripled waveguide. This is expected since the junctions would contribute to more optical losses. Interestingly, it is seen from Figure 6.12 & 6.13 that the total averaged output intensities from the end and the middle of the waveguides (Doubled total, Tripled total) from the doubled and tripled waveguide differ only slightly from each other. The intensity of the outputs of the doubled waveguide branches differ by 18% and the branches of the tripled waveguide differ from 29%, for the left branch, to 9%, for the right branch, compared to the middle branch. This uneven distribution is probably due to fabrication defects. Indeed, if more of the "extra resist" tends to be at one side of the branch, more of the light will be guided into it. Also, the alignment of the input fiber with respect to the waveguide input facet could be a factor in the light distribution. Nonetheless, the excitation light is reasonably well distributed in the branches of the doubled and tripled waveguides for the intended application. To analyze these results, beam propagation simulations were performed with the same simulated fiber source as used previously, but with the full sensors design, Figure 6.14. Also, the "extra resist" was added to both of the junctions as suggested previously. The schemes of the full doubled and tripled designs are shown in Figures 6.14 ab.
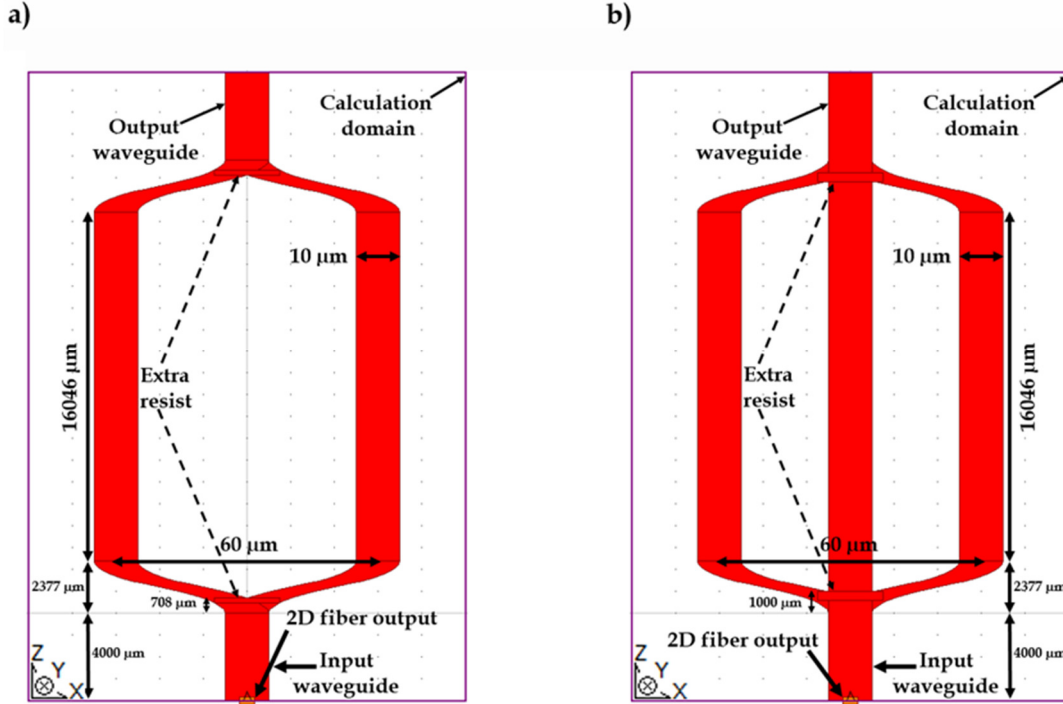
Figure 6. 14   Scheme of the a) doubled and b) tripled waveguide designs after fabrication with the simulated fiber source (Aspect ratio 200:1).

Again, since the parameters of the waveguides allow them to accept multiple modes, the simulations were performed with the effective indices related to their respective modes confined in the y direction. The results of the simulations are shown in Figure 6.15.
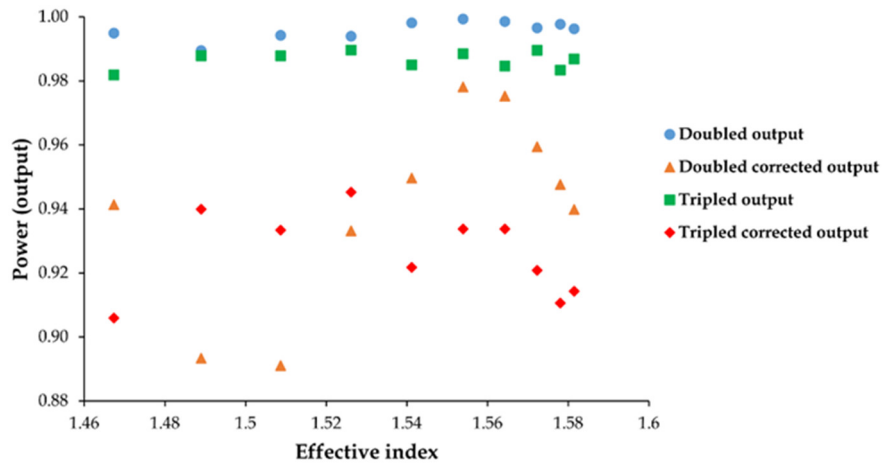
Figure 6. 15   Power at the output doubled and tripled waveguides for the effective indices related to their respective mode confined in the y direction for the original and corrected design.

Interestingly, the simulations results from Figure 6.15, show that the output power of the doubled and tripled waveguide are very near for the original and corrected design. Hence, the extra resist resulting from the fabrication doesn't affect greatly the optical losses. The experimental results in Figure 6.12 match the simulations results from Figure 6.15, by showing also that the fabricated doubled and tripled waveguide have similar optical losses than the corrected designs. However, the simulations results show that the doubled and tripled corrected designs have optical losses of 5% and 8% respectively compared to the single waveguide (power = 1). This differs from the experimental results where the optical losses are of 33% between the doubled/tripled waveguides and the single waveguide. This discrepancy could be due to the fact that the simulations are only in 2D and that the propagation in the y direction is not taken into account. Also, the roughness is not taken into account in the simulations but could affect the mode propagation and induce more optical losses at the junctions.

6.5   Fluorescence immunoassay

Now that the excitation light distribution along the branches of the splitting junctions and the optical losses of the doubled and tripled waveguide designs have been analyzed and proven suitable, the fluorescence yield from the different designs can be studied with a fluorescence evanescent wave coupling spectroscopy experiment. The experimental setup used to this effect is shown in Figure 6.16.
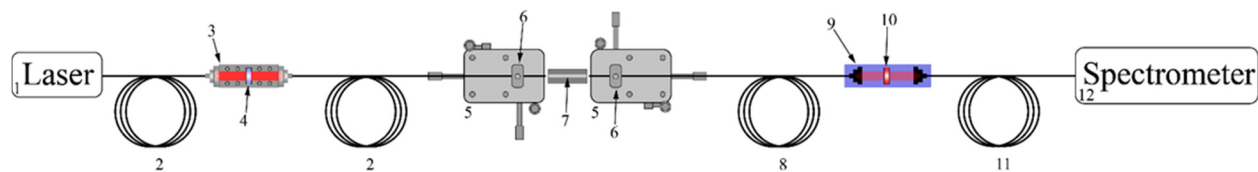
Figure 6. 16   Fluorescence evanescent wave spectroscopy experimental setup.1) Fiber-coupled laser (λ=635 nm) 2) single mode fiber 3) single mode fiber-to-fiber coupler 4) 650 nm shortpass filter 5) five-axis stage micro positioners 6) fiber holders 7) SU-8/quartz or SU-8/silica waveguide 8) mutlimode fiber (62,5 µm core) 9) multimode fiber-to-fiber coupler 10) 676-29 nm bandpass filter 11) multimode fiber (600 µm core) 12) spectrometer.

This setup relies on a 650 nm shortpass filter inserted in the single mode coupler to let

the 635 nm excitation light from the fiber-coupled laser through but at the same time blocking higher wavelengths than 650 nm, which could add to the fluorescence light making them indiscernable. Also, the 679-29 nm bandpass filter restricts even more the output signal from the waveguides, which contains the excitation and fluorescence light before it is spectrally analyzed by the spectrometer. However, before proceeding to the fluorescence immunoassay experiment, the waveguides need to undergo a treatment to immobilize the analytes to the surfaces of waveguides, Figure 6.17. Firstly the chips were rinsed thoroughly with acetone and isopropanol. Next, the chips were dried with a nitrogen jet and were subjected to oxygen plasma in a plasma chamber for 20 s to hydroxylate their surfaces, Figure 6.17a. Immediately after the plasma session, the chips were immersed in a 1% (v/v) APTES-ethanol solution at room temperature for silanization, Figure 6.17b. After an hour, the chips were rinsed with ethanol and DI water and dried with a nitrogen jet and placed in an oven at 100 ℃ for 10 min. Ensuingly, the chips were cooled down to room temperature and submerged in a solution of 1,2% (v/v) glutaraldehyde-PBS (glutaraldehyde-phosphate buffered saline) solution for 2 hours, Figure 6.17c. Then, the chips were rinsed with PBS and immersed in a solution of streptavidin-PBS of 200 µg·mL^{-1} for 8 hours, Figure 6.17d. Subsequently, the chips were rinsed with PBS and exposed to different concentrations of biotin-alexa 647 Fluor-PBS overnight. Finally, the chips were thoroughly rinsed with PBS and deionized water. The chips were always kept wet with PBS all over the surface of the waveguides for the whole duration of the experiment.
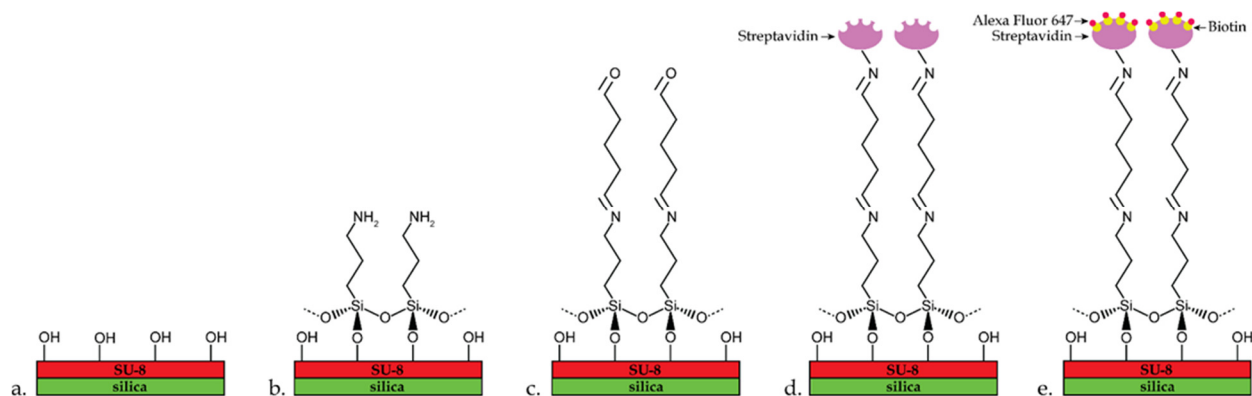
Figure 6. 17   **Schematic of the immobilization steps. a) functionalization b) silanization c) glutaraldehyde treatment d) streptavidin immobilization and e) biotin-Alexa 647 immobilization.**

It is also important to note that before the biotin-Alexa 647 immobilization, the waveguides were bleached of their intrinsic fluorescence by irradiating them with the excitation light (λ = 635 nm) at maximum power (4 mW) for 15 min. Indeed, it was demonstrated that SU-8 shows autofluorescence at visible light [199]. It was also shown that photobleaching of the SU-8 autofluorescence was possible for 635 nm light [160]. After the photobleaching of the waveguides was complete, concentrations varying from 0.1 to 250 pg·mL^{-1} of biotin-Alexa 647-PBS solution were applied to the differents sensors. The data are presented as the average of 4 measurements for each concentration with the standard deviation as error, Figure 6.18. These data were fitted with the help of the 4 parameters logistic regression model [161]:

$$F = D + \frac{(A-D)}{\left(1+\left(\frac{x}{C}\right)^B\right)} \tag{6.1}$$

Where F is the fluorescence intensity, A the lower asymptote, D the upper asymptote, B the slope factor, C the analyte concentration at the inflection point of the calibration curve, and x the analyte concentration. The fitting of the data led to the following equations:

$F = \left((6.66 - 24.09)/1 + \left(\frac{x}{44.48}\right)^{1.978}\right) + 24.09, R^2 = 0.9599,$

$F = \left((13.39 - 38.99)/1 + \left(\frac{x}{31.26}\right)^{1.966}\right) + 38.99, R^2 = 0.9936$ and

$F = \left((19.62 - 60.38)/1 + \left(\frac{x}{26.94}\right)^{1.672}\right) + 60.38, R^2 = 0.9907$ representing the calibration curves for the single, doubled, and tripled waveguides respectively. The linear dynamic ranges for each sensor were evaluated as an interval going from 20% to 80% of the value of $D - A$ [73] and summing with A since the calibration curves don't go through zero because of the non-specific binding. The linear ranges corresponds then to 22-90 pg·mL^{-1}, 16-64 pg·mL^{-1} and 12-62 pg·mL^{-1} for the single, doubled and tripled waveguides respectively. The linear regression equations were adjusted to $F = 7.84 \ln x - 14.38$, $R^2 = 0.9983$, $F = 11.45 \ln x - 13.24$, $R^2 = 0.9982$ and $F = 15.37 \ln x - 10.63$, $R^2 = 0.9978$ for the single, doubled and tripled waveguides respectively. The limits of detection were determined as the blank signal + 3σ (σ, standard deviation of the blank signal). Where

the blank signal is considered as the lower asymptote A since the calibration curves don't go through zero. Limit of detections of 15 pg·mL^{-1}, 10 pg·mL^{-1}, and 7 pg·mL^{-1} were found for the single, doubled and tripled waveguides respectively.
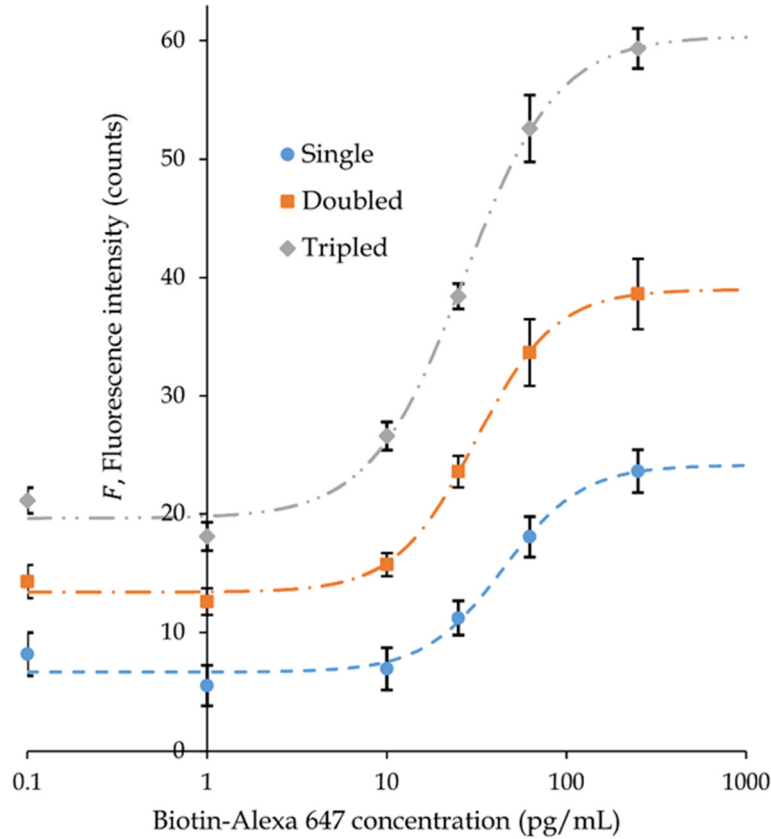
Figure 6. 18 **Calibration curves for the fluorescence evanescent spectroscopy of biotin-Alexa 647 fluor immobilized on SU-8/Silica single, doubled and tripled waveguides.**

The sensitivity of the sensors could be determined from the slope of the linear regression equations. Therefore, the increase in sensitivity from the doubled and tripled waveguides compared to the single waveguide could be known from the ratio between their respective slopes. Which result in approximately 1.5 and 2 fold increase in sensitivity for the doubled and tripled waveguides respectively compared to the single waveguide. The available area for immobilization of the labeled target (surface from the junction not exposed to the solution were substracted) are 576000 µm^2, 992000 µm^2 and 1408000 µm^2 for the single, doubled and tripled waveguides. Which translates to 1.7 and 2.4 greater area of immobilization for the doubled and tripled waveguides compared to the single waveguide.

It results in a 20 % and 40 % difference between with the experimental results for the doubled and tripled waveguides respectively. To investigate this discrepancy, simulations of the evanescently coupled and guided fluorescence light through the sensors were performed to evaluate the optical losses due to the splitting junctions.

6.6   Impact of the splitting junctions on the evanescently coupled fluorescence

As observed from the experimental results about the excitation light, the splitting junctions cause signifiant optical losses (33%) compared to the single waveguide. The simulations also showed that the splitting junctions of the doubled and tripled waveguides caused optical losses, but to a lesser extent (5% to 8%). In the same way, the splitting junctions should also cause optical losses to the evanescently coupled fluorescence light. Indeed, the evanescently coupled fluorescence light is guided through the waveguides therefore through the splitting junctions. As opposed to the excitation light that propagates first from the input of the sensors, the fluorescence light is coupled from any position on the waveguides since the Alexa 647 labeled biotin molecules are attached on the entire surface of the devices. Also, the fluorescence light couples to all the guided modes of the waveguides. Since the fluorophores are very great in number and positioned at different places on the waveguides, it won't be possible to simulate them all. To analyze the impact of the 2 splitting junctions on the guided fluorescence light, all the modes confined in the x direction for the effective indices related to the modes confined in the y direction (9 modes) are injected at the input of the sensors as shown in Figure 6.19 ac with the "Launch mode". The impact of the recombining junction (just before the output) on the fluorescence guided light from the straight waveguides were analyzed by the use of the same "Launch mode" at the end of the side straight waveguides for both the doubled and tripled waveguides, Figure 6.19be, but also for the middle straight waveguide for the tripled waveguide, Figure 6.19d. It is important to note that wherever the "Launch mode" is placed along the straight waveguides the same mode profile will appear at the end of the straight waveguides. For this reason, the "Launch mode" is placed at the end of the straight waveguides to shorten the simulation time. To resume, the "Launch mode" at the

input of the waveguides simulate the light coupled from the fluorophores at the vicinity of the input waveguides and guided through the entire sensor until the output. The same applies for the "Launch mode" at the end of the straight waveguides i.e. simulating any mode coupled and guided from anywhere on the straight waveguides to the output. Understanding that the splitting and recombining junctions are formed with 2 S-bends with very large bending radii (47 000 µm), it is a good approximation to consider them as part of the straight waveguides. Hence, it is reasonable to consider that the "Launch mode" at the end of the straight waveguides also simulates most of the fluorescence light coupled from the splitting and recombining junctions. The results from the simulations are presented in Table 6.1.
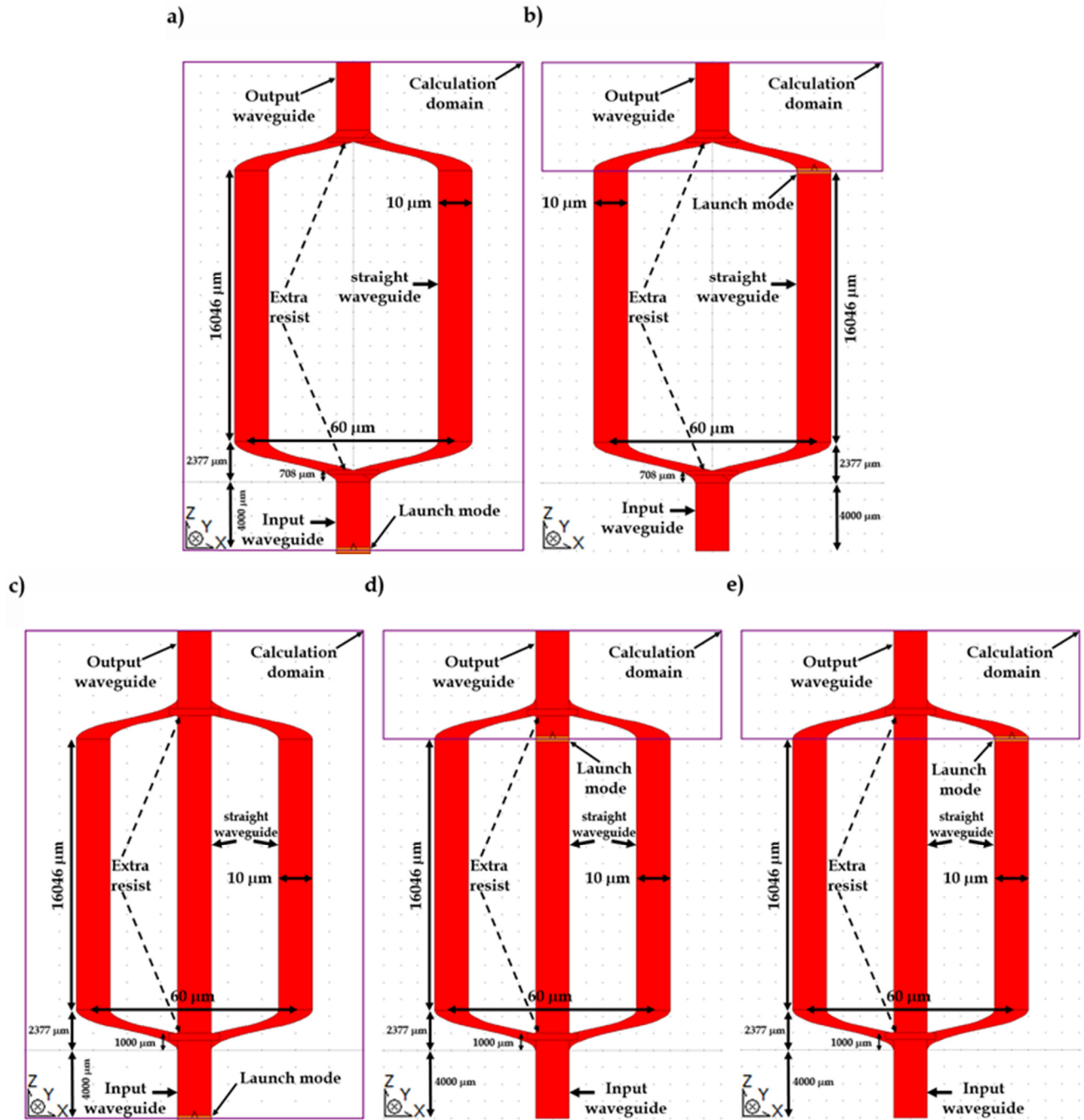
Figure 6. 19 Scheme of the doubled waveguide corrected design with the "Launch mode" at the a) input and b) end of the side straight waveguide and the tripled waveguide corrected design with the "Launch mode" at the c)input, d) middle straight and e) side straight waveguide. (Aspect ratio 200:1

Table 6. 1   Power at the output for the doubled and tripled waveguides for the "Launch mode" positionned at different locations of the sensor.

	Launch mode position		
	At input	End of middle straight waveguide	End of side straight waveguide
Doubled original design		/	
Doubled after fabrication		/	
Tripled original design			
Tripled after fabrication			

It is obvious from the data in Table 6.1 that the output powers of the higher modes coupled from the input waveguides are relatively without losses compared to the output powers of the modes coupled from the end of the straight waveguides (middle & side) which show an abrupt drop at the 11th to 14th "Launch mode" for the doubled (original design and after fabrication) waveguides and at the 6th to 9th "Launch mode" for the tripled waveguide (original design and after fabrication). This phenomenon is understandable since the 26th "Launch mode" is the last allowed mode for the slab waveguide confined in the x direction.

156

Indeed, the modes coupled from the input waveguide get split into the two or three branches of the double/triple splitters and recombine at the output. But for the modes coupled after the first splitting junction but before the second junction (represented by the "Launch mode" at the end of the straight waveguides) they keep at the same modal order until they reach the second junction. If the order of the coupled mode at the input waveguide is lower than 26, it will be guided through the waveguide for all effective indices related to the confined mode in the y direction (Mode y). When the input waveguide coupled modes pass through the first junction, they split into 2 or 3, generating 2 or 3 modes with half or third of the modal order of the initial mode and recombine after the recombining junction to recreate the initial mode. Hence, all the guided "Launch modes" for each effective indices related to the modes confined in the y direction (Mode y) are guided through the output waveguide. This also means that the "Launch modes" order at the end of the side or middle straight waveguides cannot be greater than the half or third (rounded to the lowest integer) of the highest allowed guided mode order for the doubled or tripled waveguides respectively. Hence, the drop at the 11th to the 14th "Launch modes" being 1 mode order higher than the half (rounded to the lowest integer) of the highest allowed guided mode order (19 to 25) for the effective index related to the confined mode in the y direction. Similarly for the tripled waveguide but for the 6th to the 9th "Launch modes" which are 1 mode order higher than the half (rounded to the lowest integer) of the highest allowed guided mode order (19 to 25) for the effective index related to the confined mode in the y direction. In view of these results, it will appear for a doubled or tripled waveguide that they should offer an equal guided fluorescence output than a single waveguide if it is assumed that the fluorescence light couples into all the guided modes equally and suffer no losses through the sensors. Nonetheless, assuming that in reality there will be roughness on the walls of the waveguides the higher order modes will leak more than the lower order modes. Indeed, it was reported from Tien *et al.* [201], that from the 4th mode the optical losses due to surface scattering from the roughness are 14 times higher compared to the fundamental mode. Considering the arguments for the lower optical losses of the lower guided modes compared to the higher order modes due to the roughness and the higher coupling efficiency for lower mode order, the enhancement in sensitivity of the doubled (1.5 fold) and tripled (2 fold) waveguides compared to the single

157

waveguide nearly matching the surface ratio between the doubled (1.7 fold) an tripled (2.4 fold) waveguides is comprehensible. Also, the simulations results of Table 6.1 showed that the recombining junction could limit the number of modes that could be guided through the output waveguide from the fluorescence coupled from the straight waveguides following the splitting junctions. That could explain the 20 % and 40% discrepancy between the enhancement in sensitivity (1.5-2) and the surface ratio (1.7-2.4) values.

6.7   Conclusion

Doubled and tripled waveguide designs were optimized numerically and proven to enhance the sensitivity for fluorescence evanescent wave spectroscopy. The optimal designs were also characterized experimentally, to verify the optical power distribution and losses from their configurations. Biotin-Alexa 647 concentrations as low as 10 pg·mL^{-1} and 7 pg·mL^{-1} were detected for the doubled and tripled waveguides. A 1.5 to 2 fold increase in sensitivity was found for the doubled and tripled waveguides respectively compared to a single waveguide. Also, a numerical modal study was performed to understand the impact of the splitting and recombining junctions of both configurations on the guided coupled fluorescence light from the labeled targets. These configurations could be used for multi-analyte detection using microfluidic channels unique to each waveguide to immobilize different analytes. Additionally, waveguides could also be added for this purpose if methods could be implemented for diminishing optical losses from splitting and recombining multimodal junctions with wide angles. Furthermore, preventing the losses of higher order modes could be done by modifying the geometry of the recombining junctions to allow multimodal guidance.

CHAPTER 7

CONCLUSIONS & FUTURE WORK

7.1   Overall conclusion

The purpose of this work was to enhance and study the performance of evanescent wave fluorescence spectroscopy and was realized in two manners: firstly by developing a novel fabrication process for SU-8 on quartz waveguides and secondly by designing new optical sensor geometries for increased area of immobilization.

The novel fabrication process for SU-8/quartz waveguides was proven to smooth out the roughness of the sidewalls of the waveguide reducing optical propagation losses, hence increasing the yield of the guided evanescently coupled fluorescence light from the labeled analytes. In addition to that, the increase in the refractive index of the SU-8 core due to the particular parameters of the fabrication protocol with the lower refractive index of the quartz substrate lowered the asymmetry of the waveguide compared to a standard SU-8/silica waveguide benefiting the fluorescence collection efficiency of the waveguides for fluorophores near their surface. The higher fluorescence output guided through the SU-8/quartz waveguides compared to the standard SU-8/silica waveguides was investigated numerically with two methods: by 3D FDTD simulations of emitting dimensionless current dipoles at the vicinity of the waveguides and with a calculation method combining the modal propagation approach for planar waveguides with the effective index method. Both calculation methods predicted an increase of the fluorescence collection efficiency of the SU-8/quartz waveguides fabricated with the novel protocol over the standard SU-8/silica waveguide. To our knowledge, this was the first time that such precise 3D FDTD simulations were performed to find the fluorescence collection efficiency of waveguides. Also, for the first time, a calculation method was developed to evaluate the fluorescence collection efficiency for rectangular waveguides for varying parameters.

Due to the limitations of the fabrication method to diminish the optical propagation losses or to increase the core index of the waveguides, new designs promoting a larger area for the labeled targets to be immobilized were developed. All the design were compared to a single straight waveguide in terms of sensitivity to assess their improvements. The first design, the cascaded waveguide, increased the area of immobilization of the labeled targets by using ramifications that start from a single straight input waveguide and recombines to another single straight output waveguide. The design was successful in increasing the sensitivity of the sensor but not up to its enlargement in area for labeled analyte immobilization. This was due to the great number of Y-junctions necessary for the doubling of the waveguides. Also, the more the ramifications were doubled the greater the mode order of the guided evanescently coupled fluorescence light reaching the output waveguide would be. This resulted in only part of the evanescently coupled fluorescence light to be collected. Hence, it diminished the effect of a larger immobilization area for the labeled analytes. To counter these hindrances, two new designs were developed with only 2 Y-junctions to lower the optical propagation losses and only 2 or 3 straight waveguides, making the most of the area of immobilization, to lower the mode order of the evanescently coupled fluorescence light reaching the output waveguide. The sensitivities of the doubled and tripled waveguide optical biosensors have proven to be almost proportional to the enlargement in area of immobilization compared to a single waveguide. To have a better idea of the performance of these sensors, their calibration curves for the detection of different concentration of Alexa 647 labeled biotin were plotted together as seen in Figure 7.1.
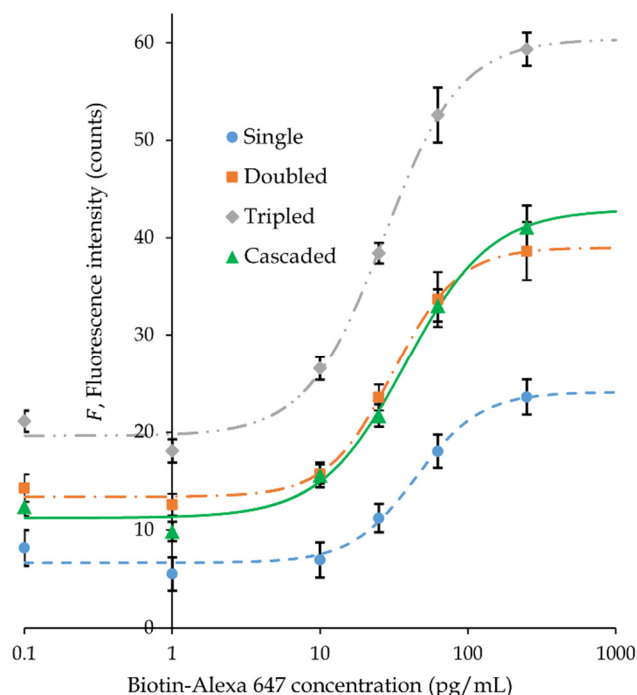
Figure 7. 1   Calibration curves for the doubled, tripled and cascaded waveguides for Alexa 647 labeled biotin detection.

Evidently, the tripled waveguide showed the greatest sensitivity (2 fold compared to the single waveguide), the lowest LOD (7 pg·mL^{-1}) and the highest fluorescence output yield compared to the other sensors. Surprisingly, the cascaded waveguide seems comparable to the doubled waveguide in terms of fluorescence output yield and sensitivity. The trend that was observed is that a balance should be kept between the number of junctions and the multiplication of the waveguides i.e. managing between the optical losses, the creation of higher order modes and the increase in area of immobilization.

In brief, this work proposed the SU-8/quartz, cascaded, doubled and the tripled waveguides as new sensing platforms for fluorescence bio detection. Also, theoretical calculations and numerical simulations accompanied with experimental testing demonstrated that these platforms were effective to enhance the fluorescence output compared to standard integrated waveguides for fluorescence spectroscopy.

161

7.2   Future work

The main emphasis for the fabrication process of the SU-8/quartz should be to perform the fabrication tasks in a humidity controlled environment to assure constant and superior performance of the waveguides. Also, the same fabrication protocol in general should be adapted for different polymers, substrates and with different dimensions to establish it as a reference for polymer optical waveguides. Future characterizations studies should provide the roughness profiles of the sidewalls of the waveguides for a better understanding of the impact from of the different fabrication processes and would allow for numerical simulations of the optical propagation losses.

Also, the 3D FDTD simulations to evaluate the fluorescence collection efficiency of the SU-8/quartz and SU-8/silica waveguide would benefit by adding the roughness profiles at the sidewalls. Indeed, it could provide simulation results that could be directly compared to the evanescent wave fluorescence spectroscopy detection results.

As for the calculation method combining the modal propagation approach for the fluorescence collection efficiency for planar waveguides and the effective index method, it should be compared with 3D FDTD simulations to have an idea of the error on the absolute and relative values obtained for the fluorescence collection efficiency of both SU-8/quartz and SU-8/silica waveguides.

The cascaded, doubled and tripled waveguides designs could be improved by reducing the optical losses from the junctions by creating slowly varying 3D tapers in between the branches which would take into account the light propagation in both transverse directions. Also, an ingenious way to limit the inability of the output waveguide to guide the higher order mode signal formed by the recombination of signals would be to gradually increase the index of refraction of the last junction until the end of the output waveguide which will contribute to support the great number of high order mode signals. The same result could be obtained by gradually tapering the final recombining junction to an output waveguide with greater dimensions which will also allow for a greater number of high order mode signals.

For future biosensing projects, the doubled and tripled waveguides are promising designs for multi-analyte detection platforms for a lab-on-a-chip system. Indeed, since they are designed with straight waveguides, each straight waveguide could be modified with antibodies specific to different analytes to be then delivered with different analytes by microfluidic channels. As reported previously, the evaluation of the purity of water requires multi-analyte detection due to the multitude of contaminants it contains. With designs similar to the doubled or tripled waveguide it would be possible to detect a multitude of contaminants but also the particularity of their designs would allow for an all planar miniaturized chip, allowing for mass production, low cost and point of care devices.

REFERENCES

[1] A. Leung, P. M. Shankar, and R. Mutharasan, "A review of fiber-optic biosensors," *Sensors and Actuators B: Chemical,* vol. 125, no. 2, pp. 688-703, 2007/08/08/ 2007.

[2] X.-D. Wang and O. S. Wolfbeis, "Fiber-Optic Chemical Sensors and Biosensors (2008–2012)," *Analytical Chemistry,* vol. 85, no. 2, pp. 487-508, 2013/01/15 2013.

[3] X. Fan, I. M. White, S. I. Shopova, H. Zhu, J. D. Suter, and Y. Sun, "Sensitive optical biosensors for unlabeled targets: A review," *Analytica Chimica Acta,* vol. 620, no. 1, pp. 8-26, 2008/07/14/ 2008.

[4] C. R. Taitt, G. P. Anderson, and F. S. Ligler, "Evanescent wave fluorescence biosensors: Advances of the last decade," *Biosensors & bioelectronics,* vol. 76, pp. 103-112, 2016.

[5] J. Homola, S. S. Yee, and G. Gauglitz, *Surface Plasmon Resonance Sensors: Review*. 1999, pp. 3-15.

[6] J. Homola, *Surface Plasmon Resonance Sensors for Detection of Chemical and Biological Species*. 2008, pp. 462-93.

[7] H. Šípová and J. Homola, "Surface plasmon resonance sensing of nucleic acids: A review," *Analytica Chimica Acta,* vol. 773, pp. 9-23, 2013/04/22/ 2013.

[8] B. E. Saleh, M. C. Teich, and B. E. Saleh, *Fundamentals of photonics*. Wiley New York, 1991.

[9] H. Mukundan *et al.*, "Waveguide-based biosensors for pathogen detection," *Sensors (Basel, Switzerland),* vol. 9, no. 7, pp. 5783-5809, 2009.

[10] V. M. N. Passaro, F. Dell'Olio, B. Casamassima, and F. De Leonardis, "Guided-Wave Optical Biosensors," *Sensors (Basel, Switzerland),* vol. 7, no. 4, pp. 508-536, 2007.

[11] H. Sohlström, K. Gylfason, and D. Hill, *Real-time label-free biosensing with integrated planar waveguide ring resonators*. 2010.

[12] L. Wang, C. Vasilev, D. P. Canniffe, L. R. Wilson, C. N. Hunter, and A. J. Cadby, "Highly confined surface imaging by solid immersion total internal reflection fluorescence microscopy," *Optics Express,* vol. 20, no. 3, pp. 3311-3324, 2012/01/30 2012.

[13] A. L. Mattheyses, S. M. Simon, and J. Z. Rappoport, "Imaging with total internal reflection fluorescence microscopy for the cell biologist," *Journal of Cell Science,* 10.1242/jcs.056218 vol. 123, no. 21, p. 3621, 2010.

[14] H. Välimäki and K. Tappura, "A novel platform for highly surface-sensitive fluorescent measurements applying simultaneous total internal reflection excitation and super critical angle detection," *Chemical Physics Letters,* vol. 473, no. 4, pp. 358-362, 2009/05/12/ 2009.

[15] T. Ruckstuhl and D. Verdes, "Supercritical angle fluorescence (SAF) microscopy," *Optics Express,* vol. 12, no. 18, pp. 4246-4254, 2004/09/06 2004.

[16] T. Pulli, M. Höyhtyä, H. Söderlund, and K. Takkinen, "One-Step Homogeneous Immunoassay for Small Analytes," *Analytical Chemistry,* vol. 77, no. 8, pp. 2637-2642, 2005/04/01 2005.

[17] M. Yamamoto, *Surface Plasmon Resonance (SPR) Theory: Tutorial*. 2001.

[18] Y. Yanase, K. Sakamoto, K. Kobayashi, and M. Hide, "Diagnosis of immediate-type allergy using surface plasmon resonance," *Optical Materials Express,* vol. 6, no. 4, pp. 1339-1348, 2016/04/01 2016.

[19] A. Valsesia, P. Colpo, T. Meziani, P. Lisboa, M. Lejeune, and F. Rossi, "Immobilization of Antibodies on Biosensing Devices by Nanoarrayed Self-Assembled Monolayers," *Langmuir,* vol. 22, no. 4, pp. 1763-1767, 2006/02/01 2006.

[20] A. Kausaite-Minkstimiene, A. Ramanaviciene, J. Kirlyte, and A. Ramanavicius, "Comparative Study of Random and Oriented Antibody Immobilization Techniques on the Binding Capacity of Immunosensor," *Analytical Chemistry,* vol. 82, no. 15, pp. 6401-6408, 2010/08/01 2010.

[21] D. H. Bunka and P. G. Stockley, "Aptamers come of age–at last," *Nature Reviews Microbiology,* vol. 4, no. 8, p. 588, 2006.

[22] J. M. Luther, P. K. Jain, T. Ewers, and A. P. Alivisatos, "Localized surface plasmon resonances arising from free carriers in doped quantum dots," *Nature materials,* vol. 10, no. 5, p. 361, 2011.

[23] N. Verellen *et al.*, "Plasmon Line Shaping Using Nanocrosses for High Sensitivity Localized Surface Plasmon Resonance Sensing," *Nano Letters,* vol. 11, no. 2, pp. 391-397, 2011/02/09 2011.

[24] S. Rebe Raz, M. G. E. G. Bremer, W. Haasnoot, and W. Norde, "Label-Free and Multiplex Detection of Antibiotic Residues in Milk Using Imaging Surface Plasmon Resonance-Based Immunosensor," *Analytical Chemistry,* vol. 81, no. 18, pp. 7743-7749, 2009/09/15 2009.

[25] W. H. Weber and C. F. Eagen, "Energy transfer from an excited dye molecule to the surface plasmons of an adjacent metal," *Optics Letters,* vol. 4, no. 8, pp. 236-238, 1979/08/01 1979.

[26] J. R. Lakowicz, J. Malicka, I. Gryczynski, and Z. Gryczynski, "Directional surface plasmon-coupled emission: a new method for high sensitivity detection," *Biochemical and Biophysical Research Communications,* vol. 307, no. 3, pp. 435-439, 2003/08/01/ 2003.

[27] I. Gryczynski, J. Malicka, Z. Gryczynski, and J. Lakowicz, *Radiative decay engineering 4. Experimental studies of surface plasmon-coupled directional emission*. 2004, pp. 170-82.

[28] T. Liebermann and W. Knoll, "Surface-plasmon field-enhanced fluorescence spectroscopy," *Colloids and Surfaces A: Physicochemical and Engineering Aspects,* vol. 171, no. 1-3, pp. 115-130, 2000.

[29] J. R. Lakowicz, "Radiative Decay Engineering: Biophysical and Biomedical Applications," *Analytical Biochemistry,* vol. 298, no. 1, pp. 1-24, 2001/11/01/ 2001.

[30] J. Enderlein and T. Ruckstuhl, *The efficiency of surface-plasmon coupled emission for sensitive fluorescence detection*. 2005, pp. 8855-65.

[31] B. Sepúlveda, P. C. Angelomé, L. M. Lechuga, and L. M. Liz-Marzán, "LSPR-based nanobiosensors," *Nano Today,* vol. 4, no. 3, pp. 244-251, 2009/06/01/ 2009.

[32] M. H. Chowdhury, K. Ray, C. D. Geddes, and J. R. Lakowicz, "Use of silver nanoparticles to enhance surface plasmon-coupled emission (SPCE)," *Chemical physics letters,* vol. 452, no. 1-3, pp. 162-167, 2008.

[33] J. S. Yuk, E. F. Guignon, and M. A. Lynes, "Highly sensitive grating coupler-based surface plasmon-coupled emission (SPCE) biosensor for immunoassay," *Analyst,* 10.1039/C3AN00135K vol. 138, no. 9, pp. 2576-2582, 2013.

[34] J. S. Yuk, G. N. Gibson, J. M. Rice, E. F. Guignon, and M. A. Lynes, "Analysis of immunoarrays using a gold grating-based dual mode surface plasmon-coupled emission (SPCE) sensor chip," *Analyst,* 10.1039/C2AN35143A vol. 137, no. 11, pp. 2574-2581, 2012.

[35] D. S Smith *et al.*, *First Observation of Surface Plasmon-Coupled Emission Due to LED Excitation*. 2005, pp. 895-900.

[36] K. Aslan and C. D. Geddes, "Metal-enhanced chemiluminescence: advanced chemiluminescence concepts for the 21st century," *Chemical Society Reviews,* 10.1039/B807498B vol. 38, no. 9, pp. 2556-2564, 2009.

[37] J. S. Yuk, E. O'Reilly, R. J. Forster, B. D. MacCraith, and C. McDonagh, "Demonstration of surface plasmon-coupled emission using solid-state electrochemiluminescence," *Chemical Physics Letters,* vol. 513, no. 1, pp. 112-117, 2011/09/06/ 2011.

[38] J. S. Yuk, M. Trnavsky, C. McDonagh, and B. D. MacCraith, "Surface plasmon-coupled emission (SPCE)-based immunoassay using a novel paraboloid array biochip," *Biosensors and Bioelectronics,* vol. 25, no. 6, pp. 1344-1349, 2010/02/15/ 2010.

[39] J. S. Yuk, B. D. MacCraith, and C. McDonagh, "Signal enhancement of surface plasmon-coupled emission (SPCE) with the evanescent field of surface plasmons on a bimetallic paraboloid biochip," *Biosensors and Bioelectronics,* vol. 26, no. 7, pp. 3213-3218, 2011/03/15/ 2011.

[40] X. Liu *et al.*, *Directional surface plasmon-coupled emission of CdTe quantum dots and its application in Hg(II) sensing*. 2012, pp. 3956-3960.

[41] D. Sarid, "Long-Range Surface-Plasma Waves on Very Thin Metal Films," *Physical Review Letters,* vol. 47, no. 26, pp. 1927-1930, 12/28/ 1981.

[42] P. Berini, "Long-range surface plasmon polaritons," *Advances in Optics and Photonics,* vol. 1, no. 3, pp. 484-588, 2009/11/01 2009.

[43] A. Kasry and W. Knoll, "Long range surface plasmon fluorescence spectroscopy," *Applied Physics Letters,* vol. 89, no. 10, p. 101106, 2006/09/04 2006.

[44] R. Slavik and J. Homola, *Ultrahigh resolution long range surface plasmon-based sensor*. 2007, pp. 10–12.

[45] D. Sarid, R. T. Deck, A. E. Craig, R. K. Hickernell, R. S. Jameson, and J. J. Fasano, "Optical field enhancement by long-range surface-plasma waves," *Applied Optics,* vol. 21, no. 22, pp. 3993-3995, 1982/11/15 1982.

[46] Y. Wang, J. Dostálek, and W. Knoll, "Long range surface plasmon-enhanced fluorescence spectroscopy for the detection of aflatoxin M1 in milk," *Biosensors and Bioelectronics,* vol. 24, no. 7, pp. 2264-2267, 2009.

[47] A. Minardo, R. Bernini, F. Mottola, and L. Zeni, "Optimization of metal-clad waveguides for sensitive fluorescence detection," *Optics Express,* vol. 14, no. 8, pp. 3512-3527, 2006/04/17 2006.

[48] M. Zourob, S. Mohr, B. J. Treves Brown, P. R. Fielden, M. B. McDonnell, and N. J. Goddard, "An Integrated Metal Clad Leaky Waveguide Sensor for Detection of Bacteria," *Analytical Chemistry,* vol. 77, no. 1, pp. 232-242, 2005/01/01 2005.

[49] M. Zourob and N. J. Goddard, "Metal clad leaky waveguides for chemical and biosensing applications," (in eng), *Biosens Bioelectron,* vol. 20, no. 9, pp. 1718-27, Mar 15 2005.

[50] N. Skivesen, R. Horvath, S. Thinggaard, N. B. Larsen, and H. C. Pedersen, "Deep-probe metal-clad waveguide biosensors," *Biosensors and Bioelectronics,* vol. 22, no. 7, pp. 1282-1288, 2007/02/15/ 2007.

[51] M. Zourob, S. Mohr, B. J. T. Brown, P. R. Fielden, M. B. McDonnell, and N. J. Goddard, "Bacteria detection using disposable optical leaky waveguide sensors," *Biosensors and Bioelectronics,* vol. 21, no. 2, pp. 293-302, 2005/08/15/ 2005.

[52] W. Lukosz, "Integrated optical chemical and direct biochemical sensors," *Sensors and Actuators B: Chemical,* vol. 29, no. 1, pp. 37-50, 1995/10/01/ 1995.

[53] W. Lukosz, "Principles and sensitivities of integrated optical and surface plasmon sensors for direct affinity sensing and immunosensing," *Biosensors and Bioelectronics,* vol. 6, no. 3, pp. 215-225, 1991/01/01/ 1991.

[54] H. M. Grandin, B. Städler, M. Textor, and J. Vörös, "Waveguide excitation fluorescence microscopy: A new tool for sensing and imaging the biointerface," *Biosensors and Bioelectronics,* vol. 21, no. 8, pp. 1476-1482, 2006/02/15/ 2006.

[55] K. Schmitt, K. Oehse, G. Sulz, and C. Hoffmann, "Evanescent field Sensors Based on Tantalum Pentoxide Waveguides - A Review," (in eng), *Sensors (Basel),* vol. 8, no. 2, pp. 711-738, Jan 6 2008.

[56] J. S. Martinez, W. K. Grace, K. M. Grace, N. Hartman, and B. I. Swanson, "Pathogen detection using single mode planar optical waveguides," *Journal of Materials Chemistry,* 10.1039/B502329G vol. 15, no. 43, pp. 4639-4647, 2005.

[57] L. Yang, S. S. Saavedra, N. R. Armstrong, and J. Hayes, "Fabrication and Characterization of Low-Loss, Sol-Gel Planar Waveguides," *Analytical Chemistry,* vol. 66, no. 8, pp. 1254-1263, 1994/04/15 1994.

[58] H. Shih-Hao and T. Fan-Gang, "Development of a monolithic total internal reflection-based biochip utilizing a microprism array for fluorescence sensing," *Journal of Micromechanics and Microengineering,* vol. 15, no. 12, p. 2235, 2005.

[59] H. Kuo-Yung, H. Heng-Tsang, and T. Fan-Gang, "Application of 3D glycerol-compensated inclined-exposure technology to an integrated optical pick-up head," *Journal of Micromechanics and Microengineering,* vol. 14, no. 7, p. 975, 2004.

[60] R. Marie *et al.*, "Immobilisation of DNA to polymerised SU-8 photoresist," *Biosensors and Bioelectronics,* vol. 21, no. 7, pp. 1327-1332, 2006/01/15/ 2006.

[61] L. Liu *et al.*, "An array fluorescent biosensor based on planar waveguide for multi-analyte determination in water samples," *Sensors and Actuators B: Chemical,* vol. 240, pp. 107-113, 2017/03/01/ 2017.

[62] L.-h. Liu, X.-h. Zhou, W.-q. Xu, B.-d. Song, and H.-c. Shi, "Highly sensitive detection of sulfadimidine in water and dairy products by means of an evanescent wave optical biosensor," *RSC Advances,* 10.1039/C4RA10501J vol. 4, no. 104, pp. 60227-60233, 2014.

[63] Z. Xiao-hong, S. Bao-dong, S. Han-chang, L. Lan-hua, G. Hong-li, and H. Miao, "An evanescent wave multi-channel immunosensor system for the highly sensitive detection of small analytes in water samples," *Sensors and Actuators B: Chemical,* vol. 198, pp. 150-156, 2014/07/31/ 2014.

[64] L. Liu, X. Zhou, R. Ma, M. He, H. Shi, and Q. Yi, "High-throughput biomolecular interaction analysis probing by an array fluorescent biosensor platform," *Sensors and Actuators B: Chemical,* vol. 259, pp. 888-893, 2018/04/15/ 2018.

[65] P. Kozma *et al.*, "A novel handheld fluorescent microarray reader for point-of-care diagnostic," *Biosensors and Bioelectronics,* vol. 47, pp. 415-420, 2013/09/15/ 2013.

[66] F. J. Aparicio *et al.*, "Silicon oxynitride waveguides as evanescent-field-based fluorescent biosensors," *Journal of Physics D: Applied Physics,* vol. 47, no. 40, p. 405401, 2014.

[67] F. López Arbeloa, V. Martínez Martínez, T. Arbeloa, and I. López Arbeloa, "Photoresponse and anisotropy of rhodamine dye intercalated in ordered clay layered films," *Journal of Photochemistry and Photobiology C: Photochemistry Reviews,* vol. 8, no. 2, pp. 85-108, 2007/10/01/ 2007.

[68] Y. Lianghong *et al.*, "Fabrication and characterization of compact silicon oxynitride waveguides on silicon chips," *Journal of Optics,* vol. 14, no. 8, p. 085501, 2012.

[69] R. Horvath, K. Cottier, H. C. Pedersen, and J. J. Ramsden, "Multidepth screening of living cells using optical waveguides," *Biosensors and Bioelectronics,* vol. 24, no. 4, pp. 799-804, 2008/12/01/ 2008.

[70] J. Ozhikandathil and M. Packirisamy, "Detection of recombinant growth hormone by evanescent cascaded waveguide coupler on silica-on-silicon," (in eng), *Journal of biophotonics,* vol. 6, no. 5, pp. 457-467, 2013/05// 2013.

[71] J. P. Golden, G. P. Anderson, S. Y. Rabbany, and F. S. Ligler, "An evanescent wave biosensor. II. Fluorescent signal acquisition from tapered fiber optic probes," *IEEE Transactions on Biomedical Engineering,* vol. 41, no. 6, pp. 585-591, 1994.

[72] B. D. Gupta, H. Dodeja, and A. K. Tomar, "Fibre-optic evanescent field absorption sensor based on a U-shaped probe," *Optical and Quantum Electronics,* vol. 28, no. 11, pp. 1629-1639, 1996/11/01 1996.

[73] L. Liu, X. Zhou, J. S. Wilkinson, P. Hua, B. Song, and H. Shi, "Integrated optical waveguide-based fluorescent immunosensor for fast and sensitive detection of microcystin-LR in lakes: Optimization and Analysis," *Scientific Reports,* vol. 7, no. 1, p. 3655, 2017/06/16 2017.

[74]   L. Jiang, K. P. Gerhardt, B. Myer, Y. Zohar, and S. Pau, "Evanescent-Wave Spectroscopy Using an SU-8 Waveguide for Rapid Quantitative Detection of Biomolecules," *Journal of Microelectromechanical Systems,* vol. 17, no. 6, pp. 1495-1500, 2008.

[75]   R. Bruck *et al.*, "Flexible thin-film polymer waveguides fabricated in an industrial roll-to-roll process," *Applied Optics,* vol. 52, no. 19, pp. 4510-4514, 2013/07/01 2013.

[76]   X. Lin, A. Hosseini, X. Dou, H. Subbaraman, and R. T. Chen, "Low-cost board-to-board optical interconnects using molded polymer waveguide with 45 degree mirrors and inkjet-printed micro-lenses as proximity vertical coupler," *Optics Express,* vol. 21, no. 1, pp. 60-69, 2013/01/14 2013.

[77]   P. Bollgruen *et al.*, "Ink-jet printed optical waveguides," *Flexible and Printed Electronics,* vol. 2, no. 4, p. 045003, 2017.

[78]   M. T. Do, T. T. N. Nguyen, Q. Li, H. Benisty, I. Ledoux-Rak, and N. D. Lai, "Submicrometer 3D structures fabrication enabled by one-photon absorption direct laser writing," *Optics Express,* vol. 21, no. 18, pp. 20964-20973, 2013/09/09 2013.

[79]   S. Bor-Yuan, H. Jui-Tang, H. Tai-Yuan, L. Kun-Pei, and C. Chang-Pin, "High resolution x-ray micromachining using SU-8 resist," *Journal of Micromechanics and Microengineering,* vol. 13, no. 5, p. 708, 2003.

[80]   B. Bilenberg *et al.*, "High resolution 100kV electron beam lithography in SU-8," *Microelectronic Engineering,* vol. 83, no. 4, pp. 1609-1612, 2006/04/01/ 2006.

[81]   A. d. Campo and C. Greiner, "SU-8: a photoresist for high-aspect-ratio and 3D submicron lithography," *Journal of Micromechanics and Microengineering,* vol. 17, no. 6, p. R81, 2007.

[82]   K. V. Nemani, K. L. Moodie, J. B. Brennick, A. Su, and B. Gimi, "In vitro and in vivo evaluation of SU-8 biocompatibility," (in eng), *Mater Sci Eng C Mater Biol Appl,* vol. 33, no. 7, pp. 4453-9, Oct 2013.

[83]   J. M. Shaw, J. D. Gelorme, N. C. LaBianca, W. E. Conley, and S. J. Holmes, "Negative photoresists for optical lithography," *IBM Journal of Research and Development,* vol. 41, no. 1.2, pp. 81-94, 1997.

[84]   J. Hammacher, A. Fuelle, J. Flaemig, J. Saupe, B. Loechel, and J. Grimm, "Stress engineering and mechanical properties of SU-8-layers for mechanical applications," *Microsystem Technologies,* vol. 14, no. 9, pp. 1515-1523, 2008/10/01 2008.

[85]   M. Aktary, M. O. Jensen, K. L. Westra, M. J. Brett, and M. R. Freeman, "High-resolution pattern generation using the epoxy novolak SU-8 2000 resist by electron beam lithography," *Journal of Vacuum Science & Technology B: Microelectronics and Nanometer Structures Processing, Measurement, and Phenomena,* vol. 21, no. 4, pp. L5-L7, 2003/07/01 2003.

[86]   K. K. Tung, W. H. Wong, and E. Y. B. Pun, "Polymeric optical waveguides using direct ultraviolet photolithography process," *Applied Physics A,* journal article vol. 80, no. 3, pp. 621-626, February 01 2005.

[87]   F. Prieto *et al.*, "An integrated optical interferometric nanodevice based on silicon technology for biosensor applications," *Nanotechnology,* vol. 14, no. 8, p. 907, 2003.

[88]   J. Halldorsson, N. B. Arnfinnsdottir, A. B. Jonsdottir, B. Agnarsson, and K. Leosson, "High index contrast polymer waveguide platform for integrated biophotonics," *Optics Express,* vol. 18, no. 15, pp. 16217-16226, 2010/07/19 2010.

[89]   B. Yang *et al.*, "Compact Arrayed Waveguide Grating Devices Based on Small SU-8 Strip Waveguides," *Journal of Lightwave Technology,* vol. 29, no. 13, pp. 2009-2014, 2011.

[90]   V. S. Kumar, S. P. Turaga, E. J. Teo, and A. A. Bettiol, "Fabrication of optical microresonators using proton beam writing," *Microelectronic Engineering,* vol. 102, pp. 33-35, 2013/02/01/ 2013.

[91]   B. Bêche, N. Pelletier, E. Gaviot, and J. Zyss, "Single-mode TE00–TM00 optical waveguides on SU-8 polymer," *Optics Communications,* vol. 230, no. 1, pp. 91-94, 2004/01/15/ 2004.

[92]   B. Yang *et al.*, "Fabrication and Characterization of Small Optical Ridge Waveguides Based on SU-8 Polymer," *Journal of Lightwave Technology,* vol. 27, no. 18, pp. 4091-4096, 2009.

[93]   M. Nordstrom, D. A. Zauner, A. Boisen, and J. Hubner, "Single-Mode Waveguides With SU-8 Polymer Core and Cladding for MOEMS Applications," *Journal of Lightwave Technology,* vol. 25, no. 5, pp. 1284-1289, 2007.

[94]   A. Borreman, S. Musa, A. A M Kok, M. B J Diemeer, and A. Driessen, *Fabrication of polymeric multimode waveguides and devices in SU-8 photoresist using selective polymerization*. 2018.

[95]   C.-S. Huang and W.-C. Wang, "Large-core single-mode rib SU8 waveguide using solvent-assisted microcontact molding," *Applied Optics,* vol. 47, no. 25, pp. 4540-4547, 2008/09/01 2008.

[96]   R. Horváth, L. R. Lindvold, and N. B. Larsen, "Reverse-symmetry waveguides: theory and fabrication," *Applied Physics B,* vol. 74, no. 4, pp. 383-393, 2002/04/01 2002.

[97]   K. Stephan, B. Gabriela, L. Michael, H. Daniel, and B. Anja, "Processing of thin SU-8 films," *Journal of Micromechanics and Microengineering,* vol. 18, no. 12, p. 125020, 2008.

[98]   S. Motahhari and J. Cameron, "The Contribution to Residual Stress by Differential Resin Shrinkage," *Journal of Reinforced Plastics and Composites,* vol. 18, no. 11, pp. 1011-1020, 1999/07/01 1999.

[99]   F. Ru and J. F. Richard, "Influence of processing conditions on the thermal and mechanical properties of SU8 negative photoresist coatings," *Journal of Micromechanics and Microengineering,* vol. 13, no. 1, p. 80, 2003.

[100]   F. Grillot, L. Vivien, S. Laval, and E. Cassan, "Propagation loss in single-mode ultrasmall square silicon-on-insulator optical waveguides," *Journal of Lightwave Technology,* vol. 24, no. 2, pp. 891-896, 2006.

[101]   R. Degl'Innocenti, A. Majkic, F. Sulser, L. Mutter, G. Poberaj, and P. Günter, "UV Second Harmonic Generation at 266 nm in He+ Implanted β-BaB2O4 Optical Waveguides," *Optics Express,* vol. 16, no. 15, pp. 11660-11669, 2008/07/21 2008.

[102] R. J. Deri and E. Kapon, "Low-loss III-V semiconductor optical waveguides," *IEEE Journal of Quantum Electronics,* vol. 27, no. 3, pp. 626-640, 1991.

[103] C. Qiu *et al.*, "Fabrication, Characterization and Loss Analysis of Silicon Nanowaveguides," *Journal of Lightwave Technology,* vol. 32, no. 13, pp. 2303-2307, 2014.

[104] D. Salazar, F. F.Castill, and J. L. Angel-Valenzuela, *Refractive index modulation of SU-8 polymer optical waveguides by means of hybrid photothermal process.* 2010, pp. 85-90.

[105] S. Agan, F. Ay, A. Kocabas, and A. Aydinli, "Stress effects in prism coupling measurements of thin polymer films," *Applied Physics A,* vol. 80, no. 2, pp. 341-345, 2005/02/01 2005.

[106] R. Bernini, N. Cennamo, A. Minardo, and L. Zeni, "Polymer-on-glass waveguide structure for efficient fluorescence-based optical biosensors," in *Integrated Optoelectronic Devices 2005*, 2005, vol. 5728, p. 11: SPIE.

[107] C. McDonagh, C. S. Burke, and B. D. MacCraith, "Optical Chemical Sensors," *Chemical Reviews,* vol. 108, no. 2, pp. 400-422, 2008/02/01 2008.

[108] C. R. Taitt, G. P. Anderson, and F. S. Ligler, "Evanescent wave fluorescence biosensors," *Biosensors and Bioelectronics,* vol. 20, no. 12, pp. 2470-2487, 2005/06/15/ 2005.

[109] M. Pospíšilová, G. Kuncová, and J. Trögl, "Fiber-Optic Chemical Sensors and Fiber-Optic Bio-Sensors," *Sensors,* vol. 15, no. 10, 2015.

[110] E. P. Schartner *et al.*, "Taming the Light in Microstructured Optical Fibers for Sensing," *International Journal of Applied Glass Science,* vol. 6, no. 3, pp. 229-239, 2015/09/01 2015.

[111] K. E. Sapsford *et al.*, "Fluorescence-based array biosensors for detection of biohazards," *Journal of Applied Microbiology,* vol. 96, no. 1, pp. 47-58, 2004/01/01 2003.

[112] M. C. Estevez, M. Alvarez, and L. M. Lechuga, "Integrated optical devices for lab-on-a-chip biosensing applications," *Laser & Photonics Reviews,* vol. 6, no. 4, pp. 463-487, 2012/07/16 2011.

[113] T. David *et al.*, "Roadmap on silicon photonics," *Journal of Optics,* vol. 18, no. 7, p. 073003, 2016.

[114] A. Fernández Gavela, D. Grajales García, C. J. Ramirez, and M. L. Lechuga, "Last Advances in Silicon-Based Optical Biosensors," *Sensors,* vol. 16, no. 3, 2016.

[115] A. Densmore *et al.*, "A Silicon-on-Insulator Photonic Wire Based Evanescent Field Sensor," *IEEE Photonics Technology Letters,* vol. 18, no. 23, pp. 2520-2522, 2006.

[116] K. D. Vos, I. Bartolozzi, E. Schacht, P. Bienstman, and R. Baets, "Silicon-on-Insulator microring resonator for sensitive and label-free biosensing," *Optics Express,* vol. 15, no. 12, pp. 7610-7615, 2007/06/11 2007.

[117] L. Eldada and L. W. Shacklette, "Advances in polymer integrated optics," *IEEE Journal of Selected Topics in Quantum Electronics,* vol. 6, no. 1, pp. 54-68, 2000.

[118] K. Lösch, "Optical polymers for telecom applications," *Macromolecular Symposia,* vol. 100, no. 1, pp. 65-69, 1995/10/01 1995.

[119] R. Bruck *et al.*, *Flexible thin-film polymer waveguides fabricated in an industrial roll-to-roll process*. 2013, pp. 4510-4514.

[120] K. Junya, Y. Shogo, H. Yutaka, and K. Naomi, "Low Loss Polymer Optical Waveguide Replicated from Flexible Film Stamp Made of Polymeric Material," *Japanese Journal of Applied Physics,* vol. 52, no. 7R, p. 072501, 2013.

[121] S. S. Zakariyah, P. P. Conway, D. A. Hutt, K. Wang, and D. R. Selviah, "CO2 laser micromachining of optical waveguides for interconnection on circuit boards," *Optics and Lasers in Engineering,* vol. 50, no. 12, pp. 1752-1756, 2012/12/01/ 2012.

[122] K. Jae-Wook, K. Joon-Sung, and K. Jang-Joo, "Optimized Oxygen Plasma Etching of Polycarbonate for Low-Loss Optical Waveguide Fabrication," *Japanese Journal of Applied Physics,* vol. 40, no. 5R, p. 3215, 2001.

[123] H. Robert, C. P. Henrik, S. Nina, S. Christer, and B. L. Niels, "Fabrication of reverse symmetry polymer waveguide sensor chips on nanoporous substrates using dip-floating," *Journal of Micromechanics and Microengineering,* vol. 15, no. 6, p. 1260, 2005.

[124] W. H. Wong, J. Zhou, and E. Y. B. Pun, "Low-loss polymeric optical waveguides using electron-beam direct writing," *Applied Physics Letters,* vol. 78, no. 15, pp. 2110-2112, 2001.

[125] H. Ma, A. K. Y. Jen, and L. R. Dalton, "Polymer-Based Optical Waveguides: Materials, Processing, and Devices," *Advanced Materials,* vol. 14, no. 19, pp. 1339-1365, 2002.

[126] Y. Sun *et al.*, "Polymer thermal optical switch for a flexible photonic circuit," *Applied Optics,* vol. 57, no. 1, pp. 14-17, 2018/01/01 2018.

[127] S.-Q. Sun *et al.*, "Design and fabrication of all-polymer thermo-optic variable optical attenuator with low power consumption," *Applied Physics A,* journal article vol. 123, no. 10, p. 646, September 18 2017.

[128] A. M. Al-Hetar, A. B. Mohammad, A. S. M. Supa'at, and Z. A. Shamsan, "MMI-MZI Polymer Thermo-Optic Switch With a High Refractive Index Contrast," *Journal of Lightwave Technology,* vol. 29, no. 2, pp. 171-178, 2011/01/15 2011.

[129] R. Dangel *et al.*, "Development of Versatile Polymer Waveguide Flex Technology for Use in Optical Interconnects," *Journal of Lightwave Technology,* vol. 31, no. 24, pp. 3915-3926, 2013/12/15 2013.

[130] L. Li *et al.*, "A Fully-Integrated Flexible Photonic Platform for Chip-to-Chip Optical Interconnects," *Journal of Lightwave Technology,* vol. 31, no. 24, pp. 4080-4086, 2013.

[131] X. Gan, H. Clevenson, and D. Englund, "Polymer Photonic Crystal Nanocavity for Precision Strain Sensing," *ACS Photonics,* vol. 4, no. 7, pp. 1591-1594, 2017/07/19 2017.

[132] M. Rosenberger, W. Eisenbeil, B. Schmauss, and R. Hellmann, "Simultaneous 2D Strain Sensing Using Polymer Planar Bragg Gratings," *Sensors (Basel, Switzerland),* vol. 15, no. 2, pp. 4264-4272, 2015.

[133] P. I. Okagbare, J. M. Emory, P. Datta, J. Goettert, and S. A. Soper, "Fabrication of a cyclic olefin copolymer planar waveguide embedded in a multi-channel poly(methyl

methacrylate) fluidic chip for evanescence excitation," *Lab on a chip,* vol. 10, no. 1, pp. 66-73, 11/04 2010.

[134]   J. W. Kim, K. J. Kim, J. A. Yi, and M. C. Oh, "Polymer Waveguide Label-Free Biosensors With Enhanced Sensitivity by Incorporating Low-Refractive-Index Polymers," *IEEE Journal of Selected Topics in Quantum Electronics,* vol. 16, no. 4, pp. 973-980, 2010.

[135]   M. Mancuso, J. M. Goddard, and D. Erickson, "Nanoporous polymer ring resonators for biosensing," *Optics Express,* vol. 20, no. 1, pp. 245-255, 2012.

[136]   J. C. Ramirez, L. M. Lechuga, L. H. Gabrielli, and H. E. Hernandez-Figueroa, "Study of a low-cost trimodal polymer waveguide for interferometric optical biosensors," *Optics Express,* vol. 23, no. 9, pp. 11985-11994, 2015/05/04 2015.

[137]   S. Aikio *et al.*, "Disposable (bio)chemical integrated optical waveguide sensors implemented on roll-to-roll produced platforms," *RSC Advances,* 10.1039/C6RA07320D vol. 6, no. 56, pp. 50414-50422, 2016.

[138]   C. S. Kuang, W. Y. Yee, and S. Shaari, "Optimized curing process for perfluorinated acrylic polymer optical waveguide," *Science and Technology of Advanced Materials,* vol. 6, no. 3, pp. 383-387, 2005/04/01/ 2005.

[139]   S. Tsuyoshi, "Fluorinated Polyimide Waveguide Fabricated Using Replication Process with Antisticking Layer," *Japanese Journal of Applied Physics,* vol. 41, no. 3R, p. 1379, 2002.

[140]   Z. Cai *et al.*, "Novel fluorinated polycarbonate negative-type photoresists for thermo-optic waveguide gate switch arrays," *Journal of Materials Chemistry C,* 10.1039/C5TC03657G vol. 4, no. 3, pp. 533-540, 2016.

[141]   H. Shug-June and Y. Hsin Her, "Novel Cyclo Olefin Copolymer Used as Waveguide Film," *Japanese Journal of Applied Physics,* vol. 44, no. 4S, p. 2541, 2005.

[142]   K. Enbutsu, M. Hikita, S. Tomaru, M. Usui, S. Imamura, and T. Maruno, "Multimode optical waveguide fabricated by UV cured epoxy resin for optical interconnection," in *Fifth Asia-Pacific Conference on ... and Fourth Optoelectronics and Communications Conference on Communications*, 1999, vol. 2, pp. 1648-1651 vol.2.

[143]   "High-resolution pattern generation using the epoxy novolak SU-8 2000 resist by electron beam lithography," vol. 21, no. 4, pp. L5-L7, 2003.

[144]   J. Hammacher, A. Fuelle, J. Flaemig, J. Saupe, B. Loechel, and J. J. M. T. Grimm, "Stress engineering and mechanical properties of SU-8-layers for mechanical applications," journal article vol. 14, no. 9, pp. 1515-1523, October 01 2008.

[145]   A. Ane *et al.*, "SU-8-based microneedles for in vitro neural applications," *Journal of Micromechanics and Microengineering,* vol. 20, no. 6, p. 064014, 2010.

[146]   W. Yuli *et al.*, "Surface graft polymerization of SU-8 for bio-MEMS applications," *Journal of Micromechanics and Microengineering,* vol. 17, no. 7, p. 1371, 2007.

[147]   J. H. Lin *et al.*, "Giant Enhancement of Upconversion Fluorescence of NaYF4:Yb3+,Tm3+ Nanocrystals with Resonant Waveguide Grating Substrate," *ACS Photonics,* vol. 2, no. 4, pp. 530-536, 2015/04/15 2015.

[148] S. Blair and Y. Chen, "Resonant-enhanced evanescent-wave fluorescence biosensing with cylindrical optical cavities," *Applied Optics,* vol. 40, no. 4, pp. 570-582, 2001/02/01 2001.

[149] Y. Jiang *et al.*, "Surface Plasmon Enhanced Fluorescence of Dye Molecules on Metal Grating Films," *The Journal of Physical Chemistry C,* vol. 115, no. 25, pp. 12636-12642, 2011/06/30 2011.

[150] A.-H. Jalal, G. Marc Andre, and P. Muthukumaran, "Silicon-free, low-loss and high contrast polymer multimode waveguides," *Journal of Micromechanics and Microengineering,* vol. 27, no. 10, p. 105006, 2017.

[151] H. Kogelnik and V. Ramaswamy, "Scaling Rules for Thin-Film Optical Waveguides," *Applied Optics,* vol. 13, no. 8, pp. 1857-1862, 1974/08/01 1974.

[152] W. Lukosz and R. E. Kunz, "Light emission by magnetic and electric dipoles close to a plane dielectric interface. II. Radiation patterns of perpendicular oriented dipoles," *Journal of the Optical Society of America,* vol. 67, no. 12, pp. 1615-1619, 1977/12/01 1977.

[153] C. K. Carniglia, L. Mandel, and K. H. Drexhage, "Absorption and Emission of Evanescent Photons*," *Journal of the Optical Society of America,* vol. 62, no. 4, pp. 479-486, 1972/04/01 1972.

[154] L. Novotny, "Allowed and forbidden light in near-field optics. I. A single dipolar light source," *Journal of the Optical Society of America A,* vol. 14, no. 1, pp. 91-104, 1997/01/01 1997.

[155] A. K. Wright and M. R. Thompson, "Hydrodynamic structure of bovine serum albumin determined by transient electric birefringence," *Biophysical journal,* vol. 15, no. 2 Pt 1, pp. 137-141, 1975.

[156] D. Marcuse, "Launching light into fiber cores from sources located in the cladding," *Journal of Lightwave Technology,* vol. 6, no. 8, pp. 1273-1279, 1988.

[157] R. Srivastava, C. Bao, and C. Gómez-Reino, "Planar-surface-waveguide evanescent-wave chemical sensors," *Sensors and Actuators A: Physical,* vol. 51, no. 2, pp. 165-171, 1995/11/01/ 1995.

[158] R. Bernini, N. Cennamo, A. Minardo, and L. Zeni, "Planar waveguides for fluorescence-based biosensing: optimization and analysis," *IEEE Sensors Journal,* vol. 6, no. 5, pp. 1218-1226, 2006.

[159] J.-H. Pai *et al.*, "Photoresist with Low Fluorescence for Bioanalytical Applications," *Analytical Chemistry,* vol. 79, no. 22, pp. 8774-8780, 2007/11/01 2007.

[160] R. Walczak, P. Śniadek, and J. Dziuban, *SU-8 photoresist as material of optical passive components integrated with analytical microsystems for real-time polymerase chain reaction*. 2011.

[161] J. W. A. Findlay and R. F. Dillard, "Appropriate calibration curve fitting in ligand binding assays," *The AAPS Journal,* vol. 9, no. 2, pp. E260-E267, 2007.

[162] G. L. Long and J. D. Winefordner, "Limit of Detection A Closer Look at the IUPAC Definition," *Analytical Chemistry,* vol. 55, no. 07, pp. 712A-724A, 1983/06/01 1983.

[163] A. COLLINGS and F. CARUSO, "BIOSENSORS: RECENT ADVANCES," *Reports on Progress in Physics,* vol. 60, no. 11, pp. 1397-1445, 1997.

[164] A. Messica, A. Greenstein, and A. Katzir, "Theory of fiber-optic, evanescent-wave spectroscopy andsensors," *Applied Optics,* vol. 35, no. 13, pp. 2274-2284, 1996/05/01 1996.

[165] F. Warken, E. Vetsch, D. Meschede, M. Sokolowski, and A. Rauschenbeutel, "Ultra-sensitive surface absorption spectroscopy using sub-wavelength diameter optical fibers," *Optics Express,* vol. 15, no. 19, pp. 11952-11958, 2007/09/17 2007.

[166] L. Wang, H. Y. Choi, Y. Jung, B. H. Lee, and K.-T. Kim, "Optical probe based on double-clad optical fiber for fluorescence spectroscopy," *Optics Express,* vol. 15, no. 26, pp. 17681-17689, 2007/12/24 2007.

[167] J. Wang and L. Wang, "An Optical Fiber Sensor for Remote pH Sensing and Imaging," vol. 66, no. 3, pp. 300-303, 2012.

[168] H. Guo, X. Zhou, Y. Zhang, B. Song, J. Zhang, and H. Shi, "Highly sensitive and simultaneous detection of melamine and aflatoxin M1 in milk products by multiplexed planar waveguide fluorescence immunosensor (MPWFI)," *Food Chemistry,* vol. 197, pp. 359-366, 2016/04/15/ 2016.

[169] S. E. McNamee, C. T. Elliott, B. Greer, M. Lochhead, and K. Campbell, "Development of a planar waveguide microarray for the monitoring and early detection of five harmful algal toxins in water and cultures," (in eng), *Environ Sci Technol,* vol. 48, no. 22, pp. 13340-9, Nov 18 2014.

[170] Z. Lai, Y. Wang, N. Allbritton, G. P. Li, and M. Bachman, "Label-free biosensor by protein grating coupler on planar optical waveguides," *Optics Letters,* vol. 33, no. 15, pp. 1735-1737, 2008/08/01 2008.

[171] C. Vannahme, S. Klinkhammer, U. Lemmer, and T. Mappes, "Plastic lab-on-a-chip for fluorescence excitation with integrated organic semiconductor lasers," *Optics Express,* vol. 19, no. 9, pp. 8179-8186, 2011/04/25 2011.

[172] M. Mendez-Astudillo, H. Takahisa, H. Okayama, and H. J. J. J. o. A. P. Nakajima, "Optical refractive index biosensor using evanescently coupled lateral Bragg gratings on silicon-on-insulator," vol. 55, no. 8S3, p. 08RE09, 2016.

[173] S. Dante, D. Duval, B. Sepúlveda, A. B. González-Guerrero, J. R. Sendra, and L. M. Lechuga, "All-optical phase modulation for integrated interferometric biosensors," *Optics Express,* vol. 20, no. 7, pp. 7195-7205, 2012/03/26 2012.

[174] J. Song, L. Chen, and B. Li, "Super-Sensitive Optical Biosensor with a Spectrometer on a Chip," *Biotechnology & Biotechnological Equipment,* vol. 27, no. 4, pp. 4040-4043, 2013/01/01 2013.

[175] L. A. Eldada, "Polymer integrated optics: promise versus practicality," in *Symposium on Integrated Optoelectronic Devices*, 2002, vol. 4642, p. 12: SPIE.

[176] A. Yariv and P. Yeh, *Optical waves in crystals*. Wiley New York, 1984.

[177] D. Marcuse, "Excitation of parabolic-index fibers with incoherent sources," *The Bell System Technical Journal,* vol. 54, no. 9, pp. 1507-1530, 1975.

[178] P. K. Tien, "Light Waves in Thin Films and Integrated Optics," *Applied Optics,* vol. 10, no. 11, pp. 2395-2413, 1971/11/01 1971.

[179] K. Okamoto, *Fundamentals of Optical Waveguides*. 2006.

[180] J. Abdul-Hadi, M. A. Gauthier, and M. Packirisamy, "Polymer on quartz waveguide sensing platform for enhanced evanescent fluorescence spectroscopy," *IEEE Photonics Journal,* pp. 1-1, 2018.

[181] X. Fan and I. M. White, "Optofluidic microsystems for chemical and biological analysis," *Nature Photonics,* Review Article vol. 5, p. 591, 09/18/online 2011.

[182] D. Erickson, S. Mandal, A. H. J. Yang, B. J. M. Cordovez, and Nanofluidics, "Nanobiosensors: optofluidic, electrical and mechanical approaches to biomolecular detection at the nanoscale," journal article vol. 4, no. 1, pp. 33-52, January 01 2008.

[183] J. Dostálek and W. J. B. Knoll, "Biosensors based on surface plasmon-enhanced fluorescence spectroscopy (Review)," journal article vol. 3, no. 3, pp. FD12-FD22, September 01 2008.

[184] M. A. Cooper, "Optical biosensors: where next and how soon?," (in eng), *Drug Discov Today,* vol. 11, no. 23-24, pp. 1061-7, Dec 2006.

[185] T. J. C. S. Hirschfeld, "Total reflection fluorescence," vol. 10, no. 5, p. 128, 1965.

[186] D. Tosi, S. Poeggel, I. Iordachita, and E. Schena, "11 - Fiber Optic Sensors for Biomedical Applications," in *Opto-Mechanical Fiber Optic Sensors*, H. Alemohammad, Ed.: Butterworth-Heinemann, 2018, pp. 301-333.

[187] Y. Shao, S. Xu, X. Zheng, Y. Wang, and W. Xu, "Optical Fiber LSPR Biosensor Prepared by Gold Nanoparticle Assembly on Polyelectrolyte Multilayer," *Sensors (Basel, Switzerland),* vol. 10, no. 4, pp. 3585-3596, 2010.

[188] S. C. Warren-Smith, H. Ebendorff-Heidepriem, T. C. Foo, R. Moore, C. Davis, and T. M. Monro, "Exposed-core microstructured optical fibers for real-time fluorescence sensing," *Optics Express,* vol. 17, no. 21, pp. 18533-18542, 2009/10/12 2009.

[189] Z. Li, Y. Xu, W. Fang, L. Tong, and L. Zhang, "Ultra-Sensitive Nanofiber Fluorescence Detection in a Microfluidic Chip," vol. 15, no. 3, p. 4890, 2015.

[190] S.-H. Hong *et al.*, "Implementation of surface plasmon resonance planar waveguide sensor system," *Microelectronic Engineering,* vol. 87, no. 5, pp. 1315-1318, 2010/05/01/ 2010.

[191] L. Shang, C. Liu, B. Chen, and K. J. A. s. Hayashi, "Plant biomarker recognition by molecular imprinting based LSPR sensor array: Performance improvement by enhanced hotspot of Au nanostructure," 2018.

[192] J. Malicka, I. Gryczynski, Z. Gryczynski, and J. R. Lakowicz, "Use of Surface Plasmon-Coupled Emission to Measure DNA Hybridization," *Journal of biomolecular screening,* vol. 9, no. 3, pp. 208-215, 2004.

[193] R. Horváth, H. C. Pedersen, N. Skivesen, D. Selmeczi, and N. B. Larsen, "Optical waveguide sensor for on-line monitoring of bacteria," *Optics Letters,* vol. 28, no. 14, pp. 1233-1235, 2003/07/15 2003.

[194] H. Guo *et al.*, "Highly sensitive and rapid detection of melamine in milk products by planar waveguide fluorescence immunosensor (PWFI)," *Sensors and Actuators B: Chemical,* vol. 194, pp. 114-119, 2014/04/01/ 2014.

[195] K. Cottier, M. Wiki, G. Voirin, H. Gao, and R. E. Kunz, "Label-free highly sensitive detection of (small) molecules by wavelength interrogation of integrated optical chips," *Sensors and Actuators B: Chemical,* vol. 91, no. 1, pp. 241-251, 2003/06/01/ 2003.

[196] J. Song *et al.*, "Electrical tracing-assisted dual-microring label‑free optical bio/chemical sensors," *Optics Express,* vol. 20, no. 4, pp. 4189-4197, 2012/02/13 2012.

[197] S. Sahu, J. Ali, P. Yupapin, and G. Singh, *Porous Silicon Based Bragg-Grating Resonator for Refractive Index Biosensor.* 2018.

[198] K. Uchiyamada, K. Okubo, M. Yokokawa, E. T. Carlen, K. Asakawa, and H. Suzuki, "Micron scale directional coupler as a transducer for biochemical sensing," *Optics Express,* vol. 23, no. 13, pp. 17156-17168, 2015/06/29 2015.

[199] J. H. Pai *et al.*, "Photoresist with low fluorescence for bioanalytical applications," (in eng), *Anal Chem,* vol. 79, no. 22, pp. 8774-80, Nov 15 2007.

[200] F. Long, M. He, A. N. Zhu, and H. C. Shi, "Portable optical immunosensor for highly sensitive detection of microcystin-LR in water samples," *Biosensors and Bioelectronics,* vol. 24, no. 8, pp. 2346-2351, 2009/04/15/ 2009.

[201] P. K. Tien, "Light waves in thin films and integrated optics," (in eng), *Appl Opt,* vol. 10, no. 11, pp. 2395-413, Nov 1 1971.

[202] P. Damborský, J. Švitel, and J. Katrlík, "Optical biosensors," *Essays in Biochemistry,* vol. 60, no. 1, pp. 91-100, 06/30 2016.

[203] C. R. Taitt and S. H. North, "17 - Total internal reflection fluorescence (TIRF) array biosensors for biothreat agents for food safety and food defense," in *High Throughput Screening for Food Safety Assessment*, A. K. Bhunia, M. S. Kim, and C. R. Taitt, Eds.: Woodhead Publishing, 2015, pp. 399-424.

[204] J. S. Yuk, E. F. Guignon, and M. A. Lynes, "Sensitivity enhancement of a grating-based surface plasmon-coupled emission (SPCE) biosensor chip using gold thickness," *Chemical Physics Letters,* vol. 591, pp. 5-9, 2014/01/20/ 2014.

[205] E. Ryckeboer, R. Bockstaele, M. Vanslembrouck, and R. Baets, "Glucose sensing by waveguide-based absorption spectroscopy on a silicon chip," *Biomedical Optics Express,* vol. 5, no. 5, pp. 1636-1648, 2014/05/01 2014.

[206] C. E. Hei *et al.*, "Remote Biosensing with Polychromatic Optical Waveguide Using Blue Light-Emitting Organic Nanowires Hybridized with Quantum Dots," *Advanced Functional Materials,* vol. 24, no. 24, pp. 3684-3691, 2014.

[207] P. Michael, S. Eginhard, B. M. A., S. M. J., O. Peter, and E. Markus, "Zeptosens' protein microarrays: A novel high performance microarray platform for low abundance protein analysis," *PROTEOMICS,* vol. 2, no. 4, pp. 383-393, 2002.

[208] K. E. Sapsford *et al.*, "Fluorescence-based array biosensors for detection of biohazards," (in eng), *J Appl Microbiol,* vol. 96, no. 1, pp. 47-58, 2004.

[209] L. Hong, H. Li, H. Yang, and K. Sengupta, "Fully Integrated Fluorescence Biosensors On-Chip Employing Multi-Functional Nanoplasmonic Optical Structures in CMOS."

[210] J. F. Li, C. Y. Li, and R. F. Aroca, "Plasmon-enhanced fluorescence spectroscopy," (in eng), *Chem Soc Rev,* vol. 46, no. 13, pp. 3962-3979, Jul 3 2017.

[211] H. P. Kao and J. S. Schoeniger, "Hollow cylindrical waveguides for use as evanescent fluorescence-based sensors: effect of numerical aperture on collected signal," *Applied Optics,* vol. 36, no. 31, pp. 8199-8205, 1997/11/01 1997.

[212] K. Tawa, T. Nakayama, and K. Kintaka, "Optimal Structure of a Plasmonic Chip for Sensitive Bio-Detection with the Grating-Coupled Surface Plasmon-Field Enhanced Fluorescence (GC-SPF)," (in eng), *Materials (Basel),* vol. 10, no. 9, Sep 11 2017.

[213] Y. Zhang *et al.*, "A compact and low loss Y-junction for submicron silicon waveguide," *Optics Express,* vol. 21, no. 1, pp. 1310-1316, 2013/01/14 2013.

[214] P. Wang, G. Brambilla, Y. Semenova, Q. Wu, and G. Farrell, *Design of an extra-low-loss broadband Y-branch waveguide splitter based on a tapered MMI structure*. 2011.

[215] S. Safavi-Naeini, Y. L. Chow, S. K. Chaudhuri, and A. Goss, "Wide angle phase-corrected Y-junction of dielectric waveguides for low loss applications," *Journal of Lightwave Technology,* vol. 11, no. 4, pp. 567-576, 1993.

[216] S. Banba and H. Ogawa, "Novel symmetrical three-branch optical waveguide with equal power division," *IEEE Microwave and Guided Wave Letters,* vol. 2, no. 5, pp. 188-190, 1992.

[217] T. Yabu, M. Geshiro, N. Minimi, and S. Sawa, "Symmetric three-branch optical power divider with a coupling cap," *Journal of Lightwave Technology,* vol. 17, no. 9, pp. 1693-1699, 1999.

[218] H. B. Lin, Y. H. Wang, and W. S. Wang, *Singlemode 1×3 integrated optical branching circuit design using microprism*. 1994, pp. 408-409.

[219] T. Wang, C.-F. Huang, and W.-S. Wang, *Wide-angle 1 x 3 optical power divider in LiNbO3 for variable power splitting*. 2003, pp. 1401-1403.

[220] L. B. Soldano and E. C. M. Pennings, "Optical multi-mode interference devices based on self-imaging: principles and applications," *Journal of Lightwave Technology,* vol. 13, no. 4, pp. 615-627, 1995.

[221] P. Qiu *et al.*, "Ultra-compact tunable graphene-based plasmonic multimode interference power splitter in mid infrared frequencies," *Science China Information Sciences,* vol. 60, no. 8, p. 082402, 2017.

[222] V. Prajzler, R. Maštera, and V. Jeřábek, *Large Core Planar 1 x 2 Optical Power Splitter with Acrylate and Epoxy Resin Waveguides on Polydimetylsiloxane Substrate*. 2014, pp. 488-495.

[223] V. Prajzler, R. Mastera, and J. Spirkova, *Large Core Three Branch Polymer Power Splitters*. 2015, pp. 885-891.